AN ARRAY OF DIRECTIONAL SENSORS (CARDIOID SENSORS OR FIGURE-8 SENSORS), DIVERSELY ORIENTATED BUT SPATIALLY COLLOCATED – THEIR BEAM-PATTERNS

CHIBUZO JOSEPH NNONYELU

PhD

The Hong Kong Polytechnic University

2018

The Hong Kong Polytechnic University
Department of Electronic and Information Engineering

An Array of Directional Sensors (Cardioid Sensors or Figure-8 Sensors), Diversely Orientated but Spatially Collocated – Their Beam-Patterns

Chibuzo Joseph NNONYELU

A thesis submitted in partial fulfilment of the requirements for the degree of Doctor of Philosophy

January, 2018

CERTIFICATE OF ORIGINALITY

I hereby declare that this thesis is my own work and that, to the best of my knowledge and belief, it reproduces no material previously published or written, nor material that has been accepted for the award of any other degree or diploma, except where due acknowledgment has been made in the text.

____ (Signed)

Chibuzo Joseph NNONYELU (Name of student)

Abstracts

This dissertation contains four related investigations:

1. A Triad of Cardioid Sensors in Orthogonal Orientation and Spatial Collocation – Its Spatial-Matched-Filter-Type Beam-Pattern:

   This work proposes a new configuration of acoustic sensors – three cardioid sensors in perpendicular orientation and spatial collocation, in order to increase the mainlobe-to-sidelobe height ratio (possibly to ∞). This study will analyze such a proposed triad's "spatial matched filter" beam-pattern that is independent of the frequency/spectrum of the incident signal. Specifically, this investigation will analytically derive (i) the mainlobe's pointing error in azimuth-elevation, (ii) the mainlobe's two-dimensional beam "width", (iii) the necessary and sufficient conditions for any sidelobe to exist, (iv) the mainlobe-to-sidelobe height ratio, and (v) the array gain. These above characteristics depend on the cardioids' "cardiodicity parameter" and on the beam's nominal "look direction". This work is first in the open literature to propose and to investigate a collocated triad of orthogonally oriented cardioids. The findings show that the proposed cardioid triad can have higher mainlobe-to-sidelobe height ratio and can avoid sidelobes altogether. Its physical compactness makes it portable for mobile deployment, indoor or outdoor. This work has been published in the *IEEE Transaction on Signal Processing* (authors include the candidate, his chief supervisor and another collaborator).

2. Cardioid Microphones/Hydrophones in a Collocated and Orthogonal Triad – A New Beamformer with No Beam-Pointing Error:

   Cardioid sensors offer low sidelobes/backlobes, compared to bi-directional sensors (like velocity-sensors). Three cardioid sensors, in orthogonal orientation and in spatial collocation, have recently been proposed in Chapter 1; and such a cardioid-triad's "spatial matched filter" beam-pattern has been analyzed therein. That beam-pattern, unfortunately, suffers pointing error, i.e. the spatial beam's actual peak direction deviates from the nominal "look direction". Instead, this study will propose a new beamformer for the abovementioned cardioidic triad to avoid beam-pointing error. Also analytically derived here is this beam-pattern's lobes' height ratio, beamwidth, directivity, and array gain. This work is under review by the *Journal of the Acoustical Society of America* (authors include the candidate, his chief supervisor and another collaborator).

3. Two Higher-Order Figure-8 Sensors in Spatial Collocation — Their "Spatial Matched Filter" Beam-Pattern:

   Higher-order figure-8 sensors have relatively high directivity and are sorted after due to this feature. Collocating directional sensor can be advantageous due to its spatial compactness and the frequency-independence of its array manifold. In this work, the "spatial matched filter" (SMF) beam-pattern of such collocated pair will be analytically studied. Due to real-world manufacturing imperfections, such pair of collocated higher-order figure-8 sensors may not be orthogonal. This work will also investigate how the non-orthogonal orientation affects the beam-pattern pointing assuming the beamformer has no knowledge of the imperfection. It is shown that non-perpendicularity would affect both the overall shape and introduce pointing bias in the spatial-matched-type beampattern of the two collocated higher-order figure-8 sensors. More importantly, this work relates the beamformer's look direction, array's skewed angle and sensor's order to the mis-pointing.

4. Directional Pointing Error in "Spatial Matched Filter" Beamforming at a Tri-Axial Velocity-Sensor due to Non-Orthogonal Axes:

   The "tri-axial velocity-sensor" has three axes that are nominally perpendicular, but may be non-perpendicular in practice, due to real-world imperfections in manufacturing or wear during operations. This work comprehensively investigates how such non-perpendicularity would affect the tri-axial velocity-sensor's azimuth-elevation beam-pattern in terms of the beam's pointing direction. Closed form expressions were developed for the pointing bias which can be used in offsetting the pointing bias introduced by the non-perpendicularity among the constituent velocity-sensors. This work was presented at the *175th Meeting of the Acoustical Society of America* in Minneapolis, Minnesota on May 7, 2018.

Publications

Journal Papers (published / under peer-review)

1. K. T. Wong, **C. J. Nnonyelu**, and Y. I. Wu, "A triad of cardioid sensors in orthogonal orientation and spatial collocation - its spatial-matched-filter-type beam-pattern," *IEEE Transactions on Signal Processing,* vol. 66, no. 4, pp. 895-906, February 2018.

2. Y. I. Wu, **C. J. Nnonyelu**, and K. T. Wong, "Cardioid microphones/hydrophones in a collocated/orthogonal triad - a new beamformer with no beam-pointing error", under review by the *Journal of the Acoustical Society of America.*

3. **C. J. Nnonyelu**, C. H. Lee, and K. T. Wong, "Two higher-order figure-8 sensors in spatial Collocation – their spatial matched filter Beam-Pattern", under preparation for submission to a peer-reviewed journal.

Conference Presentations

1. **C. J. Nnonyelu** , C. H. Lee, and K. T. Wong, "An array of two biaxial velocity-sensors of non-identical orientation – Their 'spatial matched filter' beam-pattern's pointing error", *Journal of Acoustical Society of America,* vol. 141, no. 5, pp. 3652, June 2017.

2. **C. J. Nnonyelu**, C. H. Lee, and K. T. Wong, "Directional pointing error in "spatial matched filter" beamforming at a tri-axial velocity-sensor with non-orthogonal axes", presented at the *175th Meeting of the Acoustical Society of America* in Minneapolis, May 2018.

Acknowledgments

I will remain forever grateful to:

1. **Dr. Kainam Thomas Wong** (my Chief Supervisor) - For his unquantifiable professional guidance and commitment in supervising me. For dedicating his limited time in defining the investigation, doing a comprehensive literature search, reviewing, and revising my works. I have learnt a lot from him and can never thank him enough for the opportunity.

2. **Prof. Charles Hung Lee** and **Prof. Yue Ivan Wu** - For dedicating their time assisting mathematical derivations in this thesis. Their contributions greatly helped these investigations.

3. **The Hong Kong Polytechnic University** - For providing me the financial support in the form of a studentship, a conducive learning environment and adequate resources, which enabled me to carry out my research smoothly.

4. My parents **Mr. Christian A. Nnonyelu** and **Mrs. Monica N. Nnonyelu**, my siblings, and close friends for the emotional support I received from them during my study period.

Table of Contents

List of Figures

Description of Variables and Acronyms

Variables / Acronyms	Descriptions
α	Cardioidicity index
θ	Direction of arrival's polar angle
ϕ	Direction of arrival's azimuth angle
θ_{peak}	Polar angle of the beampattern's peak
ϕ_{peak}	Azimuth angle of the beampattern's peak
θ_{look}	Beamformer's look direction's polar angle
ϕ_{look}	Beamformer's look direction's azimuth angle
$\tilde{\phi}$	Mis-orientation angle
θ_x	Mis-orientation in polar direction of the x-axis
θ_y	Mis-orientation in polar direction of the y-axis
θ_z	Mis-orientation in polar direction of the z-axis
ϕ_x	Mis-orientation in azimuthal direction of the x-axis
ϕ_y	Mis-orientation in azimuthal direction of the y-axis
ϕ_z	Mis-orientation in azimuthal direction of the z-axis
u	Direction cosine in the x axis direction
v	Direction cosine in the y axis direction
w	Direction cosine in the z axis direction
u_{look}	Beamformer's direction cosine in the x axis direction
v_{look}	Beamformer's direction cosine in the y axis direction
w_{look}	Beamformer's direction cosine in the z axis direction
B	The Beamformer's output
h_{peak}	Mainlobe's height
h_{side}	Sidelobe's height
HR	Mainlobe-to-sidelobe height ratio
BW	Half-power beamwidth
G	Array gain
G_{SNIR}	Array gain with the presence of an interference signal
D	Directivity
SNR	Signal-to-noise ratio
SNIR	Signal-to-noise-plus-interference ratio
k	Sensor order
$B^{(3+0)}$	Beampattern of tri-axial velocity sensor with no pressure sensor
$B^{(3+1)}$	Beampattern of tri-axial velocity sensor with collocated pressure sensor
$\mathbf{R}_x$	Rotation matrix with x axis as reference axis
$\mathbf{R}_y$	Rotation matrix with y axis as reference axis
$\mathbf{R}_z$	Rotation matrix with z axis as reference axis
$\mathbf{R}_2$	Rotation matrix for a tri-axial velocity sensor with a collocated pressure sensor
κ	The output of the pressure sensor in the $(3+1)$ array

Chapter 1
Introduction

1.1 Overview

A sensor array samples an incident wave field at different locations in space. The data thus obtained contain information on source's direction of arrival, phase, and frequency. Omnidirectional sensors can be placed in such array, which can provide azimuth-elevation directivity, but occupies a sizeable spatial region and whose array manifold varies with frequency. In contrast, an array of spatially collocated directional sensors can be frequency independent hence computationally simpler.

The idea of collocating directional sensors is not new, but there has been no detailed study on the performance of collocated cardioid sensors. Cardioid sensors are directional sensors which offer more directivity than figure-8 sensors. This thesis will present a comprehensive study of the beamforming performance of collocated and orthogonal cardioid sensors in terms of its pointing bias, half-power beamwidth, directivity, array gain, and mainlobe-to-sidelobe height ratio. This thesis will also present analytical studies on the beamforming performance of collocated first-order and higher-order figure-8 sensors that are not orthogonal due to manufacturing imperfection in order to show how this imperfection affects the beam's pointing bias.

1.2 General Assumptions

In this work, except otherwise stated, the following general simplifying assumptions have been made on the array, on the incident wave, and on the medium of propagation in all mathematical derivations.

Assumptions made on the array

1. *Collocation:* More than one sensor cannot be placed exactly at one point in space. Rather, the collocation is approximately realized such that the inter-sensor spacings are negligible relative to the signal wavelength to be measured. Therefore, the collocated sensor array is assumed to be a point.

2. *Orthogonality*: Perfect orthogonality is assumed between sensors in orthogonal orientation.

Assumptions made on the source and medium of propagation

1. *Homogeneity*: The medium of propagation is assumed to be homogeneous, quiescent, isotropic fluid which implies a direct propagation path.

2. *Far-field source*: The source is assumed to be far-field. The far field assumption implies the distance between the source and point of measurement is far greater than the physical dimension of the source and the array.

1.3 First-Order Cardioid Family of Microphones

The response of a cardioid microphone is given as [1][2]

$$a^{(\alpha)}(\varphi) \quad = \quad \alpha + (1-\alpha)\cos\varphi, \tag{1.3.1}$$

where $\varphi \in [0, 2\pi)$ is the angle between the incident sound wave and axis of the sensor, and $\alpha \in (0, 1)$ the *cardiodicity index*. *Cardioidicity Index* α is dimensionless where $\alpha = {}^{\tau}/_{(\tau + {}^{d}/_{c})}$ is the ratio of the front and back delay [2] where d is the separation distance between the two omnidirectional microphones, τ is the electrically(or physically)-added time-delay between the outputs of the two omnidirectional microphones, and c is the sound propagation speed in the medium. The detailed derivation of the response of a cardioid microphone is found in (Section 5.1 [2]).

There are typical values chosen for α in commercially available cardioid microphones. For the cardioid microphone response (1.3.1), maximum directivity occurs at $\alpha = 0.25$. This design is known as the *hypercardioid* pattern. Its pattern has two nulls located at $\varphi = \pm 110°$. The hypercardioid pattern provides the greatest rejection in a reverberant field, relative to main-axis pickup, of reverberant sounds arriving from random directions. This makes it the best choice for speech pickup in sound reinforcement systems.

Highest front-to-back ratio occurs at $\alpha = \frac{1}{2}(\sqrt{3} - 1)$. This design is known as the *supercardioid* microphone and has two nulls located at $\varphi = \pm 126°$. This is most desired for wide frontal angle pickup applications.

At $\alpha = 0.5$, the cardioid has a front-to-back ratio of infinity as its null occurs at $\varphi = 180°$. This design is known as the standard cardioid microphone and finds application where a complete rejection of sounds arriving from behind is unwanted such as in live performance to cancel out crowd noise.

The *subcardioid* microphones are designed with $\alpha = 0.7$. This design has the highest half-power beamwidth across α and has no null. It is sometimes loosely referred to as "forward-oriented omni" and useful for large scale scoring work. More details on the performance of unit cardioid family can be found in [1][2](Chapter 4 of [3]). Figure 1.1 shows the response of these various types of the cardioid sensors in polar coordinates.

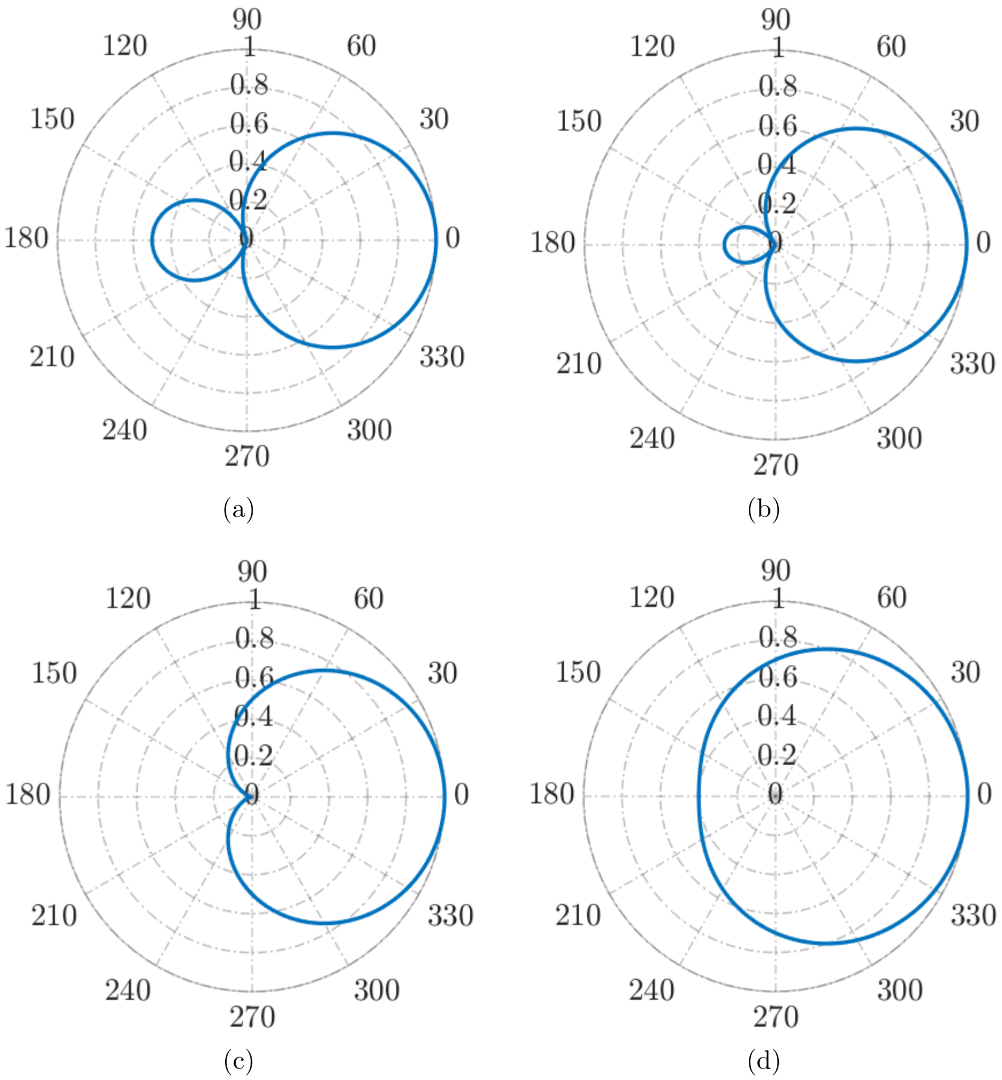

Figure 1.1: Polar plots of the far-field response of the (a) Hypercardioid $\alpha = 0.25$, (b) Supercardioid $\alpha \approx 0.37$, (c) Standard cardioid $\alpha = 0.5$, and (d) Subcardioid $\alpha = 0.7$ microphones showing their nulls and backlobe where they apply.

1.4 Higher-Order Figure-8 Microphones

The kth-order higher-order figure-8 microphone has gain response that corresponds to the kth order of the gradient of the sound pressure. The response of the kth order figure-8 sensor [4]

$$a_k = \cos^k(\psi), \tag{1.4.1}$$

where $k \in \mathcal{Z}^+$ a positive integer is the order of the microphone, and $\psi \in [0, 2\pi)$ is the angle between the incident sound wave and the axis of the sensor. Higher-order figure-8 sensors exhibit higher directionality with increasing order k which makes them desirable for application where high directivity is desired [4].

For studies on the beam-patterns and directivity index of higher-order directional sensors, refer to [5–8, 10–13]. For an application of such higher order figure-8 microphones, [9] proposed a closed-form direction of arrival estimation algorithm using higher-order sensors that are in spatial collocation and orthogonal orientation. So far, no comprehensive study has been carried out on the spatial-matched-filter type beam-pattern of such collocated higher-order sensor. Chapter 4 will analytically study the behaviour of two collocated higher-order figure-8 sensors.

1.5 Spatial-Matched-Filter Beamformer

The spatial-matched-filter beamformer is a data-independent beamformer, whereby the beamforming weights are directed to the look direction steering vector [14–18]. The output of a spatial-matched-filter beamformer,

$$B \quad = \quad \mathbf{a}(\boldsymbol{\xi}_{\text{look}})^H \, \mathbf{a}(\boldsymbol{\xi}) \tag{1.5.1}$$

where $\mathbf{a}(\boldsymbol{\xi})$ is the array manifold, $\mathbf{a}(\boldsymbol{\xi}_{\text{look}})$ is a vector of the weights for the spatial-matched-filter beamformer, $\boldsymbol{\xi}$ is the vector of parameters of the array manifold (for instance polar angle θ, azimuth angle ϕ as shown in Figure 1.2), and $\boldsymbol{\xi}_{\text{look}}$ contains the parameters of the look direction.

The maximum response of the spatial-matched-filter typically occurs when the direction of arrival matches the beamformer's look direction for an array of isotropic sensors. However, pointing bias could occur for directional sensors, e.g. in Chapter 2. The spatial-matched-filter beamformer has been applied in collocated sensor arrays such as the biaxial velocity sensor [17, 18], triaxial velocity sensors [16, 18], triaxial velocity sensor with collocated pressure sensor [18]. The effect of non-orthogonality of the axes for the biaxial first-order velocity sensor on the spatial-matched-filter beamformer has been studied in [17], which shows that the beampattern shape is unaffected by the nonorthogonality, but the peak direction is. Chapter 4 will extend this study to higher-order figure-8 sensor while Chapter 5 extends the study to a first-order figure-8 collocated triad.

1.6 Organization of the Thesis

This thesis consists of 5 main chapters, that is Chapters 1-5. Chapter 1 gives a brief overview of the first-order cardioid family of microphones, the higher-order figure-8 sensors,

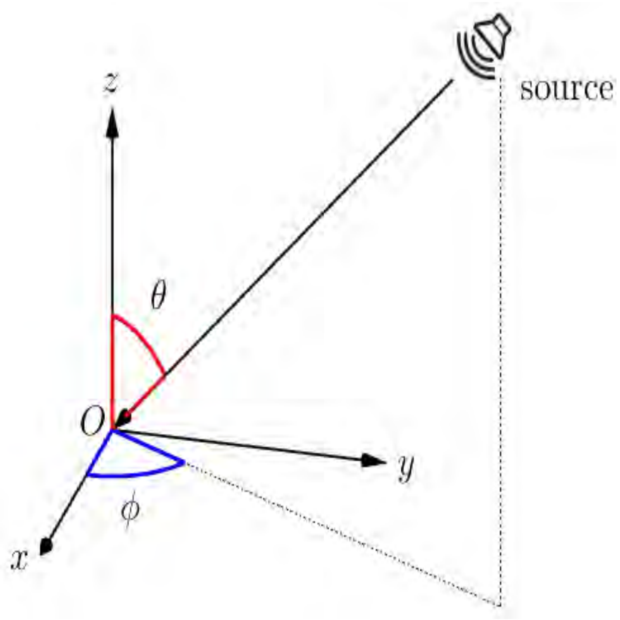

Figure 1.2: The Cartesian coordinates showing the polar angle (measured from the positive z-axis) and azimuth angle (measured from the positive x-axis) of arrival.

and spatial-matched-filter beamforming.

Chapters 2 - 3 are studies based on the first-order cardioid family of microphones while Chapters 4 - 5 are studies based on the first-order and higher-order figure-8 microphones.

Chapter 2 proposes the collocation of three first-order cardioid family of microphones that are arranged in orthogonal orientation. This spatial arrangement produces an array manifold that is independent on the incident sound wavelength. The spatial-matched-filter type beampattern of this array is analytically studied in terms of the location of the mainlobe, the presence of a sidelobe, the mainlobe-to-sidelobe height ratio, half-power beamwidth and the overall array gain. This work is the first in the open literature to propose and analytically study such array of first-order cardioid family of microphones.

Chapter 3 proposes a new beamformer to cancel the pointing bias in the spatial-matched-filter beampattern of the cardioid triad proposed in Chapter 2. The performance of this beamformer in terms of the location of its mainlobe and sidelobes, height ratio, beamwidth, directivity and overall array gain is compared to that of the spatial-matched-filter studied in Chapter 2.

Chapter 4 proposes the spatial collocation of two higher-order figure-8 sensors. The sensors in the array may not be perfectly perpendicular due to manufacturing defects. In this chapter, such arrangement is studied in terms of the pointing bias in the spatial-matched-filter beampattern.

Chapter 5 analytically studies the effect of non-orthogonality defect in collocated first order figure-8 sensors assuming the spatial-matched-filter beamformer is unaware of this non-orthogonality between the legs of the triad. The study is extended to the a tri-axial figure-8 sensor with a collocated pressure sensor. Closed form pointing bias due to the mis-orientation are derived in this work.

Finally, general conclusion based on the works presented in Chapters 2 - 5 is made in Chapter 6.

Chapter 2
A Triad of Cardioid Sensors in Orthogonal Orientation and Spatial Collocation – Its Spatial-Matched-Filter-Type Beam-Pattern

[1]

2.1 Overview

Microphones and hydrophones encounter acoustic signals that are often ultra-wideband: An acoustic signal's highest frequency is often many orders-of-magnitude above the lowest frequency (not just multiples of difference, but many orders-of-magnitude). For example, the human hearing range spans three orders-of-magnitude from 20Hz to $20,000$Hz. Hence, electronic audio signals and soundscape measurements would also need to accommodate such ultra-wide spectra. This is not to mention non-human-based acoustic sensing in military applications, where infrasound can reach down to only a few Hz but sniper shockwaves can reach above $40,000$Hz.

The acoustic signal's ultra-wide spectrum greatly complicates signal processing at an array of sensors that are spatially displaced among themselves, as the corresponding array manifold varies nonlinearly with frequency. This frequency-dependence arises from the physical displacements between sensors, which mathematically leads to "inter-sensor spatial phase factors", which are frequency-dependent. That is, an incident signal's different sub-bands would experience fundamentally different levels of directivity and sensitivity. Such complicating distortions must then be mitigated with additional signal processing, which could be computationally expensive but effective only partially.

These bothersome "spatial phase factors" could be avoided altogether, by collocating an array of directional sensors, each oriented differently to attain azimuth-elevation directivity. Mathematically, this would mean a frequency-*in*dependent array manifold.

Concerning this idea of collecting three orthogonally oriented directional sensors, it has been realized in the "acoustic vector sensor" [22], also known as a "vector hydrophone [23], or a "gradient sensor", or a "velocity-sensor triad", or a "tri-axial velocity-sensor".

[1] A large portion of this chapter is taken from [21], which is authored by the candidate, his chief supervisor, and one other coauthor.

There, the three directional sensors are first-order particle-velocity sensors. Such a tri-axial velocity-sensor has already been implemented for underwater/sea-surface acoustical applications (as the " Swallow float" [24, 25], as the "DIrectional Frequency Analysis and Recording" (DIFAR) sensor [26], as the "Perforated-ball Velocity Meter" (PVM) [27], as the "Augmented Reliable Acoustic Path" (ARAP) array [28], and in [29]), as well as for aero-acoustical applications (as the Microflown [30, 31], and in [32, 33]). For detailed literature surveys of the tri-axial velocity-sensor's hardware implementations and sea/air trials, please see [34–36]. For a literature survey of the tri-axial velocity-sensor's directivity and beam-pattern, please see [37]. This tri-axial velocity-sensor will be shown below to represent a special case of the cardioid triad to be investigated in this chapter.

2.1.1 The High Directionality of a Cardioid Sensor

One major shortcoming of the abovementioned tri-axial velocity-sensor is its flat gain-pattern [18]. Highly directive microphones are useful, especially for enhanced "random efficiency" or "reach" (i.e., for improved suppression of background noises/interference off-axis) and for a farther "distance factor" (i.e., the spatial reach of the microphone on-axis).

Among directional acoustical sensors, cardioid sensors are one of the most practical microphones/hydrophones in wide scientific and professional use. While dating back to at least the 1930s [38–40], cardioid microphones are commercially available as diverse models from various companies, including AKG 414, C519M, SE300B; Audio-Technica 42, 2020, 4033, 4050; Behringer B-2 PRO; CAD Audio GXL1200BP; Core Sound Stealthy Cardioid; DPA Microphones d:screet mini 4080;, Marshall Electronics MXL 770; Røde Microphones NT4; Sennheiser Evolution 914, 935; Shure BETA 98A, SM58; and SoundField MKV Microphone. The SoundField Microphone is a tetrahedral array of four closely spaced subcardioid or cardioid microphones, in contrast to this study's three collocated cardioids of any cardioidicity index and of orthogonal orientation.

The "cardioid" sensor obtains its name from the heart-like shape of its gain response. Mathematically, the "cardioid" gain response (see chapter 5 of [1]) equals $\alpha + (1-\alpha)\cos(\beta)$, where $\beta \in [0, \pi]$ denotes the spatial angle measured with respect to the cardioid sensor's axis. The "cardiodicity index" $\alpha \in [0, 1]$ controls the cardioid's directivity:

a) At $\alpha = 1$, an isotropic sensor results.

b) At $\alpha = 0.7$, a "subcardioid" is obtained.

c) At $\alpha = \frac{1}{2}$, it is labeled the "standard cardioid"; and this is the commonest directional pattern used in professional acoustic studios, due to its capability to suppress sound incident at the rear of the microphone.

d) At $\alpha = \frac{\sqrt{3}-1}{2} \approx 0.366025 \approx 0.37$, From equation (2.96) on page 44 of [2], $\alpha = \frac{1}{2}(\sqrt{3}-1)$ for the "supercardioid". All subsequent supercardioid plots will use this precise value.

However, many authors (such as [1] at equation (5.5) therein) uses an approximate value of $\alpha = 0.37$. the resulting "supercardioid" maximizes the frontal pick-up as a fraction of the total pickup, hence a wide frontal angular sector. It also maximizes the front-to-back ratio The front-to-back ratio is the ratio of the sensor's sensitivity to a sound wave approaching its front over that approaching its rear. .

e) At $\alpha = \frac{1}{4}$, the resulting "hypercardioid" maximizes the random efficiency in the forward direction among all first-order cardioids, thereby most effective in suppressing reverberant sounds relative to the on-axis pickup.

f) At $\alpha = 0$, a uni-axial velocity-sensor is obtained [22]. This has a "figure-8" gain pattern, where the front main lobe and the back lobe are of equal height.

2.1.2 A Triad of Cardioids in Orthogonal Orientation and in Spatial Collocation

Collocate three cardioid sensors at the origin of the Cartesian coordinates[2], and orient one each along the positive x-, y-, and z-axis.

This triad has a 3×1 array manifold of

$$\mathbf{a}^{(\alpha)}(\theta, \phi) = \begin{bmatrix} \alpha + (1-\alpha)\sin(\theta)\cos(\phi) \\ \alpha + (1-\alpha)\sin(\theta)\sin(\phi) \\ \alpha + (1-\alpha)\cos(\theta) \end{bmatrix}, \tag{2.1.1}$$

where $\theta \in [0, \pi]$ represents the polar angle of the incident acoustic wave, and $\phi \in [0, 2\pi)$ refers to the corresponding azimuth angle. At $\alpha = 0$, the above degenerates to a tri-axial velocity-sensor.

The above array manifold is *in*dependent of frequency. That is, the spatial collocation decouples the frequency dimension from the azimuth-elevation dimensions.

This idea of *collocating* diversely oriented cardioids seems to be new to the open literature, to the present authors' best knowledge.

To ease subsequent discussion, re-express (2.1.1) in terms of the Cartesian direction cosines of $u := \sin(\theta)\cos(\phi), v := \sin(\theta)\sin(\phi), w := \cos(\theta)$, such that (2.1.1) may be rewritten as

$$\mathbf{a}^{(\alpha)}(u, v, w) := \begin{bmatrix} u^{(\alpha)} \\ v^{(\alpha)} \\ w^{(\alpha)} \end{bmatrix} := \begin{bmatrix} \alpha + (1-\alpha)u \\ \alpha + (1-\alpha)v \\ \alpha + (1-\alpha)w \end{bmatrix}. \tag{2.1.2}$$

[2] The three cardioid sensors cannot occupy the same physical space, though they would effectively be collocated, relative to the wavelength of most acoustic signals. Nonetheless, please refer to [41] to explore how to correct for this inexact collocation.

Note that $u^2 + v^2 + w^2 = 1, \forall\theta, \forall\phi$; however,

$$\left(u^{(\alpha)}\right)^2 + \left(v^{(\alpha)}\right)^2 + \left(w^{(\alpha)}\right)^2 \neq 1,$$

in general for any $\alpha > 0$.

2.1.3 The Cardioid Triad's Beam-Pattern

One simple data-independent beamformer – the well known "spatial matched filter" beamformer – would set the beamforming weight vector $\mathbf{w}$ to match the steering vector pointing toward the nominal polar/azimuth "look direction" of $(\theta_{\text{look}}, \phi_{\text{look}})$, a.k.a. "steering angle". That is,

$$\begin{aligned} \mathbf{w} &= \mathbf{a}^{(\alpha)}(u_{\text{look}}, v_{\text{look}}, w_{\text{look}}) \\ &:= \begin{bmatrix} u^{(\alpha)}_{\text{look}} \\ v^{(\alpha)}_{\text{look}} \\ w^{(\alpha)}_{\text{look}} \end{bmatrix} = \alpha \begin{bmatrix} 1 \\ 1 \\ 1 \end{bmatrix} + (1-\alpha) \begin{bmatrix} u_{\text{look}} \\ v_{\text{look}} \\ w_{\text{look}} \end{bmatrix}, \end{aligned} \tag{2.1.3}$$

where $u_{\text{look}} := \sin(\theta_{\text{look}})\cos(\phi_{\text{look}})$, $v_{\text{look}} := \sin(\theta_{\text{look}})\sin(\phi_{\text{look}})$, $w_{\text{look}} := \cos(\theta_{\text{look}})$, for $\theta_{\text{look}} \in [0, \pi]$ and $\phi_{\text{look}} \in [0, 2\pi)$.

This "spatial matched filter" beamformer would output a real-valued scalar,

$$B := \mathbf{a}^{(\alpha)}(u_{\text{look}}, v_{\text{look}}, w_{\text{look}})^T \, \mathbf{a}^{(\alpha)}(u, v, w), \tag{2.1.4}$$

$$= \alpha\, g^{(\alpha)}_{\text{look}} + (1-\alpha)\left(u^{(\alpha)}_{\text{look}} u + v^{(\alpha)}_{\text{look}} v + w^{(\alpha)}_{\text{look}} w\right), \tag{2.1.5}$$

where superscript ^{T} denotes transposition, and

$$g^{(\alpha)}_{\text{look}} := u^{(\alpha)}_{\text{look}} + v^{(\alpha)}_{\text{look}} + w^{(\alpha)}_{\text{look}}. \tag{2.1.6}$$

The above beam-pattern of *collocated* but diversely oriented cardioids has not been investigated previously in the open literature, to the present authors' best knowledge. In contrast, the beam-pattern of an array of spatially *displaced/distributed* cardioid microphones/hydrophones has been much investigated, e.g., the SoundField microphone consists of four subcardioid microphones in a tetrahedral array grid, as well as [42–49]. To avoid confusion in terminology: this cardioid-triad beamforming here differs from the "cardioid beamforming" (e.g., in [54, 55]), whereby an array of pressure sensors and/or particle-velocity sensors have their measurements numerically weighted-then-added, to give a scalar output that is cardioid in the polar coordinates. Rather, this work starts with sensors that are already cardioidic in their gain responses, which would individually stay invariant over time.

2.1.4 Organization of this Chapter

The well known "spatial matched filter" beamformer of (2.1.3) turns out to have a peak direction $(\theta_{\text{peak}}, \phi_{\text{peak}})$ *not* pointing toward $(\theta_{\text{look}}, \phi_{\text{look}})$, as will be proved in Section 2.2. This mis-pointing error is analytically derived in Section 2.3.

Moreover, this beamformer may suffer from a sidelobe that may arise for certain "look directions" $(\theta_{\text{look}}, \phi_{\text{look}})$, depending on the "cardiodicity index" (α). This sidelobe arises under a set of necessary and sufficient conditions that will be derived in Section 2.2. Then, where a sidelobe exists, the mainlobe-to-sidelobe height ratio is derived in Section 2.4. This height ratio also depends again on both the sensors' "cardiodicity index" and the beamformer's reset "look direction".

Recall that the cardioid-triad's mainlobe spans two-dimensionally over the azimuth/ polar coordinates. To measure this two-dimensional mainlobe's beam "width", Section 2.5 will define a scalar metric and will analytically evaluate it. This two-dimensional beam "width" turns out to vary also with both the sensors' "cardiodicity index" and the beamformer's preset "look direction".

Section 2.6 derives the overall array gain of the cardioid triad. This array gain depends on both the sensors' "cardiodicity index" and the beamformer's preset "look direction". Section 2.8 concludes this investigation.

Regarding the acoustic vector-sensor's / vector-hydrophone's array gain, directivity, and mainlobe beamwidth — the literature could be confusing, because implicitly different definitions could be used on the composition of the acoustic vector-sensor / vector-hydrophone (e.g. whether there is a pressure-sensor, whether it is a tri-axial or a bi-axial velocity-sensor), or on the type of beamformer (not always the "spatial matched filter" beamformer here in this chapter).

2.2 To Determine if the Beam-Pattern Has Any Sidelobe

This section will analytically derive the necessary and sufficient conditions under which a sidelobe exists, for the "spatial matched filter" beamformer defined in (2.1.3) for a cardioid triad of any "cardiodicity index" $\alpha \in [0, 1]$ and of a "look direction" preset at $(\theta_{\text{look}}, \phi_{\text{look}})$.

This section's analysis will proceed as follows:

i) To locate the beam-pattern's maximum and minimum in Section 2.2.1, via the Cauchy-Schwarz inequality.

ii) Section 2.2.2: To derive the conditions under which a sidelobe exists, and to prove that a second sidelobe can never exist under any condition.

If a sidelobe does exist alongside the mainlobe, Section 2.3.1 will show how to differentiate between the two.

2.2.1 To Find the Beam-Pattern's Maximum/Minimum

From the beam pattern defined in (2.1.5),

$$B \quad = \quad \alpha g_{\text{look}}^{(\alpha)} + (1-\alpha)\tilde{B}, \tag{2.2.1}$$

where

$$\tilde{B} \quad := \quad \left[\mathbf{a}^{(\alpha)}\left(u_{\text{look}}, v_{\text{look}}, w_{\text{look}}\right)\right]^T [u,v,w]^T \tag{2.2.2}$$

represents an inner product between $\mathbf{a}^{(\alpha)}\left(u_{\text{look}}, v_{\text{look}}, w_{\text{look}}\right)$ and the steering vector $[u,v,w]^T$, subject to the previously stated constraint of $u^2+v^2+w^2=1$.

Recall that α, θ_{look}, and ϕ_{look} are preset constants. The maximum of $\tilde{B}$ in (2.2.2) (thus the maximum of B in (2.2.1)) is occurs when $[u,v,w]^T$ and $\mathbf{a}^{(\alpha)}\left(u_{\text{look}}, v_{\text{look}}, w_{\text{look}}\right)$ both point toward the same direction – this is true by the Cauchy-Schwarz inequality. Hence,

$$\left(u_{c_1}, v_{c_1}, w_{c_1}\right) \quad = \quad \frac{\left(u_{\text{look}}^{(\alpha)}, v_{\text{look}}^{(\alpha)}, w_{\text{look}}^{(\alpha)}\right)}{\sqrt{\left(u_{\text{look}}^{(\alpha)}\right)^2 + \left(v_{\text{look}}^{(\alpha)}\right)^2 + \left(w_{\text{look}}^{(\alpha)}\right)^2}}. \tag{2.2.3}$$

Likewise, the minimum of $\tilde{B}$ in (2.2.2) (thus the minimum of B in (2.2.1)) is obtained when $[u,v,w]^T$ and $\mathbf{a}^{(\alpha)}\left(u_{\text{look}}, v_{\text{look}}, w_{\text{look}}\right)$ point toward diametrically opposite directions. Hence,

$$\left(u_{c_2}, v_{c_2}, w_{c_2}\right) \quad = \quad \frac{-\left(u_{\text{look}}^{(\alpha)}, v_{\text{look}}^{(\alpha)}, w_{\text{look}}^{(\alpha)}\right)}{\sqrt{\left(u_{\text{look}}^{(\alpha)}\right)^2 + \left(v_{\text{look}}^{(\alpha)}\right)^2 + \left(w_{\text{look}}^{(\alpha)}\right)^2}}, \tag{2.2.4}$$

The above (2.2.3) and (2.2.4) hold for all $\alpha \in [0,1)$ and for all "look directions".

However, neither of these two vectors would generally correspond to the nominal "look direction" of $(\theta_{\text{look}}, \phi_{\text{look}})$. Hence, the "spatial matched filter" beamformer would generally suffer a pointing bias, which will be analytically derived in Section 2.3.

Inserting (2.2.3) and (2.2.4) into (2.2.1), the maximum and minimum of B respectively equals

$$B\big|_{(u,v,w)=\left(u_{c_1}, v_{c_1}, w_{c_1}\right)} \quad = \quad \alpha g_{\text{look}}^{(\alpha)} + (1-\alpha)\sqrt{\left(u_{\text{look}}^{(\alpha)}\right)^2 + \left(v_{\text{look}}^{(\alpha)}\right)^2 + \left(w_{\text{look}}^{(\alpha)}\right)^2}, \tag{2.2.5}$$

$$B|_{(u,v,w)=\left(u_{c_2},v_{c_2},w_{c_2}\right)} \quad = \quad \alpha g_{\text{look}}^{(\alpha)} - (1-\alpha)\sqrt{\left(u_{\text{look}}^{(\alpha)}\right)^2 + \left(v_{\text{look}}^{(\alpha)}\right)^2 + \left(w_{\text{look}}^{(\alpha)}\right)^2}, \tag{2.2.6}$$

with $g_{\text{look}}^{(\alpha)}$ is already defined in (2.1.6).

The maximum point of the beampattern $B|_{(u,v,w)=(u_{c_1},v_{c_1},w_{c_1})}$ is always non-negative. That is writing $B|_{(u,v,w)=(u_{c_1},v_{c_1},w_{c_1})}$ in terms of α and g_{look},

$$B|_{(u,v,w)=(u_{c_1},v_{c_1},w_{c_1})}\,(\alpha, g_{\text{look}}) \quad \geq \quad B|_{(u,v,w)=(u_{c_1},v_{c_1},w_{c_1})}\,(\alpha, -\sqrt{3}) \tag{2.2.7}$$

because $B|_{(u,v,w)=(u_{c_1},v_{c_1},w_{c_1})}\,(\alpha, g_{\text{look}})$ is monotonically increasing in terms of g_{look}, where

$$g_{\text{look}} \quad := \quad u_{\text{look}} + v_{\text{look}} + w_{\text{look}}. \tag{2.2.8}$$

Hence,

$$B|_{(u,v,w)=(u_{c_1},v_{c_1},w_{c_1})}\,(\alpha, -\sqrt{3}) \quad = \quad 3\alpha^2 - \sqrt{3}\alpha + (1-\alpha)|\sqrt{3}\alpha - (1-\alpha)| \tag{2.2.9}$$

The right hand side of (2.2.9) can be written as

$$\begin{aligned} & 3\alpha^2 - \sqrt{3}\alpha + (1-\alpha)|\sqrt{3}\alpha - (1-\alpha)| \\ & \qquad = \begin{cases} 2\alpha^2 + 2\alpha - 1 & \text{if } \alpha \geq \frac{1}{2}(\sqrt{3}-1) \\ \\ \left[(\sqrt{3}+1)\alpha - 1\right]^2 & \text{if } \alpha < \frac{1}{2}(\sqrt{3}-1) \end{cases} \end{aligned} \tag{2.2.10}$$

noting that both cases of the above are always greater than zero. Therefore, $B|_{(u,v,w)=(u_{c_1},v_{c_1},w_{c_1})} \geq 0$, $\forall\alpha$, $\forall\theta_{\text{look}}$, and $\forall\phi_{\text{look}}$. This fact will be used in Section 2.2.2.

2.2.2 To Derive the Conditions for a Sidelobe to Exist

A sidelobe would exist if and only if the beam-pattern B has more than one peak, obviously. In other words, if and only if the two critical points of (2.2.3)-(2.2.4) would give B values at opposite signs, i.e.,

$$B|_{(u,v,w)=\left(u_{c_1},v_{c_1},w_{c_1}\right)} B|_{(u,v,w)=\left(u_{c_2},v_{c_2},w_{c_2}\right)} \quad < \quad 0, \tag{2.2.11}$$

which is equivalent to

$$B|_{(u,v,w)=\left(u_{c_2},v_{c_2},w_{c_2}\right)} \quad < \quad 0, \tag{2.2.12}$$

because $B|_{(u,v,w)=(u_{c_1},v_{c_1},w_{c_1})} \geq 0$ as shown in (2.2.7) - (2.2.10) $\forall\alpha \in (0,1)$ and $\forall g_{\text{look}} \in [-\sqrt{3}, \sqrt{3}]$

Constraint (2.2.11) may be simplified to

$$
\begin{aligned}
(g_{\text{look}} - r_1)(g_{\text{look}} - r_2) &= \alpha^2 \left(g_{\text{look}}^{(\alpha)}\right)^2 - (1-\alpha)^2 \left[\left(u_{\text{look}}^{(\alpha)}\right)^2 + \left(v_{\text{look}}^{(\alpha)}\right)^2 + \left(w_{\text{look}}^{(\alpha)}\right)^2\right] \\
&= \left[\alpha^2(1-\alpha)^2\right] g_{\text{look}}^2 + \left[6\alpha^3(1-\alpha) - 2\alpha(1-\alpha)^3\right] g_{\text{look}} \\
&\quad + \left[9\alpha^4 - 3\alpha^2(1-\alpha)^2 - (1-\alpha)^4\right] \quad < \quad 0, \qquad (2.2.13)
\end{aligned}
$$

where the two roots equal

$$
r_1, r_2 \quad = \quad -\frac{2\alpha \mp (1-\alpha)\sqrt{-\alpha^2 - 4\alpha + 2} + 2\alpha^2 - 1}{\alpha(1-\alpha)}, \qquad (2.2.14)
$$

for all $\alpha \in (0, 1)$.

The subsequent Section 2.2.2.1 will derive the necessary condition for (2.2.12) to hold; and Section 2.2.2.2 will derive the corresponding sufficient condition. That necessary and sufficient condition will be shown to be

(i) $\alpha < \sqrt{6} - 2 \approx 0.45$, and

(ii) $g_{\text{look}} \in (r_1, r_2)$, where r_1 and r_2 are expressed in (2.2.14), each as a function of α only.

An implication of the above condition (i): The cardioid-*triad* can be sidelobe-free over the wider range of $\forall \alpha \in (\sqrt{6}-2, 1] \approx (0.45, 1]$, thereby including the particular cases of the standard cardioid and the subcardioid. The above $\alpha \in (\sqrt{6} - 2, 1]$ range is more inclusive than the $(0.5, 1]$ range wherein an *individual* cardioid would have no sidelobe.

Intuitively speaking: If α increases, each individual cardioid would become less directivity but would tend toward isotropy. The reduced directivity would lessen any sidelobe in the cardioid-triad. For the special case of the tri-axial velocity-sensor (i.e., where the "cardioidicity index" $\alpha = 0$),

1) (2.2.5)-(2.2.6) degenerate to

$$
B\big|_{(u,v,w)=\left(u_{c_1}, v_{c_1}, w_{c_1}\right)} \quad = \quad 1 \quad = \quad -B\big|_{(u,v,w)=\left(u_{c_2}, v_{c_2}, w_{c_2}\right)},
$$

thereby satisfying equation (2.2.12) above. That is, a tri-axial velocity-sensor always has a second lobe of equal height (sidelobe), regardless of the nominal "look direction" $(\theta_{\text{look}}, \phi_{\text{look}})$, which introduces π-ambiguity. Please also see [18] (p. 630).

2) (2.2.3) and (2.2.4) degenerate to give $(u_{c_1}, v_{c_1}, w_{c_1}) = -(u_{c_2}, v_{c_2}, w_{c_2})$. That is, the mainlobe and the sidelobe point in diametrically opposite directions, for any $(\theta_{\text{look}}, \phi_{\text{look}})$. This agrees with [18].

2.2.2.1 A necessary condition

Section 2.2.2 has shown that the left side of (2.2.11) may be expressed as $(g_{\text{look}} - r_1)(g_{\text{look}} - r_2)$, with r_1 and r_2 already derived in (2.2.14). As this expression is quadratic in g_{look}, it can be verified that the turning point of $(g_{\text{look}} - r_1)(g_{\text{look}} - r_2)$ is a local minimum, by taking the "second partial derivative test" as

$$\frac{\partial^2 \left[(g_{\text{look}} - r_1)(g_{\text{look}} - r_2)\right]}{\partial g_{\text{look}}^2} \;=\; 2\alpha^2(1-\alpha)^2 \;>\; 0. \tag{2.2.15}$$

To satisfy constraint (2.2.13), (2.2.15) indicates a necessary condition is that r_1 and r_2 have to be real-valued, i.e., the entry inside the square root of (2.2.13) must be non-negative. Hence, a necessary condition for the existence of a sidelobe is

$$\begin{aligned} & -\alpha^2 - 4\alpha + 2 \;>\; 0, \\ \Rightarrow \quad & -\sqrt{6} - 2 \;<\; \alpha \;<\; \sqrt{6} - 2, \end{aligned} \tag{2.2.16}$$

which is equivalent to $\alpha \in (0, \sqrt{6} - 2)$, as α cannot be negative.

2.2.2.2 A sufficient condition

The inequality (2.2.13) holds for $g_{\text{look}} \in (r_1, r_2)$, because $(g_{\text{look}} - r_1)(g_{\text{look}} - r_2)$ has been shown to have a local minimum and because it is quadratic in mathematical form.

Hence $\alpha < \sqrt{6} - 2$ and $g_{\text{look}} \in (r_1, r_2)$ together is a necessary and sufficient condition of the existence of a sidelobe.

2.3 The Beam-Pattern's Directional Pointing Offset

The cardioid triad's "spatial matched filter" beam-pattern will be analytically proved here in this section to have a peak direction of $(\theta_{\text{peak}}, \phi_{\text{peak}})$ that generally is unequal to the preset nominal "look direction" of $(\theta_{\text{look}}, \phi_{\text{look}})$. These two directions will be analytically interrelated in this section.

2.3.1 To Differentiate the Mainlobe from the Sidelobe

Section 2.2 has determined the conditions under which a sidelobe would exist, but has not yet differentiated between the mainlobe and the sidelobe. This Section 2.3.1 would achieve this.

The peak direction would be $(u_{c_1}, v_{c_1}, w_{c_1})$, if and only if

$$\left| B|_{(u,v,w)=\left(u_{c_1},v_{c_1},w_{c_1}\right)} \right| \;\;\geq\;\; \left| B|_{(u,v,w)=\left(u_{c_2},v_{c_2},w_{c_2}\right)} \right|, \tag{2.3.1}$$

which is equivalent to

$$g_{\text{look}} \;\geq\; \frac{3\alpha}{\alpha-1}. \tag{2.3.2}$$

Recall that the above g_{look} has been defined in (2.2.8).

This (2.3.2) constitutes the necessary and sufficient condition for $(u_{c_1}, v_{c_1}, w_{c_1})$ to correspond to the mainlobe. If (2.3.2) does not hold, i.e, if $g_{\text{look}} < \frac{3\alpha}{\alpha-1}$, it would be $(u_{c_2}, v_{c_2}, w_{c_2})$ that gives the mainlobe direction.

From the above and from (2.2.3)-(2.2.4), the mainlobe's peak direction

$$(u_{\text{peak}}, v_{\text{peak}}, w_{\text{peak}}) \;=\; \frac{\pm\left(u_{\text{look}}^{(\alpha)}, v_{\text{look}}^{(\alpha)}, w_{\text{look}}^{(\alpha)}\right)}{\sqrt{\left(u_{\text{look}}^{(\alpha)}\right)^2 + \left(v_{\text{look}}^{(\alpha)}\right)^2 + \left(w_{\text{look}}^{(\alpha)}\right)^2}}, \tag{2.3.3}$$

where the '+' sign applies when $g_{\text{look}} \geq \frac{3\alpha}{\alpha-1}$ else the '$-$' sign applies.

Toward analytically relating between the nominal "look direction" $(\phi_{\text{look}}, \theta_{\text{look}})$ and the actual peak direction $(\phi_{\text{peak}}, \theta_{\text{peak}})$: First, convert the peak direction's Cartesian coordinates $(u_{\text{peak}}, v_{\text{peak}}, w_{\text{peak}})$ to the spherical coordinates,

$$\cos(\theta_{\text{peak}}) \;=\; w_{\text{peak}}, \tag{2.3.4}$$

$$\cos(\phi_{\text{peak}}) \;=\; \frac{u_{\text{peak}}}{\sqrt{u_{\text{peak}}^2 + v_{\text{peak}}^2}}. \tag{2.3.5}$$

Next, substitute (2.2.3) and (2.2.4) into (2.3.4) and (2.3.5). Then, solve for θ_{peak} and ϕ_{peak}, to give (2.3.6) to (2.3.10). These are plotted versus the nominal 'look direction" in Figs. 2.1-2.4 at several common values of α.

For $g_{\text{look}} \geq \dfrac{3\alpha}{\alpha-1}$:

$$\theta_{\text{peak}} \;=\; \arccos\left(\frac{\alpha + (1-\alpha)\cos(\theta_{\text{look}})}{\sqrt{\begin{array}{l}3\alpha^2 + (1-\alpha)^2 + 2\alpha(1-\alpha) \\ \quad \{[\sin(\phi_{\text{look}}) + \cos(\phi_{\text{look}})]\sin(\theta_{\text{look}}) + \cos(\theta_{\text{look}})\}\end{array}}}\right). \tag{2.3.6}$$

$$\phi_{\text{peak}} \;=\; \arccos\left(\frac{\alpha + (1-\alpha)\cos(\phi_{\text{look}})\sin(\theta_{\text{look}})}{\sqrt{\begin{array}{l}[\alpha + (1-\alpha)\cos(\phi_{\text{look}})\sin(\theta_{\text{look}})]^2 + \\ \qquad [\alpha + (1-\alpha)\sin(\phi_{\text{look}})\sin(\theta_{\text{look}})]^2\end{array}}}\right) \tag{2.3.7}$$

$$\;=\; \arccos\left(\left[1 + \left(\frac{\alpha + (1-\alpha)\sin(\phi_{\text{look}})\sin(\theta_{\text{look}})}{\alpha + (1-\alpha)\cos(\phi_{\text{look}})\sin(\theta_{\text{look}})}\right)^2\right]^{-\frac{1}{2}}\right). \tag{2.3.8}$$

For $g_{\text{look}} < \dfrac{3\alpha}{\alpha - 1}$:

$$\theta_{\text{peak}} = \pi - \arccos\left(\frac{\alpha + (1-\alpha)\cos(\theta_{\text{look}})}{\sqrt{\begin{array}{l} 3\alpha^2 + (1-\alpha)^2 + 2\alpha(1-\alpha) \\ \quad \{[\sin(\phi_{\text{look}}) + \cos(\phi_{\text{look}})]\sin(\theta_{\text{look}}) + \cos(\theta_{\text{look}})\} \end{array}}} \right). \tag{2.3.9}$$

$$\phi_{\text{peak}} = \pi + \arccos\left(\left[1 + \left(\frac{\alpha + (1-\alpha)\sin(\phi_{\text{look}})\sin(\theta_{\text{look}})}{\alpha + (1-\alpha)\cos(\phi_{\text{look}})\sin(\theta_{\text{look}})} \right)^2 \right]^{-\frac{1}{2}} \right). \tag{2.3.10}$$

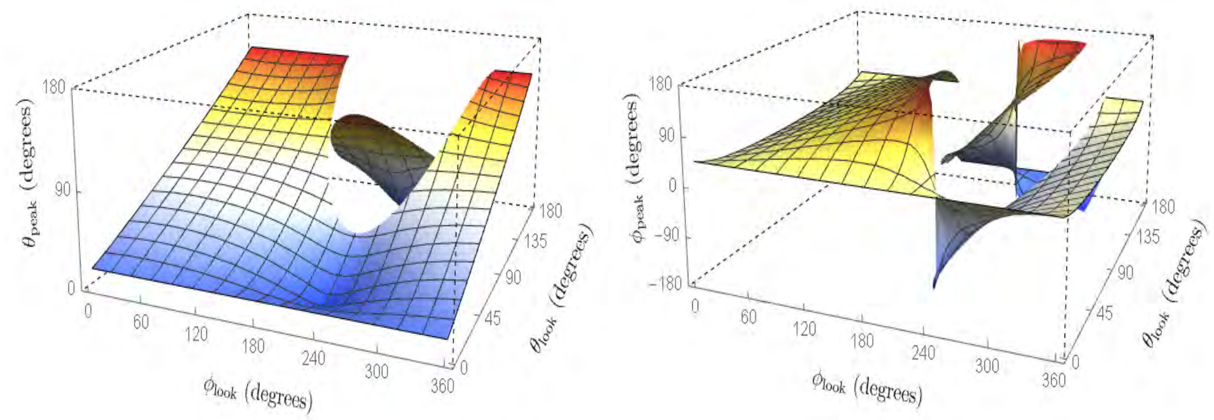

(a) (b)

Figure 2.1: (a) θ_{peak} of (2.3.6) and (2.3.9), and (b) ϕ_{peak} of (2.3.7) and (2.3.10) versus the nominal "look direction" of $(\theta_{\text{look}}, \phi_{\text{look}})$, for a triad of "hypercardioids" at a "cardioidicity index" of $\alpha = \frac{1}{4}$.

2.3.2 Geometric Interpretation of the Pointing Offset

Why is the actual peak direction $(\theta_{\text{peak}}, \phi_{\text{peak}})$ generally unequal to the nominal "look direction" $(\theta_{\text{look}}, \phi_{\text{look}})$? Below is a geometric explanation.

From (2.1.3), $\mathbf{a}^{(\alpha)}(u_{\text{look}}, v_{\text{look}}, w_{\text{look}})$ represents a vector sum of two 3×1 vectors: $[1,\ 1,\ 1]^T$ and the unit vector $[u_{\text{look}},\ v_{\text{look}},\ w_{\text{look}}]^T$ The latter represents the nominal "look direction". That is, the sum $\mathbf{a}^{(\alpha)}(u_{\text{look}}, v_{\text{look}}, w_{\text{look}})$ would point toward the nominal "look direction" only if the nominal "look direction" coincides with $[1,\ 1,\ 1]^T$. This coincidence occurs only at $(\theta_{\text{look}}, \phi_{\text{look}}) \approx (54.7°, 45°)$, $\forall\alpha$. If the nominal "look direction" points elsewhere, there would be a pointing offset, which would increase as α increases.

As α increases, $[1,\ 1,\ 1]^T$ can divert $(1-\alpha)[u_{\text{look}},\ v_{\text{look}},\ w_{\text{look}}]^T$ further from the nominal "look direction".

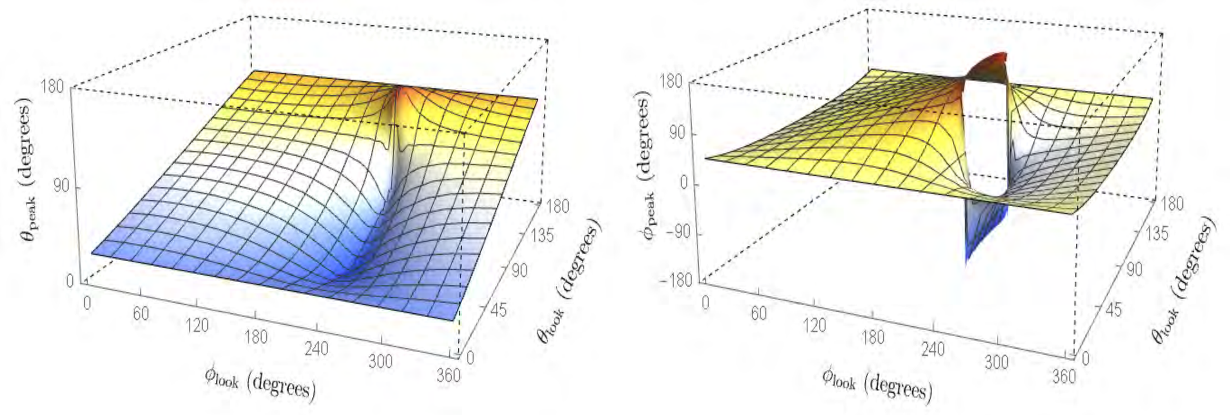

(a) (b)

Figure 2.2: (a) θ_{peak} of (2.3.6), and (b) ϕ_{peak} of (2.3.7) versus the nominal "look direction" of $(\theta_{\text{look}}, \phi_{\text{look}})$, for a triad of "supercardioids" at a "cardioidicity index" of $\alpha = \frac{\sqrt{3}-1}{2} \approx 0.366025 \approx 0.37$.

2.3.3 Abrupt Jump in the Pointing Offset Across $(\phi_{\text{look}}, \theta_{\text{look}})$

The pointing offset undergoes an abrupt jump in Figs. 2.1-2.2 as $(\phi_{\text{look}}, \theta_{\text{look}})$ varies, but not in Figs. 2.3-2.4.

Abrupt jumps occur in Figs. 2.1a and 2.1b which have $\alpha = \frac{1}{4}$ (i.e., the "hypercardioid"), and in Figs. 2.2a and 2.2b which have $\alpha = \frac{\sqrt{3}-1}{2} \approx 0.366025 \approx 0.37$ (i.e., the "supercardioid"). Abrupt jumps occur at these values of α because there exist some $(\phi_{\text{look}}, \theta_{\text{look}})$ such that $\alpha \geq \alpha_{\text{switch}}$ and there exists other $(\phi_{\text{look}}, \theta_{\text{look}})$ such that $\alpha < \alpha_{\text{switch}}$, where $\alpha_{\text{switch}} := \frac{g_{\text{look}}}{g_{\text{look}}-3}$.

However, no abrupt jump occurs anywhere in Figs. 2.3a and 2.3b which have $\alpha = \frac{1}{2}$ (i.e., the "standard cardioid"), nor anywhere in Figs. 2.4a and 2.4b which have $\alpha = 0.7$ (i.e., the "subcardioid"). This is because all possible $(\phi_{\text{look}}, \theta_{\text{look}})$ will always give $\alpha_{\text{switch}} \geq \alpha$.

2.3.4 A Closer Look at ϕ_{peak} of (2.3.8)

Figs.2.3b and 2.4b have shapes that reflect the mathematical form of (2.3.8):

{1} $\phi_{\text{peak}} - \frac{\pi}{4}$ is anti-symmetric, along $\phi_{\text{look}} \in \left[\frac{\pi}{4}, \frac{9\pi}{4}\right]$, with respect to $\frac{5\pi}{4}$, $\forall \phi_{\text{look}} \in [0, \pi]$, $\forall \theta_{\text{look}}$, $\forall \alpha > \frac{1}{2}$.

{2} At $\phi_{\text{look}} = \frac{\pi}{4}, \frac{5\pi}{4}$, the fraction in (2.3.8) equals 1, hence ϕ_{peak} would be constant over all θ_{look}.

{3} As α increases, moving from Fig. 2.3b across into 2.4b, the fraction in (2.3.8) would be less influenced by ϕ_{look}, hence ϕ_{peak} would have a narrower dynamic range with a smaller maximum ϕ_{peak} but a larger minimum ϕ_{peak}.

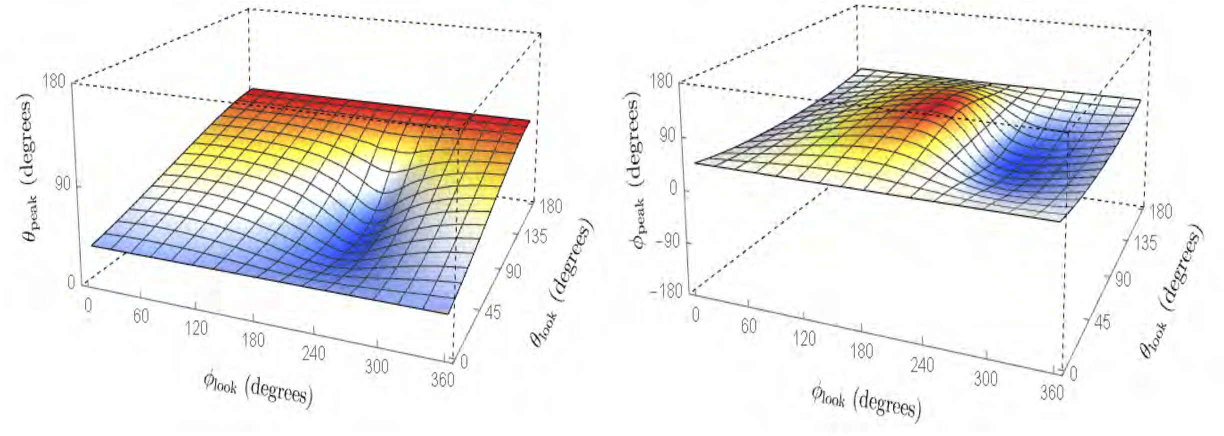

(a) (b)

Figure 2.3: (a) θ_{peak} of (2.3.6), and (b) ϕ_{peak} of (2.3.7) versus the nominal "look direction" of $(\theta_{\text{look}}, \phi_{\text{look}})$, for a triad of "standard cardioids" at a "cardioidicity index" of $\alpha = \frac{1}{2}$.

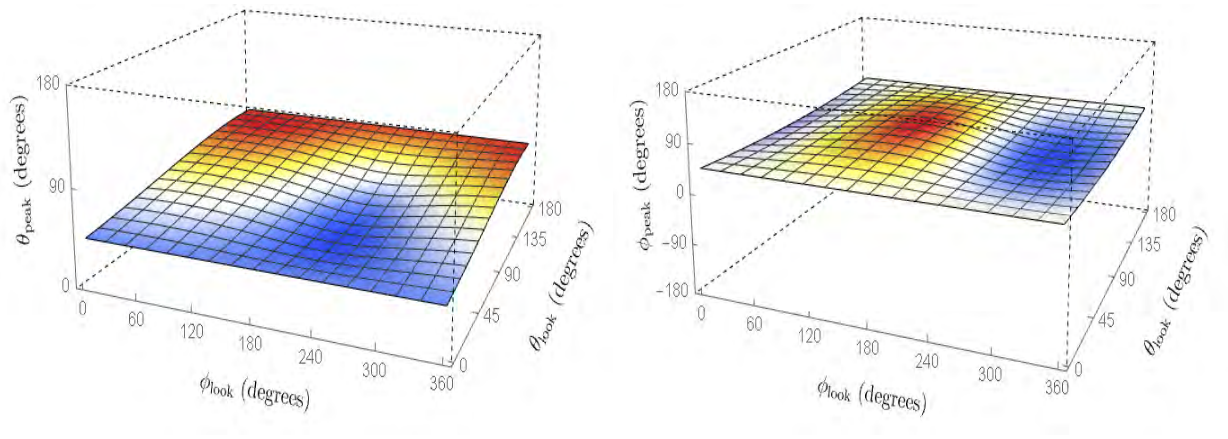

(a) (b)

Figure 2.4: (a) θ_{peak} of (2.3.6), and (b) ϕ_{peak} of (2.3.7) versus the nominal "look direction" of $(\theta_{\text{look}}, \phi_{\text{look}})$, for a triad of "subcardioids" at a "cardioidicity index" of $\alpha = 0.7$.

The minimum point of (2.3.7), along the ϕ_{look} axis, equals

$$\arg\min_{\forall \phi_{\text{look}}} \phi_{\text{peak}} \;=\; \sin^{-1}\left(\frac{\alpha - 1}{\alpha} \frac{1}{\sqrt{2}} \sin(\theta_{\text{look}}) \right) - \frac{\pi}{4}. \tag{2.3.11}$$

To analyze the implication of the above: As α increases from 0 toward 1, $\frac{1-\alpha}{\alpha}$ decreases and $\frac{\alpha-1}{\alpha}$ becomes less negative. Recall that $\sin(\theta_{\text{look}}) \geq 0, \forall \theta_{\text{look}}$. Hence, $\frac{\alpha-1}{\alpha} \frac{1}{\sqrt{2}} \sin(\theta_{\text{look}})$ gets less negative in amplitude, as (2.3.11) goes toward $0^\circ = 360^\circ$. This trend is exactly what occurs in Figs.2.3b-2.4b.

As α increases from 0.5 to 0.7, the null in Figs.2.3b-2.4b becomes shallower. This is because as α increases, $(1 - \alpha)$ decreases therefore, the component of (2.3.8) that varies with $(\theta_{\text{look}}, \phi_{\text{look}})$ has less effect on ϕ_{peak}.

The maximum point of (2.3.8) occurs at $(\theta_{\rm look}, \phi_{\rm look}) = \left(\frac{\pi}{2}, \frac{3\pi}{4} - \sin^{-1}\left(\frac{\alpha-1}{\sqrt{2}\alpha}\right)\right)$. As α increases, $\left|\frac{\alpha-1}{\sqrt{2}\alpha}\right|$ decreases, hence decreasing $\sin^{-1}\left(\frac{\alpha-1}{\sqrt{2}\alpha}\right)$ shifts the maximum point towards $(\theta_{\rm look}, \phi_{\rm look}) = \left(\frac{\pi}{2}, \frac{3\pi}{4}\right)$, $(90°, 135°)$. This effect is noticed in Figs.2.3b and 2.4b, as α increases from 0.5 to 0.7.

2.3.5 The Special Case of $\alpha = 0$, i.e., a Tri-Axial Velocity-Sensor

For the special case of the tri-axial velocity-sensor (i.e., where the "cardioidicity index" $\alpha = 0$), (2.3.6) and (2.3.7) degenerate to give $\theta_{\rm peak} = \theta_{\rm look}$ and $\phi_{\rm peak} = \phi_{\rm look}$, $\forall\,(\theta_{\rm look}, \phi_{\rm look})$. This means no pointing offset for a tri-axial velocity-sensor, in agreement with [50] (p. 327), and [51] (p. 10).

2.4 Mainlobe-to-Sidelobe Height Ratio

The mainlobe-to-sidelobe height ratio (also referred to as front-to-back ratio) as the name implies, measures the ratio of the mainlobe's height to the sidelobe's height. This metric gives an idea of how much the array amplifies signal coming from its mainlobe relative to its sidelobe.

Given (2.3.1) - (2.3.2), the mainlobe and sidelobe heights, respectively, equal to the absolute magnitude of (2.2.5) and (2.2.6). That is,

$$h_{\rm peak}, h_{\rm side} \quad = \quad \pm\,\alpha\left|g^{(\alpha)}_{\rm look}\right| + (1-\alpha)\sqrt{\left(u^{(\alpha)}_{\rm look}\right)^2 + \left(v^{(\alpha)}_{\rm look}\right)^2 + \left(w^{(\alpha)}_{\rm look}\right)^2}. \qquad (2.4.1)$$

with $+$ for $h_{\rm peak}$ and $-$ for $h_{\rm side}$.

The mainlobe-to-sidelobe height ratio (if a sidelobe exists) thus equals

$$\begin{aligned} \mathrm{HR} &:= \frac{h_{\rm peak}}{h_{\rm side}}, \\ &= \frac{\alpha\left|g^{(\alpha)}_{\rm look}\right| + (1-\alpha)\sqrt{\left(u^{(\alpha)}_{\rm look}\right)^2 + \left(v^{(\alpha)}_{\rm look}\right)^2 + \left(w^{(\alpha)}_{\rm look}\right)^2}}{-\alpha\left|g^{(\alpha)}_{\rm look}\right| + (1-\alpha)\sqrt{\left(u^{(\alpha)}_{\rm look}\right)^2 + \left(v^{(\alpha)}_{\rm look}\right)^2 + \left(w^{(\alpha)}_{\rm look}\right)^2}}. \end{aligned} \qquad (2.4.2)$$

This mainlobe-to-sidelobe height ratio is plotted versus all possible "look directions" in Fig. 2.5a, at $\alpha = \frac{1}{4}$ (i.e. a triad comprises of hypercardioids). To aid subsequent understanding of his graph's features, Fig. 2.5b plots the *main*lobe height whereas Fig. 2.5c does the same for the *side*lobe height. Please recall that these are *not* beam-patterns, but only how the height ratio / the mainlobe height / sidelobe height vary with the nominal "look direction".

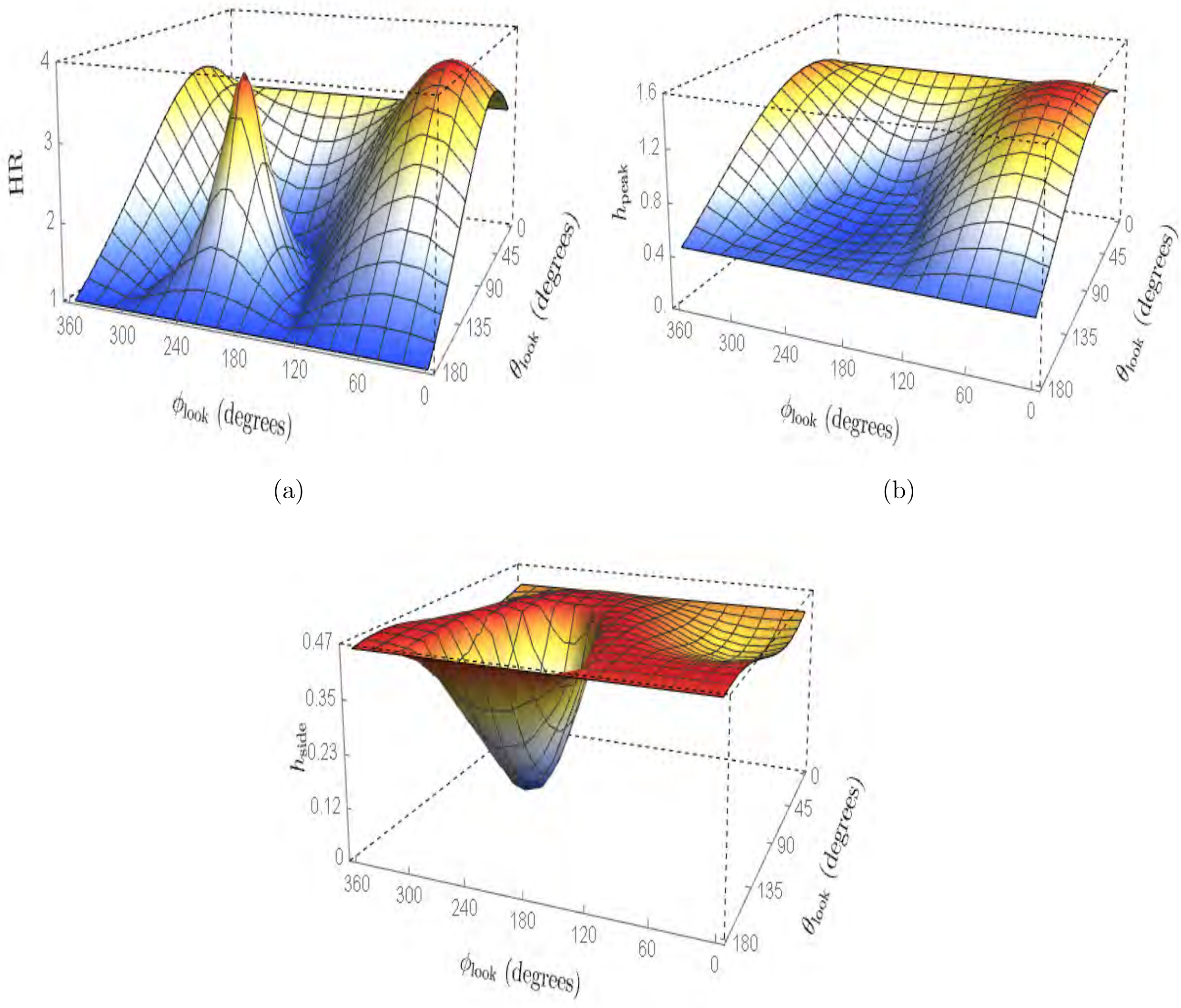

(a) (b) (c)

Figure 2.5: (a) The mainlobe-to-sidelobe height ratio (HR), (b) h_{peak}, and (c) h_{side} versus the nominal "look direction" of $(\theta_{\text{look}}, \phi_{\text{look}})$, for a triad of "hypercardioid" at a "cardioidicity index" of $\alpha = 0.25$.

The counterpart graphs for $\alpha = \frac{\sqrt{3}-1}{2} \approx 0.366025 \approx 0.37$ (i.e. a triad comprises of supercardioids). are Figs.2.6a, 2.6b, and 2.6c.

The standard-cardioid case (with $\alpha = 0.5$) and the subcardioid case (with $\alpha = 0.7$) are not plotted, because they have no sidelobe and hence no height ratio.

For the special case of the tri-axial velocity-sensor (i.e., where the "cardioidicity index" $\alpha = 0$), (3.3.3) degenerates to $\text{HR} = 1, \forall\, (\theta_{\text{look}}, \phi_{\text{look}})$. This agrees with [2] (p. 42).

Qualitative observations on the height ratio plotted in Fig. 2.5a for the triad of hypercardioids (i.e. $\alpha = \frac{1}{4}$):

HR-1 A prominent spike appears at $(\theta_{\text{look}}, \phi_{\text{look}}) = (125.4°, 225°)$. This height-ratio spike arises due to the sidelobe's very near-zero height there (i.e. $h_{\text{side}} \approx 0$), even as the mainlobe height h_{peak} varies relatively little there – as shown in Fig. 2.5c.

HR-2 At $\phi_{\text{look}} < 126^\circ$, a long ridge extends over all θ_{look}. This height-ratio ridge arises due to a similar topology in the mainlobe in Fig. 2.5b) and due to the sidelobe's relative flatness there in Fig. 2.5c.

HR-3 Fig. 2.5b consists of a flat region and a curvy/hilly region. The former corresponds to substituting the (u, v, w) of the $g_{\text{look}} < \frac{3\alpha}{\alpha-1}$ case in (2.3.3) into (2.1.5) to obtain the h_{peak} in (2.4.1), whereas the latter corresponds to substituting the subregion $\{(u, v, w)|g_{\text{look}} \geq \frac{3\alpha}{\alpha-1}\}$ for the case in (2.3.3) into (2.1.5), to obtain the h_{peak} in (2.4.1).

HR-4 Fig. 2.5c consists of a deep dip and a relatively flat region. The former corresponds to substituting the subregion $\{(u, v, w)|g_{\text{look}} \geq \frac{3\alpha}{\alpha-1}\}$ for the case in (2.3.3) into (2.1.5) to obtain the h_{side} in (2.4.1), whereas the latter corresponds to substituting the other subregion $\{(u, v, w)|g_{\text{look}} \geq \frac{3\alpha}{\alpha-1}\}$ for the case in (2.3.3) into (2.1.5) to obtain the h_{side} in (2.4.1).

Qualitative observations on the height ratio plotted in Fig. 2.6a for the triad of hypercardioids (i.e. $\alpha = \frac{\sqrt{3}-1}{2} \approx 0.366025 \approx 0.37$):

HR-5 A prominent spike appears at $(\theta_{\text{look}}, \phi_{\text{look}}) = (54.73^\circ, 45^\circ)$. This height-ratio spike arises due to the sidelobe's near-zero height there (i.e. $h_{\text{side}} \approx 0$), as shown in Fig. 2.6c.

HR-6 The height ratio becomes very large at around $\theta_{\text{look}} \in (33^\circ, 76^\circ)$ and $\phi_{\text{look}} \in (18^\circ, 72^\circ)$, because the sidelobe height is very low there about, as may be observed in Fig. 2.6c.

HR-7 There exists no spike corresponding to that in Fig. 2.5a for $\alpha = \frac{1}{4}$, because both h_{peak} and h_{side} have a deep dip around $(\theta_{\text{look}}, \phi_{\text{look}}) = (125.4^\circ, 225^\circ)$.

In conclusion, the proposed cardioid triad can increase the height ratio, from the unity value of the triaxial velocity sensor, possibly to ∞ (i.e. no sidelobe).

2.5 The Triad's Mainlobe Beam's Azimuth-Elevation "Width"

The beamwidth (3dB-beamwidth or half-power beamwidth) of the beampattern is the angular distance from the mainlobe within which the power pattern is equal to or greater than half its maximum value (i.e square of the height of the mainlobe). This section will analytically derive this "width" at 3dB below the mainlobe height.

This analysis is not straight-forward:

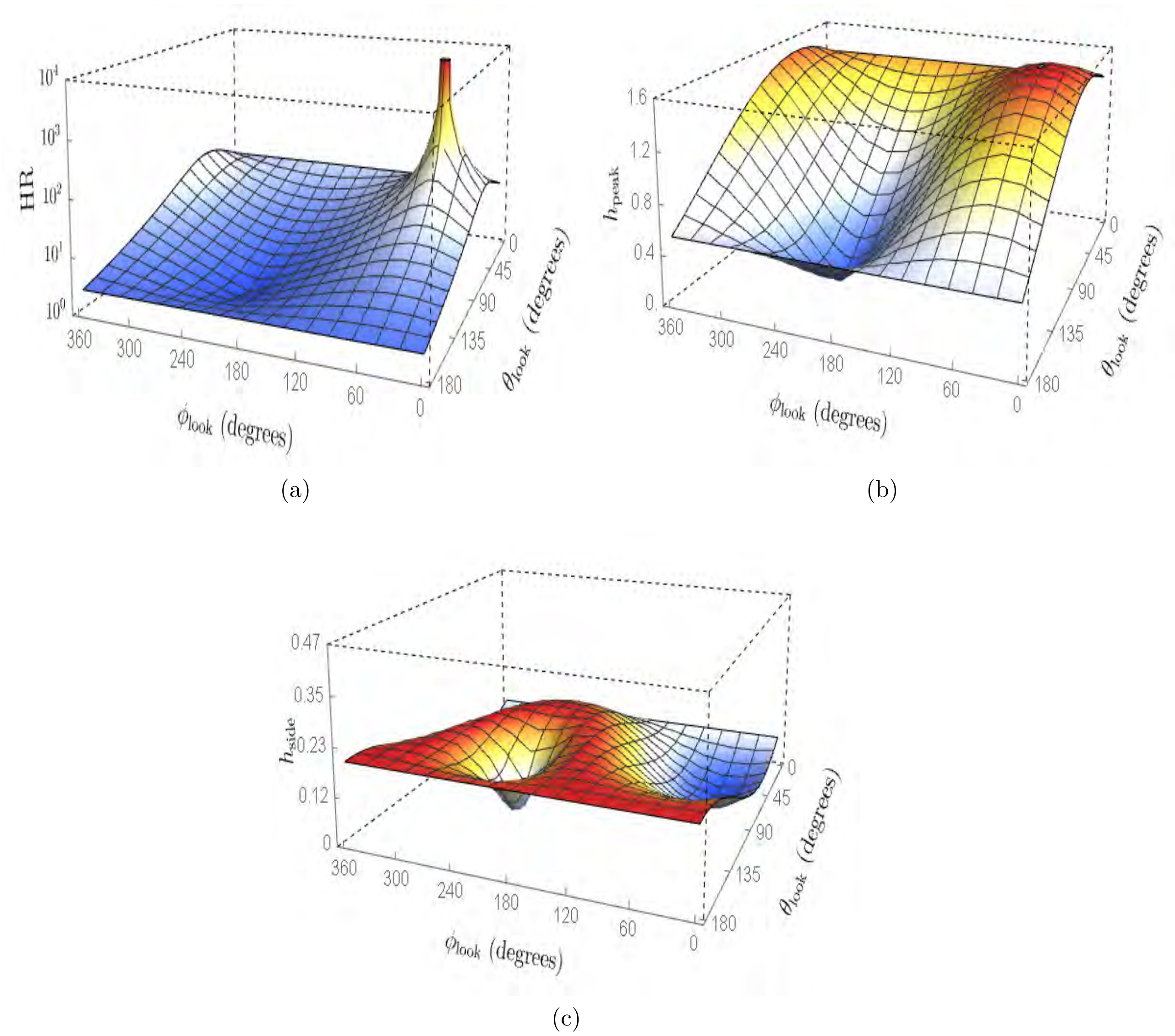

Figure 2.6: (a) The mainlobe-to-sidelobe height ratio (HR), (b) h_{peak}, and (c) h_{side} versus the nominal "look direction" of $(\theta_{\text{look}}, \phi_{\text{look}})$, for a triad of "supercardioid" at a "cardioidicity index" of $\alpha = \frac{\sqrt{3}-1}{2} \approx 0.366025 \approx 0.37$.

* As the cardioid triad's directivity is bivariate over the spherical coordinates of (θ, ϕ), the cardioid triad's mainlobe "width" is actually a two-dimensional partial surface on the unit sphere, rather than a one-dimensional width, a scalar. Nonetheless, to ease human comprehension, Section 2.5.3 will define a scalar "width" metric to measure the cardioid triad's mainlobe surface.

* However, the mainlobe height does *not* drop below the peak's half-power height, at some combination of "look direction" $(\theta_{\text{look}}, \phi_{\text{look}})$ and the "cardioidicity index" α – the exact conditions will be analytically derived in Section 2.5.1. Where the 3dB beamwidth exists, Sections 2.5.2-2.5.3 will define and will derive the 3dB beamwidth.

2.5.1 The Necessary & Sufficient Condition for the Half- Power Beamwidth to Exist

The proposed beamwidth equation is valid if the value of the minimum point on the normalized beampattern is equal to or less than $\frac{1}{\sqrt{2}} B|_{(u,v,w)=(u_{c_1},v_{c_1},w_{c_1})}$. That is,

$$B|_{(u,v,w)=(u_{c_2},v_{c_2},w_{c_2})} \leq \frac{1}{\sqrt{2}} B|_{(u,v,w)=(u_{c_1},v_{c_1},w_{c_1})} \tag{2.5.1}$$

This implies that a certain point on the beampattern will be less than the half-power value so the beamwidth can be equated to the surface area of a spherical cap.

Therefore,

$$B|_{(u,v,w)=(u_{c_1},v_{c_1},w_{c_1})} \geq \sqrt{2}\, B|_{(u,v,w)=(u_{c_2},v_{c_2},w_{c_2})}, \tag{2.5.2}$$

that is

$$\begin{aligned} \alpha g_{\text{look}}^{(\alpha)} + (1-\alpha)\sqrt{\left(u_{\text{look}}^{(\alpha)}\right)^2 + \left(v_{\text{look}}^{(\alpha)}\right)^2 + \left(w_{\text{look}}^{(\alpha)}\right)^2} \geq \\ \sqrt{2}\alpha g_{\text{look}}^{(\alpha)} - \sqrt{2}(1-\alpha)\sqrt{\left(u_{\text{look}}^{(\alpha)}\right)^2 + \left(v_{\text{look}}^{(\alpha)}\right)^2 + \left(w_{\text{look}}^{(\alpha)}\right)^2}. \end{aligned} \tag{2.5.3}$$

Re-arranging the terms,

$$\begin{aligned} (\sqrt{2}-1)\alpha g_{\text{look}}^{(\alpha)} - (\sqrt{2}+1)(1-\alpha)\sqrt{\left(u_{\text{look}}^{(\alpha)}\right)^2 + \left(v_{\text{look}}^{(\alpha)}\right)^2 + \left(w_{\text{look}}^{(\alpha)}\right)^2} &\leq 0 \\ (\sqrt{2}-1)(3\alpha^2 + \alpha(1-\alpha)g_{\text{look}}) - \\ (\sqrt{2}+1)(1-\alpha)\sqrt{3\alpha^2 + (1-\alpha)^2 + 2\alpha(1-\alpha)g_{\text{look}}} &\leq 0. \end{aligned} \tag{2.5.4}$$

Solving (2.5.4) in terms of g_{look} gives a conjugate pair,

$$\begin{aligned} g_{r_1}, g_{r_2} = & \frac{(\sqrt{2}+1)^2(1-\alpha)^2 - 3\alpha^2(\sqrt{2}-1)^2}{\alpha(\sqrt{2}-1)^2(1-\alpha)} \\ & \pm (\sqrt{2}+1)\frac{\sqrt{(6\sqrt{2}-3)\alpha^2 - 12\alpha + 6}}{\alpha(\sqrt{2}-1)^2} \end{aligned} \tag{2.5.5}$$

As g_{r_1} and g_{r_2} must be real-valued, the discriminant of the square root in (2.5.5) must be non-negative. That is,

$$(6\sqrt{2}-3)\alpha^2 - 12\alpha + 6 \geq 0. \tag{2.5.6}$$

The inequality (2.5.6) would be satisfied mathematically $\forall\alpha \notin (0.7735, 1.4142)$, i.e. $\forall\alpha \leq 0.7735$ in the present engineering analysis. This value of $\alpha = 0.7735$ approximates the exact value of $\alpha = \frac{(2-\sqrt{6-4\sqrt{2}})(1+2\sqrt{2})}{7}$, which is a basis for the subcardioid to give the highest beamwidth. The further approximated value of $\alpha = 0.7$ is used in [2] (the last paragraph on p. 40) for a single subcardioid sensor.

$g_{\text{look}} \in [-\sqrt{3}, \sqrt{3}]$, $\implies$ $g_{\text{look}} \in (\max[g_{r_1}], \min[g_{r_2}])$ $\forall \alpha \leq 0.7735$. Hence $\alpha \leq 0.7735$ is necessary and sufficient condition for the derived beamwidth expression to hold. For $\alpha > 0.7735$, all the points on the beampattern is greater than its half-power value; the beamwidth becomes constant for every look direction and is set to the area of a sphere of radius $\frac{1}{\sqrt{2}} h_{\text{peak}}$.

The necessary condition has thus been established above.

As for the sufficient condition: The condition that satisfies the inequality (2.5.4) is $g_{r_1} \leq g_{\text{look}} \leq g_{r_2}$. And this together with the necessary condition, constitutes the sufficient condition.

2.5.2 Proof of the Beam-Pattern's Rotational Symmetry About Peak Direction $(\phi_{\text{peak}}, \theta_{\text{peak}})$

The cardioid-triad's spatial-matched-filter beam-pattern, defined mathematically in (2.1.4) and (2.1.5), will be analytically shown here to be rotationally symmetric with respect to the peak direction $(\phi_{\text{peak}}, \theta_{\text{peak}})$. This characteristic will aid the next subsection to analytically derive the beamwidth.

Consider the set of all directions-of-arrival at which the beampattern B has a height of h. That is, $\{(u_h, v_h, w_h) : B|_{(u,v,w)=(u_h,v_h,w_h)} = h\}$. It holds, by definition, that

$$h \quad = \quad \alpha\, g^{(\alpha)}_{\text{look}} + (1-\alpha)\left(u^{(\alpha)}_{\text{look}} u_h + v^{(\alpha)}_{\text{look}} v_h + w^{(\alpha)}_{\text{look}} w_h\right).$$

Further define

$$\cos(\gamma_h) \quad := \quad \pm \frac{u^{(\alpha)}_{\text{look}} u_h + v^{(\alpha)}_{\text{look}} v_h + w^{(\alpha)}_{\text{look}} w_h}{\sqrt{\left(u^{(\alpha)}_{\text{look}}\right)^2 + \left(v^{(\alpha)}_{\text{look}}\right)^2 + \left(w^{(\alpha)}_{\text{look}}\right)^2}}, \tag{2.5.7}$$

where the numerator equals the inner product between the vector $[u_h, v_h, w_h]$ and the main-lobe direction (which equals $[u_{c_1}, v_{c_1}, w_{c_1}]$ if $g_{\text{look}} \geq \frac{3\alpha}{\alpha-1}$. or $[u_{c_2}, v_{c_2}, w_{c_2}]$ if $g_{\text{look}} < \frac{3\alpha}{\alpha-1}$).

Re-write (2.5.7) as

$$\cos(\gamma_h) \quad = \quad \pm \frac{h - \alpha\, g^{(\alpha)}_{\text{look}}}{(1-\alpha)\sqrt{\left(u^{(\alpha)}_{\text{look}}\right)^2 + \left(v^{(\alpha)}_{\text{look}}\right)^2 + \left(w^{(\alpha)}_{\text{look}}\right)^2}}, \tag{2.5.8}$$

which depends only on the nominal "look direction" and on the "cardioidicity index" α, but not on the particular value of (u_h, v_h, w_h). This implies that the beam-pattern's isohypse (a.k.a. isoheight) contour is a circle (in the spherical coordinates) centered at the "peak direction", for any specific α.

2.5.3 Half-Power Beam-Width - Analytically Derived in a Closed Form

As the cardioid triad's mainlobe is bivariate over the spherical coordinates of (θ, ϕ), the mainlobe "width" is actually a two-dimensional partial surface of the unit sphere, rather than a one-dimensional width. Nonetheless, to ease human comprehension, consider the surface sub-area A of the unit sphere corresponding to a beam height $h \geq h_{3\text{dB}}$. That surface sub-area (being a scalar) is defined here as the cardioid triad's mainlobe "width".

Due to the rotational symmetry of the beam-pattern under consideration (as proved in the preceding Section 2.5.2), this subregion would be a "spherical cap".[3] This "spherical cap" has a base enclosed by the circular contour where $B = h_{\text{peak}}/\sqrt{2}$, where h_{peak} is the maximum value of the beam-pattern.

Apply the rotational symmetry discovered in Section 2.5.2 to h at half power:

$$\begin{aligned} h_{3\text{dB}} &:= \frac{h_{\text{peak}}}{\sqrt{2}} \\ &= \frac{1}{\sqrt{2}}\left[\alpha g_{\text{look}}^{(\alpha)} \pm (1-\alpha)\sqrt{\left(u_{\text{look}}^{(\alpha)}\right)^2 + \left(v_{\text{look}}^{(\alpha)}\right)^2 + \left(w_{\text{look}}^{(\alpha)}\right)^2}\right]. \end{aligned} \tag{2.5.9}$$

Substitute the above into (2.5.8), giving

$$\begin{aligned} \cos(\gamma_{3\text{dB}}) &= \pm\frac{\frac{h_{\text{peak}}}{\sqrt{2}} - \alpha\, g_{\text{look}}^{(\alpha)}}{(1-\alpha)\sqrt{\left(u_{\text{look}}^{(\alpha)}\right)^2 + \left(v_{\text{look}}^{(\alpha)}\right)^2 + \left(w_{\text{look}}^{(\alpha)}\right)^2}} \\ &= \frac{1}{\sqrt{2}} \pm \frac{\alpha}{1-\alpha}\frac{1-\sqrt{2}}{\sqrt{2}}\frac{g_{\text{look}}^{(\alpha)}}{\sqrt{\left(u_{\text{look}}^{(\alpha)}\right)^2 + \left(v_{\text{look}}^{(\alpha)}\right)^2 + \left(w_{\text{look}}^{(\alpha)}\right)^2}}. \end{aligned} \tag{2.5.10}$$

For a tri-axial velocity sensor whose $\alpha = 0$, (2.5.10) above degenerates to $\frac{1}{\sqrt{2}}$.

The aforementioned "spherical cap" has a surface area equal to

$$\begin{aligned} A &= 2\pi\frac{h_{\text{peak}}}{\sqrt{2}}\left(\frac{h_{\text{peak}}}{\sqrt{2}} - \frac{h_{\text{peak}}}{\sqrt{2}}\cos\gamma_{3\text{dB}}\right) \\ &= \frac{\sqrt{2}-1}{\sqrt{2}}\pi h_{\text{peak}}^2\left[1 \pm \frac{\alpha}{1-\alpha}\frac{g_{\text{look}}^{(\alpha)}}{\sqrt{\left(u_{\text{look}}^{(\alpha)}\right)^2 + \left(v_{\text{look}}^{(\alpha)}\right)^2 + \left(w_{\text{look}}^{(\alpha)}\right)^2}}\right], \end{aligned} \tag{2.5.11}$$

[3] The "spherical cap" is also known as the "spherical dome". It is defined (pp. 69 of [56]) as the "portion of a sphere cut off by a plane".

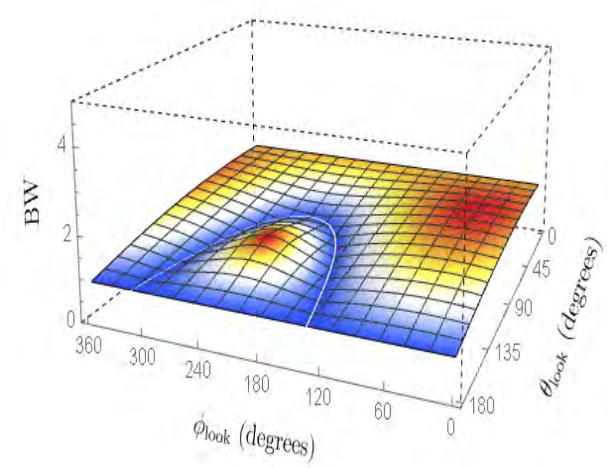

(a) $\alpha = \frac{1}{4}$, hypercardioids.

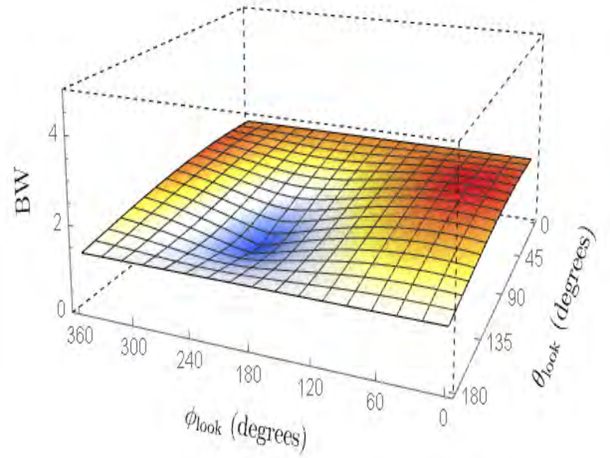

(b) $\alpha = \frac{\sqrt{3}-1}{2}$, supercardioids.

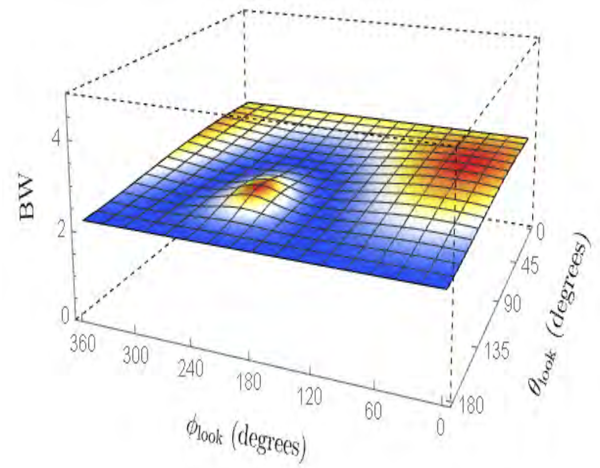

(c) $\alpha = \frac{1}{2}$, standard cardioids.

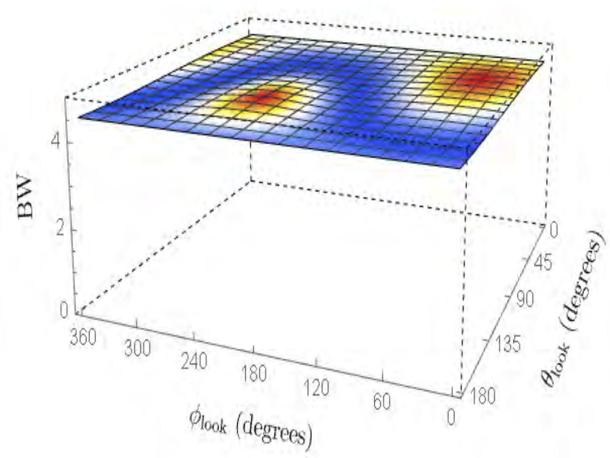

(d) $\alpha = 0.7$, subcardioids.

Figure 2.7: The beamwidth (BW) versus the nominal "look direction" $(\theta_{\text{look}}, \phi_{\text{look}})$ for various typical values of the "cardioidicity index".

where the "+" sign applies if $g_{\text{look}} \geq \frac{-3\alpha}{1-\alpha}$ (when the mainlobe points toward $(u_{c_1}, v_{c_1}, w_{c_1},))$ and the "−" sign applies (when the mainlobe points toward $(u_{c_2}, v_{c_2}, w_{c_2},))$. The third equality above is due to (2.5.10). This (2.5.11) describes the mainlobe's beam-width as a closed-form analytical expression.

The half-power beam "width" (BW) is thus given as

$$\begin{aligned} \text{BW} &:= \frac{A}{h_{\text{peak}}^2} \\ &= \frac{\sqrt{2}-1}{\sqrt{2}}\pi\left[1 \pm \frac{3\alpha^2 + \alpha(1-\alpha)g_{\text{look}}}{(1-\alpha)\sqrt{3\alpha^2 + (1-\alpha)^2 + 2\alpha(1-\alpha)g_{\text{look}}}}\right], \end{aligned} \quad (2.5.12)$$

where g_{look} has been defined in (2.2.8) to equal $\sin(\theta_{\text{look}})\cos(\phi_{\text{look}}) + \sin(\theta_{\text{look}})\sin(\phi_{\text{look}}) + \cos(\theta_{\text{look}})$.

Figs.2.7a-2.7d show how the above-derived beamwidth varies over common values of α. The beam "width" (BW) is largely determined by α, with only minor variation over $(\theta_{\text{look}}, \phi_{\text{look}})$).

In Fig. 2.7a (for $\alpha = \frac{1}{4}$) and Fig. 2.7b (for $\alpha = \frac{\sqrt{3}-1}{2} \approx 0.366025 \approx 0.37$) – in fact for any $\alpha \leq \frac{\sqrt{3}-1}{2}$ – the beam "width" is minimum at the "look direction" where $g_{\text{look}} = u_{\text{look}} + v_{\text{look}} + w_{\text{look}} = \frac{3\alpha}{\alpha-1}$. This value of g_{look} is exactly those "look directions" where the mainlobe and the sidelobe are equal in height. Generally, those "look directions" giving a taller h_{side} corresponds to a narrower BW.

In (2.5.12), the fraction's numerator and denominator both depend on the "look direction" $(\theta_{\text{look}}, \phi_{\text{look}})$ only via g_{look}, which is maximum at $(\theta_{\text{look}}, \phi_{\text{look}}) = \left(\cos^{-1}\left(3^{-1/2}\right), \frac{\pi}{4}\right) \approx (54.7°, 45°)$ but minimum at $(\theta_{\text{look}}, \phi_{\text{look}}) = \left(\pi - \cos^{-1}\left(3^{-1/2}\right), \frac{5}{4}\pi\right) \approx (125.3°, 225°)$, regardless of α. Therefore, the local maximum and minimum of the fraction term is the same as that of the numerator and denominator. This implies that the beamwidth attains its maximum (minimum) where g_{look} is maximized (minimized) in terms of θ_{look} and ϕ_{look}.

Intuitively speaking, a larger α would shift each cardioid toward isotropy, hence a broader beam for the triad as a whole, leading to a higher value as one progresses from Fig. 2.7a at $\alpha = \frac{1}{4}$ through Fig. 2.7b at $\alpha = \frac{\sqrt{3}-1}{2} \approx 0.366025 \approx 0.37$ and Fig. 2.7c at $\alpha = \frac{1}{2}$ to Fig. 2.7d at $\alpha = 0.7$.

2.6 The Cardioid Triad's Array Gain

A beamformer's "array gain", $G(\theta_{\text{look}}, \phi_{\text{look}})$ is defined as the signal-to-noise ratio (SNR) at the beamformer's output relative to that at the input – while assuming that the beamformer "looks" toward the incident source's impinging direction, and while subject to additive noise that is spatially uncorrelated but spatially uniform in power. The beamformer output's SNR thus equals

$$\text{SNR}_{\text{out}}(\theta_{\text{look}}, \phi_{\text{look}}) \quad := \quad \frac{\left[\mathbf{w}^T \mathbf{a}^{(\alpha)}(\theta_{\text{look}}, \phi_{\text{look}})\right]^2 P_s}{\|\mathbf{w}\|^2 P_n}, \tag{2.6.1}$$

where $\mathbf{w}$ refers to the beamformer's weight vector. The beamformer input's SNR simply equals P_s/P_n, where P_s denotes the incident signal's power, and P_n represents the noise power.

For the "spatial matched filter" beamformer under consideration, it has $\mathbf{w} := \mathbf{a}^{(\alpha)}(\theta_{\text{look}}, \phi_{\text{look}})$, which is defined in (2.1.3). Hence, the "array gain" equals

$$\begin{aligned} G^{(\alpha)}\left(\theta_{\text{look}}, \phi_{\text{look}}\right) &= \frac{\left[\mathbf{a}^{(\alpha)}(\theta_{\text{look}}, \phi_{\text{look}})^T \mathbf{a}^{(\alpha)}(\theta_{\text{look}}, \phi_{\text{look}})\right]^2}{\left\|\mathbf{a}^{(\alpha)}(\theta_{\text{look}}, \phi_{\text{look}})\right\|^2} \\ &= \left\|\mathbf{a}^{(\alpha)}(\theta_{\text{look}}, \phi_{\text{look}})\right\|^2 \\ &= \left[3\alpha^2 + (1-\alpha)^2\right] + 2\alpha(1-\alpha) g_{\text{look}}. \end{aligned} \tag{2.6.2}$$

Figs.2.9a-2.9d plot $G^{(\alpha)}\left(\theta_{\text{look}}, \phi_{\text{look}}\right)$, for $\alpha = \frac{1}{4}, \frac{\sqrt{3}-1}{2} \approx 0.366025 \approx 0.37, \frac{1}{2}, 0.7$, respectively.

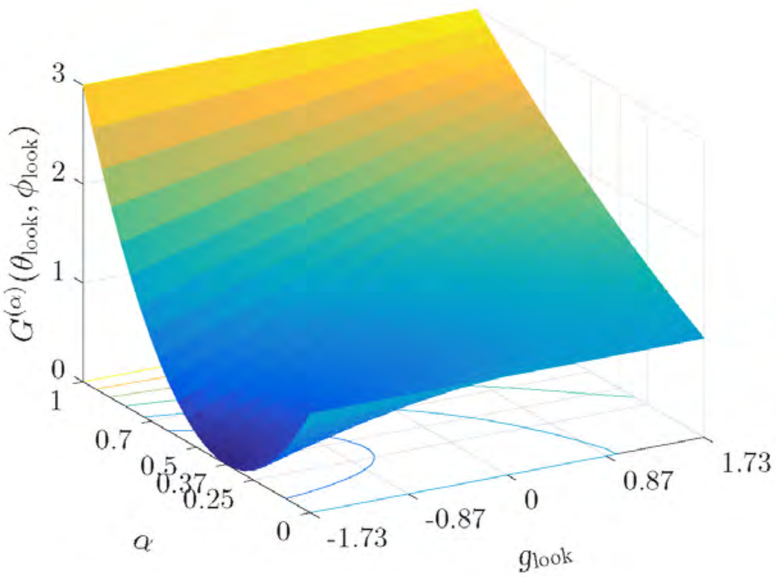

Figure 2.8: $G^{(\alpha)}(\theta_{\text{look}}, \phi_{\text{look}})$ plotted versus the "cardioidicity index" α and versus g_{look}.

Qualitative observations on the "array gain" $G^{(\alpha)}\left(\theta_{\text{look}}, \phi_{\text{look}}\right)$ of (2.6.2) and its corresponding Figs.2.9a-2.9d:

a) $G^{(\alpha)}\left(\theta_{\text{look}}, \phi_{\text{look}}\right)$ depends on the "look direction" $(\theta_{\text{look}}, \phi_{\text{look}})$ only through g_{look}, which is defined in (2.2.8). This $G^{(\alpha)}\left(\theta_{\text{look}}, \phi_{\text{look}}\right)$ monotonically increases with g_{look}, at any preset cardiodicity index α, in agreement with Fig. 2.8.

b) Concerning the general shape of $G^{(\alpha)}\left(\theta_{\text{look}}, \phi_{\text{look}}\right)$ with respect to $(\theta_{\text{look}}, \phi_{\text{look}})$ in Figs.2.9a-2.9d – This shape changes little with the cardiodicity index α, except

   b-1) a vertical displacement that varies with α through the leading term of $3\alpha^2 + (1-\alpha)^2$ in (2.6.2). This quadratic polynomial is concave upwards, with its minimum at $\alpha = \frac{\sqrt{3}-1}{2} \approx 0.366025 \approx 0.37$. Hence, the "supercardioid" triad's Fig. 2.9b has the least vertical displacement among Figs.2.9a-2.9d.

   b-2) the height variability (i.e. the difference between the maximum and the minimum of $\left\{G^{(\alpha)}\left(\theta_{\text{look}}, \phi_{\text{look}}\right), \forall \left(\theta_{\text{look}}, \phi_{\text{look}}\right)\right\}$) changes with α only through the

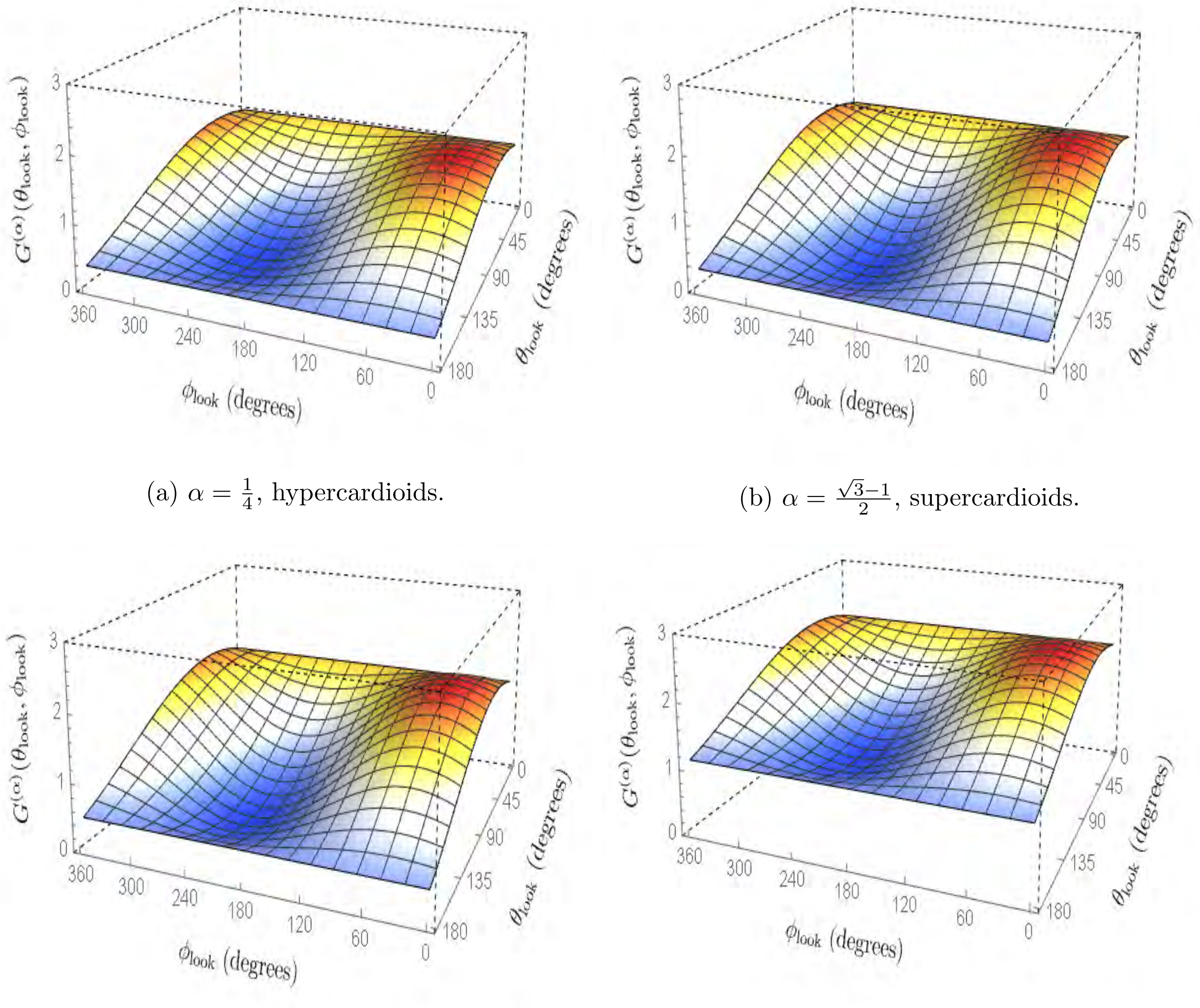

(a) $\alpha = \frac{1}{4}$, hypercardioids.

(b) $\alpha = \frac{\sqrt{3}-1}{2}$, supercardioids.

(c) $\alpha = \frac{1}{2}$, standard cardioids.

(d) $\alpha = 0.7$, subcardioids.

Figure 2.9: The array gain (G) versus the nominal "look direction" of $(\theta_{\text{look}}, \phi_{\text{look}})$ for various typical values of the "cardioidicity index".

second term's multiplicative factor of $2\alpha(1-\alpha)$, which is maximum at $\alpha = 0.5$, corresponding to the "standard cardioid" triad. This agrees with Fig. 2.9c showing the most height variability among Figs. 2.9a-2.9d.

c) At any preset "cardiodicity index" α, $G^{(\alpha)}(\theta_{\text{look}}, \phi_{\text{look}})$ (which is non-negative by definition) reaches its *min*imum of zero at

$$g_{\text{look,min}} = -\frac{3\alpha^2 + (1-\alpha)^2}{2\alpha(1-\alpha)}. \tag{2.6.3}$$

The right-hand side above is negative $\forall \alpha \in (0,1)$, but has a maximum of $-\sqrt{3}$. Hence, $g_{\text{look,min}} = -\sqrt{3}$, in agreement with Fig. 2.8. Recalling that g_{look} spans over the entire range of $[-\sqrt{3}, \sqrt{3}]$ regardless of α, $g_{\text{look,min}}$ corresponds to $[u_{\text{look,min}},$

$v_{\text{look,min}}, w_{\text{look,min}}]^T = -\frac{\sqrt{3}}{3}[1,1,1]^T$, hence $(\theta_{\text{look,min}}, \phi_{\text{look,min}}) = (125.26°, 225°)$, which represents the "look direction" that *min*imizes $G^{(\alpha)}(\theta_{\text{look}}, \phi_{\text{look}})$ for any "cardiodicity index" α.

d) At any preset "cardiodicity index" α, $G^{(\alpha)}(\theta_{\text{look}}, \phi_{\text{look}})$ is found by straightforward calculus to *max*imze at a "look direction" of $(\theta_{\text{look}}, \phi_{\text{look}}) = (54.73°, 45°)$, to a maximum value of $2[2-\sqrt{3}]\alpha^2 + 2[\sqrt{3}-1]\alpha + 1$. Hence, $g_{\text{look,max}} = \sqrt{3}$, in agreement with Fig. 2.8.

e) Intuitively speaking: If α increases, each individual cardioid's directive part of $(1-\alpha)\cos(\phi)$ would be lessen. Hence, the entire cardioid-triad's array gain would increase.

f) At a different preset "look directions" of $(\theta_{\text{look}}, \phi_{\text{look}})$, the "array gain" is minimum at possibly a different "cardiodicity index" α. This α value is found by zeroing $\dfrac{\partial}{\partial\alpha}G^{(\alpha)}(\theta_{\text{look}}, \phi_{\text{look}})$, to equal $\frac{g_{\text{look}}-1}{2g_{\text{look}}-4}$.

In the special case of the tri-axial velocity-sensor (i.e., where the "cardioidicity index" $\alpha = 0$), (2.6.2) degenerates to $G^{(0)}(\theta_{\text{look}}, \phi_{\text{look}}) = 1$, $\forall(\theta_{\text{look}}, \phi_{\text{look}})$.

2.7 The Cardioid Triad's Signal-To-Noise-Plus-Interference Ratio Gain

The beamformer's white noise gain which is the ratio of output and input SNR of the beamformer has been studied in Section 2.6. However, in most applications, aside from the signal of interest and the isotropic internal/thermal noise, other sources may be incident on the array from other specific directions. Therefore, the received signal is modelled as

$$\mathbf{y}(t) = \mathbf{a}^{(\alpha)}(\theta_s, \phi_s)s(t) + \sum_{m=1}^{M} \mathbf{a}^{(\alpha)}(\theta_m, \phi_m)v_m(t) + \mathbf{n}(t)$$

where $s(t)$ is the signal-of-interest and $v_m(t)$ is the mth interference signal. (θ_s, ϕ_s) is the direction of arrival of the signal of interest, (θ_m, ϕ_m) is the direction of arrival the mth interference.

For this analysis, it is assumed that the signal of interest, interference signals, and noise are uncorrelated. And the noise is additive white Gaussian noise with mean of zero and variance P_n. At the beamformer's input:

$$\begin{aligned} \text{SNIR} &:= \frac{P_s}{P_v + P_n} \\ &= \frac{\text{SNR}}{\text{INR}+1} \end{aligned} \tag{2.7.1}$$

where SNR $:= P_s/P_n$ is the signal-to-noise ratio, INR $:= P_v/P_n$ is the interference-to-noise ratio, $P_s = \mathrm{E}\{s(t)^2\}$ is the power of the signal of interest, $P_v = \sum_{m=1}^{M} P_{v,m} = \sum_{m=1}^{M} \mathrm{E}\{v_m(t)^2\}$ is the sum of the power of the interference signals, and $P_n = \mathrm{E}\{n(t)^2\}$ is the variance of the additive noise.

The beamformer outputs

$$\begin{aligned} B &= \mathbf{w}^T\, \mathbf{y}(t,\phi) \\ &= \mathbf{w}^T \mathbf{a}^{(\alpha)}(\theta_s,\phi_s)s(t) + \mathbf{w}^T \sum_{m=1}^{N} \mathbf{a}^{(\alpha)}(\theta_m,\phi_m)v_m(t) + \mathbf{w}^T\mathbf{n}(t) \end{aligned}$$

where $\mathbf{w} = \mathbf{a}^{(\alpha)}(\theta_{\text{look}},\phi_{\text{look}})$ is the beamforming weight vector and other variables are as previously defined.

At the output of the beamformer, the signal-to-noise-plus-interference ratio

$$\begin{aligned} \mathrm{SNIR}_o &= \frac{\mathbf{w}^T\mathbf{a}^{(\alpha)}(\theta_s,\phi_s)\mathbf{a}^{(\alpha)}(\theta_s,\phi_s)^T\mathbf{w}\ P_s}{\mathbf{w}^T\left(\sum_{m=1}^{M}\mathbf{a}^{(\alpha)}(\theta_m,\phi_m)\mathbf{a}^{(\alpha)}(\theta_m,\phi_m)^T P_{v,m}\right)\mathbf{w} + \|\mathbf{w}\|^2\ P_n} \\ &= \frac{\left(\mathbf{w}^T\mathbf{a}^{(\alpha)}(\theta_s,\phi_s)\right)^2\ \mathrm{SNR}}{\frac{1}{P_n}\sum_{m=1}^{M}\left(\mathbf{w}^T\mathbf{a}^{(\alpha)}(\theta_m,\phi_m)\right)^2 P_{v,m} + \|\mathbf{w}\|^2} \end{aligned} \tag{2.7.2}$$

By dividing (2.7.2) by (2.7.1), the beamformer's SNIR gain

$$\begin{aligned} G_{\mathrm{SNIR}} &= \frac{\mathrm{SNIR}_o}{\mathrm{SNIR}} \\ &= \frac{\left(\mathbf{w}^T\mathbf{a}^{(\alpha)}(\theta_s,\phi_s)\right)^2\ [1+\mathrm{INR}]}{\frac{1}{P_n}\sum_{m=1}^{M}\left(\mathbf{w}^T\mathbf{a}^{(\alpha)}(\theta_m,\phi_m)\right)^2 P_{v,m} + \|\mathbf{w}\|^2} \end{aligned} \tag{2.7.3}$$

Due to non-coincidence of the spatial-matched-filter beampattern (i.e true peak direction not equal to the look direction) as shown in Section 2.3, any interference arriving from the true peak direction $(\theta_{\text{peak}},\phi_{\text{peak}})$ will be amplified over the desired signal of interest arriving from the nominal look direction $(\theta_{\text{look}},\phi_{\text{look}})$. In that case, $G_{\mathrm{SNIR}} < 1$. However, with a perfect knowledge of the pointing bias, the look direction of the beamformer is chosen such that the desired signal arrives from the peak direction instead of the nominal look direction (i.e. $(\theta_s,\phi_s) = (\theta_{\text{peak}},\phi_{\text{peak}})$), (2.7.3) becomes

$$\begin{aligned} G_{\mathrm{SNIR}} &= \frac{\left(\mathbf{a}^{(\alpha)}(\theta_{\text{look}},\phi_{\text{look}})^T\mathbf{a}^{(\alpha)}(\theta_{\text{peak}},\phi_{\text{peak}})\right)^2\ [1+\mathrm{INR}]}{\frac{1}{P_n}\sum_{m=1}^{M}\left(\mathbf{a}^{(\alpha)}(\theta_{\text{look}},\phi_{\text{look}})^T\mathbf{a}^{(\alpha)}(\theta_m,\phi_m)\right)^2 P_{v,m} + \|\mathbf{a}^{(\alpha)}(\theta_{\text{look}},\phi_{\text{look}})\|^2} \\ &= \frac{\left(\alpha g_{\text{look}}^{(\alpha)} \pm (1-\alpha)\left\|\mathbf{a}^{(\alpha)}(\theta_{\text{look}},\phi_{\text{look}})\right\|\right)^2\ [1+\mathrm{INR}]}{\frac{1}{P_n}\sum_{m=1}^{M}\left(\mathbf{a}^{(\alpha)}(\theta_{\text{look}},\phi_{\text{look}})^T\mathbf{a}^{(\alpha)}(\theta_m,\phi_m)\right)^2 P_{v,m} + \|\mathbf{a}^{(\alpha)}(\theta_{\text{look}},\phi_{\text{look}})\|^2} \end{aligned} \tag{2.7.4}$$

where $g_{\text{look}}^{(\alpha)}$ is as defined in (2.1.6). It has been shown in Section 2.3.1 that for $\alpha \in (0,1)$,

$\theta \in [0, \pi]$, and $\phi \in [0, 2\pi)$, $|\mathbf{a}^{(\alpha)}(\theta_{\text{look}}, \phi_{\text{look}})^T \mathbf{a}^{(\alpha)}(\theta_{\text{peak}}, \phi_{\text{peak}})| > |\mathbf{a}^{(\alpha)}(\theta_{\text{look}}, \phi_{\text{look}})^T \mathbf{a}^{(\alpha)}(\theta, \phi)|$. Therefore, as INR increases, the numerator of (2.7.4) is greater than its denominator, hence $G_{\text{SNIR}} > 1$. For a case of single interference ($M = 1$), the SNIR gain (2.7.4) reduces to

$$G_{\text{SNIR}} \;=\; \frac{\left(\alpha g_{\text{look}}^{(\alpha)} \pm (1-\alpha) \left\|\mathbf{a}^{(\alpha)}(\theta_{\text{look}}, \phi_{\text{look}})\right\|\right)^2 \; [1 + \text{INR}]}{\text{INR}\left(\mathbf{a}^{(\alpha)}(\theta_{\text{look}}, \phi_{\text{look}})^T \mathbf{a}^{(\alpha)}(\theta_m, \phi_m)\right)^2 + \left\|\mathbf{a}^{(\alpha)}(\theta_{\text{look}}, \phi_{\text{look}})\right\|^2}, \qquad (2.7.5)$$

where $g_{\text{look}}^{(\alpha)}$ is as previously defined.

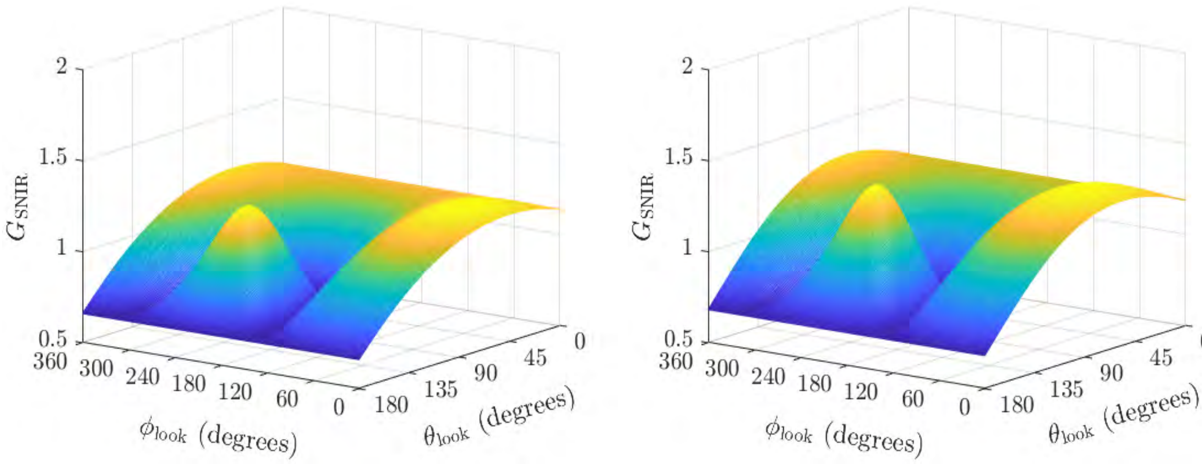

(a) INR $= -3.0103$dB, $(\delta_\theta, \delta_\phi) = (5°, 5°)$.

(b) INR $= -3.0103$dB, $(\delta_\theta, \delta_\phi) = (20°, 30°)$.

(c) INR $= 10$dB, $(\delta_\theta, \delta_\phi) = (5°, 5°)$.

(d) INR $= 10$dB, $(\delta_\theta, \delta_\phi) = (20°, 30°)$.

Figure 2.10: Array's signal-to-noise-plus-interference ratio gain (G_{SNIR}) versus the nominal "look direction" $(\theta_{\text{look}}, \phi_{\text{look}})$ for $\alpha = \frac{1}{4}$ (hypercardioid) and $(\delta_\theta, \delta_\phi)$ - the interference's offset from true peak direction $(\theta_{\text{peak}}, \phi_{\text{peak}})$.

The plots of (2.7.5) versus look direction $(\theta_{\text{look}}, \phi_{\text{look}})$ are shown in Figures 2.10 - 2.13 for various values of INR and interference's offset from the true peak direction $(\delta_\theta, \delta_\phi) := (\theta_{\text{peak}}, \phi_{\text{peak}}) - (\theta_m, \phi_m)$.

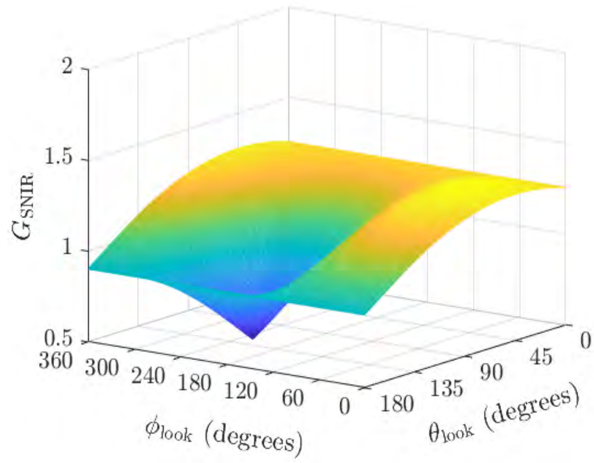

(a) INR $= -3.0103$dB, $(\delta_\theta, \delta_\phi) = (5°, 5°)$.

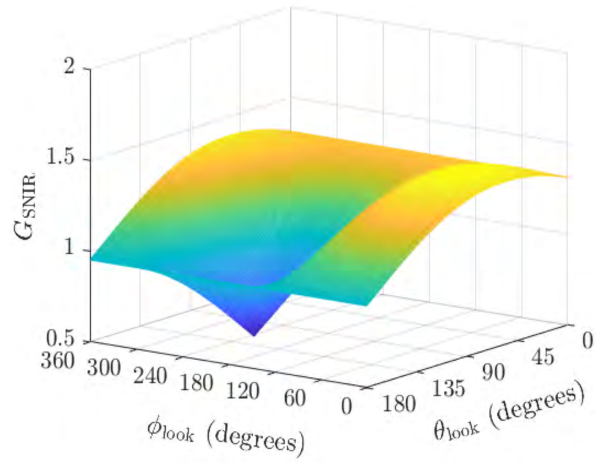

(b) INR $= -3.0103$dB, $(\delta_\theta, \delta_\phi) = (20°, 30°)$.

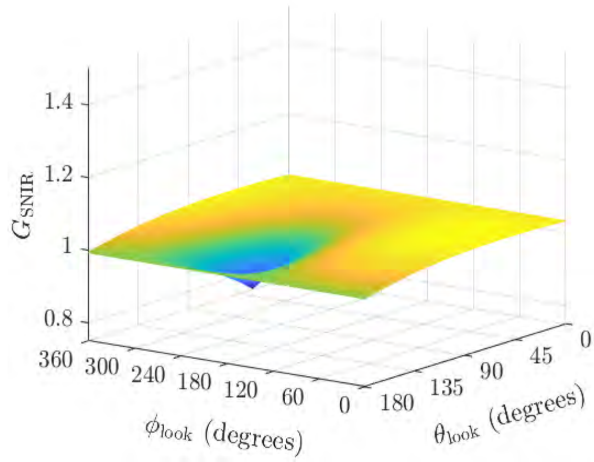

(c) INR $= 10$dB, $(\delta_\theta, \delta_\phi) = (5°, 5°)$.

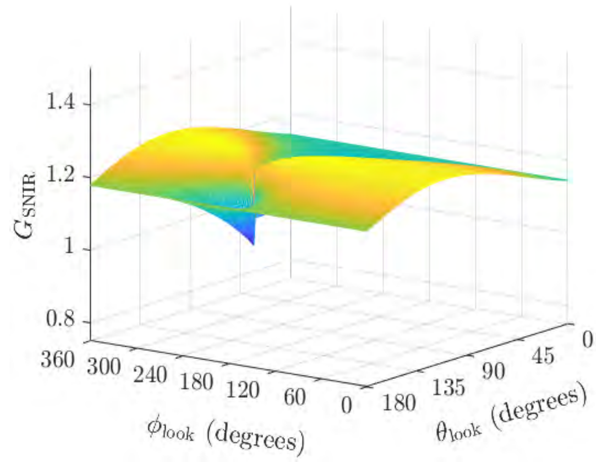

(d) INR $= 10$dB, $(\delta_\theta, \delta_\phi) = (20°, 30°)$.

Figure 2.11: Array's signal-to-noise-plus-interference ratio gain (G_{SNIR}) versus the nominal "look direction" $(\theta_{\mathrm{look}}, \phi_{\mathrm{look}})$ for $\alpha = \frac{\sqrt{3}-1}{2}$ (supercardioid) and $(\delta_\theta, \delta_\phi)$ - the interference's offset from true peak direction $(\theta_{\mathrm{peak}}, \phi_{\mathrm{peak}})$.

The array's SNIR gain increases as the angular separation of the signal of interest and interference widens. This is noticed going across (a) to (b), and (c) to (d) of Figures 2.10 - 2.13.

Generally, the SNIR gain depends on the angular separation of the source and the interference, and also the ratio of the power of the interference to the power of the thermal noise. For INR > 1, the closer the interference to the signal of interest, the lesser the SNIR gain.

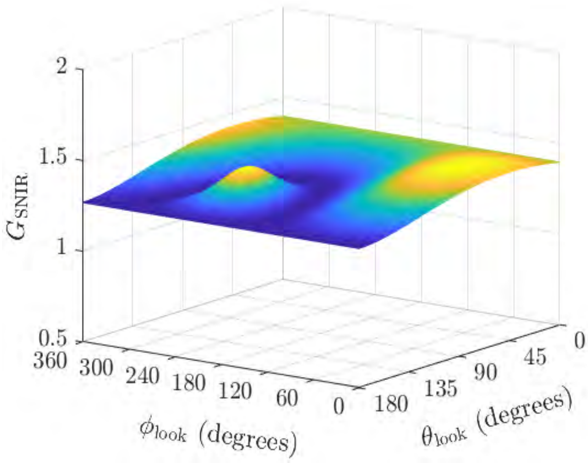

(a) INR $= -3.0103$dB, $(\delta_\theta, \delta_\phi) = (5^\circ, 5^\circ)$.

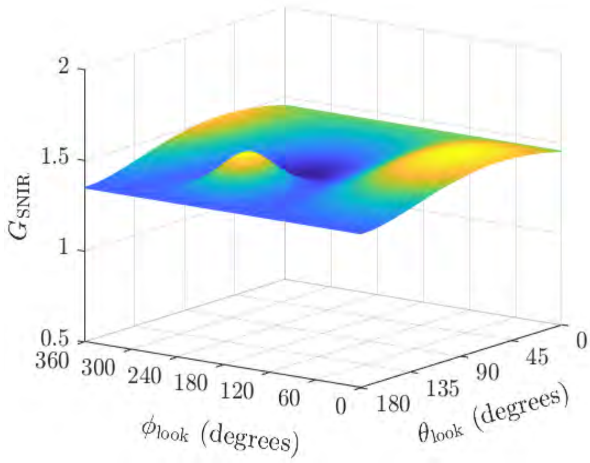

(b) INR $= -3.0103$dB, $(\delta_\theta, \delta_\phi) = (20^\circ, 30^\circ)$.

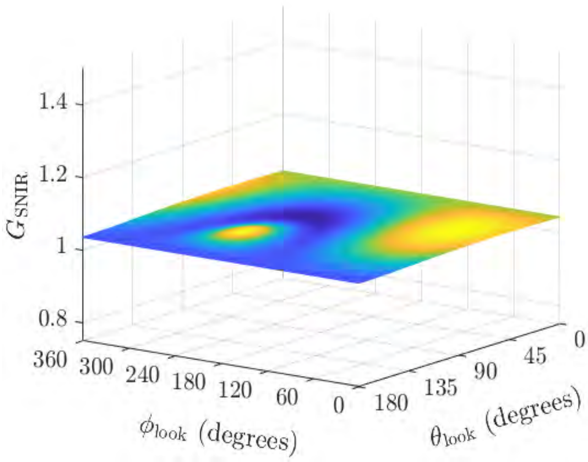

(c) INR $= 10$dB, $(\delta_\theta, \delta_\phi) = (5^\circ, 5^\circ)$.

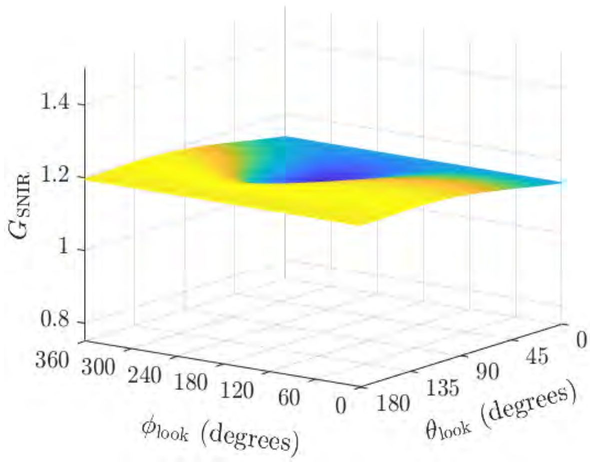

(d) INR $= 10$dB, $(\delta_\theta, \delta_\phi) = (20^\circ, 30^\circ)$.

Figure 2.12: Array's signal-to-noise-plus-interference ratio gain (G_{SNIR}) versus the nominal "look direction" $(\theta_{\text{look}}, \phi_{\text{look}})$ for $\alpha = \frac{1}{2}$ (standard cardioid) and $(\delta_\theta, \delta_\phi)$ - the interference's offset from true peak direction $(\theta_{\text{peak}}, \phi_{\text{peak}})$.

2.8 Summary

This work generalizes the customary tri-axial velocity-sensor to a cardioid triad, in that the former represents a special case of the latter when the "cardioidicity index" (α) degenerates to zero. This work is first in the open literature (to the present authors' best knowledge) to propose and to investigate a collocated triad of orthogonally oriented cardioids.

This cardioid triad's "spatial matched filter" beam-pattern can have a higher mainlobe -to-sidelobe height ratio, or can avoid sidelobes altogether if $\alpha \geq \frac{1}{2}$. The cardioid triad's array gain can also be significantly higher. A pointing offset, however, exists between the nominal "look direction" and the "spatial matched filter" beam-pattern's actual peak direction. Nonetheless, this *nominal* pointing error can be readily mitigated by the closed-

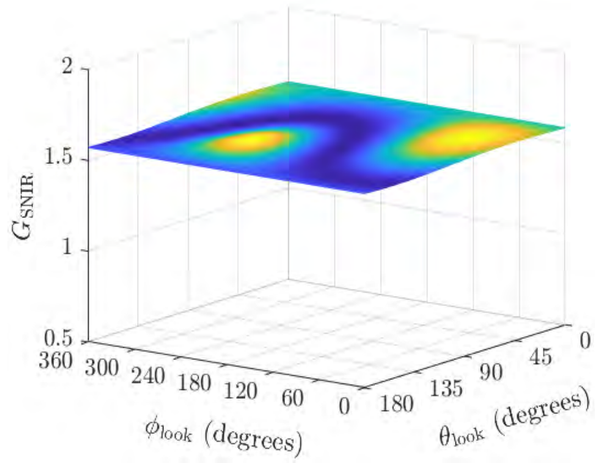

(a) INR $= -3.0103$dB, $(\delta_\theta, \delta_\phi) = (5^\circ, 5^\circ)$.

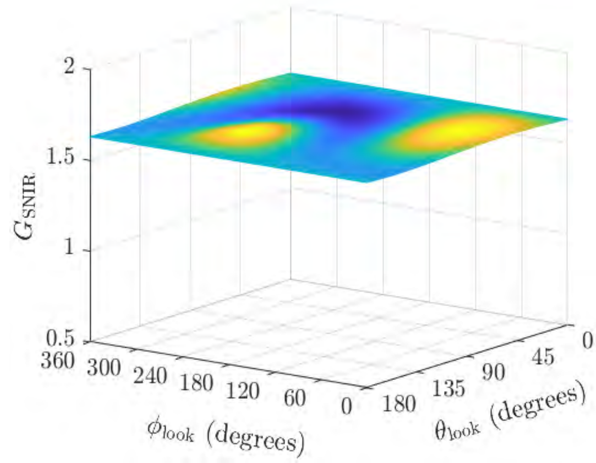

(b) INR $= -3.0103$dB, $(\delta_\theta, \delta_\phi) = (20^\circ, 30^\circ)$.

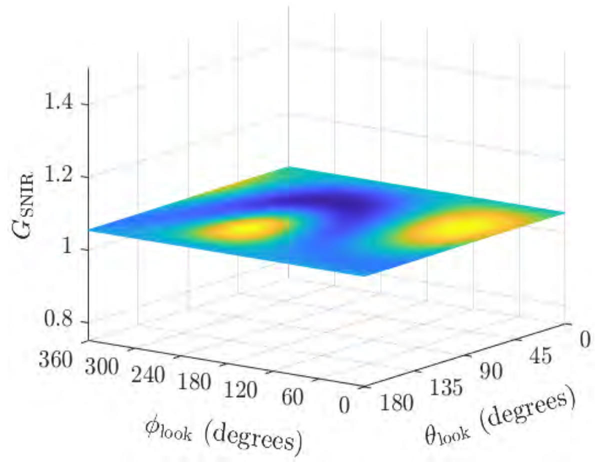

(c) INR $= 10$dB, $(\delta_\theta, \delta_\phi) = (5^\circ, 5^\circ)$.

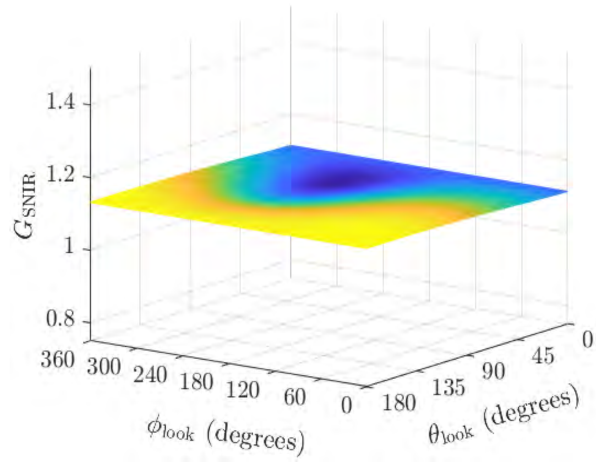

(d) INR $= 10$dB, $(\delta_\theta, \delta_\phi) = (20^\circ, 30^\circ)$.

Figure 2.13: Array's signal-to-noise-plus-interference ratio gain (G_{SNIR}) versus the nominal "look direction" $(\theta_{\text{look}}, \phi_{\text{look}})$ for $\alpha = 0.7$ (subcardioid) and $(\delta_\theta, \delta_\phi)$ - the interference's offset from true peak direction $(\theta_{\text{peak}}, \phi_{\text{peak}})$.

form formula derived in this chapter to pre-correct the nominal "look direction".

This study seems to be first to propose, for beamforming, the use of such a triad of orthogonal and collocated cardioidic sensors. Compared to the better known tri-axial velocity-sensor, this cardioidic triad could sharpen the mainlobe and could raise the peak-to-sidelobe height ratio and the array gain. Such a cardioidic triad is also physically compact, hence portable for mobile deployment, indoor or outdoor (including on the battlefield).

Chapter 3
Cardioid Microphones/Hydrophones in a Collocated and Orthogonal Triad – A New Beamformer with No Beam-Pointing Error

3.1 Overview

3.1.1 Cardioid Sensors

Cardioid sensors has a directionality shaped like a heart, hence their name. Cardioid sensors' directionality emphasizes the front side of the sensor, without the front/back directional ambiguity of "figure-8" sensors. Mathematically, the cardioid sensor's gain pattern equals $\alpha + (1-\alpha)\cos(\psi)$, where ψ refers to the incident signal's direction-of-arrival relative to the cardioid sensor's axis. In the above, α denotes the "cardioidicity index": $\alpha = 1$ gives an isotropic sensor (e.g. a pressure sensor); $\alpha = 0.7$ gives a "subcardioid"; $\alpha = 0.5$ gives a "standard cardioid"; $\alpha = \frac{\sqrt{3}-1}{2} \approx 0.366$ gives a "supercardioid"; $\alpha = \frac{1}{4}$ gives a "hypercardioid"; $\alpha = 0$ gives a uni-axial velocity-sensor.

Cardioid sensors have been in practical use for nearly a century, and have numerous commercial models in present-day use. For a brief introduction to cardioid sensors, please refer to Chapter 1.

3.1.2 A Triad of Cardioid Sensors in Orthogonal Orientation and in Spatial Collocation

Consider three cardioid sensors, all of the same cardioidicity index $\alpha \in (0,1)$, all collocating at the Cartesian origin, but each oriented along a distinct Cartesian axis. Such a triad's array manifold (2.1.1) is independent of the incident signal's frequency:

$$\mathbf{a}^{(\alpha)}(\theta,\phi) \quad := \quad \begin{bmatrix} \alpha + (1-\alpha)\sin(\theta)\cos(\phi) \\ \alpha + (1-\alpha)\sin(\theta)\sin(\phi) \\ \alpha + (1-\alpha)\cos(\theta) \end{bmatrix}, \tag{3.1.1}$$

where $\theta \in [0,\pi]$ represents the impinging acoustic wave's incident polar angle measured from the positive z-axis, and $\phi \in [0, 2\pi)$ symbolizes the incident azimuth angle measured from the positive x-axis.

To ease the ensuing analysis, define the Cartesian direction cosines along x-, y-, and z-axes :

$$\begin{aligned} u &:= \sin(\theta)\cos(\phi), \\ v &:= \sin(\theta)\sin(\phi), \\ w &:= \cos(\theta), \end{aligned}$$

which give this alternative expression to the array manifold in (3.1.1):

$$\mathbf{a}^{(\alpha)}(u,v,w) \quad := \quad \begin{bmatrix} u^{(\alpha)} \\ v^{(\alpha)} \\ w^{(\alpha)} \end{bmatrix} \quad := \quad \begin{bmatrix} \alpha + (1-\alpha)u \\ \alpha + (1-\alpha)v \\ \alpha + (1-\alpha)w \end{bmatrix}. \tag{3.1.2}$$

If $\alpha = 0$, the special case of a tri-axial vector-sensor results. If $\alpha = 1$, the special case of an isotropic sensor is obtained.

The frequency independence of the cardioid triad's array manifold means a decoupling of the azimuth-elevation spatial dimensions from the frequency dimension, thereby greatly simplifying space-time signal processing.

Despite $u^2 + v^2 + w^2 = 1$, $\forall\theta$, $\forall\phi$, the following inequality:

$$\left(u^{(\alpha)}\right)^2 + \left(v^{(\alpha)}\right)^2 + \left(w^{(\alpha)}\right)^2 \quad \neq \quad 1,$$

would generally hold $\forall\alpha > 0$.[1]

3.1.3 The Proposed Beamformer

This chapter will propose a new data-independent beamformer, as an alternative to the well known spatial-matched-filter (SMF) beamformer, which almost always suffers beam-pointing error as shown in Section 2.3 when applied to a cardioidic triad, the resulting SMF beam-pattern [21].

Instead, this chapter will propose a new beamformer, matched spatially not to the cardioidic triad's array manifold $\mathbf{a}^{(\alpha)}(\theta_{\text{look}}, \phi_{\text{look}})$ as in Chapter 1, but matched to the Cartesian direction cosines of the "look direction" $(\theta_{\text{look}}, \phi_{\text{look}})$.[2] Here, $\theta_{\text{look}} \in [0, \pi]$ symbolizes the look direction's polar angle and $\phi_{\text{look}} \in [0, 2\pi)$ denotes the look direction's azimuth angle.

[1]This becomes a equality only at $u + v + w = (1-2\alpha)/(1-\alpha)$ for $\alpha \in (0, \sqrt{3}-1]$.

[2]If and only if the cardioid sensors have $\alpha = 0$ (i.e. the cardioid triad becoming a tri-axial velocity-sensor [35, 37]), this beamforming weight vector would be matched to the triad's array manifold.

That is, the proposed beamforming weight vector is defined as

$$\mathbf{w} \quad := \quad \begin{bmatrix} u_{\text{look}} \\ v_{\text{look}} \\ w_{\text{look}} \end{bmatrix} \quad := \quad \begin{bmatrix} \cos(\phi_{\text{look}})\sin(\theta_{\text{look}}) \\ \sin(\phi_{\text{look}})\sin(\theta_{\text{look}}) \\ \cos(\theta_{\text{look}}) \end{bmatrix}, \tag{3.1.3}$$

This proposed beamformer would output a scalar:

$$\begin{aligned} B &= \mathbf{w}^T \, \mathbf{a}^{(\alpha)}(u,v,w), \\ &= \alpha \overbrace{(u_{\text{look}} + v_{\text{look}} + w_{\text{look}})}^{g_{\text{look}} \, :=} + (1-\alpha) \overbrace{(u_{\text{look}}u + v_{\text{look}}v + w_{\text{look}}w)}^{\tilde{B} \, :=}, \end{aligned} \tag{3.1.4}$$

where ^{T} represents transpose operation. The amplitude pattern in (3.1.4) can take on negative values. The most negative amplitude in B may correspond to a local peak in the magnitude pattern $|B|$.

The first term, αg_{look}, is independent of (θ, ϕ), but constitutes an amplitude offset. Hence, αg_{look} cannot affect the beamformer's pointing accuracy.

The second term, $\tilde{B}$, has been shown to produce no beam-pointing bias. For details, please refer to Section 2.2.1 . This second term, in fact, equals the spatial-matched-filter beampattern of a tri-axial velocity-sensor.

Given the above two paragraphs, the proposed new beamformer's weights would lead to no beam-pointing bias in (3.1.4).

3.1.4 Organization of this Chapter

The rest of this chapter is organized as follows: Section 3.2 will analytically derive the location(s) of the lobe(s) of the proposed beamformer output pattern. The condition where only one lobe exists will also be analytically derived. Section 3.3 will analytically derive each lobe's height. Section 3.4 will analytically derive the main lobe's "width". Section 3.5 will analytically derive the directivity. Section 3.6 will analytically derive the array gain. Section 3.8 will compare this newly proposed beamformer with the established spatial-matched-filter beamformer in terms of mainlobes height, second lobes height, height-ratio, beamwidth, and array gain. Section 3.9 will conclude this entire investigation.

3.2 Existence/Non-Existence of a Second Lobe

This section will analytically prove that a lobe always exists in the magnitude pattern $|B|$ along the nominal "look direction" if either

(i) $\alpha \in \left[0, \frac{\sqrt{3}-1}{2}\right)$, or

(ii) the "look direction" is limited to the hemisphere $u_{\text{look}} + v_{\text{look}} + w_{\text{look}} \geq 0$.

Toward this end, Section 3.2.1 will analytically derive the location(s) the amplitude pattern's (B) critical point(s) in the Cartesian spatial coordinates (u, v, w).

Then, the necessary and sufficient conditions, by which the magnitude pattern $|B|$ would have a second lobe, will then be derived in Section 3.2.3.

3.2.1 To Locate the Amplitude Pattern's Critical Points

This Section 3.2.1 will analytically prove that the amplitude pattern B

(i) always has a local maximum at $(u, v, w) = (u_{\text{look}}, v_{\text{look}}, w_{\text{look}})$, or equivalently $(\theta, \phi) = (\theta_{\text{look}}, \phi_{\text{look}})$, and

(ii) always has a local minimum at $(u, v, w) = (u_{\text{other}},\ v_{\text{other}},\ w_{\text{other}}) = (-u_{\text{look}},\ -v_{\text{look}},\ -w_{\text{look}})$, or equivalently $(\theta_{\text{other}}, \phi_{\text{other}}) = (\pi - \theta_{\text{look}}, [\pi + \phi_{\text{look}}] \mod 2\pi)$,

(iii) can never have any third critical point under any circumstance.

The beampattern of (3.1.4) depends on the impinging source's incident direction (u, v, w), only through

$$\tilde{B} \quad := \quad [u, v, w] \left[\mathbf{a} \left(u_{\text{look}}, v_{\text{look}}, w_{\text{look}} \right) \right], \tag{3.2.1}$$

which embodies an inner product between the vector $[u, v, w]^T$ and $\mathbf{a} \left(u_{\text{look}}, v_{\text{look}}, w_{\text{look}} \right)$.

This $\tilde{B}$, hence B of (3.1.4), is maximized if both $[u, v, w]^T$ and $\mathbf{a} \left(u_{\text{look}}, v_{\text{look}}, w_{\text{look}} \right)$ point toward the same direction, as stipulated by the Cauchy-Schwarz inequality.

Hence, one critical point of B lies at $(u, v, w) =$

$$\left(u_{c_1}, v_{c_1}, w_{c_1} \right) \quad = \quad \left(u_{\text{look}}, v_{\text{look}}, w_{\text{look}} \right). \tag{3.2.2}$$

On the other hand, if $[u, v, w]^T$ and $\mathbf{a} \left(u_{\text{look}}, v_{\text{look}}, w_{\text{look}} \right)$ are diametrically opposite in direction, $\tilde{B}$ (and thus B) would be minimized. Hence, a second critical point lies at $(u, v, w) =$

$$\left(u_{c_2}, v_{c_2}, w_{c_2} \right) \quad = \quad - \left(u_{\text{look}}, v_{\text{look}}, w_{\text{look}} \right), \tag{3.2.3}$$

The above (3.2.2) and (3.2.3) hold for all cardioidicity index $\alpha \in [0, 1)$ and for all "look directions" $\left(u_{\text{look}}, v_{\text{look}}, w_{\text{look}} \right)$.

Appendix A will show, via the method of Lagrange multipliers, that no third critical point can possibly exist.

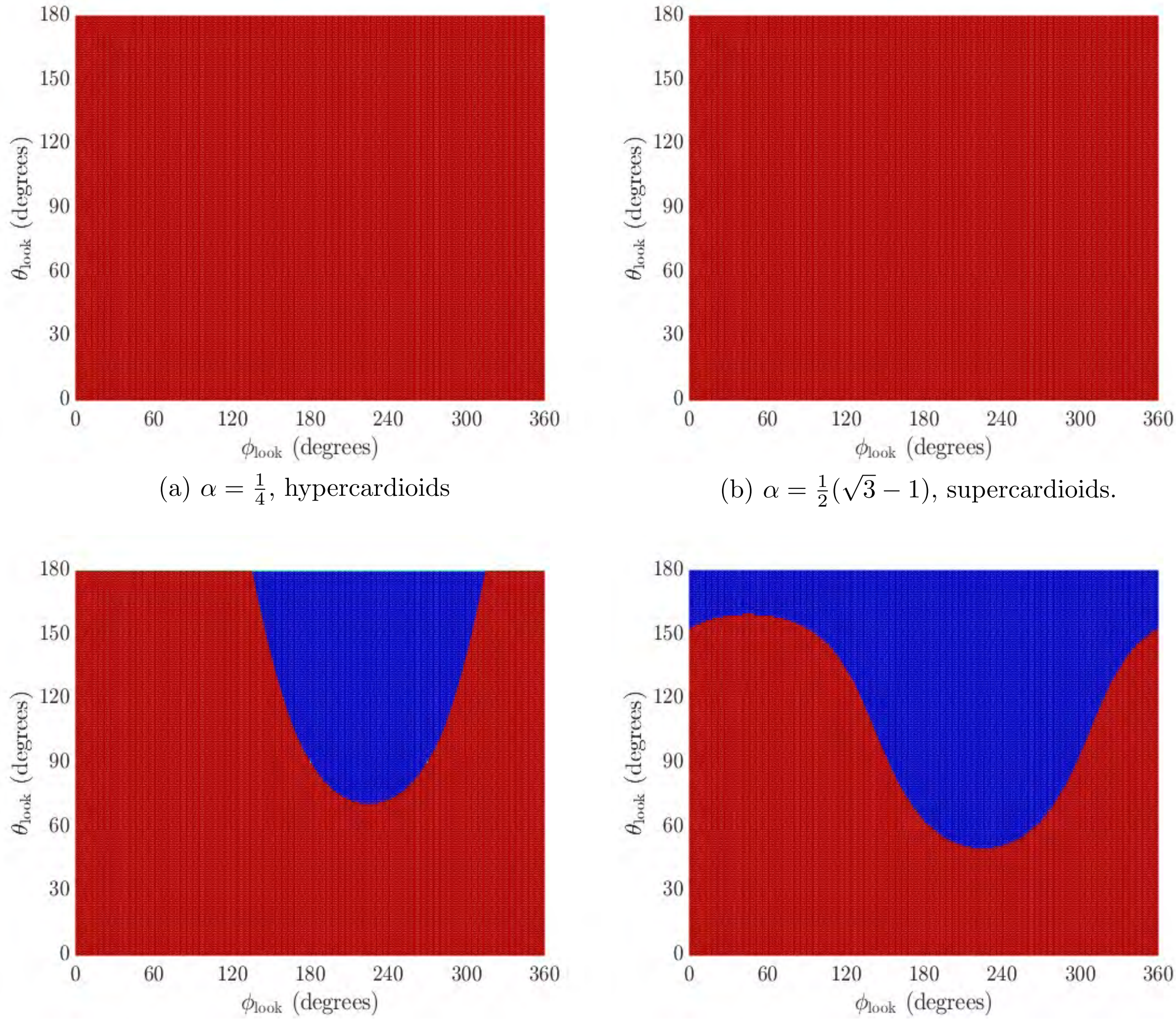

(a) $\alpha = \frac{1}{4}$, hypercardioids

(b) $\alpha = \frac{1}{2}(\sqrt{3}-1)$, supercardioids.

(c) $\alpha = \frac{1}{2}$, standard cardioids.

(d) $\alpha = 0.7$, subcardioids.

Figure 3.1: A map showing region in bivariate $(\theta_{\text{look}}, \phi_{\text{look}})$ space for which (3.2.4) holds, i.e when $|B|$ has a local peak in the look direction (red), and region where (3.2.4) does not hold (blue) for various typical values of the "cardioidicity index".

3.2.2 The Magnitude Pattern at the First Critical Point

This Section 3.2.2 shows that for $\alpha \in [0, \frac{\sqrt{3}-1}{2})$, a peak always exists in $|B|$ at $(\theta, \phi) = (\theta_{\text{look}}, \phi_{\text{look}})$ for all $(\theta_{\text{look}}, \phi_{\text{look}})$.

The "look direction" does not always have a local peak in magnitude pattern $|B|$. This section will identify the circumstances under which this occurs.

For the magnitude pattern $|B|$ to have a local peak at the "look direction",

$$\begin{aligned} B|_{(\theta,\phi)=(\theta_{\text{look}},\phi_{\text{look}})} &= \alpha g_{\text{look}} + (1-\alpha) > 0 \\ \Leftrightarrow \quad g_{\text{look}} &> (\alpha - 1)/\alpha. \end{aligned} \tag{3.2.4}$$

As the minimum value of the left side of (3.2.4) equals $-\sqrt{3}$, the inequality (3.2.4) will always be true for all g_{look} $(\forall(u_{\text{look}}, v_{\text{look}}, w_{\text{look}}))$ given α that makes the right side of (3.2.4) always less than $-\sqrt{3}$, i.e.

$$\alpha \;<\; \frac{\sqrt{3}-1}{2} \;\approx\; 0.366. \tag{3.2.5}$$

For $\alpha \in [0, \frac{1}{2}(\sqrt{3}-1))$ (3.2.4) always holds, but for $\alpha \in [\frac{1}{2}(\sqrt{3}-1), 1]$ (3.2.4) does not always hold. The region on the bivariate $(\theta_{\text{look}}, \phi_{\text{look}})$ plane for which (3.2.4) holds is filled red in Figure 3.1.

3.2.3 The Condition for a Lobe to Exist at Other than the "Look Direction"

If a lobe exists in the magnitude pattern $|B|$ outside the "look direction", that must exists at $(u, v, w) = (u_{c_2}, v_{c_2}, w_{c_2})$, which would give a local peak only if the amplitude

$$B|_{(u,v,w)=(u_{c_2},v_{c_2},w_{c_2})} \;<\; 0. \tag{3.2.6}$$

Otherwise, $(u, v, w) = (u_{c_2}, v_{c_2}, w_{c_2})$ would provide a null, not a peak in the magnitude $|B|$. The above (3.2.6) is equivalent to

$$\begin{aligned} B|_{(u,v,w)=(-u_{\text{look}},-v_{\text{look}},-w_{\text{look}})} \;&=\; \alpha\, g_{\text{look}} - (1-\alpha) \;<\; 0, \\ \Leftrightarrow\; g_{\text{look}} \;&<\; \frac{(1-\alpha)}{\alpha}, \end{aligned} \tag{3.2.7}$$

which represents the necessary and the sufficient condition for a lobe to exist at $(u, v, w) = (-u_{\text{look}}, -v_{\text{look}}, -w_{\text{look}})$. As the maximum value of the left side of (3.2.7) equals $\sqrt{3}$, the inequality (3.2.7) will always be true for all g_{look} $(\forall(u_{\text{look}}, v_{\text{look}}, w_{\text{look}}))$ given α that makes the right side of (3.2.7) always greater than $\sqrt{3}$, i.e.

$$\alpha \;<\; \frac{\sqrt{3}-1}{2} \;\approx\; 0.366. \tag{3.2.8}$$

3.2.4 Condition for two lobes to exists simultaneously

The condition for a lobe to exist in $|B|$ in the look direction has been derived in Section 3.2.2, while the condition for a lobe to exist in $|B|$ in the other direction has been derived in Section 3.2.3. The condition for the two lobes to exist simultaneously in $|B|$ is derived in this section.

Two lobes can only exist simultaneously in $|B|$ (i.e. in the look direction and other direction) if and only if the signs of the beampattern at the two critical points are mutually different, i.e.

$$\begin{aligned} B|_{(u,v,w)=(u_{\text{look}},v_{\text{look}},w_{\text{look}})}\ B|_{(u,v,w)=(u_{\text{other}},v_{\text{other}},w_{\text{other}})} &< 0 \\ [\alpha g_{\text{look}} + (1-\alpha)]\,[\alpha g_{\text{look}} - (1-\alpha)] &< 0 \\ \implies g^2_{\text{look}} < \frac{(1-\alpha)^2}{\alpha^2} \end{aligned} \tag{3.2.9}$$

$(1-\alpha) > 0$ and $\alpha > 0$, while $g_{\text{look}} \in [-\sqrt{3}, \sqrt{3}]$ hence (3.2.9) implies that $|g_{\text{look}}| < \frac{(1-\alpha)}{\alpha}$, i.e.

$$\frac{-(1-\alpha)}{\alpha} < g_{\text{look}} < \frac{(1-\alpha)}{\alpha} \tag{3.2.10}$$

which are both always satisfied for $\alpha \in [0, \frac{1}{2}(\sqrt{3}-1))$. For $\alpha \in [\frac{1}{2}(\sqrt{3}-1), 1)$ condition (3.2.9) must be satisfied for two lobes to exists simultaneously in $|B|$.

The region defined in (3.2.9) is shown in Figure 3.2.

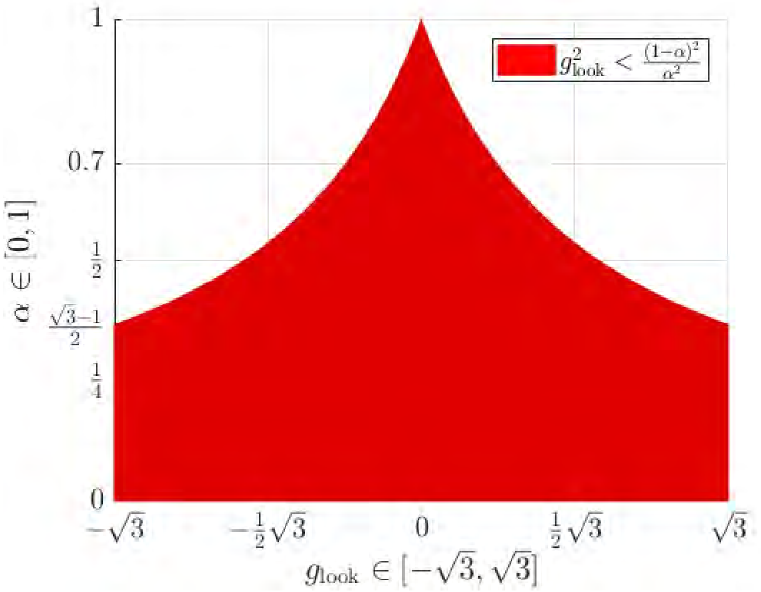

Figure 3.2: Map of $g^2_{\text{look}} < \frac{(1-\alpha)^2}{\alpha^2}$ versus α and g_{look}. The red region depicts where $g^2_{\text{look}} < \frac{(1-\alpha)^2}{\alpha^2}$ is true.

On account of (3.2.5) and (3.2.8) (which are equivalent to (3.2.9)), regardless of the "look direction", a two lobes must exist simultaneously for a triad composed of hypercardioids (which has $\alpha = \frac{1}{4}$) and indeed for any cardioids with $\alpha \in \left(0, \frac{\sqrt{3}-1}{2}\right)$.

For a triad comprising "supercardioids" (i.e. with $\alpha = \frac{\sqrt{3}-1}{2}$), or "standard cardioids" (i.e. with $\alpha = \frac{1}{2}$), or "subcardioids" (i.e. with $\alpha = 0.7$) — only one lobe would exist for those "look directions" that violate (3.2.9). [3]

[3]For a triad of "supercardioids" (i.e. with $\alpha = \frac{\sqrt{3}-1}{2}$), only those "look directions" corresponding to $g_{\text{look}} = \pm\sqrt{3}$ would not have sidelobes.

Over all possible "look directions" $\{\forall(\theta, \phi)\}$, small subregions exist where no second lobe exists (hence the height-ratio would be undefined there), because (3.2.9) is violated. For the special case of super-cardioids (i.e. $\alpha = \frac{1}{2}(\sqrt{3} - 1)$), no second lobe would exist only at $g_{\text{look}} = \pm\sqrt{3}$, meaning $(\theta_{\text{look}}, \phi_{\text{look}}) = (54.74°, 45°)$ and $(\theta_{\text{look}}, \phi_{\text{look}}) = (125.26°, 225°)$. These correspond to where the two spikes appear in the subsequent Figure 3.5c.

3.3 The Lobes' Height Ratio

The lobes' height ratio (HR) is defined here as the ratio of the "look direction" peak's height relative to the other lobe's height. This section's analysis will assume that this second lobe exists, having satisfied the condition derived in 3.2.3.

3.3.1 The Mainlobe's Height

The mainlobe's height may be found by substituting (3.2.2) into (3.1.4):

$$h_{\text{look}} \quad = \quad \alpha g_{\text{look}} + (1 - \alpha). \tag{3.3.1}$$

This h_{look} is plotted in Figures 3.4a, 3.5a, 3.6a, and 3.7a. The following observations may be made:

(i) Over all possible "look directions", h_{look} would be highest at $g_{\text{look}} = \sqrt{3}$, attaining a maximum height of $(\sqrt{3} - 1)\alpha + 1$.

Figure 3.16b shows that $h_{\text{look}} \to 0$ when both $g_{\text{look}} \to 0$ and $\alpha \to 1$. Figure 3.16b also shows that $h_{\text{look}} = 0$ for $g_{\text{look}} = \frac{1-\alpha}{\alpha}$

3.3.2 The Second Lobe's Height

The second lobe (if it exists) must point diametrically opposite the "look direction", on account of (3.2.2) and (3.2.3), Therefore, this second lobe's height equals

$$h_{\text{other}} \quad = \quad |\alpha g_{\text{look}} - (1 - \alpha)|. \tag{3.3.2}$$

This h_{other} is plotted in Figures 3.4b, 3.5b, 3.6b, and 3.7b. The following observations may be noted:

(ii) $h_{\text{other,max}} = h_{\text{other}}(g_{\text{look}} = -\sqrt{3}) = (\sqrt{3} - 1)\alpha + 1$, similarly obtained in (i) above.

(iii) Figure 3.17b shows that $h_{\text{other}}(\alpha = 1, g_{\text{look}} = 0) = 0$, and $h_{\text{other}}(\alpha, g_{\text{look}} = \frac{1-\alpha}{\alpha}) = 0$.

3.3.3 The Height Ratio

The height ratio (if a second lobe exists) equals

$$\begin{aligned} \mathrm{HR}^{(\alpha)}(g_{\mathrm{look}}) &:= \frac{h_{\mathrm{look}}}{h_{\mathrm{other}}} \\ &= \frac{|\alpha g_{\mathrm{look}} + (1-\alpha)|}{|\alpha g_{\mathrm{look}} - (1-\alpha)|}, \end{aligned} \tag{3.3.3}$$

which depends on only g_{look} and the cardiodicity index α.

The following observations may be made on (3.3.3):

(iv) Over all possible "look directions", the height ratio is minimum at $g_{\mathrm{look}} = -\sqrt{3}$, resulting in a ratio of exactly $\frac{(\sqrt{3}+1)\alpha-1}{(\sqrt{3}-1)\alpha+1}$ for $\alpha \in (0, \frac{\sqrt{3}-1}{2})$.

(v) $B|_{(u,v,w)=(u_{\mathrm{look}},v_{\mathrm{look}},w_{\mathrm{look}})} - B|_{(u,v,w)=(-u_{\mathrm{look}},-v_{\mathrm{look}},-w_{\mathrm{look}})} = 2(1-\alpha)$, regardless of the particular "look direction". This equality implies that the "look direction" (out of all possible "look directions") that gives the highest h_{look} also gives the smallest h_{other} – the same "look direction" for the largest height ratio. Over all possible "look directions", the height ratio is maximum at $g_{\mathrm{look}} = \sqrt{3}$, offering a ratio of $\frac{(\sqrt{3}-1)\alpha+1}{(\sqrt{3}+1)\alpha-1}$. This is the inverse of the height-ratio minimum in (iv) above.

(vi) The height ratio equals unity, if and only if $|g_{\mathrm{look}}| = 0$, corresponding to the blue/yellow boundary in Figure 3.3.

Figure 3.4c shows how the height ratio varies with the "look directions", for hypercardioids, which have $\alpha = 0.25$. Figure 3.5c does the same for supercardioids, which have $\alpha = \frac{1}{2}(\sqrt{3}-1)$, Figure 3.6c does same for the standard cardioids, which have $\alpha = 0.5$, and finally Figure 3.7c does same for the subcardioids which have $\alpha = 0.7$.

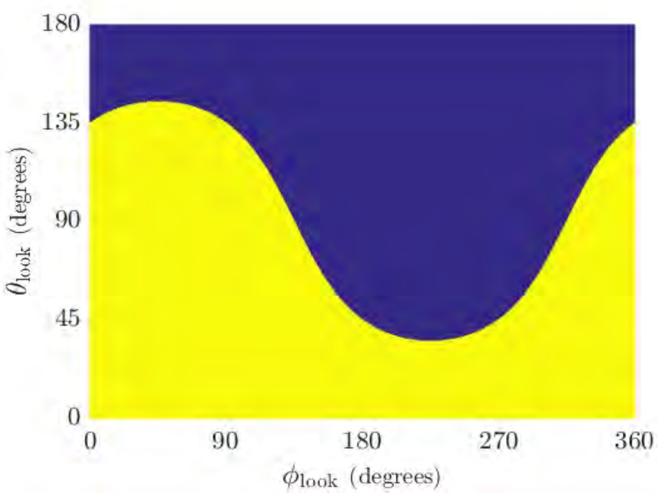

Figure 3.3: Map of g_{look} versus θ_{look} and ϕ_{look}. Yellow region depicts where $g_{\mathrm{look}} > 0$, and the blue region depicts where $g_{\mathrm{look}} < 0$. The boundary of the two regions is $g_{\mathrm{look}} = 0$.

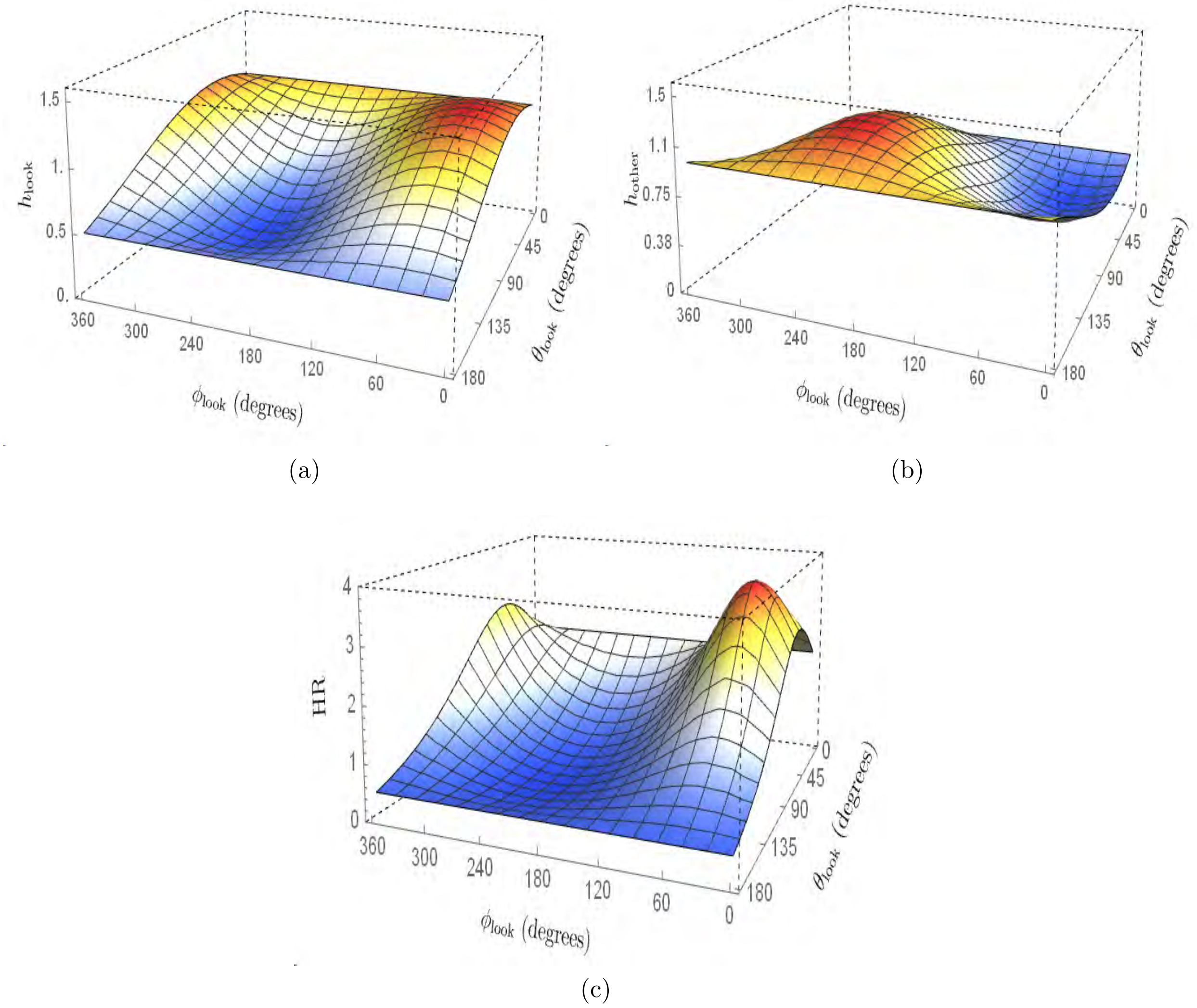

Figure 3.4: A plot of (a) h_{look}, (b) h_{other}, and (c) $H^{(\alpha)}(\theta_{\text{look}}, \phi_{\text{look}})$ versus $(\theta_{\text{look}}, \phi_{\text{look}})$ for $\alpha = \frac{1}{4}$, hypercardioids.

3.4 Half-Power Beam "Width"

The half-power beamwidth has been introduced in Section 2.5. In this section, the beamwidth is derived for the proposed beamformer.

3.4.1 Rotational Symmetry of the Beampattern

The beampattern is bivariate in terms of the spherical coordinates of θ and ϕ; hence, the mainlobe "width" is a *two*-dimensional spherical cap, rather than a *one*-dimensional width. This Section 3.4.1 will analytically prove that the beam-pattern is rotationally symmetric with respect to the "look direction".

Let (u_h, v_h, w_h) denote any set of Cartesian direction-cosines giving a beampattern

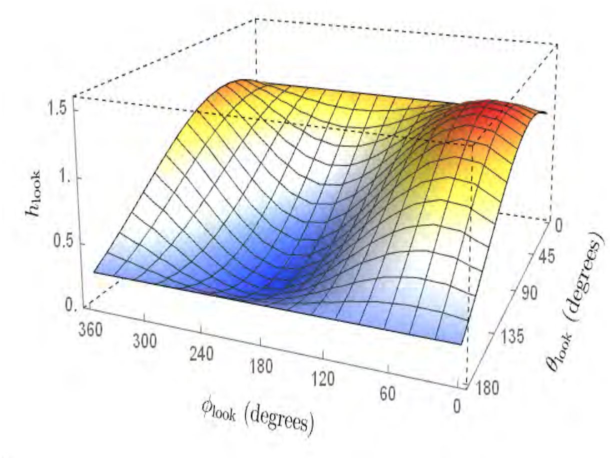

(a)

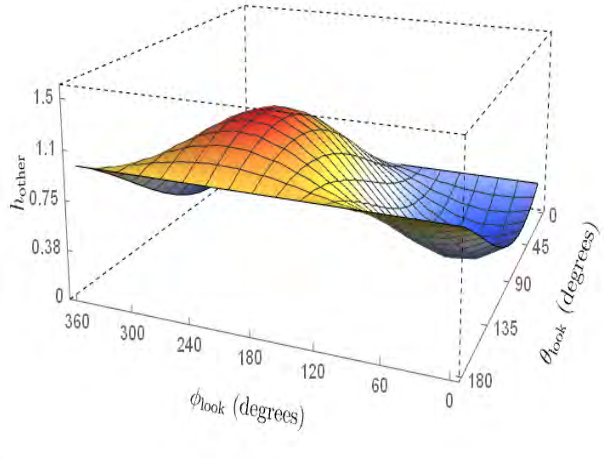

(b)

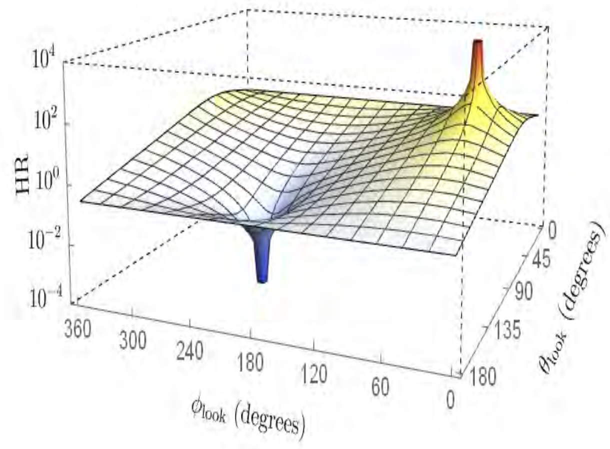

(c)

Figure 3.5: A plot of (a) h_{peak}, (b) h_{other}, and (c) $H^{(\alpha)}(\theta_{\text{look}}, \phi_{\text{look}})$ versus $(\theta_{\text{look}}, \phi_{\text{look}})$ for $\alpha = \frac{1}{2}(\sqrt{3}-1)$, supercardioids.

height of

$$\begin{aligned} h &:= B|_{(u,v,w)=(u_h,v_h,w_h)} \\ &= \alpha\, g_{\text{look}} + (1-\alpha)\,(u_{\text{look}}u_h + v_{\text{look}}v_h + w_{\text{look}}w_h). \end{aligned} \tag{3.4.1}$$

Further define

$$\cos\gamma_h \;:=\; u_{\text{look}}u_h + v_{\text{look}}v_h + w_{\text{look}}w_h, \tag{3.4.2}$$

which equals an inner product between the vectors of $[u_h, v_h, w_h]$ and $[u_{\text{look}}, v_{\text{look}}, w_{\text{look}}]$.

From (3.4.1)-(3.4.2):

$$\cos(\gamma_h) \;=\; \frac{h - \alpha\, g_{\text{look}}}{(1-\alpha)} \;\in\; [-1, 1], \tag{3.4.3}$$

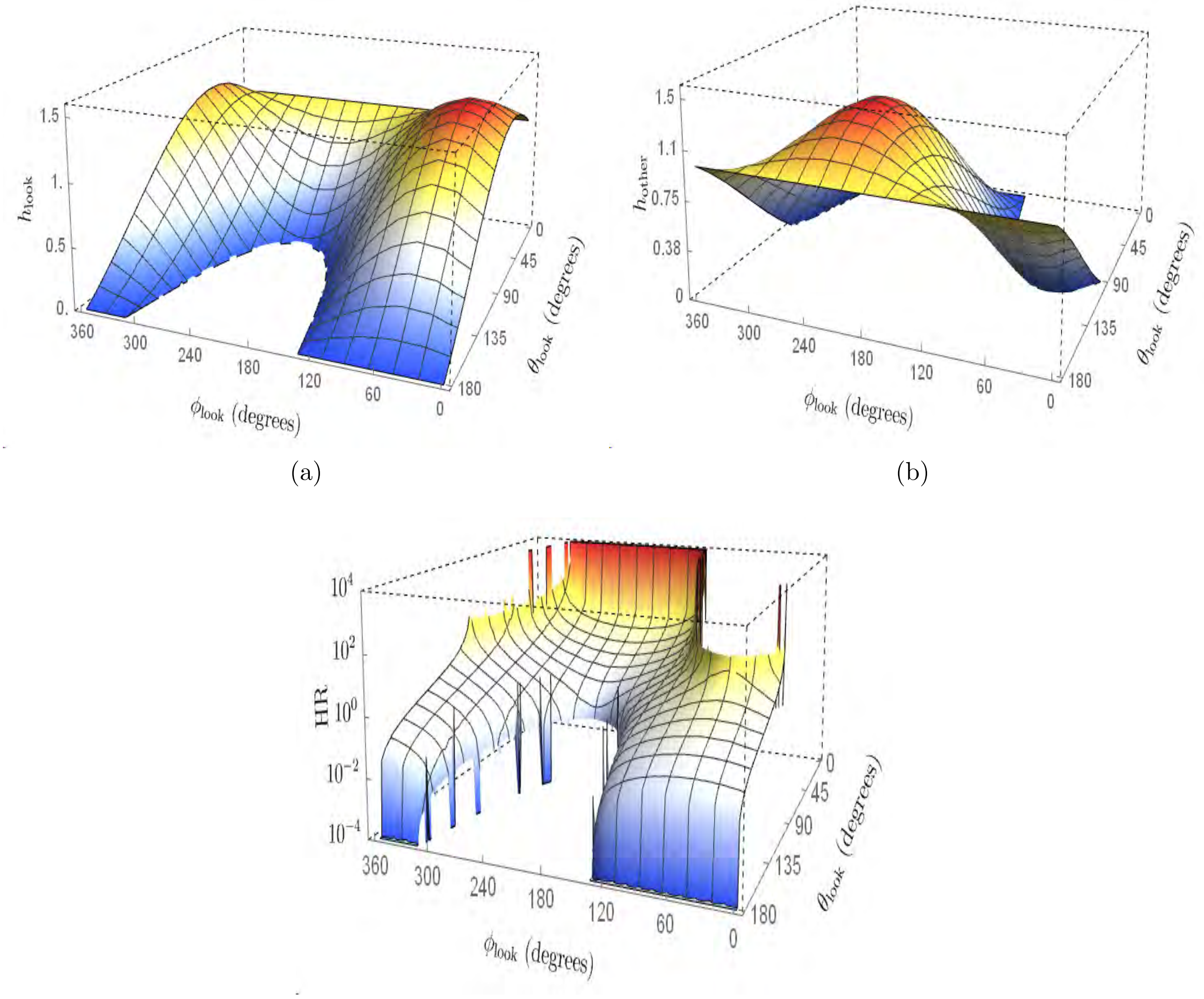

(a) (b) (c)

Figure 3.6: A plot of (a) h_{peak}, (b) h_{other}, and (c) $H^{(\alpha)}(\theta_{\text{look}}, \phi_{\text{look}})$ versus $(\theta_{\text{look}}, \phi_{\text{look}})$ for $\alpha = \frac{1}{2}$, standard cardioids.

which is satisfied by all (u_h, v_h, w_h) and only by (u_h, v_h, w_h). Therefore, for the locus of all sets of Cartesian direction cosines giving a particular beam height – that locus forms a perfect circle around the directional vector of the "look direction". Therefore, iso-height points on the beampattern forms a circular contour centered around the line from the origin O to the beampatterns peak (i.e. a line towards the peaks direction, $(\theta_{\text{look}}, \phi_{\text{look}})$).

The expression (3.4.3) is valid if its RHS is between -1 and 1 for $h = h_{\text{look}}/\sqrt{2}$. This implies that $g_{\text{look}} \in \left[\frac{(\alpha-1)}{\alpha}, \frac{(\sqrt{2}+1)}{(\sqrt{2}-1)} \frac{(1-\alpha)}{\alpha}\right]$. The implication of the above condition is that $B|_{(u,v,w)=(u_h,v_h,w_h)} \geq 0$.

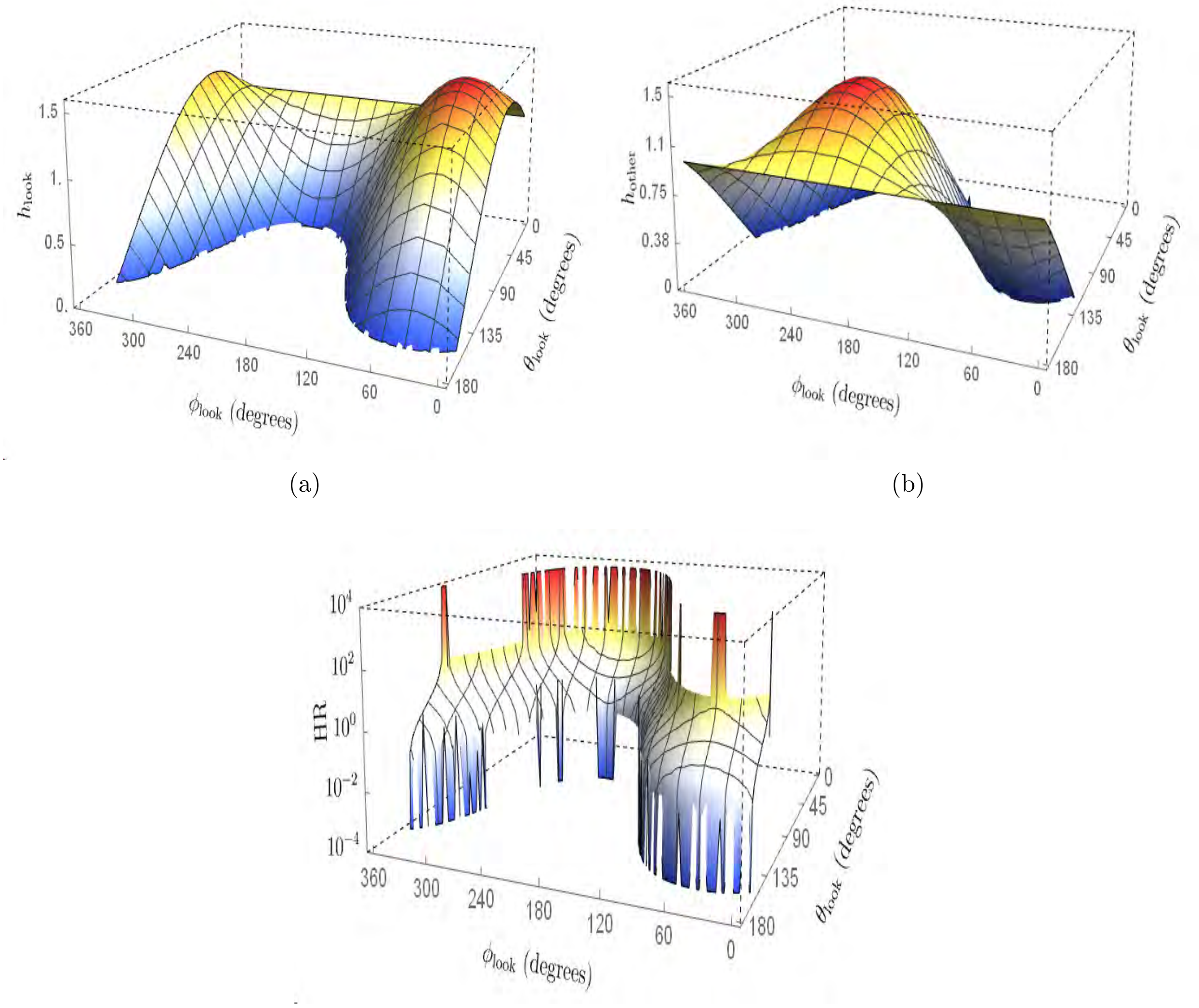

(a) (b)

(c)

Figure 3.7: A plot of (a) h_{peak}, (b) h_{other}, and (c) $H^{(\alpha)}(\theta_{\text{look}}, \phi_{\text{look}})$ versus $(\theta_{\text{look}}, \phi_{\text{look}})$ for $\alpha = 0.7$, subcardioids.

3.4.2 The Condition Under which the Beampattern is not Always Above its Half-Power Height

For the two-dimensional beam-pattern under investigation, its half-power "beamwidth" is here defined as the concerned spherical cap's surface area at a radius of $\frac{1}{\sqrt{2}} h_{\text{look}}$. The beampattern could possibly be always taller than $\frac{1}{\sqrt{2}} h_{\text{look}}$, whereby the triad could be considered as omni-directional. The beampattern could possibly be always taller than $\frac{1}{\sqrt{2}} h_{\text{look}}$, whereby the triad could be considered as omni-directional. The condition under which this occurs is derived in this Section 3.4.2.

The condition for a lobe to exist in the look direction for a given look direction and α, has been derived as $g_{\text{look}} > \frac{-(1-\alpha)}{\alpha}$ in (3.2.4). Given that (3.2.4) is obeyed, there exists at least one point on the beampattern whose height is not greater than the half-power height if the lowest point on the beam-pattern $B_{\min}$ is not greater than $B_{\max}/\sqrt{2}$. That is

$$\begin{aligned} B_{\min} &\leq \frac{1}{\sqrt{2}} B_{\max} \\ \Longrightarrow \qquad g_{\text{look}} &\leq \frac{\sqrt{2}+1}{\sqrt{2}-1} \frac{(1-\alpha)}{\alpha} \end{aligned} \tag{3.4.4}$$

Therefore, combining conditions (3.2.4) and (3.4.4)

$$g_{\text{look}} \in \left(\frac{(\alpha-1)}{\alpha}, \ \frac{(\sqrt{2}+1)}{(\sqrt{2}-1)} \frac{(1-\alpha)}{\alpha} \right] \tag{3.4.5}$$

represents the necessary and sufficient condition that $B_{\max} \geq 0$ and the beampattern is not entire above its half-power magnitude. Condition (3.4.5) is always satisfied for $\alpha \in [0, \frac{1}{2}(\sqrt{3}-1)]$ $\forall g_{\text{look}}$. This includes the hyper-cardioids and super-cardioids. The Condition (3.4.5) is not generally true for $\alpha \notin [0, \frac{1}{2}(\sqrt{3}-1)]$. This explains the blank areas in Figures 3.8c - 3.8d. Incidentally, condition (3.4.5) is mathematically equivalent to condition (3.4.3).

3.4.3 Half-Power Beamwidth Analytically Derived in Closed Form

In the subsequent discussion, the two-dimensional beamwidth is defined here as the spherical cap's area at a radius of $h_{3\text{dB}} = h_{\text{look}}/\sqrt{2} = B|_{(u,v,w)=(u_{\text{look}},v_{\text{look}},w_{\text{look}})} /\sqrt{2}$. The spherical cap's boundary is the circular contour (3.4.3) as defined in Section 3.4.1.

From (3.4.3), the half-power height makes an angle $\gamma_{3\text{dB}}$ with the peak direction's directional vector, such that

$$\cos \gamma_{3\text{dB}} = \frac{\frac{h_{\text{look}}}{\sqrt{2}} - \alpha\, g_{\text{look}}}{(1-\alpha)}. \tag{3.4.6}$$

The beamwidth (which is spherical cap's surface area) equals

$$\begin{aligned} &\text{BW}^{(\alpha)}(\theta_{\text{look}}, \phi_{\text{look}}) \\ &:= 2\pi \frac{h_{\text{look}}}{\sqrt{2}} \left(\frac{h_{\text{look}}}{\sqrt{2}} - \frac{h_{\text{look}}}{\sqrt{2}} \cos \gamma_{3\text{dB}} \right) \\ &= \pi\, h_{\text{look}}^2 \left(1 - \cos \gamma_{3\text{dB}}\right). \end{aligned} \tag{3.4.7}$$

Then substitute (3.3.1) and (3.4.6) into the (3.4.7),

$$\text{BW}^{(\alpha)}(\theta_{\text{look}}, \phi_{\text{look}}) = \frac{(2-\sqrt{2})\pi}{2} \frac{h_{\text{look}}^3}{(1-\alpha)}. \tag{3.4.8}$$

which implies that the beamwidth is directly proportional to cube of the mainlobe's height.

As α increases, $(1-\alpha)$ decreases which implies an increase in the beamwidth for a given look direction. $h_{\text{look}} = \alpha g_{\text{look}} + (1-\alpha)$ would vary less across the look directions for small values of α. This trend can be noticed as the surface plots of the beamwidth becomes less flatter as α increases from Figure 3.8a ($\alpha = \frac{1}{4}$) to Figure 3.8d ($\alpha = 0.7$).

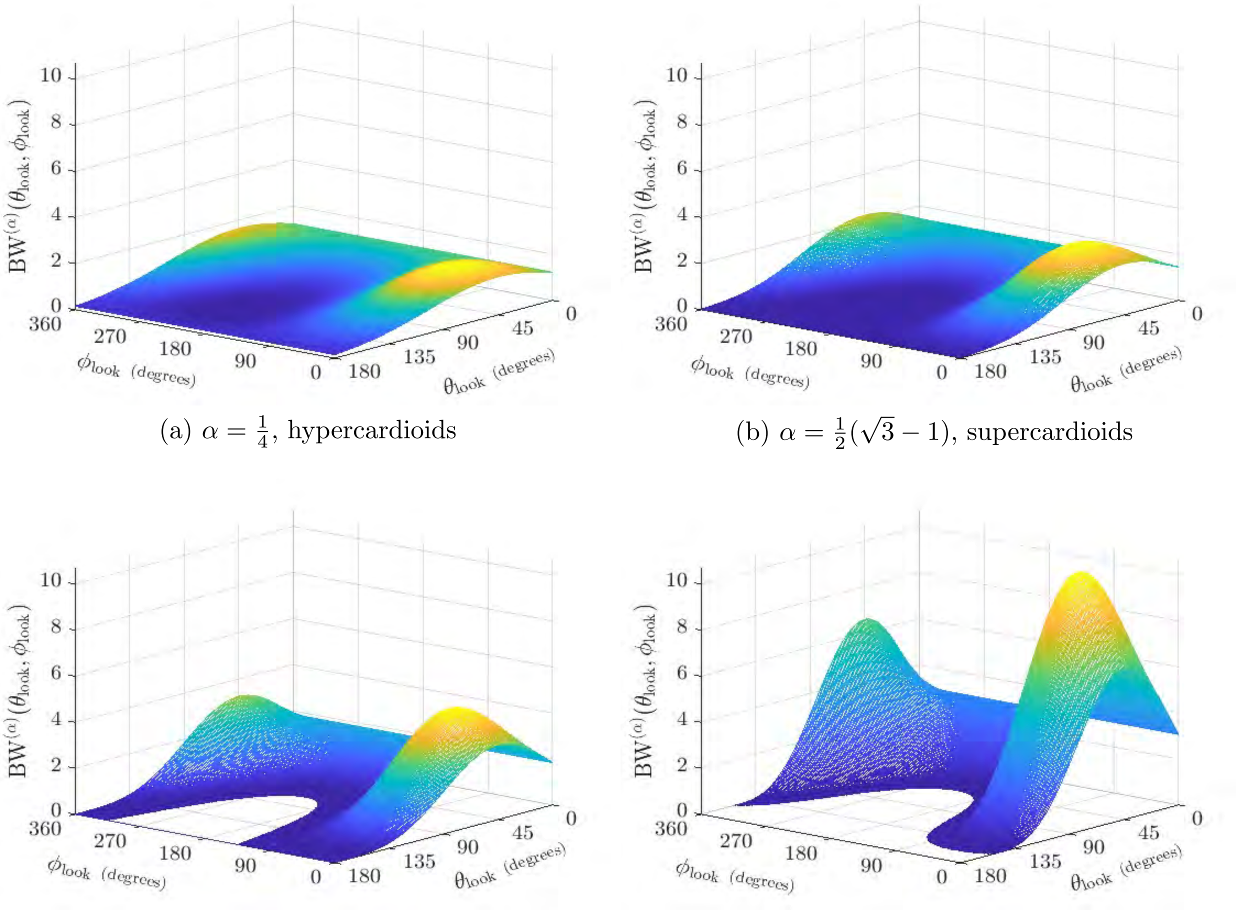

(a) $\alpha = \frac{1}{4}$, hypercardioids

(b) $\alpha = \frac{1}{2}(\sqrt{3}-1)$, supercardioids

(c) $\alpha = \frac{1}{2}$, standard cardioids

(d) $\alpha = 0.7$, subcardioids

Figure 3.8: A plot of $\mathrm{BW}^{(\alpha)}(\theta_{\text{look}}, \phi_{\text{look}})$ against $(\theta_{\text{look}}, \phi_{\text{look}})$ for various typical values of the "cardioidicity index".

3.5 Directivity

The directivity of a microphone array measures the gain of the array in a noise field against the gain of an omnidirectional microphone [2]. The noise field is usually isotropic but can, in some special cases, be modeled as cylindrical. Therefore, directivity can be defined as the ratio of the power received by the microphone in a given direction (its main response axis) to the noise power at the array due to isotropic noise. Thus an array's directivity is defined in [20] as

$$D(\theta,\phi) \;=\; \frac{|B|^2\big|_{(\theta,\phi)=(\theta_{\text{look}},\phi_{\text{look}})}}{\dfrac{1}{4\pi}\displaystyle\int_0^{\pi} d\theta \int_0^{2\pi} d\phi \sin(\theta)|B|^2}, \tag{3.5.1}$$

where $|B|^2$ is the power pattern of the array and other variables as previously defined. The numerator of (3.5.1) represents the power gain of the array in the direction of maximum response (the look direction), and the denominator of (3.5.1) represents the power of noise at the array's output due to isotropic noise field.

The power pattern

$$\begin{aligned} |B|^2 &= |\alpha\, g_{\text{look}} + (1-\alpha)(u_{\text{look}}u + v_{\text{look}}v + w_{\text{look}}w)|^2 \\ &= \alpha^2 g_{\text{look}}^2 + (1-\alpha)^2(u_{\text{look}}u + v_{\text{look}}v + w_{\text{look}}w)^2 \\ &\qquad + 2\alpha(1-\alpha)g_{\text{look}}(u_{\text{look}}u + v_{\text{look}}v + w_{\text{look}}w), \end{aligned} \tag{3.5.2}$$

and it holds that

$$|B|^2\big|_{(\theta,\phi)=(\theta_{\text{look}},\phi_{\text{look}})} \;=\; \alpha^2 g_{\text{look}}^2 + 2\alpha(1-\alpha)g_{\text{look}} + (1-\alpha)^2. \tag{3.5.3}$$

Substitute u, v, w from Section 3.1.2 into (3.5.2), and then further substitute (3.5.2) and (3.5.3) into (3.5.1). Thereafter, integration with respect to (θ,ϕ):

$$\begin{aligned} D^{(\alpha)}(\theta_{\text{look}},\phi_{\text{look}}) &= \frac{\alpha^2 g_{\text{look}}^2 + 2\alpha(1-\alpha)\, g_{\text{look}} + (1-\alpha)^2}{\alpha^2\, g_{\text{look}}^2 + \frac{1}{3}(1-\alpha)^2} \\ &= 1 + 2(1-\alpha)\frac{3\alpha\, g_{\text{look}} + (1-\alpha)}{3\alpha^2\, g_{\text{look}}^2 + (1-\alpha)^2}, \end{aligned} \tag{3.5.4}$$

recalling that g_{look} represents a bivariate function of $(\theta_{\text{look}},\phi_{\text{look}})$.

At $\alpha = 1$, the cardioidic triad degenerates to an isotropic sensor, giving $D^{(\alpha)}(\theta_{\text{look}},\phi_{\text{look}}) = 1$. For $\alpha = 0$ (i.e. the triad of cardoiids degenerating to a tri-axial velocity sensor): $D^{(\alpha)}(\theta_{\text{look}},\phi_{\text{look}}) = 3$.

3.5.1 Condition Under Which $D^{(\alpha)}(g_{\text{look}}) > 3$ (i.e. Greater than a Tri-Axial Velocity-Sensor's Directivity)

From (3.5.4),

$$D^{(\alpha)}(\theta_{\text{look}},\phi_{\text{look}}) \;=\; 1 + 2(1-\alpha)\left(\frac{(1-\alpha) + 3\alpha\, g_{\text{look}}}{3\alpha^2\, g_{\text{look}}^2 + (1-\alpha)^2}\right) \;>\; 3, \tag{3.5.5}$$

which is equivalent to $g_{\text{look}} \in \left(0, \frac{1-\alpha}{\alpha}\right)$.

3.5.2 To Identify the "Look Direction" that Maximizes Directivity

At any preset cardioidicity index α, the "look direction" that gives the maximum directivity may be identified as follows:

$$\max_{g_{\text{look}} \in [-\sqrt{3}, \sqrt{3}]} D^{(\alpha)}(g_{\text{look}}) \equiv \max_{g_{\text{look}} \in [-\sqrt{3}, \sqrt{3}]} \tilde{D}^{(\alpha)}(g_{\text{look}}), \tag{3.5.6}$$

where

$$\tilde{D} \quad = \quad \frac{(1-\alpha) + 3\alpha\, g_{\text{look}}}{3\alpha^2\, g_{\text{look}}^2 + (1-\alpha)^2}. \tag{3.5.7}$$

Next,

$$\frac{\partial \tilde{D}}{\partial\, g_{\text{look}}} \quad = \quad \frac{g_{\text{look}}^2 + 3\left(\frac{1-\alpha}{\alpha}\right)^2 - 2\, g_{\text{look}}\left(\frac{1-\alpha}{\alpha} + g_{\text{look}}\right)}{\left[g_{\text{look}}^2 + 3\left(\frac{1-\alpha}{\alpha}\right)^2\right]^2} \quad = \quad 0$$

implies that $g_{\text{look}} = \frac{(1-\alpha)}{3\alpha}$ and $-\frac{(1-\alpha)}{\alpha}$. At the two critical points of (3.5.7):

$$D^{(\alpha)}(g_{\text{look}}) \quad = \quad \begin{cases} 0, & \text{for } g_{\text{look}} = -\frac{(1-\alpha)}{\alpha} \\ 4, & \text{for } g_{\text{look}} = \frac{(1-\alpha)}{3\alpha} \end{cases} \tag{3.5.8}$$

Therefore, the second critical point at $g_{\text{look}} = \frac{(1-\alpha)}{3\alpha}$ maximizes the directivity. Hence, $\max_{g_{\text{look}} \in [-\sqrt{3}, \sqrt{3}]} D^{(\alpha)}(g_{\text{look}}) = 4$. This can also be seen in the directivity plots of Figures 3.9.

The maximum directivity occurs when $(u_{\text{look}}, v_{\text{look}}, w_{\text{look}})$ lies on the Cartesian plane defined by

$$g_{\text{look}} \quad := \quad u_{\text{look}} + v_{\text{look}} + w_{\text{look}} \quad = \quad \frac{(1-\alpha)}{3\alpha}.$$

3.6 Array Gain

A beamformer's "array gain", $G(\theta_{\text{look}}, \phi_{\text{look}})$ is defined as the signal-to-noise ratio (SNR) at the beamformer's output relative to that at the input, while assuming that the beamformer "looks" toward the incident source's impinging direction, and while subject to additive noise that has equal intensity and statistical independence across the various sensors. [4] A higher array gain in a given direction (> 1) basically means that the using more than one microphone improves the signal-to-noise ratio compared to using just one microphone in

[4] Please see equation (2.34) on p. 25 of [52], equation (2.185) on p. 65 of [20], and (2.22) equation p. 24 of [53].

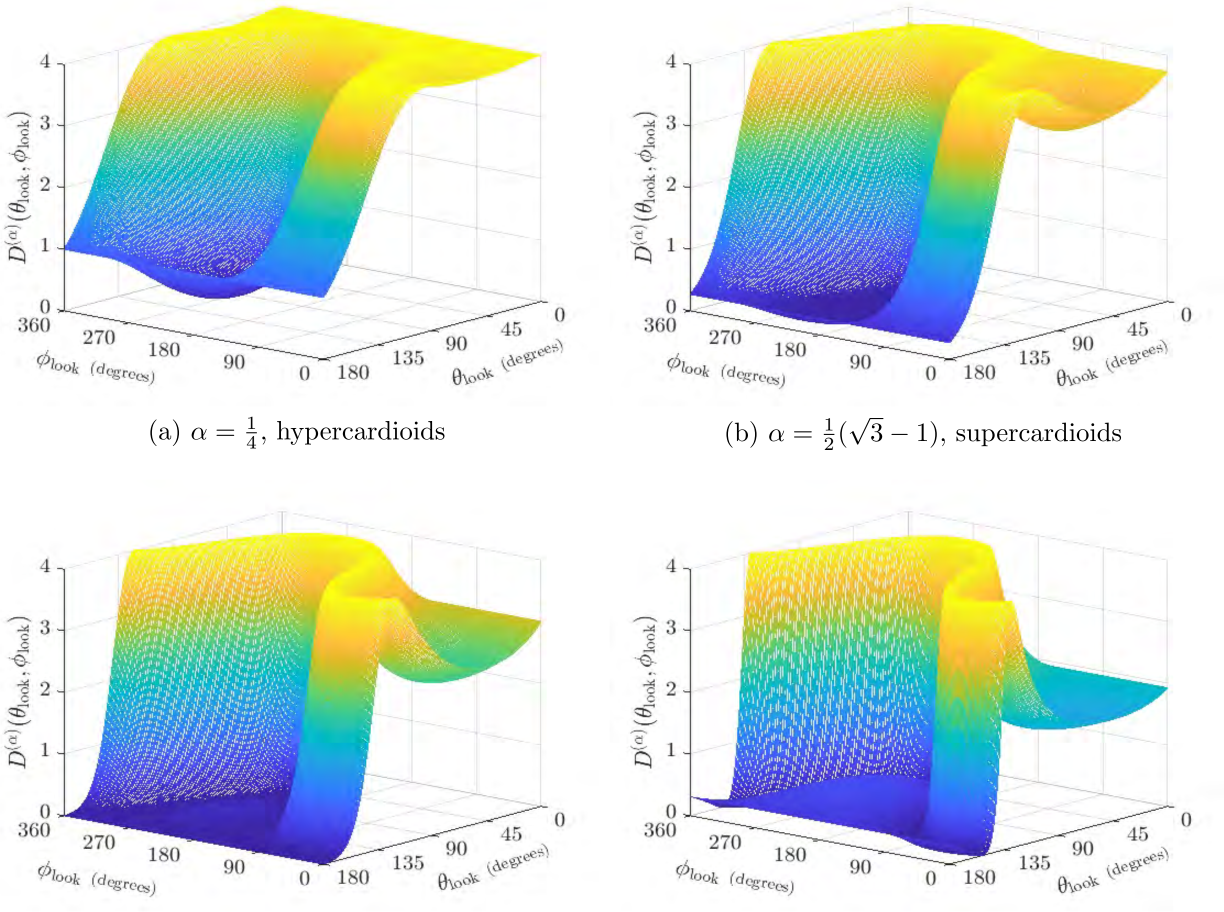

(a) $\alpha = \frac{1}{4}$, hypercardioids

(b) $\alpha = \frac{1}{2}(\sqrt{3}-1)$, supercardioids

(c) $\alpha = \frac{1}{2}$, standard cardioids

(d) $\alpha = 0.7$, subcardioids

Figure 3.9: A plot of $D^{(\alpha)}(\theta_{\text{look}}, \phi_{\text{look}})$ against $(\theta_{\text{look}}, \phi_{\text{look}})$ for various typical values of the "cardioidicity index".

that given direction. The direction of choice is in the maximum-response axis direction.

Define the beamformer input's signal-to-noise ratio as

$$\text{SNR}_{\text{in}} \quad := \quad \frac{P_s}{P_n},$$

where P_s and P_n denote the signal power and noise power, respectively. The beamformer output's signal-to-noise ratio equals

$$\text{SNR}_{\text{out}} \quad = \quad \frac{\left[\mathbf{w}^T\,\mathbf{a}^{(\alpha)}(\theta_{\text{look}}, \phi_{\text{look}})\right]^2\;P_s}{\|\mathbf{w}\|^2 P_n}. \tag{3.6.1}$$

At the beamformer's weighting vector $\mathbf{w} := \mathbf{a}(\theta_{\text{look}}, \phi_{\text{look}})$, as defined in (3.1.3), the array gain equals

$$
\begin{aligned}
G^{(\alpha)}(\theta_{\text{look}}, \phi_{\text{look}}) &= \frac{\text{SNR}_{\text{out}}}{\text{SNR}_{\text{in}}} \\
&= \left[\mathbf{a}(\phi_{\text{look}}, \theta_{\text{look}})^T \, \mathbf{a}^{(\alpha)}(\phi_{\text{look}}, \theta_{\text{look}})\right]^2 \\
&= (\alpha \, g_{\text{look}} - \alpha + 1)^2 \\
&= \alpha^2 g_{\text{look}}^2 + 2\alpha(1-\alpha) g_{\text{look}} + (1-\alpha)^2. \qquad (3.6.2)
\end{aligned}
$$

The array gain $G^{(\alpha)}(\theta_{\text{look}}, \phi_{\text{look}})$ is plotted against the "look direction" $(\theta_{\text{look}}, \phi_{\text{look}})$ at various values of α in Figures 3.11a-3.11d.

To determine, at any given α, the maximum array gain among all possible "look direction", apply the Lagrangian method: The two stationary points of (3.6.2) are then obtained as

$$
(u_{L_1}, v_{L_1}, w_{L_1}) = \left(\frac{\sqrt{3}}{3}, \frac{\sqrt{3}}{3}, \frac{\sqrt{3}}{3}\right), \qquad (3.6.3)
$$

$$
(u_{L_2}, v_{L_2}, w_{L_2}) = \left(-\frac{\sqrt{3}}{3}, -\frac{\sqrt{3}}{3}, -\frac{\sqrt{3}}{3}\right). \qquad (3.6.4)
$$

These respectively imply $(\theta_{\text{look}}, \phi_{\text{look}}) = (54.73^\circ, 45^\circ)$ and $(\theta_{\text{look}}, \phi_{\text{look}}) = (125.26^\circ, 225^\circ)$, and $g_{\text{look}} = \sqrt{3}$ and $-\sqrt{3}$. As $G^{(\alpha)}(g_{\text{look}} = \sqrt{3}) > G^{(\alpha)}(g_{\text{look}} = -\sqrt{3})$, (3.6.3) corresponds to the "look direction" of the maximum array gain.

Hence, the "look direction" that maximizes the array gain (among all "look directions") is independent of α, though that maximum array gain itself depends on α as follows:

$$
\begin{aligned}
G^{(\alpha)}(g_{\text{look}} = \sqrt{3}) &= (\alpha\sqrt{3} + (1-\alpha))^2 \\
&= 3\alpha^2 + 2\sqrt{3}\alpha(1-\alpha) + (1-\alpha)^2 \\
&= [4 - 2\sqrt{3}]\alpha^2 + [2\sqrt{3} - 2]\alpha + 1. \qquad (3.6.5)
\end{aligned}
$$

$G^{(\alpha)}(g_{\text{look}} = \sqrt{3})$ (3.6.5) shows that the maximum array gain is quadratic with regard to α, the maximum array gain actually increases monotonically within the range of $\alpha \in (0, 1)$. Please see Figure 3.10.

3.7 Signal-To-Noise-Plus-Interference Ratio Gain

The signal-to-noise-plus-interference ratio gain has been developed in Section 2.7 for the spatial-matched-filter beamformer. This section will extend analysis to the beamformer proposed in this chapter.

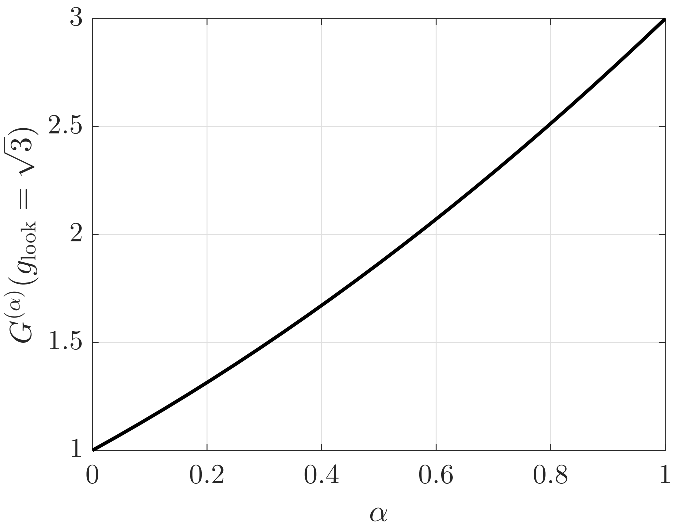

Figure 3.10: Plot of the $G^{(\alpha)}(g_{\text{look}} = \sqrt{3})$ against α.

From (2.7.3) in Section 2.7

$$G_{\text{SNIR}} = \frac{\left(\mathbf{w}^T \mathbf{a}^{(\alpha)}(\theta_s, \phi_s)\right)^2 \; [1 + \text{INR}]}{\frac{1}{P_n}\sum_{m=1}^{M} \left(\mathbf{w}^T \mathbf{a}^{(\alpha)}(\theta_m, \phi_m)\right)^2 P_{v,m} + \|\mathbf{w}\|^2} \tag{3.7.1}$$

For the proposed beamformer, $\mathbf{w} = \mathbf{a}(\theta_{\text{look}}, \phi_{\text{look}})$, therefore, (3.7.1) becomes

$$\begin{aligned} G_{\text{SNIR}} &= \frac{\left(\mathbf{a}(\theta_{\text{look}}, \phi_{\text{look}})^T \mathbf{a}^{(\alpha)}(\theta_{\text{look}}, \phi_{\text{look}})\right)^2 \; [1 + \text{INR}]}{\frac{1}{P_n}\sum_{m=1}^{M} \left(\mathbf{a}(\theta_{\text{look}}, \phi_{\text{look}})^T \mathbf{a}^{(\alpha)}(\theta_m, \phi_m)\right)^2 P_{v,m} + \|\mathbf{a}(\theta_{\text{look}}, \phi_{\text{look}})\|^2} \\ &= \frac{\left(\alpha g_{\text{look}} + (1-\alpha)\right)^2 \; [1 + \text{INR}]}{\frac{1}{P_n}\sum_{m=1}^{M} \left(\alpha g_{\text{look}} + \mathbf{a}(\theta_{\text{look}}, \phi_{\text{look}})^T \mathbf{a}(\theta_m, \phi_m)\right)^2 P_{v,m} + 1} \end{aligned} \tag{3.7.2}$$

where g_{look} is as defined in (3.1.4). It has been shown in Section 3.2.1 that for $\alpha \in (0, 1)$, $\theta \in [0, \pi]$, and $\phi \in [0, 2\pi)$, $|\mathbf{a}(\theta_{\text{look}}, \phi_{\text{look}})^T \mathbf{a}^{(\alpha)}(\theta_{\text{look}}, \phi_{\text{look}})| > |\mathbf{a}(\theta_{\text{look}}, \phi_{\text{look}})^T \mathbf{a}^{(\alpha)}(\theta, \phi)|$. Therefore, as INR increases, the numerator of (3.7.2) is greater than its denominator, hence $G_{\text{SNIR}} > 1$. For a case of single interference ($M = 1$), the SNIR gain reduces to

$$G_{\text{SNIR}} = \frac{\left(\alpha g_{\text{look}} + (1-\alpha)\right)^2 \; [1 + \text{INR}]}{\text{INR}\left(\alpha g_{\text{look}} + \mathbf{a}(\theta_{\text{look}}, \phi_{\text{look}})^T \mathbf{a}(\theta_m, \phi_m)\right)^2 + 1}, \tag{3.7.3}$$

where g_{look} is as previously defined.

The plots of (3.7.3) versus look direction $(\theta_{\text{look}}, \phi_{\text{look}})$ are shown in Figures 3.12 - 3.15 for various values of INR and interference's offset from the look direction $(\delta_\theta, \delta_\phi) := (\theta_{\text{look}}, \phi_{\text{look}}) - (\theta_m, \phi_m)$.

The array's SNIR gain increases for a given INR as the angular separation of the signal of interest and interference widens. This is noticed going across (a) to (b), and (c) to (d)

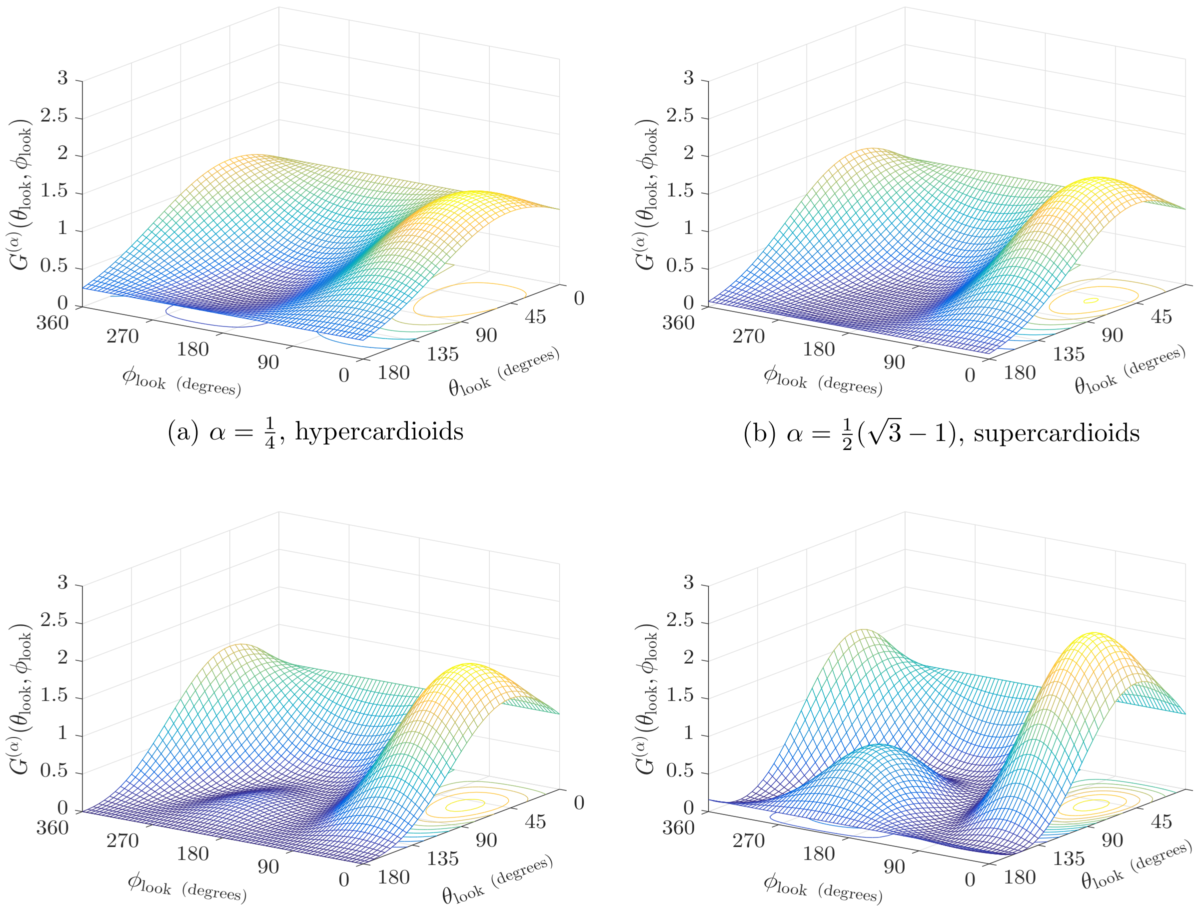

(a) $\alpha = \frac{1}{4}$, hypercardioids

(b) $\alpha = \frac{1}{2}(\sqrt{3} - 1)$, supercardioids

(c) $\alpha = \frac{1}{2}$, standard cardioids

(d) $\alpha = 0.7$, subcardioids

Figure 3.11: A plot of $G^{(\alpha)}(\theta_{\text{look}}, \phi_{\text{look}})$ against $(\theta_{\text{look}}, \phi_{\text{look}})$ for various typical values of the "cardioidicity index".

of Figures 3.12 - 3.15. Generally, the SNIR gain depends on the angular separation of the source and the interference, and also the ratio of the power of the interference to the power of the thermal noise. For INR > 1, the closer the interference to the signal of interest, the lesser the SNIR gain. But when compared to that of the spatial-matched-filter proposed in Chapter 2, it becomes evident that generally, the beamformer proposed in this chapter experiences more SNIR attenuation.

3.8 Comparing this Unbiased Beam-Pattern with the Earlier Spatial-Matched-Filter Beam- Pattern

3.8.1 Beam-Pointing Error

In the present beamformer's magnitude pattern, there is no pointing error (in that a peak always exists at the look direction $(\theta_{\text{look}}, \phi_{\text{look}})$) if

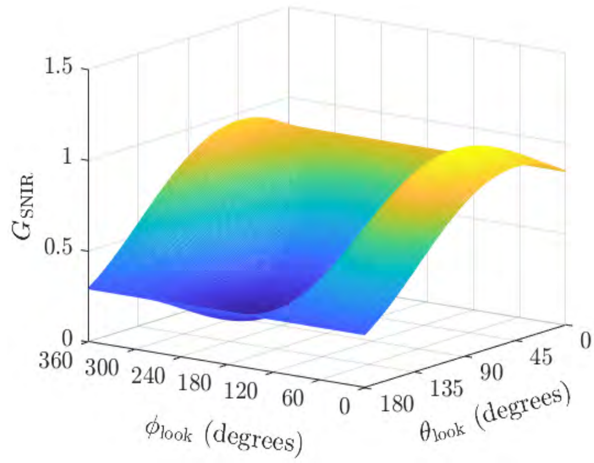

(a) INR $= -3.0103$dB, $(\delta_\theta, \delta_\phi) = (5°, 5°)$.

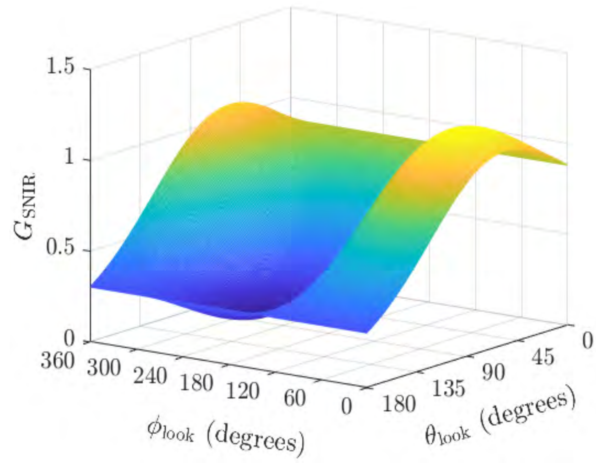

(b) INR $= -3.0103$dB, $(\delta_\theta, \delta_\phi) = (20°, 30°)$.

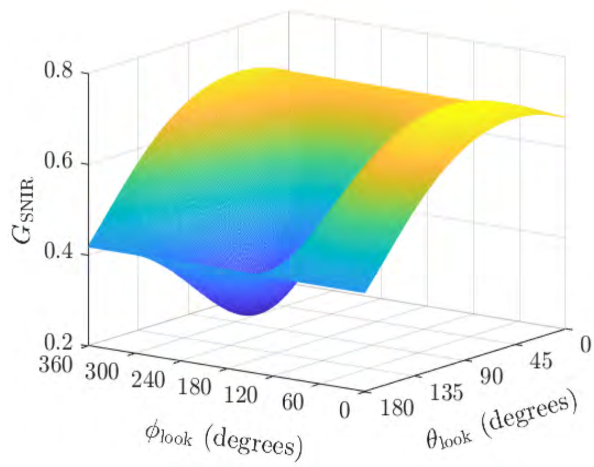

(c) INR $= 10$dB, $(\delta_\theta, \delta_\phi) = (5°, 5°)$.

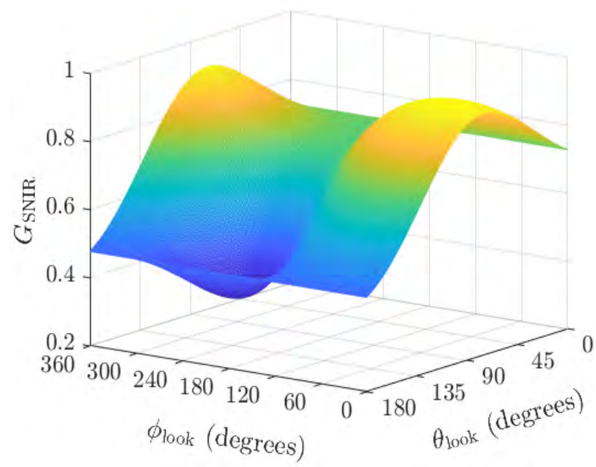

(d) INR $= 10$dB, $(\delta_\theta, \delta_\phi) = (20°, 30°)$.

Figure 3.12: Array's signal-to-noise-plus-interference ratio gain (G_{SNIR}) versus the nominal "look direction" $(\theta_{\text{look}}, \phi_{\text{look}})$ for $\alpha = \frac{1}{4}$ (hypercardioid) and $(\delta_\theta, \delta_\phi)$ - the interference's offset from true peak direction $(\theta_{\text{peak}}, \phi_{\text{peak}})$.

(i) if $\alpha \in \left[0, \frac{\sqrt{3}-1}{2}\right)$ – e.g. hypercardioids – for any "look direction" anywhere on the entire sphere, or

(ii) if $\alpha \in [0, 1)$ and the "look direction" is limited to an hemisphere defined by $u_{\text{look}} + v_{\text{look}} + w_{\text{look}} \geq 0$.

In contrast, the spatial-matched-filter beampattern in Chapter 1 (refer to Section 2.2.2) would generally have a pointing bias.[5] That pointing bias, furthermore, varies with α and with the particular look direction.[6]

[5]More precisely, the spatial-matched-filter beampattern would *always* have a pointing bias except for the degenerate case of $\alpha = 0$ (that renders each cardioid a uni-axial velocity-sensor), and except the one "look direction" of $(\theta_{\text{look}}, \phi_{\text{look}}) = (54.7°, 45°)$, $\forall \alpha > 0$.

[6]Please refer to equations (2.3.6) - (2.3.10).

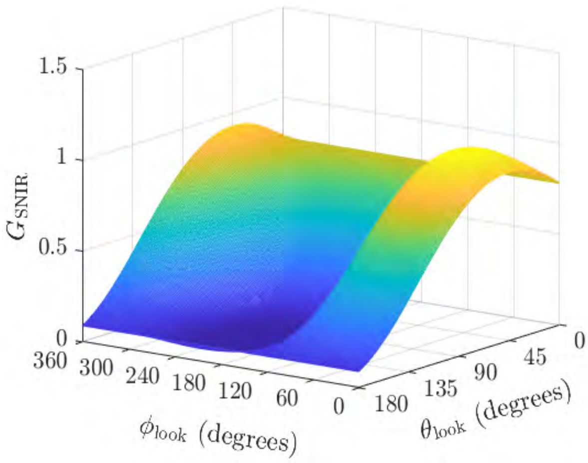

(a) INR $= -3.0103$dB, $(\delta_\theta, \delta_\phi) = (5°, 5°)$.

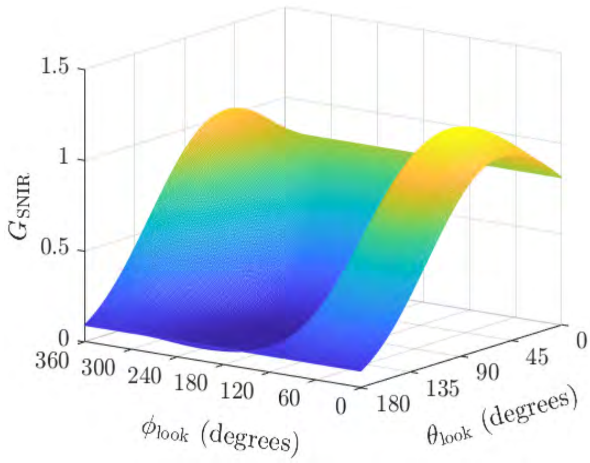

(b) INR $= -3.0103$dB, $(\delta_\theta, \delta_\phi) = (20°, 30°)$.

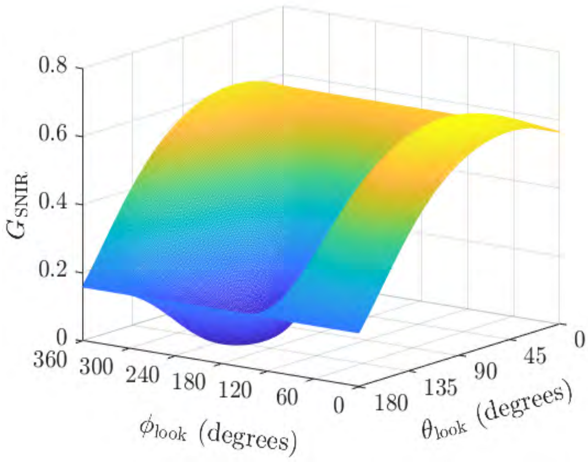

(c) INR $= 10$dB, $(\delta_\theta, \delta_\phi) = (5°, 5°)$.

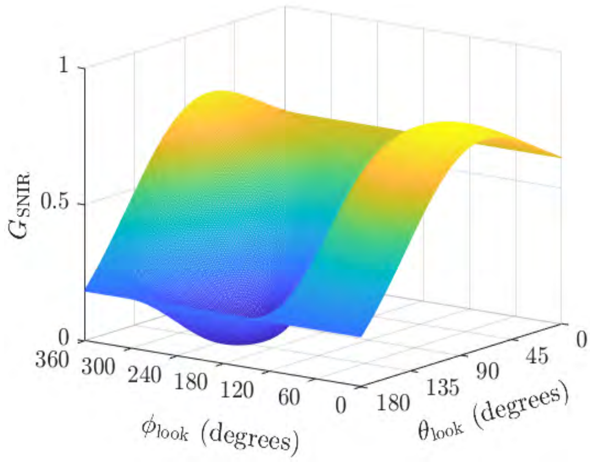

(d) INR $= 10$dB, $(\delta_\theta, \delta_\phi) = (20°, 30°)$.

Figure 3.13: Array's signal-to-noise-plus-interference ratio gain (A_{SNIR}) versus the nominal "look direction" $(\theta_{\text{look}}, \phi_{\text{look}})$ for $\alpha = \frac{\sqrt{3}-1}{2}$ (supercardioid) and $(\delta_\theta, \delta_\phi)$ - the interference's offset from true peak direction $(\theta_{\text{peak}}, \phi_{\text{peak}})$.

3.8.2 Existence of a Second Lobe

The present magnitude pattern would have a second lobe under the sufficient and necessary condition in (3.2.9), which holds $\forall \alpha \in \left(0, \frac{\sqrt{3}-1}{2}\right]$ and $\forall(\theta_{\text{look}}, \phi_{\text{look}})$.

In contrast, the spatial-matched-filter beam-pattern would have a sidelobe only for the wider range of $\alpha \in \left(0, \sqrt{6}-2\right)$ and only if g_{look} therein satisfies further conditions. For full details, please refer to equation (18) of [21].

From another perspective: Both a triad of hyper-cardioids $\left(\alpha = \frac{1}{4}\right)$ and a triad of super-cardioids $\left(\alpha = \frac{1}{2}\left(\sqrt{3}-1\right)\right)$ must necessarily have two lobes in both beam-patterns for all "look directions".

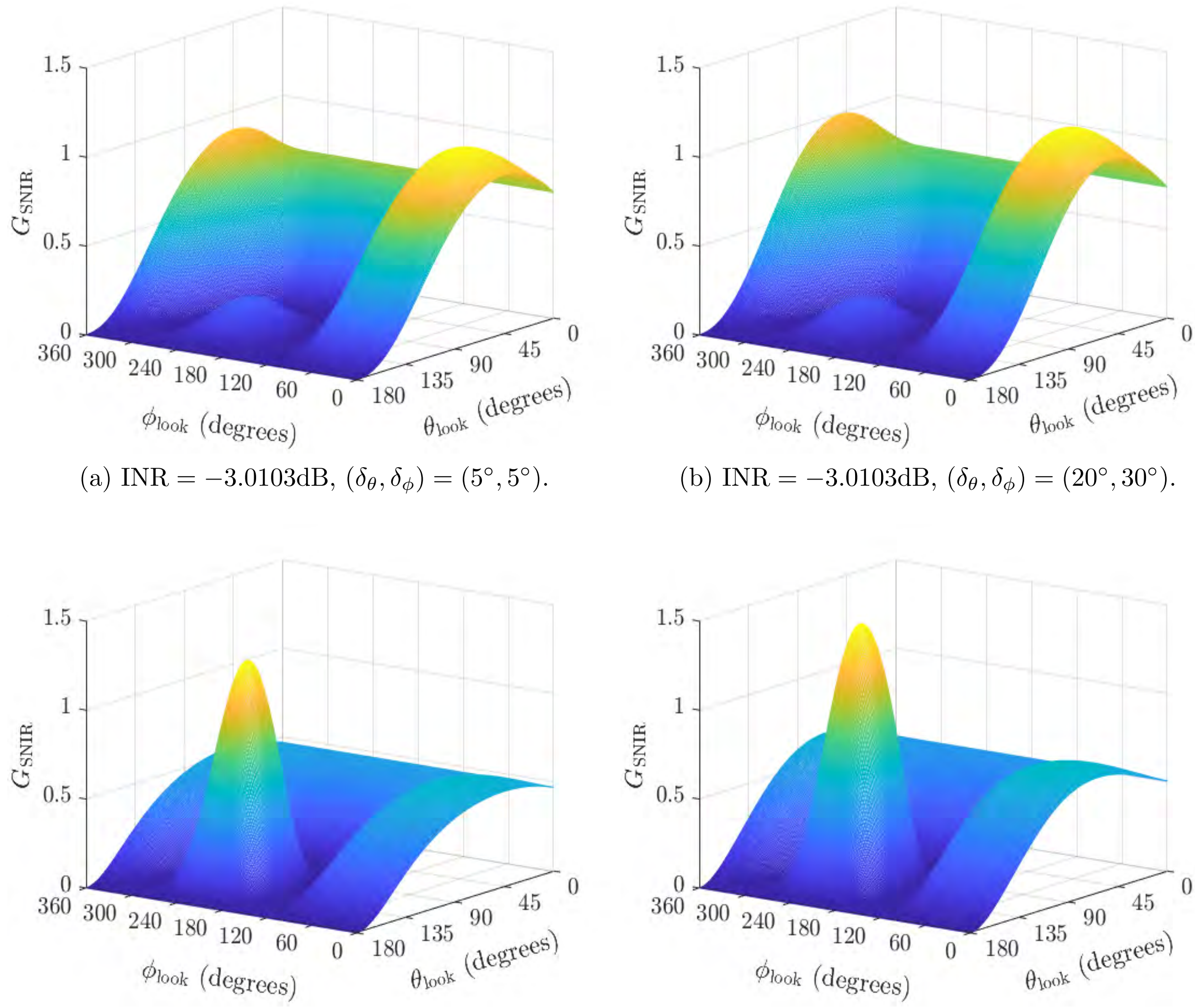

(a) INR $= -3.0103$dB, $(\delta_\theta, \delta_\phi) = (5°, 5°)$.

(b) INR $= -3.0103$dB, $(\delta_\theta, \delta_\phi) = (20°, 30°)$.

(c) INR $= 10$dB, $(\delta_\theta, \delta_\phi) = (5°, 5°)$.

(d) INR $= 10$dB, $(\delta_\theta, \delta_\phi) = (20°, 30°)$.

Figure 3.14: Array's signal-to-noise-plus-interference ratio gain (A_{SNIR}) versus the nominal "look direction" $(\theta_{\text{look}}, \phi_{\text{look}})$ for $\alpha = \frac{1}{2}$ (standard cardioid) and $(\delta_\theta, \delta_\phi)$ - the interference's offset from true peak direction $(\theta_{\text{peak}}, \phi_{\text{peak}})$.

3.8.3 Lobes' Height Ratio

Over those values of $(\alpha, g_{\text{look}})$ where the height ratio is defined for both the present magnitude pattern and the spatial-matched-filter beam-pattern, both beam-patterns share these similarities:

(i) For each beam-pattern individually, the "look direction" that gives the tallest main-lobe is also the "look direction" that gives the shortest second lobe.

(ii) The height ratio is undefined if either $g_{\text{look}} = \pm\sqrt{3}$ or $\alpha = \frac{\sqrt{3}-1}{2}$.

As α increases while g_{look} is kept constant, $h_{\text{look}}(\alpha, g_{\text{look}})$ in/decreases monotonically according to Figure 3.16b, $h_{\text{other}}(\alpha, g_{\text{look}})$ in/decreases monotonically according to Figure

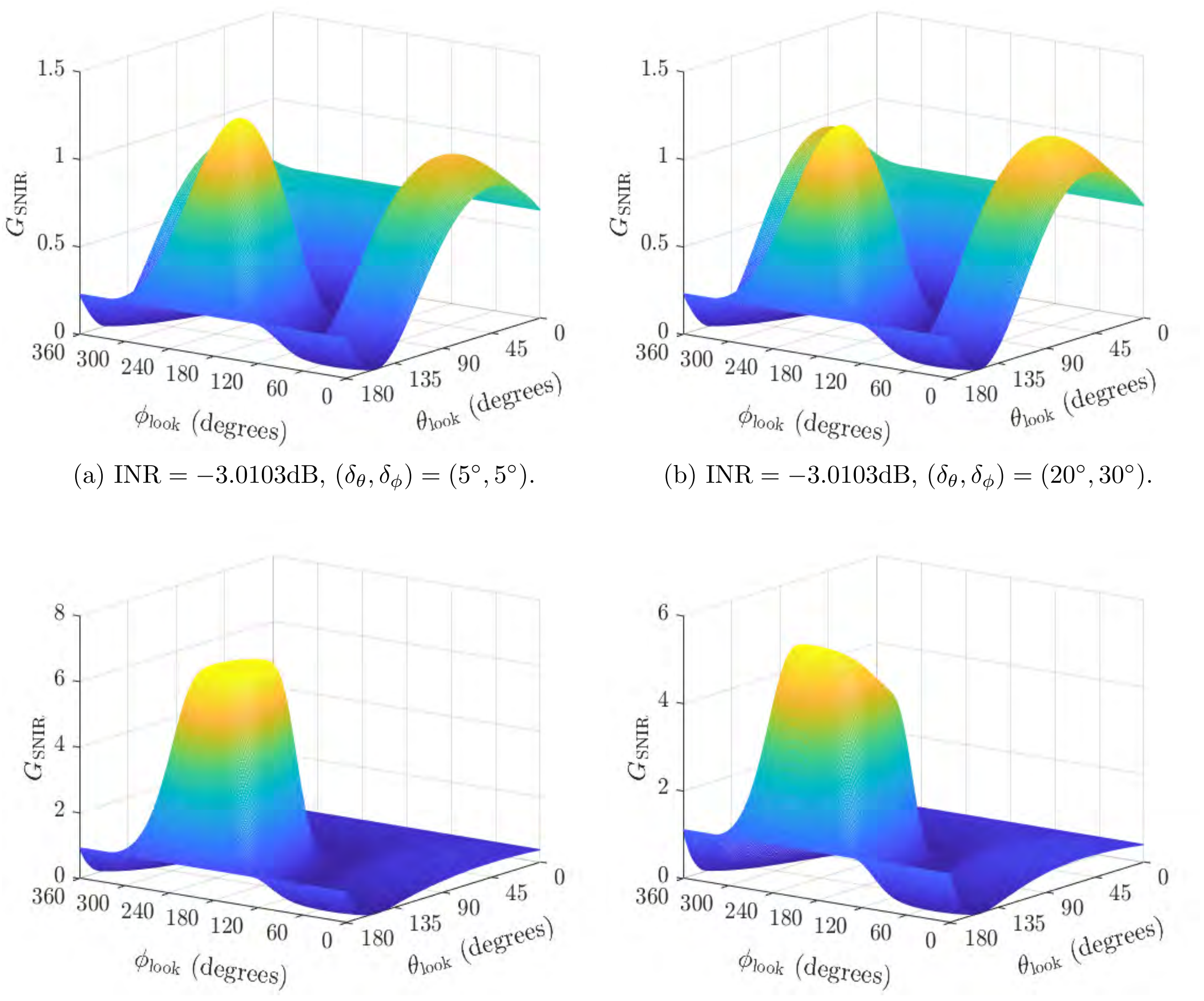

(a) INR $= -3.0103$dB, $(\delta_\theta, \delta_\phi) = (5°, 5°)$.

(b) INR $= -3.0103$dB, $(\delta_\theta, \delta_\phi) = (20°, 30°)$.

(c) INR $= 10$dB, $(\delta_\theta, \delta_\phi) = (5°, 5°)$.

(d) INR $= 10$dB, $(\delta_\theta, \delta_\phi) = (20°, 30°)$.

Figure 3.15: Array's signal-to-noise-plus-interference ratio gain (G_{SNIR}) versus the nominal "look direction" $(\theta_{\text{look}}, \phi_{\text{look}})$ for $\alpha = 0.7$ (subcardioid) and $(\delta_\theta, \delta_\phi)$ - the interference's offset from true peak direction $(\theta_{\text{peak}}, \phi_{\text{peak}})$.

3.17b, $\text{HR}^{(\alpha)}(g_{\text{look}})$ in/decreases monotonically according to Figure 3.18b. Whether increases or decreases – that depends on the particular value of g_{look}. This monotonic variation in $\text{HR}(\alpha, g_{\text{look}})$ with α, however, does not occur in the spatial-matched-filter beam-pattern as seen in Figure 3.16a.

3.8.4 Mainlobe's Half-Power Beamwidth

Figure 3.19 show that both beam-patterns vary little with g_{look} at small α. As α increases, the spatial-matched-filter beamwidth increases until $\alpha \approx 0.77$, at which the entire beam-pattern is taller than the half-power height, rendering the beamwidth to become undefined. Please see Figure 3.19a. In contrast, the present magnitude pattern's beamwidth exists $\forall\alpha$ for at least some g_{look}.

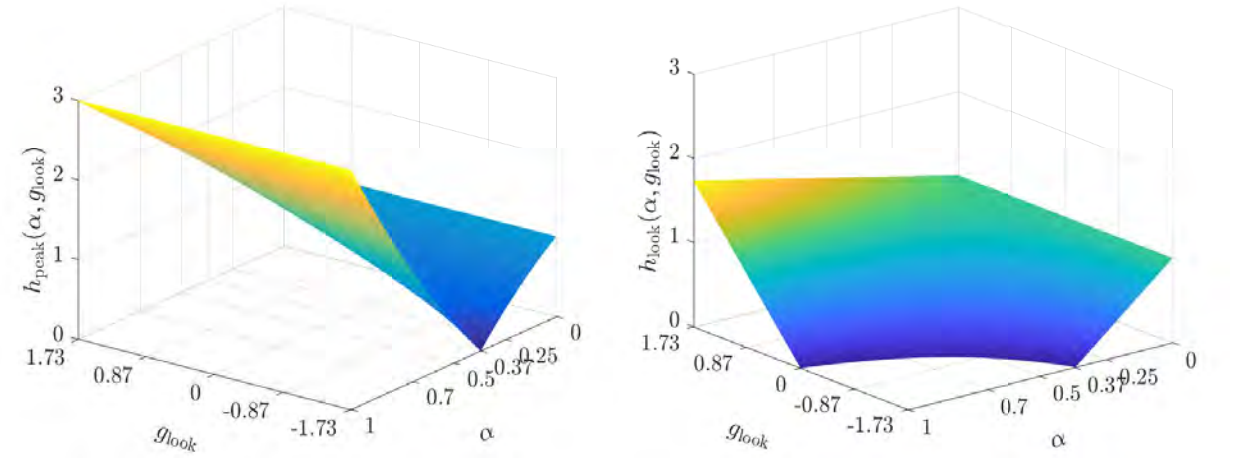

(a) (b)

Figure 3.16: Beam-pattern's mainlobe's height $h_{\mathrm{look}}(\alpha, g_{\mathrm{look}})$ against "cardioidicity index" α and g_{look} for (a) the spatial-matched-filter beam-pattern, and (b) the current magnitude pattern.

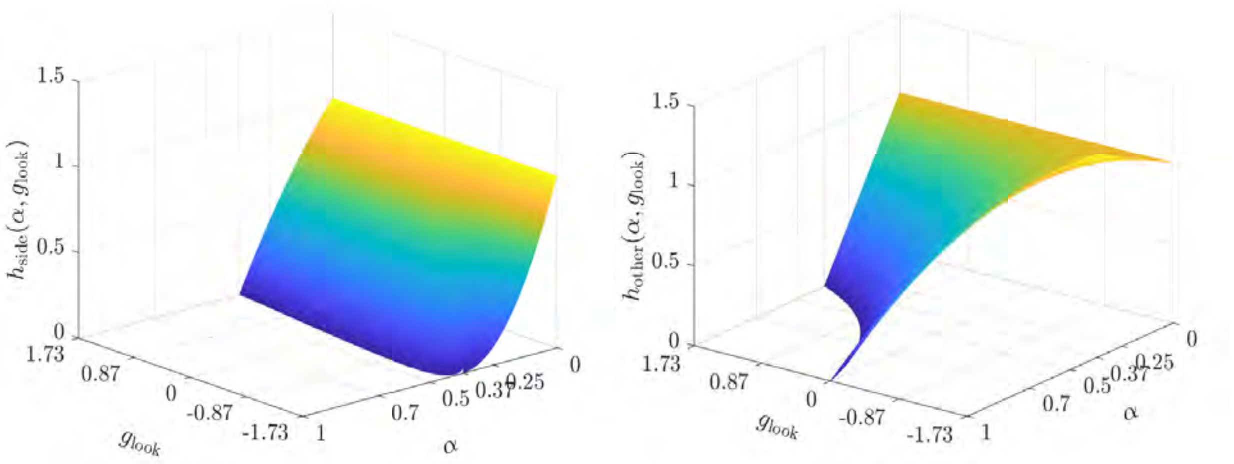

(a) (b)

Figure 3.17: Beam-pattern's second lobe's height $h_{\mathrm{other}}(\alpha, g_{\mathrm{look}})$ against "cardioidicity index" α and g_{look} for (a) the spatial-matched-filter beam-pattern, and (b) the current magnitude pattern.

The spatial-matched-filter beam-pattern is all zero if $\alpha = \frac{1}{2}(\sqrt{3} - 1)$ and $g_{\mathrm{look}} = -\sqrt{3}$ simultaneously hold

3.8.5 Array Gain

Both beam-patterns' maximum array gains equal 3, in $\{\forall\alpha, \forall g_{\mathrm{look}}\}$. The spatial-matched-filter beam-pattern's array gain equals zero only if both $\alpha = \frac{1}{2}(\sqrt{3} - 1)$ and $g_{\mathrm{look}} = -\sqrt{3}$

[6]Chapter 1 uses the symbol BW which has already been normalized by h^2_{peak}.

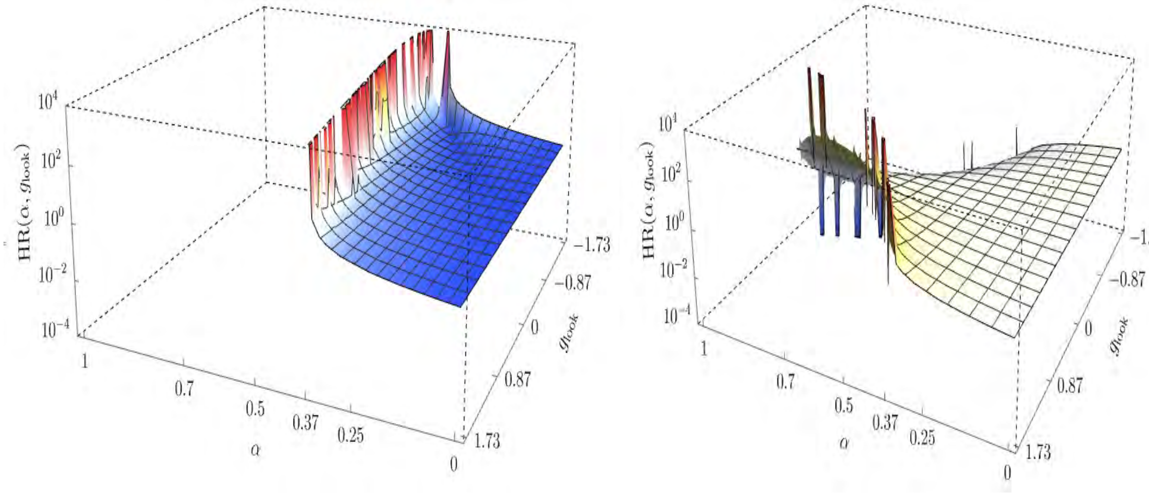

(a) (b)

Figure 3.18: Main-to-second lobe height ratio $\mathrm{HR}(\alpha, g_{\mathrm{look}})$ against "cardioidicity index" α and g_{look} for (a) the spatial-matched-filter beam-pattern, and (b) the current magnitude pattern.

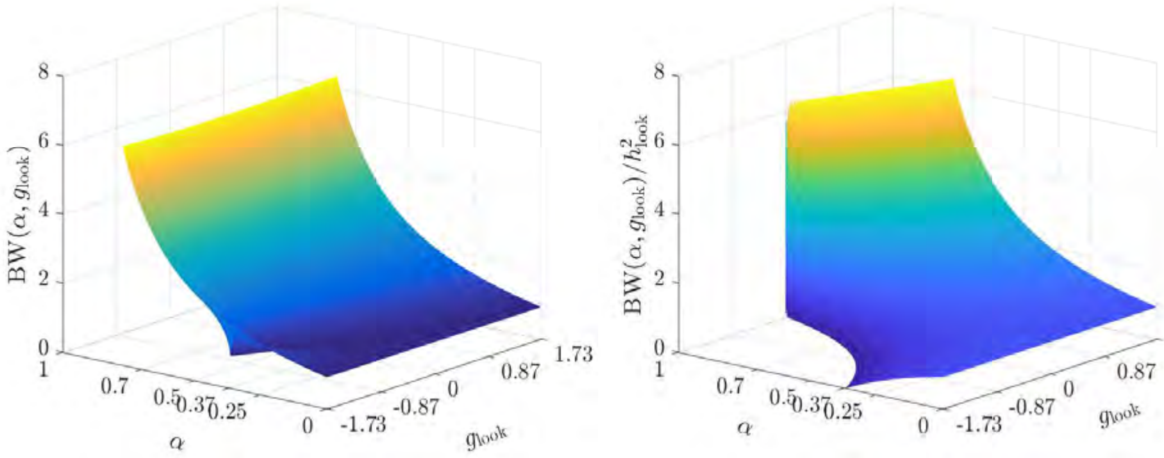

(a) (b)

Figure 3.19: Mainlobe's half-power beamwidth $\mathrm{BW}(\alpha, g_{\mathrm{look}})$ against "cardioidicity index" α and g_{look} for (a) the spatial-matched-filter beam-pattern, and (b) the current magnitude pattern. [7]

are simultaneously true. Please refer to Figure 3.20a.

The current magnitude pattern's array gain $G^{(\alpha)}(\theta_{\mathrm{look}}, \phi_{\mathrm{look}})$ would equal zero for more combinations of α and g_{look}. That is, whenever $g_{\mathrm{look}} = \frac{\alpha-1}{\alpha}$, which graphically represented as an arc in Figure 3.20b.

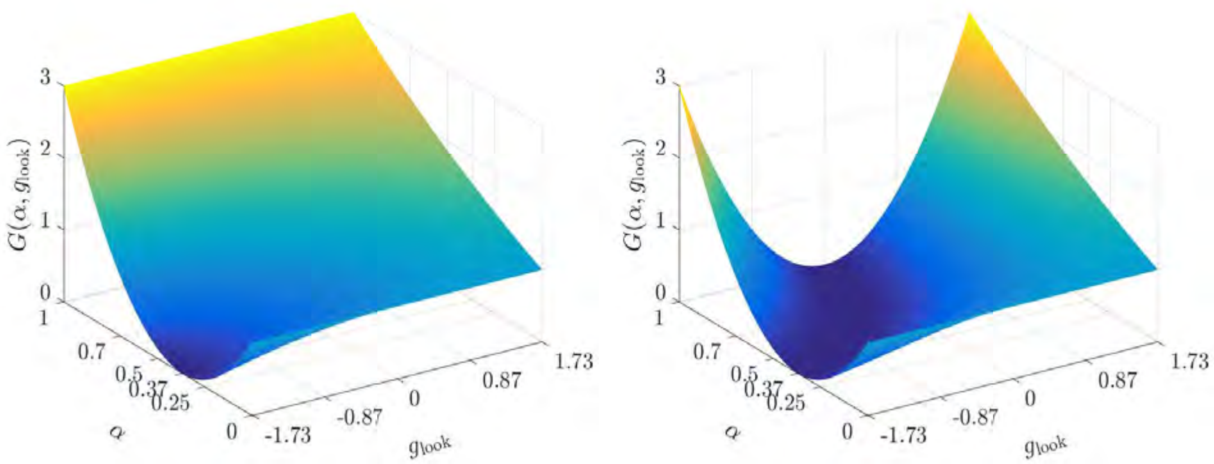

(a) (b)

Figure 3.20: Array gain $G(\alpha, g_{\mathrm{look}})$ against "cardioidicity index" α and g_{look} for (a) the spatial-matched-filter beam-pattern, and (b) the current magnitude pattern.

3.9 Summary

Cardioid hydrophones/microphones provide low backlobes/sidelobes, relative to figure-8 bi-directional sensors (such as velocity-sensors). Collocating three perpendicularly oriented cardioids would render the triad's array manifold independent of the incident signal's frequency and spectrum, thereby decoupling the azimuth-elevation dimensions from the frequency dimension, leading to great simplification in any real-time signal processing. This study proposes the first data-independent beamformer without pointing bias. This new beamformer's height ratio, beamwidth, directivity, and array gain are also analytically derived in this chapter.

Chapter 4
Two Higher-Order Figure-8 Sensors in Spatial Collocation — Their "Spatial Matched Filter" Beam-Pattern

4.1 Overview

4.1.1 Differential Sensors

Highly directive microphones/hydrophones could enhance "random efficiency" (i.e., could better suppress background noises/interference off-axis) and could increase the "distance factor" (i.e., the microphone's/hydrophone's spatial reach on-axis). One type of directional microphones/hydrophones is the differential sensor.

A *first*-order differential sensor (a.k.a. a "pressure gradient" sensor) often implemented by measuring the pressure difference across a diaphragm's two sides. This first-order spatial finite difference is proportional to the acoustical particle velocity; therefore the first-order differential sensor is also called a uni-axial "velocity sensor" or a "velocity hydrophone". This first-order differential sensor would have a dipole-like directional response of $\cos(\phi)$, where $\phi \in [0, 2\pi)$ denotes the incident source's incident angle measured with respect to the sensor axis. This is labeled "figure-8", because the $\cos(\phi)$ gain response resembles the digit "8". This response is bidirectional in nature, sensitive equally to incident energy from the front as well as from the back, but little sideway pickup.

The above-mentioned *first*-order differential sensor could be generalized to the a kth order, by (chapter 8.5 of [39], chapter 2.2 of [2]) measuring pressure field at $k+1$ closely spaced points along a straight line, then by computing the kth-order finite difference among them in order to approximate a measurement of the kth-order partial derivative of the pressure field [64,65]). A kth-order differential sensor has a directional gain response equal to the kth-order spatial derivative of the pressure field. More mathematically, a k-order differential sensor would have a directional response of $\cos^k(\phi)$.

The frequency response of these higher-order sensors limits their applications. The kth order sensor depends on ω^k which makes them more sensitive to high frequency sounds hence attenuating lower frequency sounds along with noise [1]. This limits their applications to high-frequency sound sensing such as in some musical instruments or measuring engine noises. Also hearing aids benefits from higher-order figure-8 microphones due to their abilities to be pick up close sound sources while attenuating distant source sources in a noisy or reverberant environments. Miniaturized higher-order microphones also finds applications as microphones for telephones, computers, portable digital devices, camcorders, and surveillance systems [75].

Some higher-order figure-8 sensors have been realized dating as far back as 1942 to 2008. The second-order bi-directional sensors have been realized in [7, 74, 75, 77–83]. The third-order has been designed and realized in (Section 5.3 in [2]), [74–76], while the Fifth-order has been implemented in [73]. Choice of the best kth-order depends on availability, frequency of the source, and the proximity of the source relative to the sensor.

4.1.2 A Bi-Axial Pair of Differential Sensors in Spatial Collocation and Perpendicular Orientation

First-order differential sensors have been used for decades as a collocated *pair* in perpendicular orientation, giving an array manifold of

$$\mathbf{a}_1(\phi) = \begin{bmatrix} \cos(\phi) \\ \sin(\phi) \end{bmatrix}. \tag{4.1.1}$$

The above array manifold has a key advantage of independence from the frequency/ spectrum/ bandwidth of the incident signal, thereby decoupling the frequency coordinate from the direction-of-arrival coordinate. Such a pair is sometimes called a "u-u probe". It has been implemented in hardware [59, 60, 67], while its directivity and beampattern have been studied in [68, 70]. Direction-finding formulas have been advanced for it in [9]. Please refer to [66] for a literature review. Incidentally, first-order differential sensors have been used in a collocated and perpendicular *triad*, called a "tri-axial velocity-sensor", or a "velocity-sensor triad", or a "vector sensor", or a "vector hydrophone". The effect of non-perpendicularity in such tri-axial velocity sensors is studied in Chapter 5. For comprehensive reviews of the "tri-axial velocity-sensor" literature, please consult [34, 36, 71].

Similarly, for a bi-axial pair of k-th order differential sensors in spatial collocation and perpendicular orientation, the pair's array manifold is equal to

$$\mathbf{a}_k(\phi) = \begin{bmatrix} \cos^k(\phi) \\ \sin^k(\phi) \end{bmatrix}. \tag{4.1.2}$$

This array manifold retains the frequency-decoupling advantage of (4.1.1).

4.1.3 A Bi-Axial Pair of Differential Sensors in Spatial Collocation but *Arbitrary* Orientation

Perfectly perpendicular axes are, however, an idealization unachievable in practice. If the x-axis rotates on the x-y plane counter-clockwise by an angle of $\tilde{\phi}$ (see Figure 4.1), the corresponding rotation matrix is

$$\mathbf{R}(\tilde{\phi}) = \begin{bmatrix} \cos(\tilde{\phi}) & -\sin(\tilde{\phi}) \\ 0 & 1 \end{bmatrix}. \tag{4.1.3}$$

The non-perpendicular but collocated pair of differential sensors would then have an array manifold of

$$\begin{aligned} \tilde{\mathbf{a}}_k(\phi, \tilde{\phi}) &= \mathbf{R}(\tilde{\phi})\, \mathbf{a}_k(\phi) \\ &= \begin{bmatrix} \cos(\tilde{\phi}) & -\sin(\tilde{\phi}) \\ 0 & 1 \end{bmatrix} \begin{bmatrix} \cos^k(\phi) \\ \\ \sin^k(\phi) \end{bmatrix} \\ &= \begin{bmatrix} \cos(\tilde{\phi}) \cos^k(\phi) - \sin(\tilde{\phi}) \sin^k(\phi) \\ \\ \sin^k(\phi) \end{bmatrix}. \end{aligned} \tag{4.1.4}$$

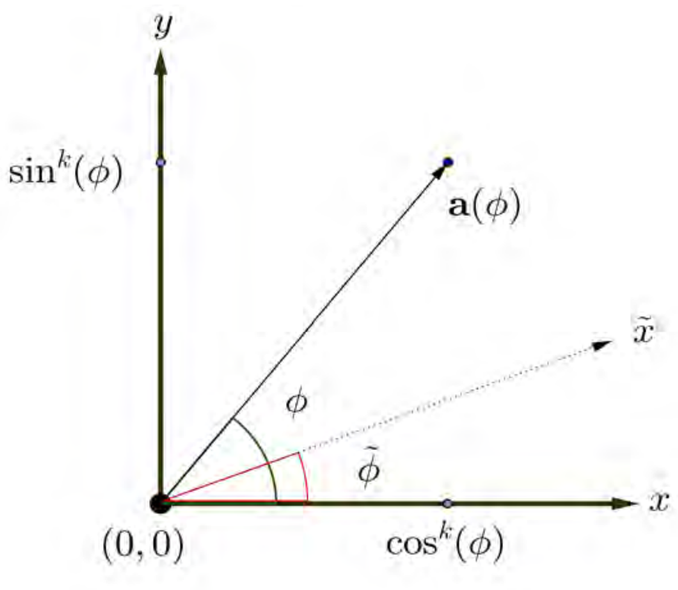

Figure 4.1: A bi-axial pair of high-order differential sensors with the horizontal axis rotated counterclockwise through $\tilde{\phi}$.

4.1.4 "Spatial Matched Filter" Beamforming on a Bi-Axial Pair of Collocated Differential Sensors

"Spatial matched filter" (SMF) beamforming is common in data-independent beamforming. It weights-and-sums the individual channels' measurements, by matching the beamforming weights to the array's spatial steering vector weights for the pre-set/fixed "look direction". If the interference and the additive noise together are statistically 1) zero-mean, 2) spatially uncorrelated, and 3) uncorrelated with the desired signal incident from the pre-set "look direction" – then this "spatial matched filter" beamformer would maximize its output signal-to-noise ratio (SNR) [57].

If the "spatial matched filter" beamformer has no prior knowledge of any non-orthogonality between the two axes but presumes them to be orthogonal, the beampattern would then equal

$$B_k^{(2+0)}(\phi, \phi_L, \tilde{\phi}) \quad = \quad \frac{\mathbf{a}_k(\phi_L)^T\,\mathbf{R}(\tilde{\phi})\,\mathbf{a}_k(\phi)}{\max\limits_{\phi}\left|\mathbf{a}_k(\phi_L)^T\,\mathbf{R}(\tilde{\phi})\,\mathbf{a}_k(\phi)\right|}. \tag{4.1.5}$$

The "spatial match filter" beampattern – for the special but important biaxial case at $k = 1$ (i.e., the u-u probe) and with non-perpendicular axes – has already been analyzed in [17]. There, it is analytically proved that a directional pointing error would be incurred, but the overall beam pattern would otherwise stay the same as in the perpendicular case. Incidentally, for a *triad* of *first*-order differential sensors that are collocated in space and perpendicular in orientation, the "spatial matched filter" beam-pattern has been analyzed in [18]. This work will generalize the analysis in [17] on a bi-axial pair of differential sensors to any arbitrary order k.

4.1.5 Organization of This Chapter

Section 4.2 will derive the location of the beampattern's peak and analytically derive the pointing bias in terms of the axes' skew angle $\tilde{\phi}$, the pre-set "look direction" ϕ_L, and the differential sensor order k of the two collocated higher-order non-perpendicular figure-8 sensors. Section 4.3 will re-express the skewed pair's array manifold in (4.1.4) to an alternative mathematical form more conductive for subsequent analysis and also will analyze the different sub-functions realized by the simplification of the beampattern in and how each of these functions affects the beampattern. Section 4.4 reduces the beampattern to 3 degree-of-freedom to facilitate the study of the effect of non-perpendicularity. Section 4.5 finally concludes the investigation.

4.2 To Derive the Beampattern's Pointing Bias

The location of the beampattern's peak is derived in Section 4.2.1. The pointing error is then analytically studied in terms of the look direction ϕ_L, mis-orientation angle $\tilde{\phi}$, and the sensor order k in Sections 4.2.2 and 4.2.3. Section 4.2.2 will study the pointing error for first-order collocated figure-8 bi-axial sensor, i.e $k = 1$. The pointing error for $k > 1$ will be defined in Section 4.2.3 and analyzed subsequently.

4.2.1 To Derive the Beampattern's Peak

The peak of the beampattern (4.1.5) is located at –noting that its denominator is functionally independent on ϕ

$$\begin{aligned}
\phi_{\text{peak}} &= \arg\max_{\phi\in[0,2\pi)]} \left\{ \underbrace{\mathbf{a}_k(\phi_L)^T \; \mathbf{R}(\tilde{\phi})}_{:=\mathbf{u}_k(\phi_L,\tilde{\phi})^T} \; \mathbf{a}_k(\phi) \right\} \\
&= \arg\max_{\phi\in[0,2\pi)]} \left\{ \mathbf{u}_k(\phi_L,\tilde{\phi})^T \; \mathbf{a}_k(\phi) \right\} \\
&= \arg\max_{\phi\in[0,2\pi)]} \left\{ \underbrace{u_1 \cos^k(\phi) + u_2 \sin^k(\phi)}_{:=\hat{B}_k} \right\} \\
&= \arg\max_{\phi\in[0,2\pi)]} \; \hat{B}_k,
\end{aligned} \tag{4.2.1}$$

where

$$\mathbf{u}_k(\phi_L,\tilde{\phi}) = \begin{bmatrix} u_1 \\ u_2 \end{bmatrix} = \begin{bmatrix} \cos^k(\phi_L)\cos(\tilde{\phi}) \\ \sin^k(\phi_L) - \cos^k(\phi_L)\sin(\tilde{\phi}) \end{bmatrix}. \tag{4.2.2}$$

Applying the first derivative test to the maximization problem (4.2.1) to find the critical points of $\hat{B}$, $\frac{\partial \hat{B}_k}{\partial \phi}$ is set to zero and the following sets of solutions are obtained

$$\phi_{c1} = n\frac{\pi}{2}, \quad n = 0, 1, 2, 3 \tag{4.2.3}$$

$$\phi_{c2} = \tan^{-1}\left(\left[\frac{u_1}{u_2}\right]^{\frac{1}{k-2}} \right), \tag{4.2.4}$$

as the critical points of $\hat{B}$.

For $k = 1$, the maximum occurs at $\phi = \phi_{c2}$ since $\phi_{c1} \subset \phi_{c2}$, i.e

$$\begin{aligned} \phi_{\text{peak}}^{k=1} &= \tan^{-1}\left(\frac{u_2}{u_1}\right) \\ &= \tan^{-1}\left(\frac{\sin^k(\phi_L) - \cos^k(\phi_L)\sin(\tilde{\phi})}{\cos^k(\phi_L)\cos(\tilde{\phi})}\right) \end{aligned} \tag{4.2.5}$$

For $k > 1$, note that $\mathbf{a}_k(\phi)$ is 2×1 in size and is plotted in Figure 4.2 for $k = 3$ and $k = 4$. As k increases, $\|\mathbf{a}_k(\phi)\|_2$ becomes more concave. For all $k > 1$, $\|\mathbf{a}_k(\phi)\|_2$ is largest at $\phi = 0°, 90°, 180°, 270°$, therefore,

$$\begin{aligned} \phi_{\text{peak}}^{k>1} &= \phi_{c1} \\ &= \{0°, 90°, 180°, 270°\} \end{aligned} \tag{4.2.6}$$

Now that the peak locations have been obtained, we consider the denominator of (4.1.5) as $\left|\hat{B}\right|_{\max}$. To ease subsequent exposition, make the definition indicated below

$$\begin{aligned} \left|\hat{B}_k\right|_{\max} &:= \max_{\phi} \left|\hat{B}_k\right|, \\ &= \max_{\phi \in [0, 2\pi)]} \left|u_1 \cos^k(\phi) + u_2 \sin^k(\phi)\right| \end{aligned} \tag{4.2.7}$$

For $k = 1$, substitute (4.2.5) into (4.2.7) and

$$\left|\hat{B}_{k=1}\right|_{\max} = \|\mathbf{u}(\phi_L, \tilde{\phi})\|_2. \tag{4.2.8}$$

The analysis differs for $k > 1$. Inside the $|\cdot|$ of (4.2.7), the 2×1 potential steering vector of $\mathbf{a}_k(\phi)$ is projected onto the 2×1 skewed pair's look direction vector of $\mathbf{u}_k(\phi_L, \tilde{\phi})$. This vector projection gives a nonnegative scalar $\left|\hat{B}_k\right|$ which indicates the measured strength of the impinging signal. The incident angle ϕ that maximizes $\left|\hat{B}_k\right|$, as shown in Figure 4.2a, must be the apexes of the $\mathbf{a}_k(\phi)$ closest to $\mathbf{u}_k(\phi_L, \tilde{\phi})$. Here, $\left|\hat{B}_k\right|_{\max}$ is the maximum of all possible projections $\forall\phi$, for a preset ϕ_L and a preset $\tilde{\phi}$ (for even k, $\mathbf{a}_k(\phi)$ only exists in the first quadrant as shown in Figure 4.2b). Therefore,

$$\left|\hat{B}_{k>1}\right|_{\max} = \max_{\phi = 0°, 90°, 180°, 270°} \left|u_1 \cos^k(\phi) + u_2 \sin^k(\phi)\right|. \tag{4.2.9}$$

Note that $\cos(0) = -\cos(180°) = 1$ and $\sin(0) = \sin(180°) = 0$. Also $\cos(90°) = \cos(270°) = 0$ and $\sin(90°) = -\sin(270°) = 1$. Therefore,

$$\begin{aligned} \left|\hat{B}_{k>1}\right|_{\max} &= \max\{|u_1|, |u_2|\} \\ &= \|\mathbf{u}_k(\phi_L, \tilde{\phi})\|_\infty \end{aligned} \tag{4.2.10}$$

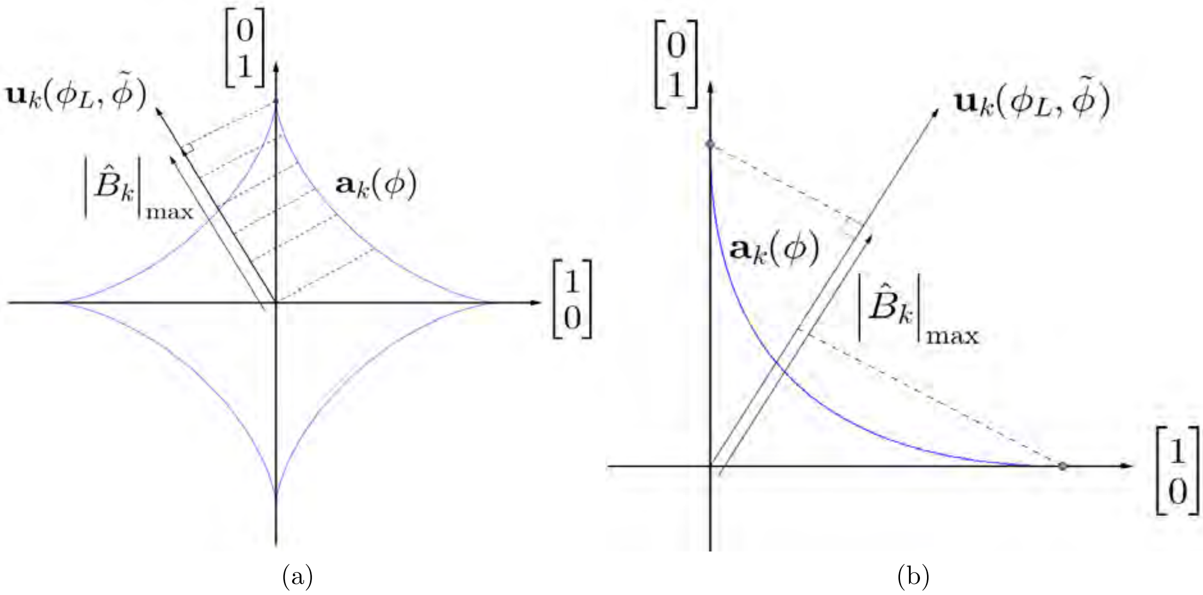

Figure 4.2: A diagrammatic proof of maximum projection of $\mathbf{a}_k(\phi)$ on $\mathbf{u}_k(\phi_L, \tilde{\phi})$ for (a) $k = 3$, and (b) $k = 4$ which can be generalized to all odd $k > 1$ and all even $k > 1$, respectively.

Generally, from (4.2.8) and (4.2.10),

$$\left|\hat{B}_k\right|_{\max} \;=\; ||\mathbf{u}_k(\phi_L, \tilde{\phi})||_p, \tag{4.2.11}$$

where $||\cdot||_p$ is the p-norm, and

$$p \;:=\; \begin{cases} 2, & \text{for } k = 1 \;; \\ \infty, & \text{for } k > 1 \end{cases} . \tag{4.2.12}$$

The simplified denominator (4.2.11)-(4.2.12) will be used in Section 4.3.2 to further simplify the beampattern.

4.2.2 Pointing Bias for First-Order ($k = 1$) Case

The beampattern's peak points in the look direction ϕ_L for a perfectly perpendicular case. This section will extend the work done in [17] – when the two figure-8 sensors are not perpendicular. Towards that we define the pointing bias as

$$\begin{aligned} \phi_{\text{bias}} \;&:=\; \phi_L - \phi_{\text{peak}}^{k=1} \\ &=\; \phi_L - \tan^{-1}\left(\frac{\sin^k(\phi_L) - \cos^k(\phi_L)\sin(\tilde{\phi})}{\cos^k(\phi_L)\cos(\tilde{\phi})}\right) \\ &=\; \phi_L - \tan^{-1}\left(\tan(\phi_L)\sec(\tilde{\phi}) - \tan(\tilde{\phi})\right) \end{aligned} \tag{4.2.13}$$

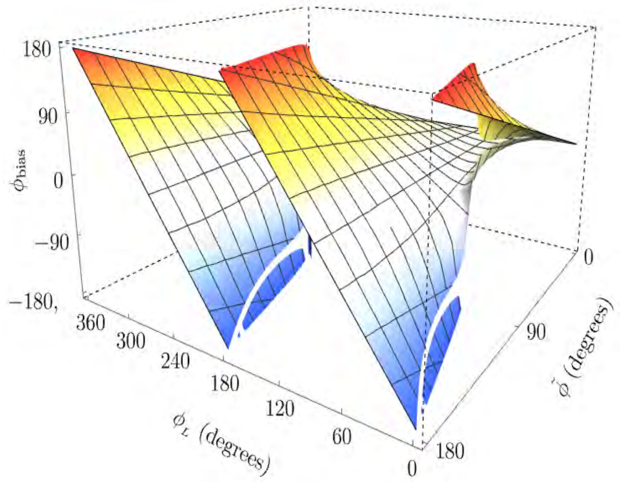

Figure 4.3: Plot of $\phi_{\rm bias}$ versus look direction ϕ_L and mis-orientation angle $\tilde{\phi}$ for $k = 1$.

Qualitative observations on the pointing bias $\phi_{\rm bias}$ versus ϕ_L and $\tilde{\phi}$ – see Figure 4.3:

{1.} The pointing bias is π-periodic with respect to ϕ_L.

{2.} $\phi_{\rm bias} = 0$ when $\phi_L = 90^\circ$ and 270°. This is because in this analysis, the vertical axis is assumed to remain perpendicular to the true horizontal axis.

{3.} For $\phi_L = 0^\circ$ or 180°, the pointing bias is equal to the mis-orientation angle $\tilde{\phi}$.

{4.} The pointing bias is zero for ϕ_L and $\tilde{\phi}$ that obey

$$\phi_L = \tan^{-1}\left(\frac{\sin\tilde{\phi}}{1-\cos\tilde{\phi}}\right)$$

4.2.3 Pointing Bias for Higher-Order ($k > 1$) Case

It is proved in Section 4.2.1 that the mainlobe of two collocated higher-order figure-8 sensor array can only point in either of 0°, 90°, 180°, and 270° for odd values of k, or combinations of $\{0^\circ$ and $180^\circ\}$, or $\{90^\circ$ and $270^\circ\}$ for even values of k – even for a perfectly perpendicular case. Due to this phenomenon, the pointing bias introduced due to non-perpendicularity of the two sensors is defined differently from the first-order case.

How do the look direction ϕ_L, axes' skew angle $\tilde{\phi}$ and sensor order k affect the pointing bias? By the definition of the infinity norm, $\|\mathbf{u}_k(\phi,\tilde{\phi})\|_\infty$ must equal the absolute magnitude of either entry in the 2×1 vector $\mathbf{u}_k(\phi,\tilde{\phi})$. More precisely, $\|\mathbf{u}_k(\phi,\tilde{\phi})\|_\infty = \max\left\{\left|\left[\mathbf{u}_k(\phi_L,\tilde{\phi})\right]_1\right|, \left|\left[\mathbf{u}_k(\phi_L,\tilde{\phi})\right]_2\right|\right\}$. Here we analyze what entry of $\mathbf{u}_k(\phi,\tilde{\phi})$ is larger in magnitude at what values of $\{\phi_L,\tilde{\phi},k\}$.

$$\begin{aligned} \left|\left[\mathbf{u}_k(\phi_L,\tilde{\phi})\right]_1\right| \;&\geq\; \left|\left[\mathbf{u}_k(\phi_L,\tilde{\phi})\right]_2\right|, \\ \Leftrightarrow\quad \cos(2\tilde{\phi}) + 2\sin(\tilde{\phi})\tan^k(\phi_L) - \tan^{2k}(\phi_L) \;&\geq\; 0, \end{aligned} \tag{4.2.14}$$

which is quadratic in $\tan^k(\phi_L)$. Hence, (4.2.14) is equivalent to

$$\left[\tan^k \phi_L - \sqrt{2}\sin(\tilde{\phi}+45^\circ)\right]\left[\tan^k \phi_L + \sqrt{2}\cos(\tilde{\phi}+45^\circ)\right] \leq 0, \tag{4.2.15}$$

$$\Leftrightarrow \tan^k \phi_L \in \left[-\sqrt{2}\cos(\tilde{\phi}+45^\circ), \sqrt{2}\sin(\tilde{\phi}+45^\circ)\right]. \tag{4.2.16}$$

Therefore, it holds $\forall k > 1$ that for

$$\tan^k(\phi_L) \in \left[-\sqrt{2}\cos(\tilde{\phi}+45^\circ), \sqrt{2}\sin(\tilde{\phi}+45^\circ)\right], \tag{4.2.17}$$

$$\left\|\mathbf{u}_k\left(\phi,\tilde{\phi}\right)\right\|_\infty = \left|\left[\mathbf{u}_k\left(\phi_L,\tilde{\phi}\right)\right]_1\right|,$$

which directly implies that the mainlobe of the beampattern points in 0° or 180°.

Alternatively, the beampattern will point in 90° and 270° if and only if

$$\tan^k(\phi_L) \notin \left[-\sqrt{2}\cos(\tilde{\phi}+45^\circ), \sqrt{2}\sin(\tilde{\phi}+45^\circ)\right], \tag{4.2.18}$$

i.e.

$$\left\|\mathbf{u}_k\left(\phi,\tilde{\phi}\right)\right\|_\infty = \left|\left[\mathbf{u}_k\left(\phi_L,\tilde{\phi}\right)\right]_2\right|.$$

In perfectly perpendicularity, the beampattern will point in

$$\phi_{\text{peak}} = \begin{cases} \begin{cases} 0^\circ & \text{if } \phi_L \in [-45^\circ, 45^\circ] \\ 90^\circ & \text{if } \phi_L \in [45^\circ, 135^\circ] \\ 180^\circ & \text{if } \phi_L \in [135^\circ, 225^\circ] \\ 270^\circ & \text{if } \phi_L \in [225^\circ, 315^\circ] \end{cases}, & \text{for odd } k \\ \\ \begin{cases} 0^\circ, 180^\circ & \text{if } \phi_L \in [-45^\circ, 45^\circ] \cup [135^\circ, 225^\circ] \\ 90^\circ, 270^\circ & \text{if } \phi_L \in [45^\circ, 135^\circ] \cup [225^\circ, 315^\circ] \end{cases}, & \text{for even } k \end{cases}. \tag{4.2.19}$$

Under perfect conditions, given, say $\phi_L = 30^\circ$ and any even $k > 1$, the beampattern will point to 0° and 180°, according to (4.2.19). But according to (4.2.17), given $k = 2$ and $\tilde{\phi} = -35^\circ$, the region described in (4.2.17) becomes $[-1.393, 0.246]$. Then $\tan^2(30^\circ) = 0.333 \notin [-1.393, 0.246]$, and according to (4.2.18) implies the beampattern points in 90° and 270° instead, hence a pointing error. Plots of the relationship between ϕ_L, $\tilde{\phi}$, k, and pointing bias are shown in Figure 4.4 for $k = 2, ..., 5$.

Observations made on Figure 4.4:

{1.} The mainlobe points mainly in the vertical direction, i.e. 90° and 270° as there are more blue areas than yellow. Mainly due to the same reason given in item {2.} of Section 4.2.2.

{2.} For $\phi_L \in [45, 90]$ and $[225, 315]$, the beampattern points only in the vertical direction irrespective of the value of the misorientation angle ϕ_L. Similar to point {2.} in Section 4.2.2.

{3.} The pointing error reduces as k increases. This can be observed between Figures 4.4a and 4.4c where the shape of the yellow areas curves less as k increases from 2 to 4. Similar trend can be noticed for odd values of k, i.e from Figure 4.4b and 4.4d.

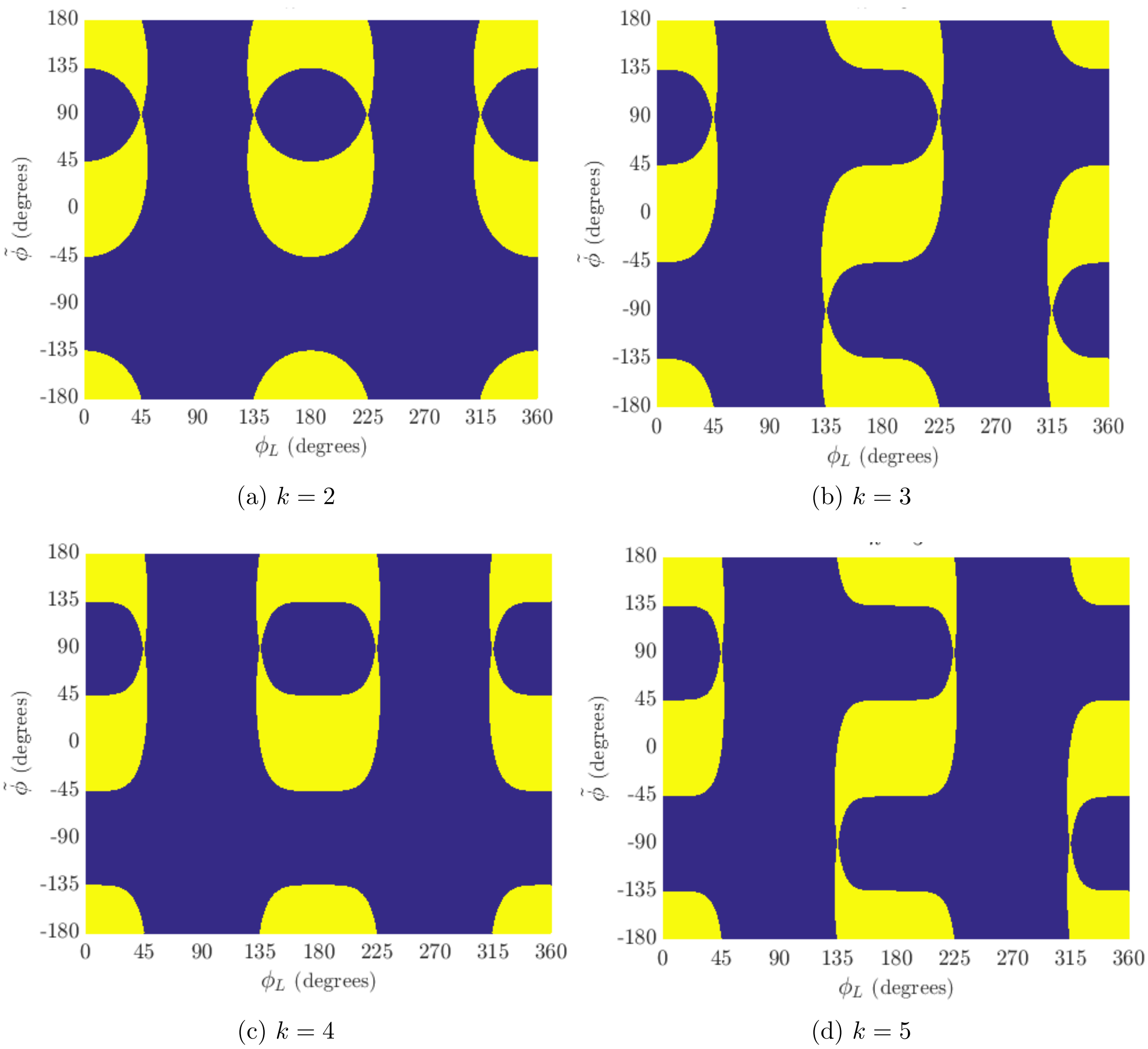

(a) $k = 2$

(b) $k = 3$

(c) $k = 4$

(d) $k = 5$

Figure 4.4: A map depicting the regions in $(\phi_L, \tilde{\phi})$ where the mainlobe points in $\{0°, 180°\}$ in yellow, and $\{90°, 270°\}$ in blue for different values of $k > 1$.

4.3 Further Analyzing the Beampattern

The location of the peak of the beampattern, hence the pointing bias have been derived and analyzed in Section 4.2. In this section, the beampattern is further analyzed by expressing it in form of magnitude and phase sub-functions to facilitate analogy between the higher-order and first-order figure-8 sensors' beampatterns.

4.3.1 To Mathematically Relate the Higher-Order $\mathbf{a}_k(\phi)$ to the First-Order $\mathbf{a}_1(\phi)$

To facilitate subsequent analysis, the kth-order array manifold $\mathbf{a}_k(\phi)$ in (4.1.2) is re-expressed here in a mathematically more convenient form, in terms of the first-order array manifold $\mathbf{a}_1(\phi)$, as follows:

$$\begin{aligned} \mathbf{a}_k(\phi) &= \beta_k(\phi)\ \mathbf{a}_1(\xi_k(\phi)) \\ &= \beta_k(\phi) \begin{bmatrix} \cos(\xi_k(\phi)) \\ \sin(\xi_k(\phi)) \end{bmatrix}, \quad \forall \phi \in [0, 2\pi), \end{aligned} \tag{4.3.1}$$

where

$$\beta_k(\phi) := \sqrt{\sin^{2k}(\phi) + \cos^{2k}(\phi)}, \tag{4.3.2}$$

$$\xi_k(\phi) := \tan^{-1}(\sin^k(\phi)/\cos^k(\phi)). \tag{4.3.3}$$

This transformation is based upon the preservation of the ratio of the horizontal and vertical components of a vector defined in 2-D Cartesian Coordinates. Any vector in the 2-D Cartesian Coordinates is be defined by a magnitude function and a phase function. The validity of (4.3.1)-(4.3.3) is analytically proved in Appendix B. This insight is new to the open literature. That (4.1.2) may be alternatively expressed as (4.3.1)-(4.3.3) is unsurprising: (4.1.2) may be interpreted to define a vector in a two-dimensional Cartesian space. Such a vector can be fully described by its magnitude ($\beta_k(\phi)$) and its phase ($\xi_k(\phi)$).

This (4.3.1) maintains the ratio of $\frac{[\mathbf{a}_k(\phi)]_2}{[\mathbf{a}_k(\phi)]_1} = \frac{[\mathbf{a}(\xi_k(\phi))]_2}{[\mathbf{a}(\xi_k(\phi))]_1}$, where $[\cdot]_1$ and $[\cdot]_2$ denotes the 1st and 2nd entries of the enclosed vector, respectively.

4.3.2 To Re-Express the Beampattern in Sub-Functions

The beampattern of (4.1.5) has a denominator that is functionally independent of the source's incident direction (ϕ). This denominator thus affects the beampattern as a magnitude-scaling factor, which does vary with the axes' skew angle ($\tilde{\phi}$) and the beampattern's "look direction" (ϕ_L).

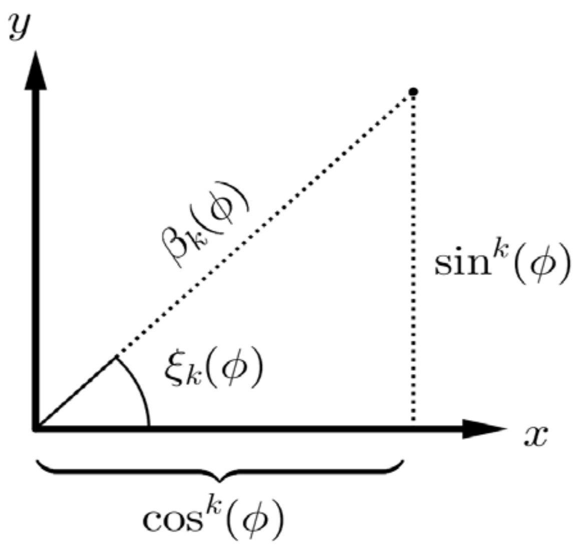

Figure 4.5: The geometric relationship between ϕ and $\xi_k(\phi)$.

Denoting this denominator has been shown in (4.2.11) in Section 4.2.1 to be

$$\left|\hat{B}_k\right|_{\max} = \begin{cases} \|\mathbf{R}(\tilde{\phi})^T \mathbf{a}_k(\phi_L)\|_2, & \text{if } k = 1 \\ \\ \|\mathbf{R}(\tilde{\phi})^T \mathbf{a}_k(\phi_L)\|_\infty, & \text{if } k > 1. \end{cases} \tag{4.3.4}$$

Substitute (4.3.4) into (4.1.5),

$$B_k^{(2+0)}(\phi, \phi_L, \tilde{\phi}) = \frac{\mathbf{u}_k(\phi_L, \tilde{\phi})^T \, \mathbf{a}_k(\phi)}{||\mathbf{u}_k(\phi_L, \tilde{\phi})||_p}. \tag{4.3.5}$$

where

$$p = \begin{cases} 2, & k = 1 \\ \infty, & k > 1 \end{cases} \tag{4.3.6}$$

Multiplying both numerator and denominator of (4.3.5) by $\|\mathbf{u}_k(\phi_L, \tilde{\phi})\|_2$

$$B_k^{(2+0)}(\phi, \phi_L, \tilde{\phi}) = \frac{\|\mathbf{u}_k(\phi_L, \tilde{\phi})\|_2}{\|\mathbf{u}_k(\phi_L, \tilde{\phi})\|_p} \frac{\mathbf{u}_k(\phi_L, \tilde{\phi})^T}{\|\mathbf{u}_k(\phi_L, \tilde{\phi})\|_2} \, \mathbf{a}_k(\phi). \tag{4.3.7}$$

The first fraction above is functionally independent of ϕ for all k and equals unity for $k = 1$ and any other constant with respect to ϕ when $k > 1$.

The second fraction is also functionally independent of ϕ for all k. Moreover, it is a unit vector in two-dimensional Cartesian space; and any such a unit vector may be represented as $\begin{bmatrix} \cos(\cdot) \\ \sin(\cdot) \end{bmatrix}$ with same phase angle inside both trigonometric functions. Hence, write

$$\begin{aligned} \frac{\mathbf{u}_k(\phi_L,\tilde{\phi})}{\|\mathbf{u}_k(\phi_L,\tilde{\phi})\|_2} &= \begin{bmatrix} \cos(\chi_k(\phi_L,\tilde{\phi})) \\ \sin(\chi_k(\phi_L,\tilde{\phi})) \end{bmatrix} && (4.3.8) \\ &= \mathbf{a}(\chi_k(\phi_L,\tilde{\phi})), && (4.3.9) \end{aligned}$$

where

$$\chi_k(\phi_L,\tilde{\phi}) \;:=\; \tan^{-1}\left(\frac{[\mathbf{u}_k(\phi_L,\tilde{\phi})]_2}{[\mathbf{u}_k(\phi_L,\tilde{\phi})]_1}\right) \;\in\; [-\pi,\pi]. \tag{4.3.10}$$

Substituting (4.3.1)-(4.3.3) and (4.3.8) all into (4.3.7),

$$\begin{aligned} B_k^{(2+0)}(\phi,\phi_L,\tilde{\phi}) &= \frac{\|\mathbf{u}_k(\phi_L,\tilde{\phi})\|_2}{||\mathbf{u}_k(\phi_L,\tilde{\phi})||_p}\beta_k(\phi)\ \mathbf{a}(\chi_k(\phi_L,\tilde{\phi}))^T\mathbf{a}(\xi_k(\phi)) \\ &= \overbrace{\frac{\|\mathbf{u}_k(\phi_L,\tilde{\phi})\|_2}{||\mathbf{u}_k(\phi_L,\tilde{\phi})||_p}}^{\upsilon_k(\phi_L,\tilde{\phi}):=}\beta_k(\phi)\ \cos(\xi_k(\phi)-\chi_k(\phi_L,\tilde{\phi})) \\ &= \upsilon_k(\phi_L,\tilde{\phi})\ \beta_k(\phi)\ \cos(\xi_k(\phi)-\chi_k(\phi_L,\tilde{\phi})), && (4.3.11) \end{aligned}$$

where $\beta_k(\phi)$, $\xi_k(\phi)$, and $\chi_k(\phi_L,\tilde{\phi})$ are defined respectively in (4.3.2), (4.3.3), and (4.3.10).

The beampattern is thus decomposed into a nonnegative magnitude factor of $\upsilon_k(\phi_L,\tilde{\phi})$ $\beta_k(\phi)$ and the cosine of a phase difference of $\xi_k(\phi)-\chi_k(\phi_L,\tilde{\phi})$. Though the magnitude factor of $\upsilon_k(\phi_L,\tilde{\phi})\beta_k(\phi)$ is quadri-variate, $\upsilon_k(\phi_L,\tilde{\phi})$ is only trivariate and is independent of ϕ, whereas $\beta_k(\phi)$ is only bivariate. Likewise, though the phase $\xi_k(\phi)-\chi_k(\phi_L,\tilde{\phi})$ is quadri-variate, $\xi_k(\phi)$ is only bivariate and $\chi_k(\phi_L,\tilde{\phi})$ is only trivariate and is independent of ϕ. Each of these factors or terms will be analyzed in the subsequent sections.

4.3.3 Analysis of Magnitude-Scaling Factor of $\beta_k(\phi)$

The nonnegative multiplicative factor of $\beta_k(\phi)$ is independent of the axial skew angle of $\tilde{\phi}$ and independent of the pointing direction ϕ_L. The variation of $\beta_k(\phi)$ with ϕ is shown in Figure 4.6 for various sensor-orders k. Four lobes exist for all $k>1$, with heights equal to 1 and centered around $\phi=0°$, $90°$, $180°$, $270°$, with nulls of heights equal to $\sqrt{2^{1-k}}$ at $\phi=45°$, $135°$, $225°$, $315°$. Please refer to Appendix C.1 for proof of the null location and height.

The lobes sharpens in width as the sensor order k increases, i.e. $\beta_k(\phi)\geq\beta_{k+1}(\phi)$, $\forall\phi$, $\forall k\geq 1$. The analytical proof is given in Appendix C.2.

Recall that the beam-pattern's magnitude-scaling multiplicative factor of $\upsilon_k(\phi_L,\tilde{\phi})\beta_k(\phi)$

varies with the incident source's direction-of-arrival ϕ only through $\beta_k(\phi)$. This implies that the directivity of a pair of $k > 1$ figure-8 sensors (whether orthogonally oriented or not) is limited to four sector around $\phi = 0°, 90°, 180°, 270°$.

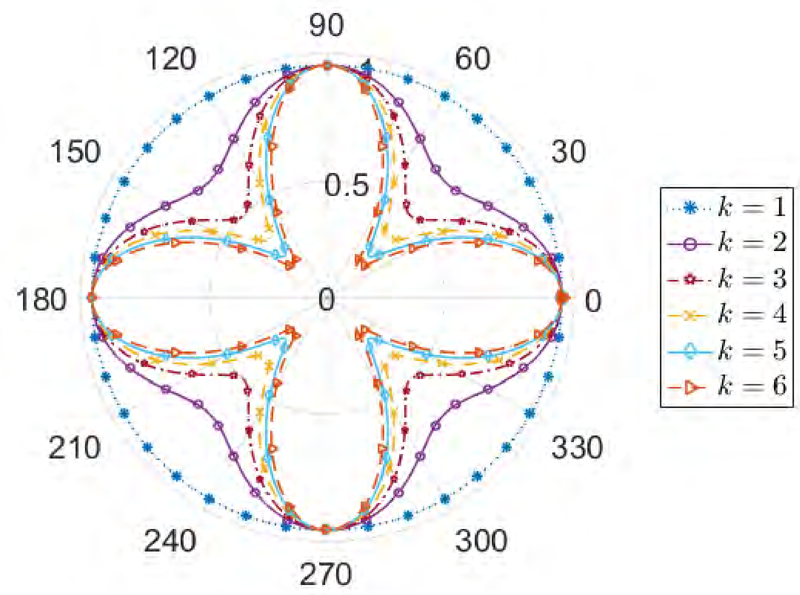

Figure 4.6: How $\beta_k(\phi)$ varies with an incident emitter's azimuth direction-of-arrival ϕ, at various figure-8 sensor order k.

4.3.4 Analysis of Magnitude-Scaling Factor of $\upsilon_k(\phi_L, \tilde{\phi})$

The magnitude-scaling factor of $\upsilon_k(\phi_L, \tilde{\phi})$ is independent of the source's azimuth direction-of-arrival ϕ; hence, $\upsilon_k(\phi_L, \tilde{\phi})$ does *not* affect the beamformer's azimuth-pattern shape but only magnitude-scales the entire pattern.

For $k = 1$, $\upsilon_k(\phi_L, \tilde{\phi}) = 1$ for all ϕ_L and all $\tilde{\phi}$. For $k > 1$, by the definition of infinity norm, when

$$\left\| \mathbf{u}_k\left(\phi, \tilde{\phi}\right) \right\|_\infty = \left| \left[\mathbf{u}_k\left(\phi_L, \tilde{\phi}\right) \right]_1 \right|, \tag{4.3.12}$$

$$\begin{aligned} \upsilon_k(\phi_L, \tilde{\phi}) &= \sqrt{1 + \left(\frac{[\mathbf{u}_k(\phi_L, \tilde{\phi})]_2}{[\mathbf{u}_k(\phi_L, \tilde{\phi})]_1} \right)^2} \\ &= \sqrt{1 + \tan^2(\chi_k(\phi_L, \tilde{\phi}))}, \\ &= |\sec(\chi_k(\phi_L, \tilde{\phi}))| \end{aligned} \tag{4.3.13}$$

Alternatively, when

$$\left\|\mathbf{u}_k\left(\phi,\tilde{\phi}\right)\right\|_\infty \;=\; \left|\left[\mathbf{u}_k\left(\phi_L,\tilde{\phi}\right)\right]_2\right|, \tag{4.3.14}$$

$$\begin{aligned}
\upsilon_k(\phi_L,\tilde{\phi}) &= \sqrt{1+\left(\frac{[\mathbf{u}_k(\phi_L,\tilde{\phi})]_2}{[\mathbf{u}_k(\phi_L,\tilde{\phi})]_1}\right)^2} \\
&= \sqrt{1+\cot^2(\chi_k(\phi_L,\tilde{\phi}))}, \\
&= |\csc(\chi_k(\phi_L,\tilde{\phi}))|
\end{aligned} \tag{4.3.15}$$

$\upsilon_k(\phi_L,\tilde{\phi})$ is functionally dependent on k, ϕ_L, and $\tilde{\phi}$, therefore, how do k, ϕ_L, and $\tilde{\phi}$ influence (4.3.12) and (4.3.14)? This is answered in Section 4.2.3.

Plots of $\upsilon_k(\phi_L,\tilde{\phi})$ versus $(\phi_L,\tilde{\phi})$ are shown in Figure 4.7 for various values of k. As absolute value secant or co-secant functions, the minimum values of $\upsilon_k(\phi_L,\tilde{\phi}) = 1$ as can be seen in Figure 4.7. This implies that $\upsilon_k(\phi_L,\tilde{\phi})$ does not downscale the beampattern. The maximum value of $\upsilon_k(\phi_L,\tilde{\phi}) = \sqrt{2}$ which occurs when $|\sec(\chi_k(\phi_L,\tilde{\phi}))| = |\csc(\chi_k(\phi_L,\tilde{\phi}))|$.

The transitions between secant and cosecant $\upsilon_k(\phi_L,\tilde{\phi})$ is more rapid at lower values of k as can be observed across Figures 4.7b - 4.7f. This translates to less changes in the beampattern with increasing k as ϕ_L and $\tilde{\phi}$ are varied.

4.3.5 Analysis of the Phase Term $\xi_k(\phi)$

Figure 4.8 shows how $\xi_k(\phi)$ varies with the incident emitter's direction-of-arrival ϕ, at various figure-8 sensor orders of $k = 1, 2, \cdots, 6$.

For even values of k: $\xi_k(\phi)$ ranges over $[0, \frac{\pi}{2}], \forall\phi \in [0, 2\pi)$, but $\xi_k(\phi)$ mostly clusters around the values of $0°$ and $90°$. Appendix D.1 analytically proves that this clustering becomes tighter around these two values, as k increases.

For odd values of k: $\xi_k(\phi)$ spans over the entire $[0, 2\pi)$, but mostly clusters around the values of $0°$, $90°$, $180°$, and $270°$. Appendix D.2 analytically proves that this clustering becomes tighter around these four values, as k increases.

The above properties of $\xi_k(\phi)$ will be shown in Section 4.3.7 to steer the beam toward one of the four direction-of-arrival sectors identified in Section 4.3.3.

4.3.6 Analyzing the Phase Term $\chi_k(\phi_L,\tilde{\phi})$

$\chi_k(\phi_L,\tilde{\phi})$ for a given k and $|\tilde{\phi}|$ close to zero, varies with ϕ_L similarly as $\xi_k(\phi)$ varies with ϕ. This is shown by expressing $\chi_k(\phi_L,\tilde{\phi})$ in terms of $\xi_k(\cdot)$ as

$$\chi_k(\phi_L,\tilde{\phi}) = \tan^{-1}\left(\tan(\xi_k(\phi_L))\sec(\tilde{\phi}) - \tan(\tilde{\phi})\right)$$

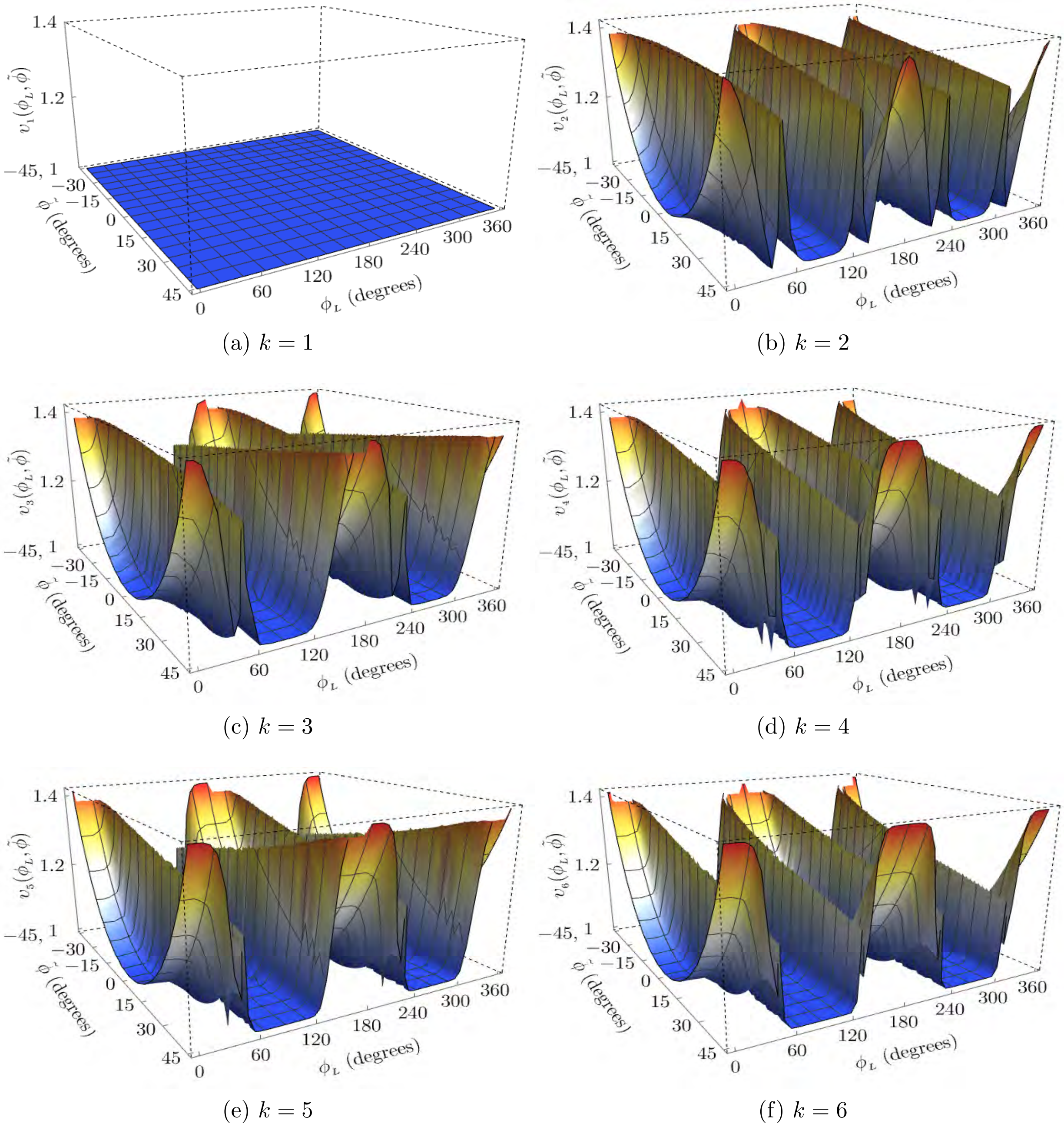

Figure 4.7: $\upsilon_k(\phi_L, \tilde{\phi})$ versus ϕ_L and $\tilde{\phi}$ for various values of order k.

As $\tilde{\phi} \to 0$, $\tan(\phi) \to 0$ and $\sec(\tilde{\phi}) \to 1$, hence $\chi_k(\phi_L, \tilde{\phi}) \to \xi_k(\phi_L)$.

Observations on Figure 4.9: As odd k increases, the shape become more rectangular, more staircase-like. As even k increases, the shape become more rectangular, more square-wave-like. This staircase-like or square-wave-like trend implies that there will be no change in the shape of the beampattern within the flat surface even while varying the look-direction ϕ_L within the flat region.

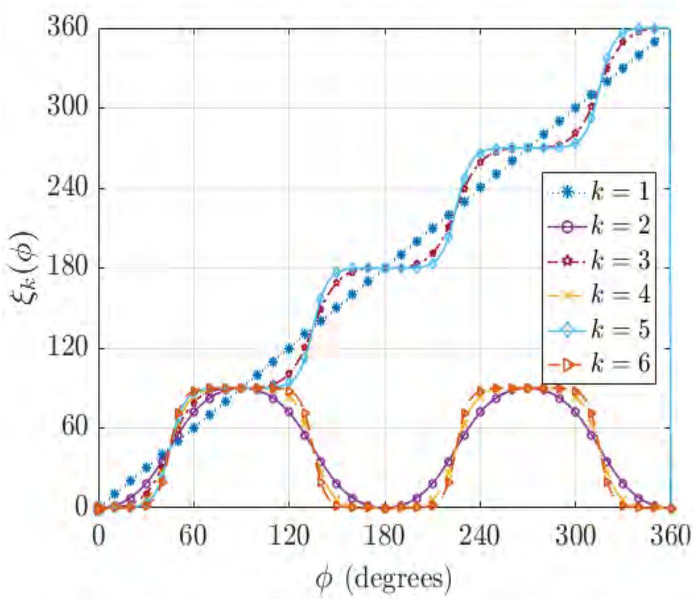

Figure 4.8: How $\xi_k(\phi)$ varies with the incident emitter's direction-of-arrival ϕ, at various figure-8 sensor order k.

4.3.7 Analyzing $\cos\left(\xi_k(\phi) - \chi_k(\phi_L, \tilde{\phi}\right)$

The phase terms of $\xi_k(\phi)$ and $\chi_k\left(\phi_L, \tilde{\phi}\right)$ together affect the beam-pattern through $\cos\left(\xi_k(\phi)\right.$ $\left.-\chi_k(\phi_L, \tilde{\phi})\right)$.

For even k: Section 4.3.5 has shown that $\xi_k(\phi)$ mostly clusters around 0° and 90°. Hence, by selecting ϕ_L suitably (for any given $\tilde{\phi}$ and any given k), it is possible to render $\cos\left(\xi_k(\phi) - \chi_k(\phi_L, \tilde{\phi})\right) = 1$ for all ϕ. Pick out either $\phi \approx 0^\circ, 180^\circ$ versus $\phi \approx 90^\circ, 270^\circ$.

For odd k: Section 4.3.5 has shown that $\xi_k(\phi)$ mostly clusters around 0°, 90°, 180°, and 270°. Hence, by selecting ϕ_L suitably (for any given $\tilde{\phi}$ and any given k), it is possible to render $\cos\left(\xi_k(\phi) - \chi_k(\phi_L, \tilde{\phi})\right) = 1$ for all ϕ. Pick out either $\phi \approx 0^\circ$ versus $\phi \approx 90^\circ$ versus $\phi \approx 180^\circ$ versus $\phi \approx 270^\circ$.

4.4 Reducing the Beampattern to 3 Degree-of-Freedom for $k > 1$

Up to this point, the beampattern is expressed in terms of 4 independent variables, k, ϕ, $\tilde{\phi}$, and ϕ_L. In this section, the simplification of $v_k(\phi_L, \tilde{\phi})$ in Section 4.3.4 for $k > 1$ will be applied to group $\tilde{\phi}$ and ϕ_L as one independent variable, thereby reducing the beampattern to 3 degree-of-freedom.

Substituting (4.3.12) into (4.3.11), the beampattern is written as

$$B_{k,1}^{(2+0)}(\phi, \chi) \quad = \quad |\sec(\chi)|\beta_k(\phi)\cos(\xi_k(\phi) - \chi). \qquad (4.4.1)$$

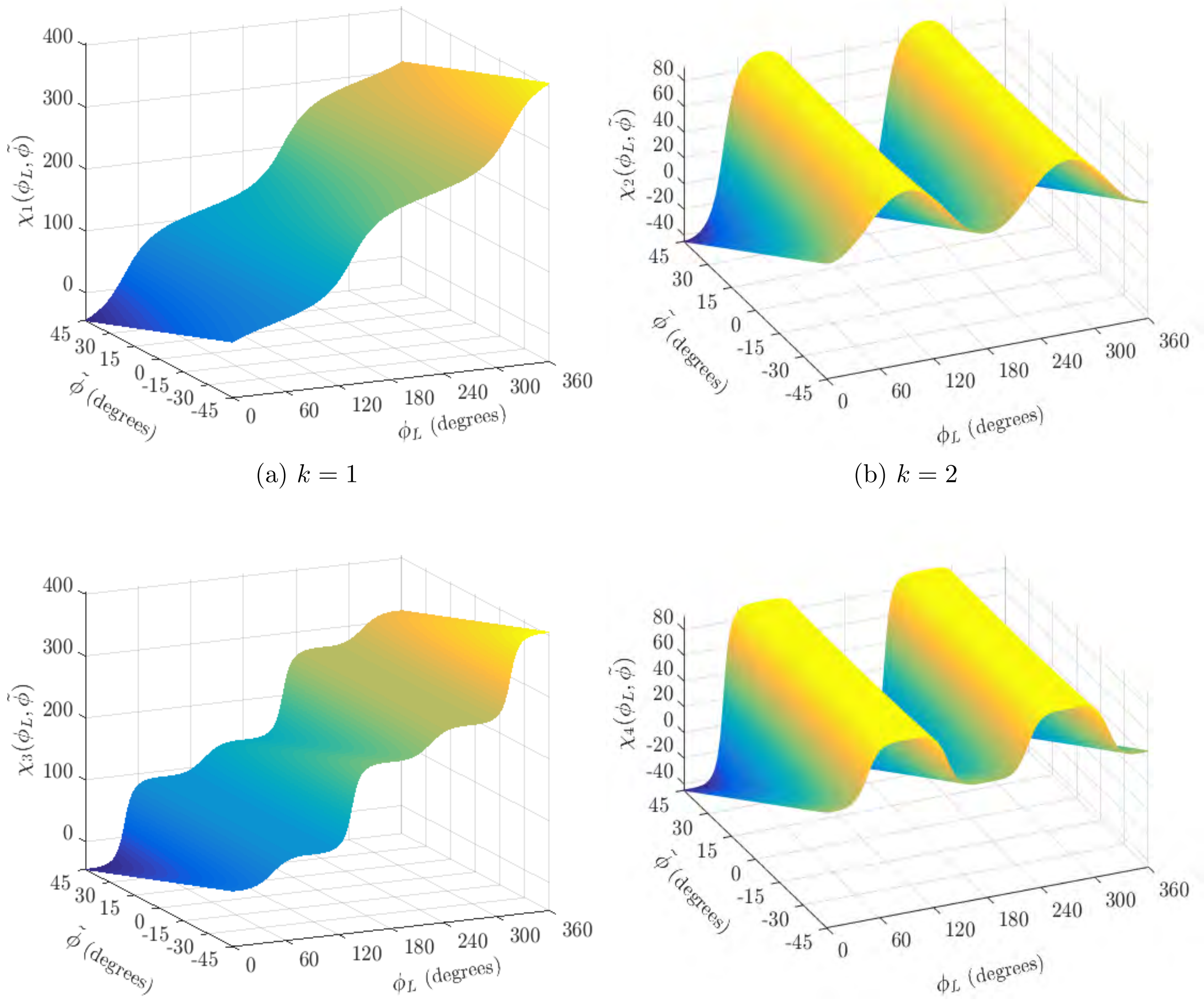

(a) $k = 1$ (b) $k = 2$

(c) $k = 3$ (d) $k = 4$

Figure 4.9: Plot of $\chi_k(\phi_L, \tilde{\phi})$ versus ϕ_L and $\tilde{\phi}$ for various values of sensor order k.

Alternatively, substituting (4.3.14) into (4.3.11), the beampattern is written as

$$B_{k,2}^{(2+0)}(\phi, \chi) \quad = \quad |\csc(\chi)|\beta_k(\phi)\cos(\xi_k(\phi) - \chi). \tag{4.4.2}$$

Note that $\chi_k(\phi_L, \tilde{\phi})$ is written as χ in (4.4.1) and (4.4.2) eliminating its functional dependence on ϕ_L and $\tilde{\phi}$ since the two do not occur anywhere in (4.4.1) outside $\chi_k(\phi_L, \tilde{\phi})$, thereby reducing the degrees-of-freedom from 4 to 3. However, it is important to note that the beampattern's can be equal to either (4.4.1) and (4.4.2), depending on ϕ_L and $\tilde{\phi}$. Please refer to Section 4.2.3 for the condition, which depends ϕ_L, $\tilde{\phi}$, and k, for which the beampattern can either be (4.4.1) or (4.4.2).

Notwithstanding the challenges presented by the dependence of χ on ϕ_L and $\tilde{\phi}$, the two different beampatterns can be studied independently to have a general knowledge of the variation of the beampattern with respect to ϕ and the combined effects of non-perpendicularity ($\tilde{\phi}$) and look direction (ϕ_L).

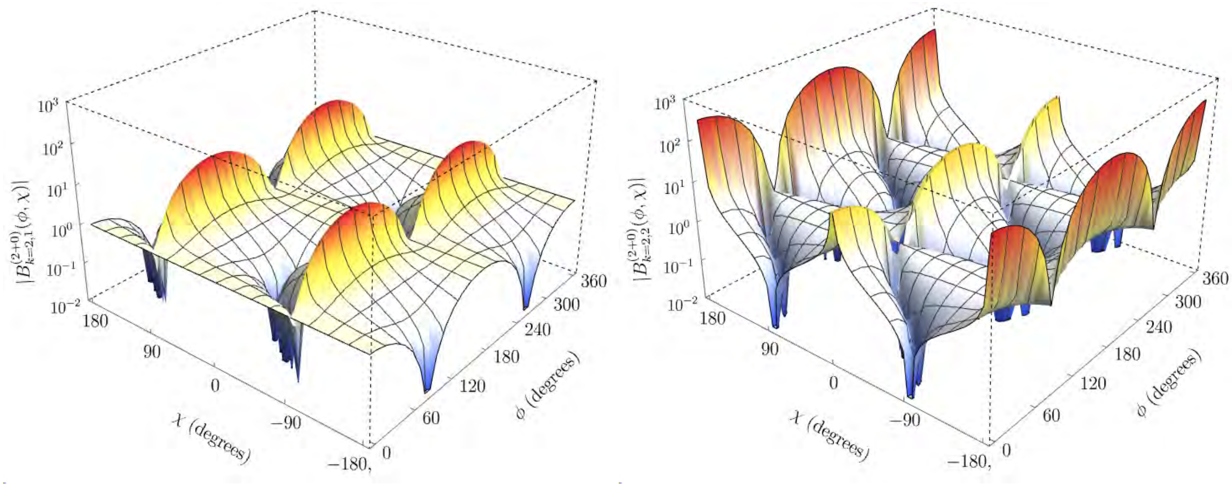

(a) (b)

Figure 4.10: Plot of (a) $|B^{(2+0)}_{k,1}(\phi,\chi)|$ and (b) $|B^{(2+0)}_{k,2}(\phi,\chi)|$ versus ϕ and χ for $k = 2$, with logarithmic vertical axis.

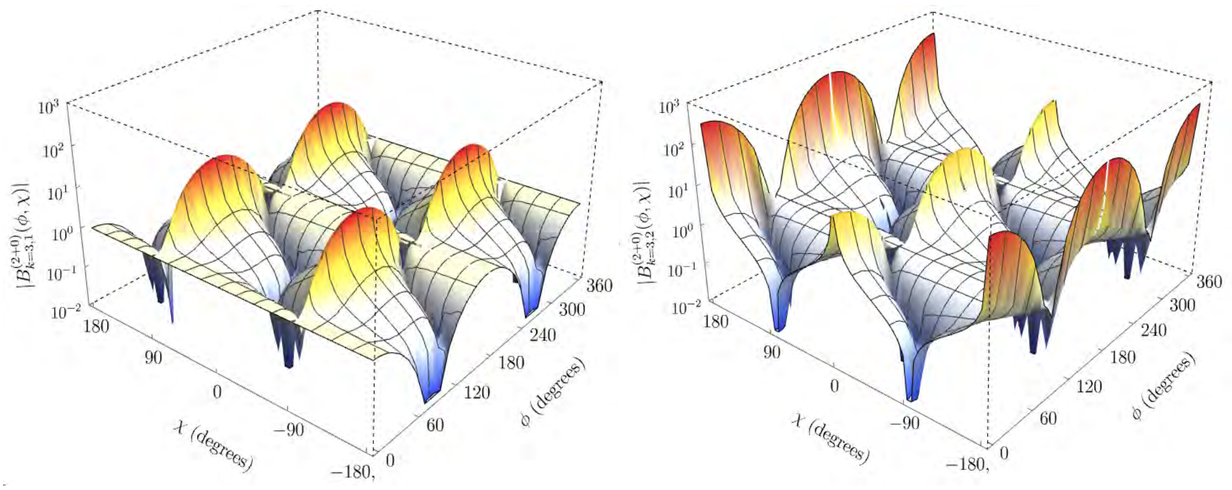

(a) (b)

Figure 4.11: Plot of (a) $|B^{(2+0)}_{k,1}(\phi,\chi)|$ and (b) $|B^{(2+0)}_{k,2}(\phi,\chi)|$ versus ϕ and χ for $k = 3$, with logarithmic vertical axis.

Qualitative observations on $|B^{(2+0)}_{k,1}(\phi,\chi)|$ of Figure 4.10a, 4.11a, 4.12a, and 4.13a:

(i.) The width of the mainlobes remains unchanged for most part of the surfaces away from $\chi = \pm 90°$. This is the region where the beampattern switches from $|B^{(2+0)}_{k,1}(\phi,\chi)|$ to $|B^{(2+0)}_{k,2}(\phi,\chi)|$.

(ii.) As k increases, the switching region described in (i.) becomes less prominent. This implies less rapid switching in the direction of the mainlobe increases as k increases.

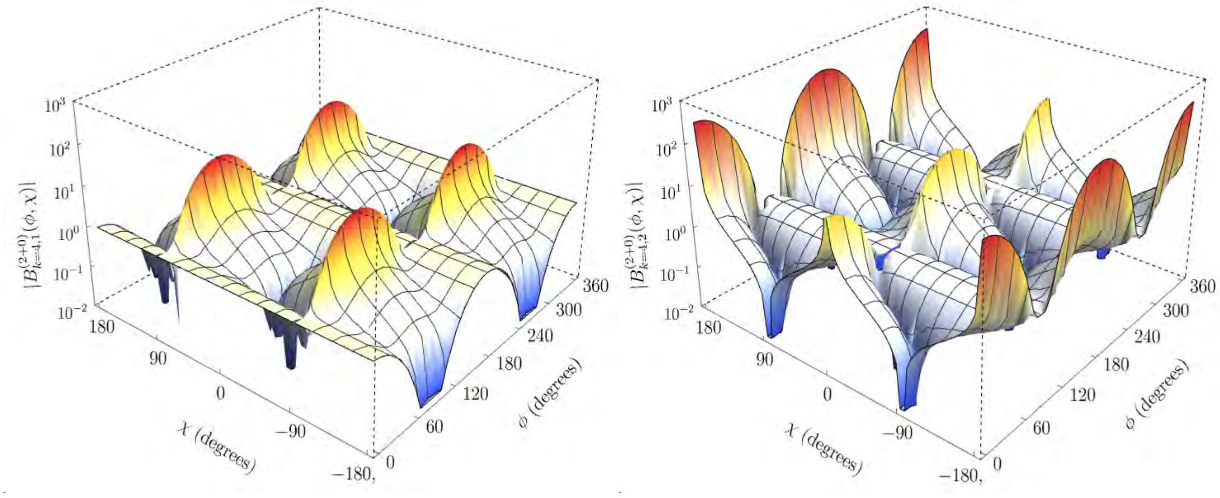

(a) (b)

Figure 4.12: Plot of (a) $|B_{k,1}^{(2+0)}(\phi, \chi)|$ and (b) $|B_{k,2}^{(2+0)}(\phi, \chi)|$ versus ϕ and χ for $k = 4$, with logarithmic vertical axis.

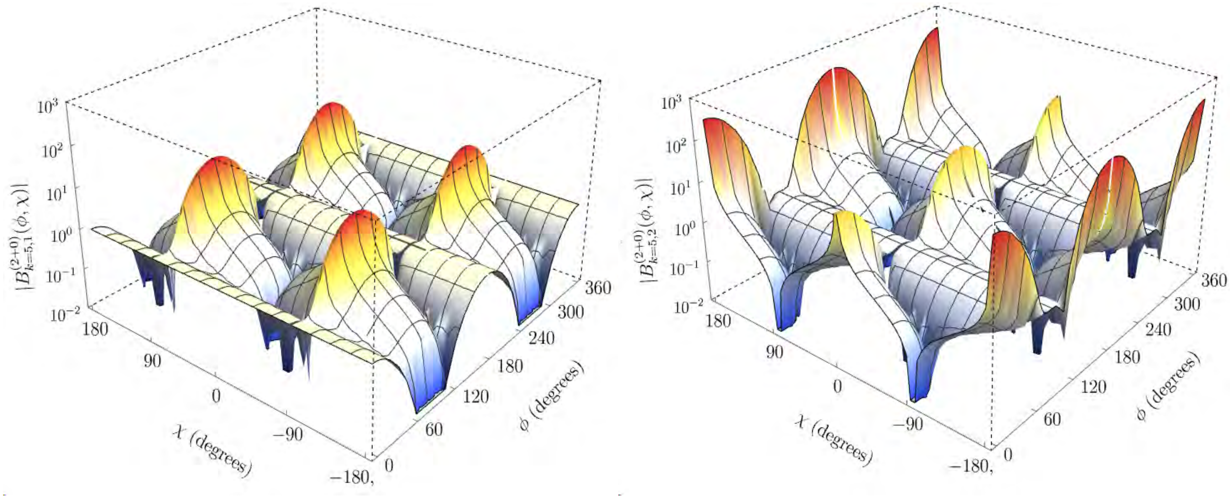

(a) (b)

Figure 4.13: Plot of (a) $|B_{k,1}^{(2+0)}(\phi, \chi)|$ and (b) $|B_{k,2}^{(2+0)}(\phi, \chi)|$ versus ϕ and χ for $k = 5$, with logarithmic vertical axis.

(iii.) The lobes, in terms of direction of arrival ϕ, becomes narrower for a given χ as k increases. This is expected as the directivity of the figure-8 sensor increases with sensor order k.

Qualitative observations on $|B_{k,2}^{(2+0)}(\phi, \chi)|$ of Figure 4.10b, 4.11b, 4.12b, and 4.13b:

(iv.) A sidelobe is introduced next to the mainlobe for odd values of k. Please see Figures 4.11b and 4.13b.

(v.) The depth of the null between the sidelobe described in (iv.) deepens as odd values of k increases. Please see Figures 4.11b and 4.13b.

(vi.) The sidelobe described in (iv.) becomes more prominent as χ deviates from 0 for a given odd k.

(vii.) The mainlobe lobe of $|B_{k,2}^{(2+0)}(\phi, \chi)|$ becomes narrower as k increases. This is due to the reason mentioned in (iii.).

4.5 Summary

This work has shown that for an array of two collocated higher-order figure-8 sensors which are/are not in orthogonal orientation (with the beamformer unaware of the non-perpendicularity), its spatial-matched-filter-type beampattern will only point in horizontal or vertical directions. More importantly, this work relates the look direction, array's skewed angle and sensor order to the mis-pointing of the array's beampattern.

More interestingly, this work pioneers the expression of the higher-order figure-8 sensors in form of first-order figure-8 sensors, which provides a way of mathematically relating the behaviors of the two categories of figure-8 sensors.

If the two higher-order figure-8 sensors are collocated with an isotropic sensor (like a pressure sensor), that triad's beam pointing bias would remain the same as analyzed above. This is on account of the analysis available in Section 2.2 of [17], by simply changing $\mathbf{a}^{(2+0)}(\cdot)$ there in [17] by the $\mathbf{a}_k(\cdot)$ here in this work.

Chapter 5

Directional Pointing Error in "Spatial Matched Filter" Beamforming at a Tri-Axial Velocity-Sensor due to Non-Orthogonal Axes

5.1 Overview

5.1.1 A Tri-Axial Velocity-Sensor

A "tri-axial velocity sensor" (also called a "velocity-sensor triad", a "pressure gradient sensor", an "acoustic vector-sensor", or a "vector hydrophone") measures an incident acoustic field by its underlying 3×1 particle-velocity vector. Such a "tri-axial velocity-sensor" has an array manifold of [22, 69, 72]

$$\mathbf{a}^{(3+0)}(\phi, \theta) = \begin{bmatrix} \cos\phi \sin\theta \\ \sin\phi \sin\theta \\ \cos\theta \end{bmatrix}, \qquad (5.1.1)$$

where $\theta \in [0, \pi]$ denotes the polar arrival direction (also known as the zenith angle) defined with respect to the positive z-axis, and $\phi \in [0, 2\pi)$ symbolizes the azimuth arrival direction defined with respect to the positive x-axis. The above array manifold offers azimuth-elevation bivariate spatial directivity, plus independence from the frequency/ spectrum/ bandwidth of the incident signal. This allows any associate signal processing to decouple the time/frequency coordinates from the direction-of-arrival coordinates. Furthermore, the spatial collocation of all three constituent sensors (i.e., the three *uni*-axial velocity-sensors) leads to a physical compactness that facilitates deployment and mobility.

This "tri-axial velocity-sensor" has been implemented in hardware, sometimes with a collocating pressure-sensor. The "tri-axial velocity-sensor" is available commercially, as the"Uniaxial P-U Probe from AcousTech Inc. (Fort Wayne, Indiana, U.S.A.) for the underwater propagation medium, and as the " Ultimate Sound Probe" from Microflown Technologies (Arnhem, The Netherlands) and as "Vector Intensity Probe" from G.R.A.S. Sound and Vibration A/S (Holte, Denmark) for the air acoustics. The "tri-axial velocity-sensor" has been used in sea trials or aeroacoustic field tests, and has many signal-processing algorithms tailored for it — please see [34, 36, 71] for comprehensive reviews of the research literature.

5.1.2 "Spatial Matched Filter" Beamforming on a Tri-Axial Velocity-Sensors

Spatial-matched-filter beamforming has been introduced and discussed in Section 1.5, and further in Section 4.1.4. The tri-axial velocity-sensor's "spatial matched filter" beampattern has been analyzed in [16, 18], under the assumption of perfect orthogonality among the three axes.

For non-perpendicular axes, which may arise due to manufacturing / fabrication / deployment imperfections: the "spatial match filter" beampattern has been analyzed in the open literature only for a *bi*-axial velocity-sensor (i.e., the u-u probe) under *uni*variate axial non-orthogonality [17], but not yet for the *tri*-axial velocity-sensor. There in [17], the *bi*-axial velocity-sensor is analytically proved to incur a directional pointing error, but the overall beam pattern would otherwise be same as in the perpendicular case.

This chapter will generalize the analysis in [17] to a *tri*-axial velocity-sensor, with or without the collocating pressure-sensor, under *tetra*variate axial non-orthogonality.

5.1.3 A Tri-Axial Velocity-Sensor with *Non*-Orthogonal Orientation

Perfect orthogonality is an idealization that is unattainable in practical systems. Without loss of generality: among the tri-axial velocity-axis' three axes, only two may be taken to have mis-oriented, with the remaining axis serving as a "reference" coordinate.

5.1.4 Organization of This Chapter

Section 5.2 develops the rotation matrix to capture the non-perpendicularity among the sensors. The preliminary analysis in Section 5.2 is common to all three cases in Sections 5.2.3, 5.2.2, and 5.2.4. Section 5.3 will analytically derive the pointing error in closed form, explicitly in terms of the tri-axial velocity-sensor's axial mis-orientation angles of $(\phi_x, \theta_x, \phi_y, \theta_y, \phi_z, \theta_z)$ and in terms of the beamformer's pre-set "look direction" (ϕ_L, θ_L). Section 5.7 will do the same for a tri-axial velocity-sensor that is collocated with pressure-sensor as a four-component sensing system. Finally, Section 5.8 will conclude this investigation.

5.2 The Geometry of Axial Mis-Orientation

5.2.1 Capturing Rotations of Each Axis

This section contains the rotations that would take x-, y-, z- axes to $\tilde{x}$-, $\tilde{y}$-, $\tilde{z}$- directions respectively. The rotation of a vector through an angle ψ about the x-, y-, and z-axis are captured in the basic rotation matrix

$$\mathbf{T}_x(\psi) = \begin{bmatrix} 1 & 0 & 0 \\ 0 & \cos\psi & -\sin\psi \\ 0 & \sin\psi & \cos\psi \end{bmatrix}, \tag{5.2.1}$$

$$\mathbf{T}_y(\psi) = \begin{bmatrix} \cos\psi & 0 & \sin\psi \\ 0 & 1 & 0 \\ -\sin\psi & 0 & \cos\psi \end{bmatrix}, \tag{5.2.2}$$

and

$$\mathbf{T}_z(\psi) = \begin{bmatrix} \cos\psi & -\sin\psi & 0 \\ \sin\psi & \cos\psi & 0 \\ 0 & 0 & 1 \end{bmatrix} \tag{5.2.3}$$

respectively.

The x-axis is directed to a new $\tilde{x}$-direction (please see Figure 5.1) by $\mathbf{T}_{yz}(\theta_x, \phi_x)$ obtained by a rotation of

(i.) θ_x about the nominal y-axis captured in $\mathbf{T}_y(\theta_x)$ and,

(ii.) ϕ_x about the nominal z-axis captured in $\mathbf{T}_z(\phi_x)$,

therefore,

$$\begin{aligned} \mathbf{T}_{\mathrm{yz}}(\theta_x, \phi_x) &= \mathbf{T}_z(\phi_x)\,\mathbf{T}_y(\theta_x) \\ &= \begin{bmatrix} \cos\phi_x\cos\theta_x & -\sin\phi_x & \cos\phi_x\sin\theta_x \\ \cos\theta_x\sin\phi_x & \cos\phi_x & \sin\phi_x\sin\theta_x \\ -\sin\theta_x & 0 & \cos\theta_x \end{bmatrix} \end{aligned} \tag{5.2.4}$$

To take y-axis to $\tilde{y}$-direction, which points in a direction ϕ_y and θ_y away from y-axis (see Figure 5.1) the resultant rotation matrix $\mathbf{T}_{\mathrm{xz}}(\theta_y, \phi_y)$ is obtained by a rotation of

(i.) θ_y about the nominal x-axis captured in $\mathbf{T}_x(\theta_y)$ and, (ii.) ϕ_y about the nominal z-axis captured in $\mathbf{T}_z(\phi_y)$,

therefore,

$$\begin{aligned}\mathbf{T}_{\mathrm{xz}}(\theta_y, \phi_y) &= \mathbf{T}_z(\phi_y)\mathbf{T}_x(\theta_y) \\ &= \begin{bmatrix} \cos\phi_y & -\sin\phi_y\cos\theta_y & \sin\phi_y\sin\theta_y \\ \sin\phi_y & \cos\phi_y\cos\theta_y & -\cos\phi_y\sin\theta_y \\ 0 & \sin\theta_y & \cos\theta_y \end{bmatrix}\end{aligned} \tag{5.2.5}$$

Finally, the z-axis is directed to a new $\tilde{z}$-direction by $\mathbf{T}_{yz}(\theta_z, \phi_z)$ obtained by a rotation of

(i.) θ_z about the nominal y-axis captured in $\mathbf{T}_y(\theta_z)$ and,

(ii.) ϕ_z about the nominal z-axis captured in $\mathbf{T}_z(\phi_z)$,

therefore,

$$\begin{aligned}\mathbf{T}_{\mathrm{yz}}(\theta_z, \phi_z) &= \mathbf{T}_z(\phi_z)\ \mathbf{T}_y(\theta_z) \\ &= \begin{bmatrix} \cos\phi_z\cos\theta_z & -\sin\phi_z & \cos\phi_z\sin\theta_z \\ \cos\theta_z\sin\phi_z & \cos\phi_z & \sin\phi_z\sin\theta_z \\ -\sin\theta_z & 0 & \cos\theta_z \end{bmatrix}\end{aligned} \tag{5.2.6}$$

5.2.2 Geometry with the x-Axis Being the Reference Axis

In this section, the x-axis is adopted as the reference axis (see Figure 5.2) hence only the y-axis and z-axis are mis-oriented.

The y-axis is rotated by (5.2.5), and the z-axis is rotated by (5.2.6). Therefore, the overall rotation effect is modeled as

$$\mathbf{R}_x(\phi_y, \theta_y, \phi_z, \theta_z) = \begin{bmatrix} [\mathbf{I}_3]_{1,i} \\ [\mathbf{T}_{\mathrm{xz}}(\theta_y, \phi_y)^T]_{2,i} \\ [\mathbf{T}_{yz}(\theta_z, \phi_z)^T]_{3,i} \end{bmatrix} \tag{5.2.7}$$

$i = 1, 2, 3$, where $\mathbf{I}_3$ is a 3×3 identity matrix which represents no transformation was done on the x-axis (reference axis), $[\cdot]_{i,j}$ is the entry on the i-th row and j-th column of matrix, and ^{T} represents matrix transposition.

$$\mathbf{R}_x(\phi_y, \theta_y, \phi_z, \theta_z) = \begin{bmatrix} 1 & 0 & 0 \\ -\sin\phi_y\cos\theta_y & \cos\phi_y\cos\theta_y & \sin\theta_y \\ \cos\phi_z\sin\theta_z & \sin\phi_z\sin\theta_z & \cos\theta_z \end{bmatrix}, \tag{5.2.8}$$

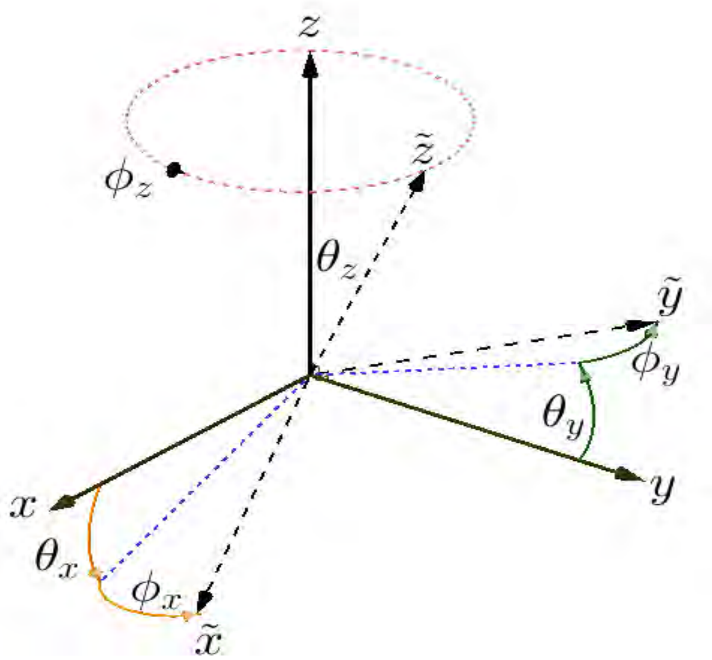

Figure 5.1: The tri-axial velocity-sensor, with mis-orientation in its x-axis, y-axis, and z-axis. The six mis-orientation angles are (ϕ_x, θ_x) to parameterize the mis-orientation of the x-axis to the $\tilde{x}$-axis, (ϕ_y, θ_y) to parameterize the mis-orientation of the y-axis to the $\tilde{y}$-axis, and (ϕ_z, θ_z) to parameterize the mis-orientation of the z-axis to the $\tilde{z}$-axis

where ϕ_y, and θ_y are the azimuth and elevation angle of the $\tilde{y}$-axis with respect to the y-axis, and ϕ_z and θ_z are the azimuth and elevation angle of the $\tilde{z}$-axis relative to the x-y-z-coordinates.

A non-orthogonal tri-axial velocity-sensor whose x-axis is taken as reference axis would have this array manifold:

$$\tilde{\mathbf{a}}_x^{(3+0)}(\phi, \theta, \phi_y, \theta_y, \phi_z, \theta_z) \quad = \quad \mathbf{R}_x(\phi_y, \theta_y, \phi_z, \theta_z)\ \mathbf{a}^{(3+0)}(\phi, \theta). \tag{5.2.9}$$

5.2.3 Geometry with the y-Axis Being the Reference Axis

If the y-axis is adopted as the reference axis, and x- and z-axes are taken to non-orthogonal to y-axis as shown in Figure 5.3, the overall rotation effect is captured as

$$\mathbf{R}_y(\phi_x, \theta_x, \phi_z, \theta_z) \quad = \quad \begin{bmatrix} [\mathbf{T}_{\mathrm{yz}}(\theta_x, \phi_x)^T]_{1,i} \\ [\mathbf{I}_3]_{2,i} \\ [\mathbf{T}_{\mathrm{yz}}(\theta_z, \phi_z)^T]_{3,i} \end{bmatrix} \tag{5.2.10}$$

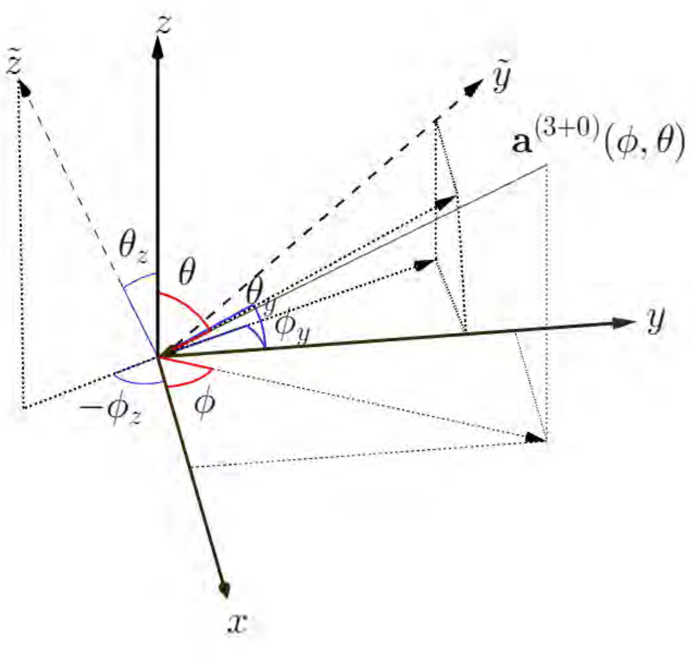

Figure 5.2: The tri-axial velocity-sensor, with *tetra*variate mis-orientation in its y-axis and z-axis. The four mis-orientation angles are (ϕ_y, θ_y) to parameterize the mis-orientation of the y-axis to the $\tilde{y}$-axis, and (ϕ_z, θ_z) to parameterize the mis-orientation of the z-axis to the $\tilde{z}$-axis.

$i = 1, 2, 3$, and other variables as previously defined.

$$\mathbf{R}_y(\phi_x, \theta_x, \phi_z, \theta_z) \quad = \quad \begin{bmatrix} \cos\phi_x \cos\theta_x & \sin\phi_x \cos\theta_x & -\sin\theta_x \\ 0 & 1 & 0 \\ \cos\phi_z \sin\theta_z & \sin\phi_z \sin\theta_z & \cos\theta_z \end{bmatrix}, \tag{5.2.11}$$

where ϕ_x, and θ_x are the azimuth and elevation angle of the $\tilde{x}$-axis, and ϕ_z and θ_z are the azimuth and elevation angle of the $\tilde{z}$-axis, relative to the x-y-z-coordinates, that is the mis-orientation angles.

A non-orthogonal tri-axial velocity-sensor whose y-axis is adopted as reference axis would have this array manifold:

$$\tilde{\mathbf{a}}_y^{(3+0)}(\phi, \theta, \phi_x, \theta_x, \phi_z, \theta_z) \quad = \quad \mathbf{R}_y(\phi_x, \theta_x, \phi_z, \theta_z)\, \mathbf{a}^{(3+0)}(\phi, \theta). \tag{5.2.12}$$

5.2.4 Geometry with the z-Axis Being the Reference Axis

Here, the z-axis is taken as the reference axis while the x-axis is mis-oriented by ϕ_x (azimuthally from the nominal x-axis) and θ_x(downwards from the normal x-y plane); and y-axis is mis-oriented by ϕ_y (azimuthally from the nominal y-axis) and θ_y (above the normal x-y plane) as shown in Figure 5.4.

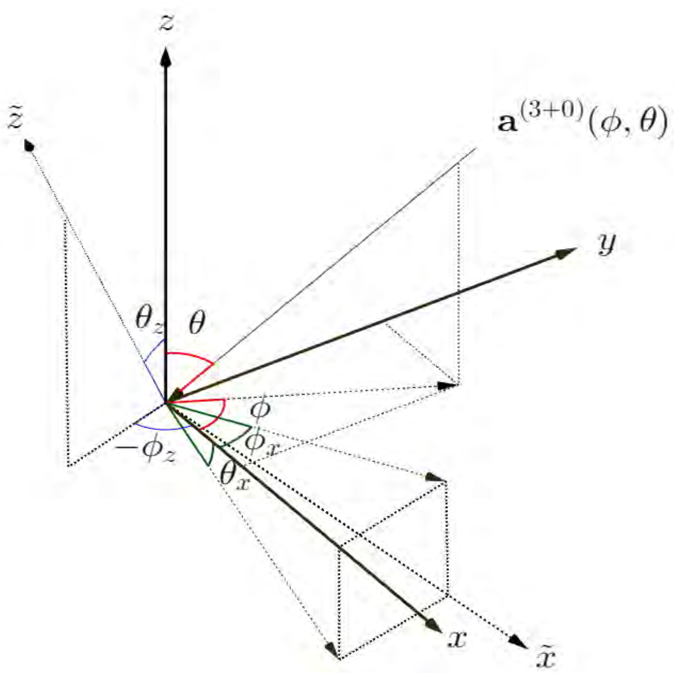

Figure 5.3: The tri-axial velocity-sensor, with *tetra*variate mis-orientation in its x-axis and z-axis. The four mis-orientation angles are (ϕ_x, θ_x) to parameterize the mis-orientation of the x-axis to the $\tilde{x}$-axis, and (ϕ_z, θ_z) to parameterize the mis-orientation of the z-axis to the $\tilde{z}$-axis.

The overall rotation effect is modeled as

$$\mathbf{R}_z(\phi_x, \theta_x, \phi_y, \theta_y) = \begin{bmatrix} [\mathbf{T}_x(\theta_x, \phi_x)^T]_{1,i} \\ [\mathbf{T}_y(\theta_y, \phi_y)^T]_{2,i} \\ [\mathbf{I}_3]_{3,i} \end{bmatrix} \tag{5.2.13}$$

$i = 1, 2, 3$, and other variables as previously defined. Hence,

$$\mathbf{R}_z(\phi_x, \theta_x, \phi_y, \theta_y) = \begin{bmatrix} \cos\phi_x \cos\theta_x & \sin\phi_x \cos\theta_x & -\sin\theta_x \\ -\sin\phi_y \cos\theta_y & \cos\phi_y \cos\theta_y & \sin\theta_y \\ 0 & 0 & 1 \end{bmatrix}, \tag{5.2.14}$$

where ϕ_x, and θ_x are the azimuth and elevation angle of the $\tilde{x}$-axis, and ϕ_y and θ_y are the azimuth and elevation angle of the $\tilde{y}$-axis, relative to the x-y-z-coordinates, that is the mis-orientation angles.

A non-orthogonal tri-axial velocity-sensor whose z-axis is adopted as reference axis would have this array manifold:

$$\tilde{\mathbf{a}}_z^{(3+0)}(\phi, \theta, \phi_x, \theta_x, \phi_y, \theta_y) = \mathbf{R}_z(\phi_x, \theta_x, \phi_y, \theta_y)\, \mathbf{a}^{(3+0)}(\phi, \theta). \tag{5.2.15}$$

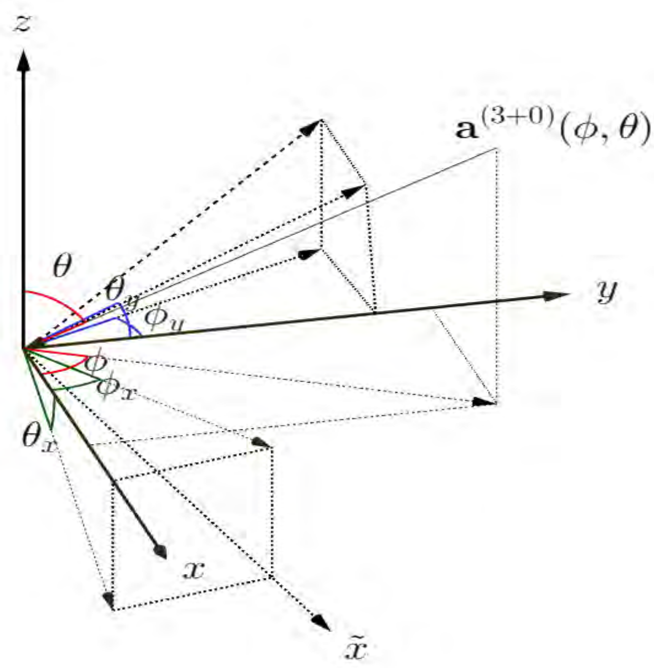

Figure 5.4: The tri-axial velocity-sensor, with *tetra*variate mis-orientation in its x-axis and y-axis. The four mis-orientation angles are (ϕ_x, θ_x) to parameterize the mis-orientation of the x-axis to the $\tilde{x}$-axis, and (ϕ_y, θ_y) to parameterize the mis-orientation of the y-axis to the $\tilde{y}$-axis.

5.3 Toward an Analytical Derivation of the Beamformer's Pointing Error

Suppose that "spatial matched filter" beamforming is performed on a *non*-orthogonal tri-axial velocity-sensor corresponding to any of the three cases in Sections 5.2.3, 5.2.2, and 5.2.4, but with*out* any awareness of that non-orthogonality. That is, the beamforming weight vector is spatially matched to (5.1.1), instead of to (5.2.9), (5.2.12), or (5.2.15). Therefore, the beampattern equals

$$\begin{aligned} B^{(3+0)}(\phi,\theta,\phi_{\xi'_1},\theta_{\xi'_1},\phi_{\xi'_2},\theta_{\xi'_2}) &= \frac{\mathbf{a}^{(3+0)}(\phi_L,\theta_L)^T\ \tilde{\mathbf{a}}_\xi^{(3+0)}(\phi,\theta)}{\max\limits_{\phi,\theta}\left[\mathbf{a}^{(3+0)}(\phi_L,\theta_L)^T\ \tilde{\mathbf{a}}_\xi^{(3+0)}(\phi,\theta)\right]}, \\ &= \frac{\mathbf{a}^{(3+0)}(\phi_L,\theta_L)^T\ \mathbf{R}_\xi(\phi_{\xi'_1},\theta_{\xi'_1},\phi_{\xi'_2},\theta_{\xi'_2})\ \mathbf{a}^{(3+0)}(\phi,\theta)}{\max\limits_{\phi,\theta}\left[\mathbf{a}^{(3+0)}(\phi_L,\theta_L)^T\ \mathbf{R}_\xi(\phi_{\xi'_1},\theta_{\xi'_1},\phi_{\xi'_2},\theta_{\xi'_2})\ \mathbf{a}^{(3+0)}(\phi,\theta)\right]}, \end{aligned} \tag{5.3.1}$$

where ξ is any of $\{x,y,z\}$, and ξ' is the other two of $\{x,y,z\}$ that is not ξ (i.e. if $\xi=y$, $\xi'_1=x$ and $\xi'_2=z$), $\phi_L\in[0,2\pi)$ and $\theta_L\in[0,\pi]$ denote the beamformer's look azimuth angle and the look polar angle, respectively. Applying the equality condition of the Cauchy-Schwarz inequality, the denominator in (5.3.1) may be re-written as $\left\|\mathbf{R}_\xi(\phi_{\xi'},\theta_{\xi'})^T\ \mathbf{a}^{(3+0)}(\phi_L,\theta_L)\right\|$.

Consequentially,

$$
\begin{aligned}
& B^{(3+0)}(\phi, \theta, \phi_L, \theta_L, \phi_{\xi_1'}, \theta_{\xi_1'}, \phi_{\xi_2'}, \theta_{\xi_2'}) \\
& \quad = \frac{\left(\mathbf{R}_\xi(\phi_{\xi_1'}, \theta_{\xi_1'}, \phi_{\xi_2'}, \theta_{\xi_2'})^T \, \mathbf{a}^{(3+0)}(\phi_L, \theta_L)\right)^T}{\left\|\mathbf{R}_\xi(\phi_{\xi_1'}, \theta_{\xi_1'}, \phi_{\xi_2'}, \theta_{\xi_2'})^T \, \mathbf{a}^{(3+0)}(\phi_L, \theta_L)\right\|} \, \mathbf{a}^{(3+0)}(\phi, \theta).
\end{aligned} \tag{5.3.2}
$$

The fraction in (5.3.2) is a unit-vector, but any unit-vector may be mathematically represented as a point on a unit-radius sphere centered upon the Cartesian origin. Any such a particular unit-vector can be uniquely identified by two angles, say $(\phi_{B,\xi}, \theta_{B,\xi})$, in the spherical coordinates; and this $(\phi_{B,\xi}, \theta_{B,\xi})$ may be defined with reference to any point on the unit-sphere, say with reference to (ϕ_L, θ_L), the beamformer's "look direction". In other words, the fraction in (5.3.2) may be expressed as the 3×1 vector,

$$
\mathbf{u}_\xi := \begin{bmatrix} \cos(\phi_L - \phi_{B,\xi}) \sin(\theta_L - \theta_{B,\xi}) \\ \sin(\phi_L - \phi_{B,\xi}) \sin(\theta_L - \theta_{B,\xi}) \\ \cos(\theta_L - \theta_{B,\xi}) \end{bmatrix}, \tag{5.3.3}
$$

$$
\equiv \frac{\mathbf{R}_\xi(\phi_{\xi_1'}, \theta_{\xi_1'}, \phi_{\xi_2'}, \theta_{\xi_2'})^T \, \mathbf{a}^{(3+0)}(\phi_L, \theta_L)}{\left\|\mathbf{R}_\xi(\phi_{\xi_1'}, \theta_{\xi_1'}, \phi_{\xi_2'}, \theta_{\xi_2'})^T \, \mathbf{a}^{(3+0)}(\phi_L, \theta_L)\right\|} \tag{5.3.4}
$$

which may be expressed as

$$
\mathbf{u}_\xi = \mathbf{a}^{(3+0)}(\phi_L - \phi_{B,\xi}, \theta_L - \theta_{B,\xi}). \tag{5.3.5}
$$

All these imply that

$$
B^{(3+0)}(\phi, \theta, \phi_L, \theta_L, \phi_{B,\xi}, \theta_{B,\xi}) = \mathbf{a}^{(3+0)}(\phi_L - \phi_{B,\xi}, \theta_L - \theta_{B,\xi})^T \, \mathbf{a}^{(3+0)}(\phi, \theta), \tag{5.3.6}
$$

where $(\phi_{B,\xi}, \theta_{B,\xi})$ represent the directional bias with ξ as reference axis due to the mis-orientation $\phi_{\xi_1'}, \theta_{\xi_1'}, \phi_{\xi_2'}, \theta_{\xi_2'}$.

Next, express $(\phi_{B,\xi}, \theta_{B,\xi})$ in terms of the mis-orientation angles of $\phi_{\xi_1'}, \theta_{\xi_1'}, \phi_{\xi_2'}, \theta_{\xi_2'}$. [1] From (5.3.3) the followings are be obtained:

$$
\begin{aligned}
\tan(\phi_L - \phi_{B,\xi}) &= \frac{[\mathbf{u}_\xi]_2}{[\mathbf{u}_\xi]_1}, && (5.3.7) \\
\cos(\theta_L - \theta_{B,\xi}) &= [\mathbf{u}_\xi]_3, && (5.3.8)
\end{aligned}
$$

it holds that

$$
\begin{aligned}
\phi_{B,\xi} &= \phi_L - \tan^{-1}\left(\frac{[\mathbf{u}_\xi]_2}{[\mathbf{u}_\xi]_1}\right) && (5.3.9) \\
\theta_{B,\xi} &= \theta_L - \cos^{-1}[\mathbf{u}_\xi]_3, && (5.3.10)
\end{aligned}
$$

[1]For perfect orthogonal triad, $\phi_{\xi_1'} = \theta_{\xi_1'} = \phi_{\xi_2'} = \theta_{\xi_2'} = 0$, it holds that pointing biases $\phi_{B,\xi} = \theta_{B,\xi} = 0$.

where $[\mathbf{u}_\xi]_1$, $[\mathbf{u}_\xi]_2$, and $[\mathbf{u}_\xi]_3$ are respectively the first, second, and third entries of vector $\mathbf{u}_\xi$, which is obtained from the expansion of (5.3.4).

The new form of expressing the beampattern (5.3.6) implies that in a mutually collocated non-orthogonal velocity sensor triad whose spatial-matched-filter beamformer is unaware of the non-perpendicularity between the legs of sensor, the shape of the beampattern remains unchanged but the effective look direction will mis-point by an offset $(\phi_{B,\xi}, \theta_{B,\xi})$ which depends on the look direction (ϕ_L, θ_L) and angle of deviation of the legs from the nominal Cartesian axes. The pointing error defined in (5.3.9) and (5.3.10) will be used subsequently to develop the pointing biases with each axis as the reference axis in subsequent sections.

5.4 Beamformer's Pointing Error – If the x-Axis is the Reference-Axis

In this section, the x-axis is taken as the reference axis, hence $\xi = x$, then $\xi_1' = y$, and $\xi_2' = z$. Thus expanding (5.3.4),

$$\mathbf{u}_x = \frac{\begin{bmatrix} \cos\phi_L \sin\theta_L + \cos\phi_z \cos\theta_L \sin\theta_z - \cos\theta_y \sin\phi_L \sin\phi_y \sin\theta_L \\ \cos\theta_L \sin\phi_z \sin\theta_z + \cos\phi_y \cos\theta_y \sin\phi_L \sin\theta_L \\ \cos\theta_L \cos\theta_z + \sin\phi_L \sin\theta_L \sin\theta_y \end{bmatrix}}{\sqrt{\begin{array}{r} 1 - \cos\theta_y \sin(2\phi_L) \sin\phi_y \sin^2\theta_L + \cos\phi_L \cos\phi_z \sin(2\theta_L) \sin\theta_z \\ + \cos\theta_y \sin\phi_L \sin(\phi_z - \phi_y) \sin(2\theta_L) \sin\theta_z \\ + \sin\phi_L \cos\theta_z \sin(2\theta_L) \sin\theta_y \end{array}}}. \tag{5.4.1}$$

Defining

$$\begin{aligned} \gamma_x &:= \left\| \mathbf{R}_x(\phi_y, \theta_y, \phi_z, \theta_z)^T \, \mathbf{a}^{(3+0)}(\phi_L, \theta_L) \right\| \\ &= \sqrt{\begin{array}{r} 1 - \cos\theta_y \sin(2\phi_L) \sin\phi_y \sin^2\theta_L + \cos\phi_L \cos\phi_z \sin(2\theta_L) \sin\theta_z \\ + \cos\theta_y \sin\phi_L \sin(\phi_z - \phi_y) \sin(2\theta_L) \sin\theta_z \\ + \sin\phi_L \cos\theta_z \sin(2\theta_L) \sin\theta_y \end{array}}, \end{aligned} \tag{5.4.2}$$

as the denominator of (5.4.1). Then (5.4.1) is expressed as

$$\mathbf{u}_x = \frac{1}{\gamma_x} \begin{bmatrix} \cos\phi_L \sin\theta_L + \cos\phi_z \cos\theta_L \sin\theta_z - \cos\theta_y \sin\phi_L \sin\phi_y \sin\theta_L \\ \cos\theta_L \sin\phi_z \sin\theta_z + \cos\phi_y \cos\theta_y \sin\phi_L \sin\theta_L \\ \cos\theta_L \cos\theta_z + \sin\phi_L \sin\theta_L \sin\theta_y \end{bmatrix}. \tag{5.4.3}$$

From (5.3.9), (5.3.10), and (5.4.3), the azimuthal and elevation pointing biases with

x-axis as the reference axis are given as

$$\phi_{B,x} = \phi_L - \tan^{-1}\left(\frac{\cos\theta_L\sin\phi_z\sin\theta_z + \cos\phi_y\cos\theta_y\sin\phi_L\sin\theta_L}{\begin{array}{r}\cos\phi_L\sin\theta_L + \cos\phi_z\cos\theta_L\sin\theta_z \\ -\cos\theta_y\sin\phi_L\sin\phi_y\sin\theta_L\end{array}}\right) \tag{5.4.4}$$

and

$$\theta_{B,x} = \theta_L - \cos^{-1}\left(\frac{\cos\theta_L\cos\theta_z + \sin\phi_L\sin\theta_L\sin\theta_y}{\gamma_x}\right), \tag{5.4.5}$$

respectively.

5.4.1 The Special Case of Only the z-Axis Leg is Mis-Oriented

Considering a case where $\phi_y = \theta_y = 0$ (only the z-axis is mis-oriented), (5.4.4) and (5.4.5) degenerate to

$$\phi_{B,x,y} = \phi_L - \tan^{-1}\left(\frac{\sin\phi_L\sin\theta_L + \sin\phi_z\sin\theta_z\cos\theta_L}{\cos\phi_L\sin\theta_L + \cos\phi_z\sin\theta_z\cos\theta_L}\right) \tag{5.4.6}$$

and

$$\theta_{B,x,y} = \theta_L - \cos^{-1}\left(\frac{\cos\theta_L\cos\theta_z}{\sqrt{1 + \sin\theta_z\cos(\phi_L - \phi_z)\sin(2\theta_L)}}\right), \tag{5.4.7}$$

respectively. [2]

Given a mis-orientation of the z-axis (θ_z, ϕ_z), which look direction gives no azimuthal pointing bias (i.e. $\phi_{B,x,y} = 0$)?

1. For $\theta_L = \frac{\pi}{2}$ and $\phi_L \in [0, 2\pi)$, (5.4.6) equals to zero. That is, for signal impinging horizontally from any azimuth, the azimuthal pointing is zero.

2. For $\phi_L = \phi_z$ and $\theta_L < \tan^{-1}(-\sin\theta_z)$, the azimuthal pointing bias is zero. This is shown as the contour line below the green circle in Figure 5.5.

3. For $\phi_L = \phi_z + \pi$ and $\theta_L > \tan^{-1}(\sin\theta_z)$, the azimuthal pointing bias is zero. This is shown as the contour line above the red circle in Figure 5.5.

Alternatively, given a mis-orientation of the z-axis (θ_z, ϕ_z), which look direction gives the highest azimuthal pointing bias?

1. For $\phi_L = \phi_z$ and $\theta_L > \tan^{-1}(-\sin\theta_z)$, the azimuthal pointing bias is maximum. This is shown as the contour line above the green circle in Figure 5.5.

[2] The subscript notation, $\phi_{B,x,y}$ means the azimuthal bias when x-axis and y-axis has no mis-orientation.

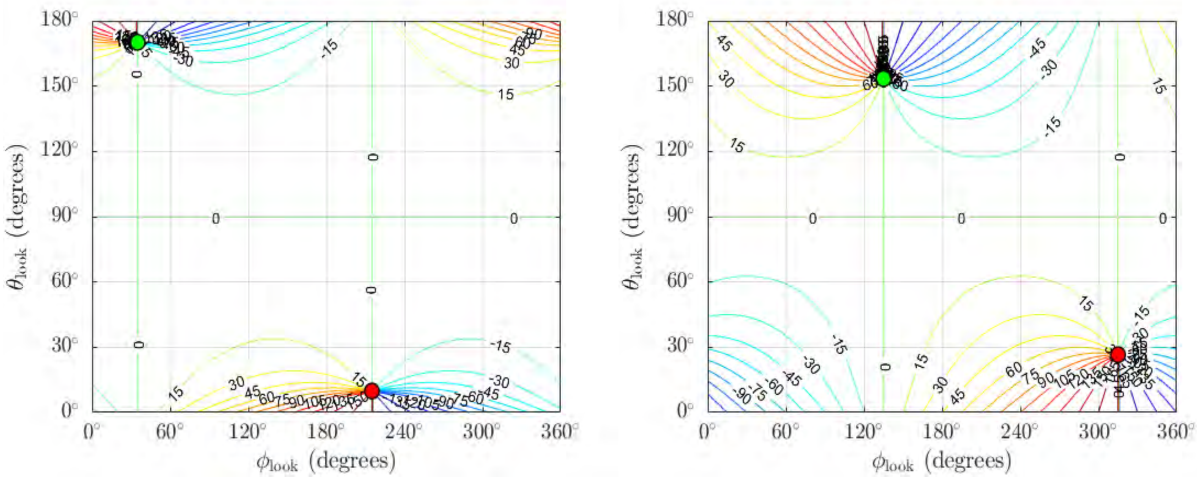

Figure 5.5: Contour plots of $\phi_{B,x,y}$ i.e (5.4.6) versus look direction (θ_L, ϕ_L) for (a) $(\theta_z, \phi_z) = (10°, 35°)$, and (b) $(\theta_z, \phi_z) = (30°, 135°)$.

2. For $\phi_L = \phi_z + \pi$ and $\theta_L < \tan^{-1}(\sin\theta_z)$, the azimuthal pointing bias is maximum. This is shown as the contour line below the red circle in Figure 5.5.

5.4.1.1 One Angle θ_z is Mis-Oriented, i.e. $\phi_z = 0$

Here by setting $\phi_z = 0$ in (5.4.6) and (5.4.7), the $\tilde{z}$-axis lies on the xOz plane, then

$$\phi_{B,x,y,\phi_z} = \phi_L - \tan^{-1}\left(\frac{\sin\phi_L \sin\theta_L}{\cos\phi_L \sin\theta_L + \sin\theta_z \cos\theta_L}\right) \tag{5.4.8}$$

$$\theta_{B,x,y,\phi_z} = \theta_L - \cos^{-1}\left(\frac{\cos\theta_L \cos\theta_z}{\sqrt{1 + \sin\theta_z \cos\phi_L \sin(2\theta_L)}}\right) \tag{5.4.9}$$

5.4.1.2 One Angle ϕ_z is Mis-Oriented, i.e. $\theta_z = 0$

Here by setting $\theta_z = 0$ in (5.4.6) and (5.4.7),

$$\phi_{B,x,y,\theta_z} = 0 \tag{5.4.10}$$

$$\theta_{B,x,y,\theta_z} = 0 \tag{5.4.11}$$

There is no mis-orientation for this case due to the way the mis-orientation is modeled on the Cartesian coordinate –i.e. existence of ϕ_z is dependent on θ_z.

5.4.2 The Special Case of Only the y-Axis Leg is Mis-Oriented

In this degenerate case, only the y-axis is mis-oriented, hence by setting $\phi_z = \theta_z = 0$, (5.4.4) and (5.4.5) reduce to

$$\phi_{B,x,z} = \phi_L - \tan^{-1}\left(\frac{\cos\phi_y \cos\theta_y}{\cot\phi_L - \sin\phi_y \cos\theta_y}\right) \tag{5.4.12}$$

$$\theta_{B,x,z} = \theta_L - \cos^{-1}\left(\frac{\cos\theta_L + \sin\theta_y \sin\phi_L \sin\theta_L}{\sqrt{1 - \cos\theta_y \sin(2\phi_L)\sin\phi_y \sin^2\theta_L + \sin\phi_L \sin(2\theta_L)\sin\theta_y}}\right) \tag{5.4.13}$$

Note that $\phi_{B,x,z}$ (5.4.12) is independent of θ_L, similar to $\phi_{B,y,z}$ (5.5.6).

5.4.2.1 One Angle θ_y is Mis-Oriented, i.e. $\phi_y = 0$

Here by setting $\phi_y = 0$ in (5.4.12) and (5.4.13), the $\tilde{y}$-axis lies on the yOz plane

$$\phi_{B,x,z,\phi_y} = \phi_L - \tan^{-1}(\cos\theta_y \tan\phi_L) \tag{5.4.14}$$

$$\theta_{B,x,z,\phi_y} = \theta_L - \cos^{-1}\left(\frac{\cos\theta_L + \sin\theta_y \sin\phi_L \sin\theta_L}{\sqrt{1 + \sin\phi_L \sin(2\theta_L)\sin\theta_y}}\right) \tag{5.4.15}$$

5.4.2.2 One Angle ϕ_y is Mis-Oriented, i.e. $\theta_y = 0$

Here by setting $\theta_y = 0$ in (5.4.12) and (5.4.13), the $\tilde{y}$-axis lies on the xOy plane

$$\phi_{B,x,z,\theta_y} = \phi_L - \tan^{-1}\left(\frac{\cos\phi_y}{\cot\phi_L - \sin\phi_y}\right) \tag{5.4.16}$$

$$\theta_{B,x,z,\theta_y} = \theta_L - \cos^{-1}\left(\frac{\cos\theta_L}{\sqrt{1 - \sin(2\phi_L)\sin\phi_y \sin^2\theta_L}}\right) \tag{5.4.17}$$

5.5 Beamformer's Pointing Error – If the y-Axis is the Reference-Axis

In this section, the y-axis is taken as the reference axis, hence $\xi = y$ then $\xi'_1 = x$, and $\xi'_2 = z$. Thus expanding (5.3.4),

$$\mathbf{u}_y = \frac{\begin{bmatrix} \cos\phi_x \cos\theta_x \cos\phi_L \sin\theta_L + \cos\phi_z \sin\theta_z \cos\theta_L \\ \sin\phi_L \sin\theta_L + \sin\phi_z \sin\theta_z \cos\theta_L + \sin\phi_x \cos\theta_x \cos\phi_L \sin\theta_L \\ \cos\theta_z \cos\theta_L - \sin\theta_x \cos\phi_L \sin\theta_L \end{bmatrix}}{\sqrt{\begin{array}{r} 1 + \cos\theta_x \sin(2\phi_L) \sin\phi_x \sin^2\theta_L + \sin\phi_L \sin\phi_z \sin(2\theta_L) \sin\theta_z \\ + \cos\theta_x \cos\phi_L \cos(\phi_x - \phi_z) \sin(2\theta_L) \sin\theta_z \\ - \cos\phi_L \cos\theta_z \sin(2\theta_L) \sin\theta_x \end{array}}}. \tag{5.5.1}$$

Defining

$$\begin{aligned} \gamma_y &:= \left\| \mathbf{R}_y(\phi_x, \theta_x, \phi_z, \theta_z)^T \, \mathbf{a}^{(3+0)}(\phi_L, \theta_L) \right\| \\ &= \sqrt{\begin{array}{r} 1 + \cos\theta_x \sin(2\phi_L) \sin\phi_x \sin^2\theta_L + \sin\phi_L \sin\phi_z \sin(2\theta_L) \sin\theta_z \\ + \cos\theta_x \cos\phi_L \cos(\phi_x - \phi_z) \sin(2\theta_L) \sin\theta_z \\ - \cos\phi_L \cos\theta_z \sin(2\theta_L) \sin\theta_x \end{array}}\ , \end{aligned} \tag{5.5.2}$$

as the denominator of (5.5.1). Then (5.5.1) is expressed as

$$\mathbf{u}_y = \frac{1}{\gamma_y} \begin{bmatrix} \cos\phi_x \cos\theta_x \cos\phi_L \sin\theta_L + \cos\phi_z \sin\theta_z \cos\theta_L \\ \sin\phi_L \sin\theta_L + \sin\phi_z \sin\theta_z \cos\theta_L + \sin\phi_x \cos\theta_x \cos\phi_L \sin\theta_L \\ \cos\theta_z \cos\theta_L - \sin\theta_x \cos\phi_L \sin\theta_L \end{bmatrix}. \tag{5.5.3}$$

From (5.3.9), (5.3.10), and (5.5.3),

$$\phi_{B,y} = \phi_L - \tan^{-1}\left(\frac{\begin{array}{r} \sin\phi_L \sin\theta_L + \sin\phi_z \sin\theta_z \cos\theta_L + \\ \sin\phi_x \cos\theta_x \cos\phi_L \sin\theta_L \end{array}}{\cos\phi_x \cos\theta_x \cos\phi_L \sin\theta_L + \cos\phi_z \sin\theta_z \cos\theta_L} \right) \tag{5.5.4}$$

$$\theta_{B,y} = \theta_L - \cos^{-1}\left(\frac{\cos\theta_z \cos\theta_L - \sin\theta_x \cos\phi_L \sin\theta_L}{\gamma_y} \right) \tag{5.5.5}$$

5.5.1 The Special Case of Only the z-Axis Leg is Mis-Oriented

Considering a case of $\theta_x = \phi_x = 0$ (only z-axis is mis-oriented), (5.5.4) and (5.5.5) degenerate to (5.4.6) and (5.4.7) respectively as given in Section 5.4.1.

A case of one angle θ_z mis-oriented, i.e. $\phi_z = 0$ has been derived in Section 5.4.1.1. And the case of angle ϕ_z mis-oriented, i.e. $\theta_z = 0$ has been derived in Section 5.4.1.2.

5.5.2 The special case of only the x-axis Leg is mis-oriented

Considering a case of $\theta_z = \phi_z = 0$ (only x-axis is mis-oriented), (5.5.4) and (5.5.5) degenerate to

$$\phi_{B,y,z} = \phi_L - \tan^{-1}\left(\tan\phi_x + \frac{\tan\phi_L}{\cos\phi_x\cos\theta_x}\right) \tag{5.5.6}$$

and

$$\theta_{B,y,z} = \theta_L - \cos^{-1}\left(\frac{\cos\theta_L - \sin\theta_x\cos\phi_L\sin\theta_L}{\sqrt{\sin(2\phi_L)\sin^2\theta_L\cos\theta_x\sin\phi_x + 1 - \sin(2\theta_L)\sin\theta_x\cos\phi_L}}\right), \tag{5.5.7}$$

respectively.

Note that (5.5.6) is not dependent on θ_L, which incidentally occurs in (5.4.12) as well. Therefore, as long as the z-axis is perfectly perpendicular, the pointing bias in the azimuth angle will be independent of the look direction's polar angle θ_L.

5.5.2.1 One Angle θ_x is Mis-Oriented, i.e. $\phi_x = 0$

Here by setting $\phi_x = 0$ in (5.5.6) and (5.5.7), the $\tilde{x}$-axis lies on the xOz plane,

$$\phi_{B,y,z,\phi_x} = \phi_L - \tan^{-1}\left(\frac{\tan\phi_L}{\cos\theta_x}\right). \tag{5.5.8}$$

$$\theta_{B,y,z,\phi_x} = \theta_L - \cos^{-1}\left(\frac{\cos\theta_L - \sin\theta_x\cos\phi_L\sin\theta_L}{\sqrt{1 - \sin(2\theta_L)\sin\theta_x\cos\phi_L}}\right). \tag{5.5.9}$$

5.5.2.2 One Angle ϕ_x is Mis-Osriented, i.e. $\theta_x = 0$

Here by setting $\theta_x = 0$ in (5.5.6) and (5.5.7), the $\tilde{z}$-axis lies on the xOy plane,

$$\phi_{B,y,z,\theta_x} = \phi_L - \tan^{-1}\left(\tan\phi_x + \frac{\tan\phi_L}{\cos\phi_x}\right). \tag{5.5.10}$$

$$\theta_{B,y,z,\theta_x} = \theta_L - \cos^{-1}\left(\frac{\cos\theta_L}{\sqrt{1+\sin(2\phi_L)\sin^2\theta_L\sin\phi_x}}\right). \tag{5.5.11}$$

Note that (5.5.10) is similar to the case of a bi-axial first-order sensor analyzed in Chapter 4 since there is no elevation mis-orientation.

5.6 Beamformer's Pointing Error – If the z-Axis is the Reference-Axis

If the z-axis is taken as the reference axis, then we set $\xi = z$, and then $\xi_1' = x$, and $\xi_2' = y$. Thus expanding (5.3.4),

$$\mathbf{u}_z = \frac{\begin{bmatrix} \cos\phi_x\cos\theta_x\cos\phi_L\sin\theta_L - \sin\phi_y\cos\theta_y\sin\phi_L\sin\theta_L \\ \cos\phi_y\cos\theta_y\sin\phi_L\sin\theta_L + \sin\phi_x\cos\theta_x\cos\phi_L\sin\theta_L \\ \cos\theta_L - \cos\phi_L\sin\theta_x\sin\theta_L + \sin\theta_y\sin\phi_L\sin\theta_L \end{bmatrix}}{\sqrt{\begin{array}{r} 1-\sin(2\phi_L)\sin^2\theta_L[\sin\theta_x\sin\theta_y+\cos\theta_x\cos\theta_y\sin(\phi_y-\phi_x)]+ \\ \sin(2\theta_L)(\sin\theta_y\sin\phi_L-\sin\theta_x\cos\phi_L) \end{array}}}. \tag{5.6.1}$$

Defining the denominator of (5.6.1) as

$$\gamma_z := \sqrt{\begin{array}{r} 1-\sin(2\phi_L)\sin^2\theta_L[\sin\theta_x\sin\theta_y+\cos\theta_x\cos\theta_y\sin(\phi_y-\phi_x)]+ \\ \sin(2\theta_L)(\sin\theta_y\sin\phi_L-\sin\theta_x\cos\phi_L) \end{array}} \tag{5.6.2}$$

then

$$\mathbf{u}_z = \frac{1}{\gamma_z}\begin{bmatrix} \cos\phi_x\cos\theta_x\cos\phi_L\sin\theta_L - \sin\phi_y\cos\theta_y\sin\phi_L\sin\theta_L \\ \cos\phi_y\cos\theta_y\sin\phi_L\sin\theta_L + \sin\phi_x\cos\theta_x\cos\phi_L\sin\theta_L \\ \cos\theta_L - \cos\phi_L\sin\theta_x\sin\theta_L + \sin\theta_y\sin\phi_L\sin\theta_L \end{bmatrix}. \tag{5.6.3}$$

From (5.3.9), (5.3.10), and (5.6.3), $\phi_{B,z}$ and $\theta_{B,z}$ are explicitly expressed as

$$\phi_{B,z} = \phi_L - \tan^{-1}\left(\frac{\cos\phi_y\cos\theta_y\sin\phi_L\sin\theta_L + \sin\phi_x\cos\theta_x\cos\phi_L\sin\theta_L}{\cos\phi_x\cos\theta_x\cos\phi_L\sin\theta_L - \sin\phi_y\cos\theta_y\sin\phi_L\sin\theta_L}\right), \tag{5.6.4}$$

$$\theta_{B,z} = \theta_L - \cos^{-1}\left(\frac{\cos\theta_L - \cos\phi_L\sin\theta_x\sin\theta_L + \sin\theta_y\sin\phi_L\sin\theta_L}{\gamma_z}\right). \tag{5.6.5}$$

5.6.1 A Special Case of $\phi_x = \phi_y$ and $\theta_x = \theta_y = 0$

This leads to a perfectly orthogonal tri-axial sensor. This is so because $\phi_x = \phi_y$ with $\theta_x = \theta_y = 0$ means equal azimuthal mis-orientation in the same direction, hence the orthogonality between the x-axis and the y-axis is retained, i.e. $\tilde{x}$-axis is orthogonal with $\tilde{y}$-axis. Therefore, substituting $\phi_y = \phi_x$ and $\theta_y = \theta_y = 0$ in (5.6.4), and (5.6.5)

$$\phi_{B,z} \quad = \quad -\phi_x \quad = \quad -\phi_y, \tag{5.6.6}$$

and

$$\theta_{B,z} \quad = \quad 0, \tag{5.6.7}$$

respectively. This implies there is no elevation angle error while azimuthal error is the value of the rotation along the azimuth.

The special case of only y-axis is mis-oriented i.e. $\phi_x = \theta_x = 0$ been derived in Section 5.4.2. The degenerate case of one-angle θ_y mis-oriented, i.e. $\phi_y = 0$ has been derived in Section 5.4.2.1. The degenerate case of one-angle ϕ_y mis-oriented, i.e. $\theta_y = 0$ has been derived in Section 5.4.2.2.

The special case of only x-axis is mis-oriented i.e. $\phi_y = \theta_y = 0$ has been derived in Section 5.5.2. For degenerate cases of one-angle mis-orientation: $\theta_x \neq 0$ (but $\phi_x = 0$) has been in Section 5.5.2.1, while $\phi_x \neq 0$ (but $\theta_x = 0$) has been derived in Section 5.5.2.2.

5.7 Pointing Error for the Tri-Axial Figure-8 Sensors Collocated with a Pressure-Sensor

The "tri-axial velocity-sensor" is often used with a pressure-sensor, collocated with the triad. Such a quad system would have the following 4×1 array manifold for a source impinging from the far field: [22, 69, 72]

$$\mathbf{a}^{(3+1)}(\phi, \theta) \quad = \quad \begin{bmatrix} \cos\phi \sin\theta \\ \sin\phi \sin\theta \\ \cos\theta \\ \kappa \end{bmatrix}, \tag{5.7.1}$$

where $\kappa > 0$ represents the gain of the pressure-sensor relative to that of the "tri-axial velocity-sensor". The superscript $^{(3+1)}$ indicates the "3" triaxial velocity-sensors and "1" pressure-sensor. As the pressure-sensor and "tri-axial velocity-sensor" are implemented often with different transducer technologies, these channels' voltages need normalization. The value of κ depends on this normalization.

Now, consider the case of the three axes being non-orthogonal. The rotation matrix becomes 4×4:

$$\mathbf{R}_2(\phi_{\xi_1'}, \theta_{\xi_1'}, \phi_{\xi_2'}, \theta_{\xi_2'}) \;=\; \begin{bmatrix} \mathbf{R}_\xi & \mathbf{0}_{3\times 1} \\ \mathbf{0}_{3\times 1}^T & 1 \end{bmatrix}. \tag{5.7.2}$$

where $\mathbf{0}_{3\times 1}$ is a three-entries column vector of zeros, and $\mathbf{R}_\xi$ is as previously defined and described in Section 5.3.

The "spatial matched beamforming" weight vector, while mistakenly assuming axial orthogonality, equals

$$\mathbf{a}^{(3+1)}(\phi_L, \theta_L) \;=\; \begin{bmatrix} \cos\phi_L \sin\theta_L \\ \sin\phi_L \sin\theta_L \\ \cos\theta_L \\ \kappa \end{bmatrix}. \tag{5.7.3}$$

The beamformer output equals

$$\begin{aligned} &B^{(3+1)}(\phi, \theta, \phi_L, \theta_L, \phi_{\xi_1'}, \theta_{\xi_1'}, \phi_{\xi_2'}, \theta_{\xi_2'}) \\ &\quad := \frac{\mathbf{a}^{(3+1)}(\phi_L, \theta_L)^T \; \mathbf{R}_2(\phi_{\xi_1'}, \theta_{\xi_1'}, \phi_{\xi_2'}, \theta_{\xi_2'}) \; \mathbf{a}^{(3+1)}(\phi, \theta)}{\max\limits_{\phi,\theta} \left[\mathbf{a}^{(3+1)}(\phi_L, \theta_L)^T \; \mathbf{R}_2(\phi_{\xi_1'}, \theta_{\xi_1'}, \phi_{\xi_2'}, \theta_{\xi_2'}) \; \mathbf{a}^{(3+1)}(\phi, \theta)\right]}. \end{aligned} \tag{5.7.4}$$

The denominator and numerator of the above are rewritten in such a way that the portion of the expressions from the triaxial velocity sensors and the pressure sensor are separated. Therefore,

$$\begin{aligned} &B^{(3+1)}(\phi, \theta, \phi_L, \theta_L, \phi_{\xi_1'}, \theta_{\xi_1'}, \phi_{\xi_2'}, \theta_{\xi_2'}) \\ &\quad = \frac{\kappa^2 + \mathbf{a}^{(3+0)}(\phi_L, \theta_L)^T \; \mathbf{R}(\phi_{\xi_1'}, \theta_{\xi_1'}, \phi_{\xi_2'}, \theta_{\xi_2'}) \; \mathbf{a}^{(3+0)}(\phi, \theta)}{\kappa^2 + \max\limits_{\phi,\theta} \left[\mathbf{a}^{(3+0)}(\phi_L, \theta_L)^T \; \mathbf{R}(\phi_{\xi_1'}, \theta_{\xi_1'}, \phi_{\xi_2'}, \theta_{\xi_2'}) \; \mathbf{a}^{(3+0)}(\phi, \theta)\right]}. \end{aligned} \tag{5.7.5}$$

Similar to the operation in Section 5.3, applying Cauchy-Schwarz inequality to the second term of the denominator of (5.7.5), the beampattern is expressed as

$$
\begin{aligned}
& B^{(3+1)}(\phi,\theta,\phi_L,\theta_L,\phi_{\xi_1'},\theta_{\xi_1'},\phi_{\xi_2'},\theta_{\xi_2'}) \\
&= \frac{\kappa^2 + \left[\mathbf{a}^{(3+0)}(\phi_L,\theta_L)\right]^T \ \mathbf{R}(\phi_{\xi_1'},\theta_{\xi_1'},\phi_{\xi_2'},\theta_{\xi_2'})\ \mathbf{a}^{(3+0)}(\phi,\theta)}{\kappa^2 + \underbrace{\left\|\mathbf{R}(\phi_x,\theta_x,\phi_z,\theta_z)^T\ \mathbf{a}^{(3+0)}(\phi_L,\theta_L)\right\|}_{\gamma_\xi}}, \\
&= \frac{\kappa^2 + \left[\mathbf{a}^{(3+0)}(\phi_L,\theta_L)\right]^T \ \mathbf{R}(\phi_{\xi_1'},\theta_{\xi_1'},\phi_{\xi_2'},\theta_{\xi_2'})\ \mathbf{a}^{(3+0)}(\phi,\theta)}{\kappa^2 + \gamma_\xi}, \\
&= \frac{\kappa^2 + \gamma_\xi \dfrac{\left[\mathbf{a}^{(3+0)}(\phi_L,\theta_L)\right]^T \ \mathbf{R}(\phi_{\xi_1'},\theta_{\xi_1'},\phi_{\xi_2'},\theta_{\xi_2'})}{\gamma_\xi}\ \mathbf{a}^{(3+0)}(\phi,\theta)}{\kappa^2 + \gamma_\xi}.
\end{aligned}
$$

Replace the fraction in the numerator with $\mathbf{u}$ (which has already been defined in (5.3.3)). Then,

$$
\begin{aligned}
& B^{(3+1)}(\phi,\theta,\phi_L,\theta_L,\phi_{B,\xi},\theta_{B,\xi}) \\
&= \frac{\kappa^2 + \gamma_\xi\ \mathbf{u}_\xi^T\ \mathbf{a}^{(3+0)}(\phi,\theta)}{\kappa^2+\gamma_\xi}, \\
&= \frac{\kappa^2 + \gamma_\xi\ \left[\mathbf{a}^{(3+0)}(\phi_L-\phi_{B,\xi},\theta_L-\theta_{B,\xi})\right]^T \mathbf{a}^{(3+0)}(\phi,\theta)}{\kappa^2+\gamma_\xi}, \\
&= \frac{\kappa^2}{\kappa^2+\gamma_\xi} + \frac{\gamma_\xi}{\kappa^2+\gamma_\xi}\left[\mathbf{a}^{(3+0)}(\phi_L-\phi_{B,\xi},\theta_L-\theta_{B,\xi})\right]^T \mathbf{a}^{(3+0)}(\phi,\theta), \\
&= \frac{\kappa^2}{\kappa^2+\gamma_\xi} + \frac{\gamma_\xi}{\kappa^2+\gamma_\xi} B^{(3+0)}(\phi,\theta,\phi_L,\theta_L,\phi_{B,\xi},\theta_{B,\xi}),
\end{aligned}
\tag{5.7.6}
$$

where $\phi_{B,\xi}$ and $\theta_{B,\xi}$ are previously defined in (5.3.9) and (5.3.10), respectively. These γ_ξ, $\phi_{B,\xi}$ and $\theta_{B,\xi}$ are all *in*dependent of the direction-of-arrival (ϕ,θ).

If κ equals zero, $B^{(3+1)}(\phi,\theta,\phi_L,\theta_L,\phi_{B,\xi},\theta_{B,\xi})$ above becomes the earlier (5.3.6) in Section 5.3. Incidentally, $B^{(3+1)}(\phi,\theta,\phi_L,\theta_L,\phi_{B,\xi},\theta_{B,\xi})$ maximizes to 1 and minimizes to $\dfrac{\kappa^2-\gamma_\xi}{\kappa^2+\gamma_\xi}$, because maximum of $B^{(3+0)}(\phi,\theta,\phi_L,\theta_L,\phi_{B,\xi},\theta_{B,\xi})$ is equal to one and its minimum equals to -1.

Equation (5.7.6) implies that the beam-patterns, with and without the pressure-sensor, differ only by a scaling factor of $\dfrac{\gamma}{\kappa^2+\gamma_\xi}$ and an offset of $\dfrac{\kappa^2}{\kappa^2+\gamma_\xi}$. This scaling factor and offset each depends on the tri-axial velocity-sensor's axial mis-orientations and on the beamformer's look direction, therefore the mis-orientation changes the shape of the beampattern while mis-pointing the lobe. However, this scaling factor and this offset do not affect the beam-patterns' pointing error, with or without the pressure-sensor. This invariance may be intuitively expected, as the pressure-sensor itself is isotropic, with no directivity.

5.8 Summary

This work has analyzed the beampattern of collocated triaxial velocity sensors whose legs are not orthogonal and its spatial-matched-filter is unaware of the non-perpendicularity. The non-perpendicularity does not affect the effective shape of the beampattern but only offsets it lobe by an amount that is dependent on the degree of mis-orientations of the axes. This effect is not the case when the triaxial velocity sensor is collocated with a pressure sensor as the shape of the beampattern changes depending on the degree of mis-orientation.

Closed-form expressions have been derived for the pointing biases which are useful for offsetting pointing bias in non-perpendicular vector sensor.

Chapter 6
Conclusion

This thesis has presented four studies:

1. A Triad of Cardioid Sensors in Orthogonal Orientation and Spatial Collocation – Its Spatial-Matched-Filter-Type Beam-Pattern

2. Cardioid Microphones/Hydrophones in a Collocated and Orthogonal Triad – A New Beamformer with No Beam-Pointing Error

3. Two Higher-Order Figure-8 Sensors in Spatial Collocation — Their "Spatial Matched Filter" Beam-Pattern

4. Directional Pointing Error in "Spatial Matched Filter" Beamforming at a Tri-Axial Velocity-Sensor due to Non-Orthogonal Axes

The first two studies in Chapters 2 - 3 are based on the first-order cardioid family of microphones while the last two studies presented in Chapters 4 - 5 are based on the first-order and higher-order figure-8 microphones.

Chapter 2 proposes the collocation of first-order cardioid family of microphones that are placed in orthogonal orientation. This spatial arrangement produces an array manifold that is independent on the incident sound wavelength. The spatial-matched-filter type beampattern of this array is analytically studied in terms of the location of the mainlobe, the presence of a sidelobe, the mainlobe-to-sidelobe height ratio, half-power beamwidth and the overall array gain. This work is the first in the open literature to propose and analytically study such array of first-order cardioid family of microphones. The findings show that the proposed cardioid triad can have higher mainlobe-to-sidelobe height ratio and can avoid sidelobes altogether. Its physical compactness makes it portable for mobile deployment, indoor or outdoor.

Chapter 3 proposes a new beamformer to cancel the pointing bias in the spatial-matched-filter beampattern of the cardioid triad proposed in Chapter 2. The performance of this beamformer in terms of the location of its mainlobe and sidelobes, height ratio, beamwidth, directivity and overall array gain is compared to that of the spatial-matched-filter studied in Chapter 2. This new beamformer gave close performance to the spatial-matched-filter type beamformer studied in Chapter 2 while offering a bias-free beam pointing.

Chapter 4 proposes the spatial collocation of two higher-order figure-8 sensors. The sensors in the array may not be perfectly perpendicular due to manufacturing defects. In this work, such arrangement is studied in terms of the pointing bias in the spatial-matched-filter beampattern. It was found that higher-order collocated pair of figure-8 sensors will point in discrete direction whether perpendicular or non-perpendicular. More importantly, this study relates the look direction, array's skewed angle and sensor order to the mis-pointing of the array's beampattern. This study also pioneered a way of mathematically relating the array manifold of the collocated higher-order figure-8 dyad to that of the collocated first-order figure-8 dyad. This paved way for critical study of this array configuration.

Lastly, Chapter 5 analytically studies the effect of non-orthogonality in collocated first order figure-8 sensors assuming the spatial-matched-filter beamformer is unaware of this non-orthogonality between the legs of the triad. This non-orthogonality can be as a result of imperfection in manufacturing or wear during used, for instance in towed arrays. The study is extended to the a tri-axial figure-8 sensor with a collocated pressure sensor. Closed form pointing biases due to the mis-orientation are derived in this work.

Future works can study how the non-orthogonality between the axes of the collocated and supposedly orthogonal Figure-8 sensors would affect signal detection and parameter estimation performances. This can be done for a case of a unit triad and can be extended to arrays of the triad. Further work can also develop a direction of arrival estimation algorithm based on the proposed cardioid triad - single unit or in phased array.

Appendices

Appendix A
To Show There Can Only be Two Peaks in the Beampattern (3.1.4)

A peak is a critical point in the beampattern with respect to (θ, ϕ). To obtain the number of such critical points that exists in the beampattern, consider the beam pattern defined in (3.1.4). Its critical point (u_c, v_c, w_c) satisfies $\underset{-1\leq u,v,w\leq 1}{\arg\max}\ B$

$$= \underset{-1\leq u,v,w\leq 1}{\arg\max}\ \alpha g_{\text{look}} + (1-\alpha)(\overbrace{u_{\text{look}}u + v_{\text{look}}v + w_{\text{look}}w}^{\tilde{B}:=}) \tag{A.0.1}$$

subject to $u^2 + v^2 + w^2 = 1$. The equality in (A.0.1) holds true because α, $u_{\text{look}}, v_{\text{look}}$, and w_{look} are preset constants in this optimization.

The Lagrangian is formulated as

$$\mathcal{L}(u, v, w, \lambda) \ := \ u_{\text{look}}u + v_{\text{look}}v + w_{\text{look}}w + \lambda(u^2 + v^2 + w^2 - 1), \tag{A.0.2}$$

of which

$$\tfrac{\partial}{\partial u}\mathcal{L}(u, v, w, \lambda) \ = \ u_{\text{look}} + 2\lambda u; \qquad \tfrac{\partial}{\partial v}\mathcal{L}(u, v, w, \lambda) \ = \ v_{\text{look}} + 2\lambda v,$$

$$\tfrac{\partial}{\partial w}\mathcal{L}(u, v, w, \lambda) \ = \ w_{\text{look}} + 2\lambda w; \quad \tfrac{\partial}{\partial \lambda}\mathcal{L}(u, v, w, \lambda) \ = \ u^2 + v^2 + w^2 - 1.$$

Setting the above partial derivatives to zero, the critical points of $\tilde{B}$ exist at $(u, v, w) = (u_c, v_c, w_c)$. From setting the first three partial derivatives to zero

$$(u_c, v_c, w_c) \ = \ -\frac{1}{2\lambda}(u_{\text{look}}, v_{\text{look}}, w_{\text{look}}). \tag{A.0.3}$$

Substituting u_c, v_c and w_c into $u_c^2 + v_c^2 + w_c^2 = 1$, one obtains

$$\frac{1}{2\lambda} \ = \ \pm 1. \tag{A.0.4}$$

Hence there exist exactly two critical points:

$$(u_{c_1}, v_{c_1}, w_{c_1}) \ = \ (u_{\text{look}}, v_{\text{look}}, w_{\text{look}}), \tag{A.0.5}$$

$$(u_{c_2}, v_{c_2}, w_{c_2}) \ = \ -(u_{\text{look}}, v_{\text{look}}, w_{\text{look}}). \tag{A.0.6}$$

Appendix B
Analytical Proof of Array Manifold's Trig Order Conversion

The validity of (4.3.1)-(4.3.3) is verified below: the unit vector in the direction of $\mathbf{a}_k(\phi)$

$$\hat{\mathbf{a}}_k(\phi) \quad := \quad \frac{1}{\beta_k(\phi)}\mathbf{a}_k(\phi), \tag{B.0.1}$$

where $\mathbf{a}_k(\phi) := \left[\cos^k(\phi),\ \sin^k(\phi)\right]^T$ (as defined in (4.1.2)), $\beta_k(\phi) := \|\mathbf{a}_k(\phi)\|_2 = \sqrt{\cos^{2k}(\phi) + \sin^{2k}(\phi)}$, $k \in \mathbb{Z}^+$ and $\phi \in [0, 2\pi)$.

The unit vector $\hat{\mathbf{a}}_k(\phi)$ can be transformed into a unit vector of phase-shifted first-order cosine and sine entries, while preserving the ratio of the entries in the transform pair. That is,

$$\hat{\mathbf{a}}_k(\phi) \quad = \quad \frac{1}{\beta(\phi)}\mathbf{a}_k(\phi) \quad = \quad \mathbf{a}(\xi_k(\phi)), \tag{B.0.2}$$

where

$$\mathbf{a}(\xi_k(\phi)) \quad := \quad \begin{bmatrix} \cos(\xi_k(\phi)) \\ \sin(\xi_k(\phi)) \end{bmatrix}. \tag{B.0.3}$$

Because the ratio of entries is preserved in the transformation of (B.0.2),

$$\frac{\left[\mathbf{a}_k^{(\beta)}(\phi)\right]_2}{\left[\mathbf{a}_k^{(\beta)}(\phi)\right]_1} \quad = \quad \frac{[\mathbf{a}(\phi)]_2}{[\mathbf{a}(\phi)]_1}, \quad \Longrightarrow \quad \tan^k(\phi) \quad = \quad \tan(\xi_k(\phi)). \tag{B.0.4}$$

From (B.0.2)

$$\begin{aligned} \frac{1}{\beta_k(\phi)}\mathbf{a}_k(\phi) \quad &= \quad \mathbf{a}(\xi_k(\phi)) \\ \mathbf{a}_k(\phi) \quad &= \quad \beta_k(\phi)\ \mathbf{a}(\xi_k(\phi)), \\ \mathbf{a}_k(\phi) \quad &= \quad \begin{bmatrix} \cos^k(\phi) \\ \sin^k(\phi) \end{bmatrix} \quad = \quad \beta_k(\phi) \begin{bmatrix} \cos(\xi_k(\phi)) \\ \sin(\xi_k(\phi)) \end{bmatrix}, \end{aligned} \tag{B.0.5}$$

where $\beta_k(\phi) := \sqrt{\cos^{2k}(\phi) + \sin^{2k}(\phi)}$ and $\xi_k(\phi) = \tan^{-1}(\sin^k(\phi)/\cos^k(\phi))$.

Appendix C
On the Magnitude Scaling $\beta_k(\phi)$

C.1 Lower Limit of $\beta_k(\phi)$ $\forall\phi$ for a Given k

To find the lower limit a $\beta_k(\phi)$ $\forall\phi$, the first-order derivative test is used to obtain the critical points of $\beta_k(\phi)$ w.r.t ϕ. The second-derivative test is then used to ascertain the nature of these critical points (i.e local max/min points).

For $k = 1, 2, 3, ...,$ $\sin^{2k}\phi + \cos^{2k}\phi > 0,\ \forall\phi$, therefore,

$$\arg\min_{\phi\in[0,360^\circ)} \beta_k(\phi) \equiv \arg\min_{\phi\in[0,360^\circ)} \beta_k^2(\phi) \tag{C.1.1}$$

Applying the first derivative test,

$$\frac{\partial\beta_k^2(\phi)}{\partial\phi} = 2k\sin\phi\cos\phi\left[\sin^{2k-2}(\phi) - \cos^{2k-2}(\phi)\right] \tag{C.1.2}$$

For $k = 1$, (C.1.2) is equal to zero which implies that $\beta_k(\phi)$ is constant with respect to ϕ for $k = 1$.

For $k \geq 2$, equating (C.1.2) to zero and solving for ϕ gives to two sets of critical points

$$\phi_{c1} = (2n+1)\frac{\pi}{4} \tag{C.1.3}$$

$$\phi_{c2} = n\frac{\pi}{2} \tag{C.1.4}$$

where $n = 0, 1, 2, 3$. That is $\phi_{c1} = \{45^\circ, 135^\circ, 225^\circ, 315^\circ\}$ and $\phi_{c2} = \{0^\circ, 90^\circ, 180^\circ, 270^\circ\}$.

According to the second derivative test

$$\begin{aligned}\frac{\partial^2\beta_k^2(\phi)}{\partial\phi^2} = 2k\Big[&(2k-1)\sin^2\phi\cos^2\phi\left(\sin^{2k-4}(\phi) + \cos^{2k-4}(\phi)\right) \\ &- \left(\sin^{2k}(\phi) + \cos^{2k}(\phi)\right)\Big].\end{aligned} \tag{C.1.5}$$

Substituting ϕ_{c1} (C.1.3) in (C.1.5)

$$\left.\frac{\partial^2\beta_k^2(\phi)}{\partial\phi^2}\right|_{\phi=\phi_{c1}} = \frac{8k(k-1)}{2^k} \implies\ > 0 \tag{C.1.6}$$

implies that ϕ_{c1} is a local minimum point.

Similarly, substituting ϕ_{c2} (C.1.4) in (C.1.5)

$$\left.\frac{\partial^2 \beta_k^2(\phi)}{\partial \phi^2}\right|_{\phi=\phi_{c1}} = -2k \implies < 0 \tag{C.1.7}$$

implies that ϕ_{c2} is a local maximum point.

Finally, the lower limit of $\beta_k(\phi)$ for $\phi \in [0, 2\pi)$ for a given k

$$\begin{aligned}\beta_k(\phi = \phi_{c1}) &= \sqrt{\sin^{2k}\left((2n+1)\frac{\pi}{4}\right) + \cos^{2k}\left((2n+1)\frac{\pi}{4}\right)} \\ &= \sqrt{2^{1-k}}.\end{aligned} \tag{C.1.8}$$

Therefore, the lower limit of $\beta_k(\phi)$ occurs at $\phi = \{45°, 135°, 225°, 315°\}$ and its value at these location equal to $\sqrt{2^{1-k}}$. When $k = 1$, (C.1.8) is equal to 1.

C.2 Analytical Proof that $\beta_k(\phi) \geq \beta_{k+1}(\phi)$, $\forall\phi$, $k \geq 1$

For all values of k, $2k$ is even integer, hence $\cos^{2k}(\phi) + \sin^{2k}(\phi) > 0, \forall\phi$. The square value of $\beta_k(\phi)$ thus exists without absolute magnitude. Hence, to show that $\beta_k(\phi) \geq \beta_{k+1}(\phi)$, is equivalent to showing that $\beta_k(\phi)^2 \geq \beta_{k+1}^2(\phi)$.

Therefore,

$$\begin{aligned}& \beta_k(\phi)^2 \geq \beta_{k+1}^2(\phi), \\ \Leftrightarrow\ & \beta_k(\phi)^2 - \beta_{k+1}^2(\phi) \geq 0.\end{aligned} \tag{C.2.1}$$

The left hand side of (C.2.1) is equivalent to

$$\begin{aligned}\beta_k(\phi)^2 - \beta_{k+1}^2(\phi) &= \cos^{2k}(\phi) + \sin^{2k}(\phi) - \cos^{2(k+1)}(\phi) - \sin^{2(k+1)}(\phi) \\ &= \cos^{2k}(\phi)\sin^2(\phi) + \sin^{2k}(\phi)\cos^2(\phi) \\ &= \sin^2(\phi)\cos^2(\phi)\left(\cos^{2k-2}(\phi) + \sin^{2k-2}(\phi)\right) \\ &= \frac{1}{4}\sin^2(2\phi)\ \beta_{k-1}^2(\phi).\end{aligned} \tag{C.2.2}$$

The first term of (C.2.2) $\sin^2(2\phi)$ is always greater than zero, likewise the second term of (C.2.2) $\beta_{k-1}^2(\phi)$, which implies that (C.2.2) is always greater than zero. Which in turn implies that $\beta_k(\phi)^2 \geq \beta_{k+1}^2(\phi)$, which also implies that $\beta_k(\phi) \geq \beta_{k+1}(\phi)$ for all k.

Appendix D
Analysis of How $\xi_k(\phi)$ Varies with the Figure-8 Sensor's Order k

D.1 For even values of k

For even $k = k_n = 2n$, the following analytically proves that $\xi_{k_{n+1}}(\phi) \geq \xi_{k_n}(\phi), \forall k_n = 2n, n = 1, 2, ...$ for $\phi \in \left[\frac{\pi}{4}, \frac{3\pi}{4},\right] \cup \left[\frac{5\pi}{4}, \frac{7\pi}{4},\right]$.

$$\begin{aligned} & \xi_{k_{n+1}}(\phi) \geq \xi_{k_n}(\phi) \\ \Leftrightarrow \quad & \xi_{k_{n+1}}(\phi) - \xi_{k_n}(\phi) \quad \geq \quad 0 \end{aligned} \tag{D.1.1}$$

The inequality (D.1.1) is equivalent to

$$\cos(2\phi) \quad \leq \quad 0 \tag{D.1.2}$$

$$\Leftrightarrow \quad \phi \quad \in \quad \left[\frac{\pi}{4}, \frac{3\pi}{4}\right], \quad \pi \text{ periodic.} \tag{D.1.3}$$

$\xi_{k_{n+1}}(\phi) \geq \xi_{k_n}(\phi)$.

For even $k = k_n = 2n$, the above proof also shows that $\xi_{k_{n+1}}(\phi) \leq \xi_{k_n}(\phi), \forall k_n = 2n, n = 1, 2, ...$ for $\phi \notin \left[\frac{\pi}{4}, \frac{3\pi}{4},\right] \cup \left[\frac{5\pi}{4}, \frac{7\pi}{4},\right]$.

D.2 For odd values of k

For odd $k = k_m = 2m + 1, \quad$ m = 1, 2, ..., the following analytically proves that $\xi_{k_{m+1}}(\phi) \geq \xi_{k_m}(\phi)$ for $\phi \in \left[\frac{\pi}{4}, \frac{\pi}{2}\right], \frac{\pi}{2}$periodic.

$$\begin{aligned} & \xi_{k_{2m+3}}(\phi) \geq \xi_{k_{2m+1}}(\phi) \\ \Leftrightarrow \quad & \xi_{k_{2m+3}}(\phi) - \xi_{k_{2m+1}}(\phi) \quad \geq \quad 0 \end{aligned} \tag{D.2.1}$$

The inequality (D.2.1) is equivalent to

$$\sin(4\phi) \quad \leq \quad 0 \tag{D.2.2}$$

$$\Leftrightarrow \quad \phi \quad \in \quad \left[\frac{\pi}{4}, \frac{\pi}{2}\right], \quad \frac{\pi}{2} \text{ periodic.} \tag{D.2.3}$$

$\xi_k(\phi) \in [0, 90°]$ for even values of k. Also for even k, $\chi_k(\phi_L, \tilde{\phi}) \in [-45°, 90°]$, this limits the resultant argument of the cosine function $\xi_k(\phi) - \chi_k(\phi) \in [-45°, 180°]$.

For odd values of k, $\xi_k(\phi) \in [0, 360°)$, and same for $\chi_k(\phi_L, \tilde{\phi}) \in [0, 360°)$

Bibliography

[1] J. M. Eargle, *"The Microphone Book ,"* 2 ed., Focal Press: Oxford, United Kingdom, 2005.

[2] Y. A. Huang and J. Benesty, *Audio Signal Processing for Next-Generation Multimedia Communication*, Kluwer Academic Publishers, Boston, 2004.

[3] J. M. Eargle, *"Handbook of Recording Engineering,"* 4 ed., Springer: New York, 2003.

[4] H. F. Olson, "Gradient microphones", *Journal of Acoustical Society of America,* vol. 17, no. 3, pp. 192-198, 1946.

[5] B. R. Beavers, and R. Brown, "Third order gradient microphone for speech reception," *Journal of Audio Engineering Society,* vol. 18, no. 6, pp. 636-640, December 1970.

[6] G. M. Sessler and J. E. West, "Second-order gradient unidirectional microphones utilizing an electret transducer," *Journal of Audio Engineering Society,* vol. 58, no. 1, pp. 273-278, Jul. 1975

[7] A. J. Brouns, "Second-order gradient noise-cancelling microphone," in *Proceeding of IEEE International Conference on Acoustic Speech Signal Processing*, 1981, pp. 786-789.

[8] G. S. Kang and D. A. Heide, "Acoustic noise reduction for speech communication (second-order gradient microphone)," in *Proceedings of IEEE International Symposium Circuits System,* vol. 4. Jul. 1999, pp. 556-559.

[9] Y. Song and K. T. Wong, "Closed-form direction finding using collocated but orthogonally oriented higher-order acoustic sensors," *IEEE Sensors Journal,* vol. 12, no. 8, pp. 2604-2608, August 2012.

[10] P. C. Hines, A. L. Rosenfeld, B. H. Maranda, and D. L. Hutt, "Evaluation of the endfire response of a superdirective line array in simulated ambient noise environments," in *Proceedings of IEEE Oceans Conference,* vol. 3. 2000, pp. 1489-1292.

[11] R. Aubauer and D. Leckschat, "Optimized second-order gradient microphone for hands-free speech recordings in cars," *Speech Communication,* vol. 34, no. 1-2, pp. 13-23, Apr. 2001.

[12] B. A. Cray, V. M. Evora, and A. H. Nuttall, “Highly directional acoustic receivers,” *Journal of Acoustical Society of America,* vol. 113, no. 3, pp. 1527-1533, March 2003.

[13] D. J. Schmidlin, “Directionality of generalized acoustic sensors of arbitrary order,” *Journal of Acoustical Society of America,* vol. 121, no. 6, pp. 3569-3578, June 2007.

[14] E. Jan, P. Svaizer, and J. L. Flanagan, “Matched-filter processing of microphone array for spatial volume selectivity”, *IEEE International Symposium on Circuits and Systems, 1995*, Seattle, April, 2015.

[15] J. Liu, K.-S Kim, and M. F. Insana, “SNR comparisons of beamforming strategies”, *IEEE Transaction on Ultrasonics, Ferroelectrics, and Frequency Control,* vol. 54, no. 5, pp. 1010-1017, May 2007.

[16] T. -C. Lin, K. T. Wong, M. O. Cordel, and J. P. Ilao, “Beamforming pointing error of a triaxial velocity sensor under gain uncertainties,” *Journal of Acoustical Society of America*, vol. 140, no. 3, pp. 1675-1685, September 2016.

[17] C. H. Lee, H. R. L. Lee, K. T. Wong, and M. Razo, “The spatial-matched-filter beam pattern of a biaxial non-orthogonal velocity sensor,” *Journal of Sound and Vibration,* vol. 367, pp. 250-255, April 2016.

[18] K. T. Wong and H. Chi, “Beam patterns of an underwater acoustic vector hydrophone located away from any reflecting boundary,” *IEEE Journal of Oceanic Engineering,* vol. 27, no. 3, pp. 628-637, July 2002.

[19] D. Laneuville and O. Cuilliére, “Non linear estimation in sonar tracking,” in proceeding of *1997 European Control Conference (ECC)*, Brussels, pp. 2150-2155, 1997.

[20] H. L. Van Trees, *Detection, Estimation, and Modulation Theory, Part IV, Optimum Array Processing* New York: Wiley, 2004.

[21] K. T. Wong, C. J. Nnonyelu and Y. I. Wu, “A Triad of Cardioid Sensors in Orthogonal Orientation and Spatial Collocation – Its Spatial-Matched-Filter-Type Beam-Pattern”, *IEEE Transaction of Signal Processing,* vol. 66, no. 4, pp. 895-906, February 2018.

[22] A. Nehorai and E. Paldi, “Acoustic vector-sensor array processing,” *IEEE Transactions on Signal Processing*, vol. 42, no. 10, pp. 2481-2491, September 1994.

[23] K. T. Wong and M. D. Zoltowski, “Closed-form underwater acoustic direction-finding with arbitrarily spaced vector-hydrophones at unknown locations,” *IEEE Journal of Oceanic Engineering*, vol. 22, no. 3, pp. 566-575, July 1997.

[24] G. L. D'Spain, W. S. Hodgkiss and G. L. Edmonds, "Energetics of the deep ocean's infrasonic sound field," *Journal of the Acoustical Society of America*, vol. 89, no. 3, pp. 1134-1158, March 1991.

[25] G. L. D'Spain, W. S. Hodgkiss and G. L. Edmonds, "The simultaneous measurement of infrasonic acoustic particle velocity and acoustic pressure in the ocean by freely drifting Swallow floats," *IEEE Journal of Oceanic Engineering*, vol. 16, no. 1, pp. 195-207, April 1991.

[26] J. C. Nickles, G. Edmonds, R. Harriss, F. Fisher, W. S. Hodgkiss, J. Giles and G. D'Spain, "A vertical array Of directional acoustic sensors," *IEEE Oceans Conference*, vol. 1, pp. 340-345, 1992.

[27] V. Mathew, V. G. Indichandy and S. K. Bhattacharyya, "A perforated-ball velocity meter for underwater kinematics measurement in waves and current," *International Symposium on Underwater Technology*, pp. 218-223, 2000.

[28] J. F. McEachern, J. A. McConnell, J. Jamieson and D. Trivett, "ARAP - deep ocean vector sensor research array," *IEEE Oceans Conference*, 2006.

[29] J. C. Shipps and K. Deng, "A miniature vector sensor for line array applications," *IEEE Oceans Conference*, vol. 5, pp. 2367-2370, 2003.

[30] H.-E. de Bree, W. F. Druyvesteyn, E. Berenschot and M. Elwenspoek, "Three-dimension sound intensity measurements using Microflown particle velocity sensors," *IEEE International Conference on Electro Mechanical Systems*, pp. 124-129, 1999.

[31] D. R. Yntema, W. F. Druyvesteyn and M. Elwenspoek, "A four particle velocity sensor device," *Journal of the Acoustical Society of America*, vol. 119, no. 2, pp. 943-951, February 2006.

[32] J. W. Parkins, S. D. Sommerfeldt and J. Tichy, "Error analysis of a practical energy density sensor," *Journal of Acoustical Society of America*, vol. 108, no. 1, pp. 211-222, July 2000.

[33] M. E. Lockwood and D. L. Jones, "Beamformer performance with acoustic vector sensors in air," *Journal of the Acoustical Society of America*, vol. 119, no. 1, pp. 608-619, January 2006.

[34] P. K. Tam and K. T. Wong, "Cramér-Rao bounds for direction finding by an acoustic vector-sensor under non-ideal gain-phase responses, Non-Collocation, or Non-Orthogonal Orientation," *IEEE Sensors Journal*, vol. 9, no. 8, pp. 969-982, August 2009.

[35] K. T. Wong, "Acoustic Vector-Sensor "Blind" beamforming and geolocation for FFH-sources," *IEEE Transactions on Aerospace and Electronic Systems*, vol. 46, no. 1, pp. 444-449, January 2010.

[36] Y. I. Wu and K. T. Wong, "Acoustic near-field source localization by two passive anchor nodes," *IEEE Transactions on Aerospace and Electronic Systems*, vol. 48, no. 1, pp. 159-169, January 2012.

[37] Y. I. Wu, K. T. Wong, S.-k. Lau, X. Yuan and S.-k. Tang, "A directionally tunable but frequency-invariant beamformer on an acoustic velocity-sensor triad to enhance speech perception," *Journal of the Acoustical Society of America*, vol. 131, no. 5, pp. 3891-3902, May 2012.

[38] R. P. Glover, "A Review of cardioid type unidirectional microphones," *Journal of the Acoustical Society of America*, vol. 11, no. 3, pp. 296-302, January 1940.

[39] H. F. Olson, *Acoustical Engineering*, New York, U.S.A.: D. Van Nostrand and Company, 1957.

[40] H. F. Olson, "The quest for directional microphones at RCA," *Journal of the Audio Engineering Society*, vol. 28, no. 11, pp. 776-786, November 1980.

[41] C. Faller and M. Kolundzija, "Design and limitations of non-coincidence correction filters for Soundfield Microphones," *Audio Engineering Society Convention 126*, 2009.

[42] W. Soede, A. J. Berkhou and F. A. Bilsen, "Development of a directional hearing instrument based on array technology," *Journal of Acoustical Society of America*, vol. 94, no. 2, part 1, pp. 785-798, August 1993.

[43] R. W. Stadler and W. M. Rabinowitz, "On the potential of fixed arrays for hearing aids," *Journal of Acoustical Society of America*, vol. 94, no. 3, part 1, pp. 1332-1342, September 1993.

[44] C. Liu and S. Sideman, "Simulation of fixed microphone arrays for directional hearing aids," *Journal of Acoustical Society of America*, vol. 100, no. 2, part 1, pp. 848-856, August 1996.

[45] J. Chen, L. Shue, K. Phua and H. Sun, "Theoretical comparisons of dual microphone systems," *IEEE International Conference on Acoustics, Speech, and Signal Processing*, vol. IV, pp. 73-76, 2004.

[46] G. Haralabus and A. Baldacci, "Unambiguous triplet array beamforming and calibration algorithms to facilitate an environmentally adaptive active sonar concept" *IEEE Oceans Conference*, 2006.

[47] L. del-Val, A. Izquierdo, J. J. Villacorta, M. I. Jimenez and M. Raboso, “Sidelobe evaluation of cardioid-patterned sensor array,” *European Microwave Conference*, pp. 1046-1049, 2008.

[48] D. Y. Levin, E. A. P. Habets and S. Gannot, “A generalized theorem on the average array directivity factor,” *IEEE Signal Processing Letters*, vol. 20, no. 9, pp. 877-880, September 2013.

[49] H. Gazzah, J.P. Delmas and S. M. Jesus, ”Direction-finding arrays of directional sensors for randomly located sources,” *IEEE Transactions on Aerospace and Electronic Systems*, vol. 52, no. 4, pp. 1995-2003, August 2016.

[50] B. A. Cray and A. H. Nuttall, “Directivity factors for linear arrays of velocity sensors,” *Journal of Acoustical Society of America*, vol. 110, no. 1, pp. 324-331, July 2001.

[51] B. A. Cray and A. H. Nuttall, “A Comparison of Vector-Sensing and Scalar-Sensing Linear Arrays,” *NUWC-NPT Technical Report 10,632*, Naval Undersea Warfare Center Division Newport, Rhode Island, U.S.A., January 1997.

[52] J. Benesty & J. Chen, *Study and Design of Differential Microphone Arrays*, vol 6, New York, U.S.A.: Springer, 2013.

[53] M. Brandstein & D. Ward, *Microphone Arrays: Signal Processing Techniques and Applications*, Berlin, Germany: Springer-Verlag, 2001.

[54] W. R. Woszczyk, “A microphone technique applying to the principle of second-order gradient unidirectionality,” *Journal of the Audio Engineering Society*, vol. 32, no. 7/8, pp. 507-530, August 1984.

[55] J. Groen, S. P. Beerens, R. Been, Y. Doisy and E. Noutary, “Adaptive portstarboard beamforming of triplet sonar arrays,” *IEEE Journal of Oceanic Engineering*, vol. 30, no. 2, pp. 348-359, April 2005.

[56] A. D. Polyanin and A. V. Manzhirov, *Handbook of Mathematics for Engineers and Scientists*, Chapman and Hall / CRC Press, 2006.

[57] B. D. Van Veen & K. M. Buckley, “Beamforming: a versatile approach to spatial filtering,” *IEEE Acoustics, Speech & Signal Processing Magazine*, vol. 5, no. 2, pp. 4-24, April 1988.

[58] K. J. Bastyr, G. C. Lauchle & J. A. McConnell, “Development of a velocity gradient underwater acoustic intensity sensor,” *Journal of the Acoustical Society of America*, vol. 106, no. 6, pp. 3178-3188, December 1999.

[59] J. A. McConnell, G. C. Lauchle & T. B. Gabrielson, "Two geophone underwater acoustic intensity probe", U.S. Patent, January 2001.

[60] R. Raangs, W. F. Druyvesteyn & H. E. de Bree, "A low cost intensity probe," *Audio Engineering Society Convention*, 2001.

[61] H. E. de Bree, T. Basten & D. Yntema, "A single broad banded 3D beamforming sound probe," *German Annual Conference on Acoustics*, 2008.

[62] H. E. de Bree & J. Wind, "A particle velocity gradient beam forming system," *U.S. National Noise Control Conference*, 2010.

[63] M. K. Awad & K. T. Wong, "Recursive least-squares source-tracking using one acoustic vector-sensor," *IEEE Transactions on Aerospace and Electronic Systems*, vol. 48, no. 4, pp. 3073-3083, October 2012.

[64] A. Y. Olenko and K. T. Wong, "Noise statistics of a higher order directional sensor, realized by computing finite differences spatially across multiple isotropic sensors," *IEEE Transactions on Aerospace and Electronic Systems*, vol. 49, no. 4, 2792-2798, October 2013.

[65] A. Y. Olenko and K. T. Wong, "Noise statistics across the three axes of a tri-axial velocity sensor constructed of pressure sensors," *IEEE Transactions on Aerospace and Electronic Systems*, vol. 51, no. 2, pp. 843-852, April 2015.

[66] Y. Song, K. T. Wong, and Y. Li, "Direction finding using a biaxial particle velocity sensor," *Journal of Sound and Vibration*, vol. 340, pp. 354-367, 2015.

[67] K. J. Bastyr, G. C. Lauchle & J. A. McConnell, "Development of a velocity gradient underwater acoustic intensity sensor," *Journal of the Acoustical Society of America*, vol. 106, no. 6, pp. 3178-3188, December 1999.

[68] H. E. de Bree, T. Basten & D. Yntema, "A single broad banded 3D beamforming sound probe," *German Annual Conference on Acoustics*, 2008.

[69] Y. I. Wu, K. T. Wong & S.-K. Lau, "The acoustic vector-sensor's near-field array-manifold," *IEEE Transactions on Signal Processing*, vol. 58, no. 7, pp. 3946-3951, July 2010.

[70] H. E. de Bree & J. Wind, "A particle velocity gradient beam forming system," *U.S. National Noise Control Conference*, 2010.

[71] M. K. Awad & K. T. Wong, "Recursive least-squares source-tracking using one acoustic vector-sensor," *IEEE Transactions on Aerospace and Electronic Systems*, vol. 48, no. 4, pp. 3073-3083, October 2012.

[72] Y. I. Wu, S.-K. Lau, and K. T. Wong, "Near-field/far-field array manifold of an acoustic vector-sensor near a reflecting boundary," *Journal of the Acoustical Society of America*, vol. 139, no. 6, pp. 3159-3176, June 2016.

[73] P. C. Hines, A. L. Rosenfeld, B. H. Maranda, and D. L. Hutt, "Evaluation of the endfire response of a superdirective line array in simulated ambient noise environments," in *OCEANS 2000 MTS/IEEE Conference and Exhibition*, Rhode Island, 2000, pp. 1489-1494.

[74] A. M. Wiggins, "Higher order pressure gradient microphone system having adjustable polar response pattern," U.S. patent 2,896,189, July 21, 1959.

[75] R. Miles, "High-order directional microphone diaphragm," U.S. patent 6,963,653, November 8, 2005.

[76] B. R. Beavers and R. Brown, "Third order gradient microphone for speech reception," in *38th Convention of the Audio Engineering Society,* Los Angeles, 1970, pp. 636-640.

[77] H. E. de Bree, "An overview of microflown technologies," *Acta acustica united with Acustica,* vol. 89, 163172, January 2003.

[78] H. F. Olson, "Electroacoustical signal translating apparatus," U.S. patent 2,301,744, May 31, 1941.

[79] A. M. Wiggins, "Second order differential microphone," U.S. patent 2,529,467, November 07, 1950.

[80] A. M. Wiggins, "Second order differential microphone," U.S. patent 2,552,878, May 15, 1951.

[81] M. M. Rosenfeld, "Pressure gradient transducers," U.S. patent 3,068,328, December 11, 1962.

[82] D. M. Warren and S. C. Thompson, "Microphone array having a second order directional pattern," U.S. patent application 2003/014283, July 31, 2003.

[83] S. A. Klinke, "Directional microphone arrangement and method for signal processing in a directional microphone arrangement," U.S. patent application 2003/0174852, September 18, 2003.